Self-consistent non-linear description of radio-frequency wave propagation and of the edge of a magnetized plasma

Jonathan Jacquot

Collegium Sciences et Technologies *École doctorale EMMA (n ° 409)*

THÈSE

pour l'obtention du titre de

DOCTEUR de l'UNIVERSITÉ DE LORRAINE

Spécialité : Physique

présentée par :

Jonathan JACQUOT

Description non-linéaire auto-cohérente de la propagation d'ondes radiofréquences et de la périphérie d'un plasma magnétisé

Thèse soutenue publiquement le 20 Novembre 2013 à Nancy devant le jury composé de:

Président du jury	
Dr. Pascal CHABERT	Directeur de recherche, Ecole Polytechnique, Palaiseau
Rapporteurs	
Dr. Steve WUKITCH	Directeur de Recherche, MIT/PSFC (USA)
Pr. Jean-Marie NOTERDAEME	Professeur des Universités, Université de Gent (Belgique)
Examinateurs	
Dr. Kristel CROMBE	Chercheur, Ecole Royale Militaire (Belgique)
Dr. Xavier LITAUDON	Représentant CEA, HDR, Chef du service SCCP IRFM, Cadarache
Directeur de thése	
Pr. Stéphane HEURAUX	Professeur des Universités, Université de Lorraine
Co-directeur de thése	
Dr. Laurent COLAS	Chercheur CEA, HDR, IRFM, Cadarache
Invités	
Pr. Bruno DESPRES	Professeur des Universités, Université Paris VI
Dr. Patrick JOLY	Directeur de recherche, INRIA, Palaiseau

Institut de Recherche sur la Fusion par confinement Magnétique
CEA Cadarache 13108 Saint-Paul-lez-Durance, France

Université de Lorraine - Pôle M4: matière, matériaux, métallurgie, mécanique

"Une personne qui n'a jamais commis d'erreurs n'a jamais tenté d'innover."
"A person who never made a mistake never tried anything new."

Albert Einstein, Theoretical Physicist (1879 - 1955).

Remerciements/Acknowledgments

Arrivé à la fin de cette thèse, il est de tradition de remercier les personnes, collègues, amis qui ont contribué à la réalisation de cette thèse par leur support, encouragement non seulement sur le plan scientifique mais aussi sur les plans humain, relationnel, psychologique. C'est avec une certaine émotion et fierté que j'écris cette dernière page de mon manuscrit (même si elle vient en premier) ainsi qu'avec une certaine nostalgie quand je pense au tout début de ma thèse en novembre 2010. Déjà 3 ans ont passé. Mais je sais que je continuerai de travailler avec certains.

Tout d'abord, je tiens à sincèrement remercier Alain Bécoulet et Xavier Litaudon de m'avoir accueilli à l'IRFM malgré ma candidature tardive. Ils étaient à l'époque chef et chef-adjoint du SCCP. Merci aussi à Roland Magne, mon chef de groupe, le GCHF. Ils ont depuis pris du galon. Les tâches et objectifs, qui m'avaient été confiées, ont été partiellement accomplis. Pour le reste, beaucoup plus ardu, d'autres tâches sont apparues en cours de route et une collaboration européenne (dont je fais partie dans le cadre de mon Post-Doc à l'IPP Garching) se met en place. Je tiens également à remercier le SCCP de la confiance accordée en proposant mon nom pour présenter au nom du service et de l'institut les activités autours des antennes ICRH lors de la conférence RF Topical 2013 à Sorrento. Ce papier invité englobait non seulement mon travail de modélisation mais également le travail en amont d'expérimentateurs. Cela m'a donné beaucoup de travail supplémentaire qui ont été valorisé dans ma thèse, dans un papier en cours de publication. De nombreuses répétitions ont aussi été nécessaires afin d'être prêt le jour J.

Je tiens aussi à remercier les secrétaires du SCCP, Valérie Icard, Stéphanie Villechavrolle qui a été remplacée plus tard par Nathalie Borio. Leur aide en de multiples occasions pour les démarches administrative et autres soucis en tout genre a été très appréciée. Un exemple qui me vient à l'esprit est parmi les derniers. Il concerne l'organisation des moyens de transport du jury pour ma soutenance de thèse à Nancy.

A ce propos, je souhaiterais exprimer ma gratitude à mes deux rapporteurs, Jean-Marie Noterdaeme et Steve Wukitch. Je vous remercie de m'avoir fait l'honneur d'avoir tout d'abord accepté cette indispensable et lourde tâche que représente la lecture d'un manuscrit de thèse et d'avoir ensuite évalué et jugé mon manuscrit de thèse. Merci pour l'intérêt que vous avez porté à ce manuscrit et pour le temps que vous y avez consacré. J'ai beaucoup apprécié vos commentaires. Je tiens aussi à remercier Jean-Marie de m'avoir accepté en Post-Doc dans son département à Garching afin de poursuivre mon travail dans la même thématique tout en me permettant de diversifier mes activités par une participation aux campagnes expérimentales sur ASDEX-Upgrade. Cette dernière partie a été impossible à réaliser à Cadarache du fait d'éléments planifiés (travaux sur la ligne 400kV) et imprévus (incident sur le transformateur 400kV). I would like to thank Steve Wukitch for coming all the way from Boston to Nancy for my PhD defence and then to a visit in Cadarache the next day. I hope the situation gets better at MIT for Alcator C-Mod and that you can stay in the field. I hope to see you at the next RF Topical Conference in the US.

Je voudrais également remercier les autres membres du jury. Je vais être amené à collaborer de manière assez proche avec Kritel dans le cadre d'Ishtar à Garching dont elle est project leader. J'ai beaucoup apprécié la présence et les questions de nos collègues mathématiciens, Bruno Després et Patrick Joly que j'ai perçu comme étant très intrigués par la physique des plasmas et des gaines RF. J'espère qu'ils ont mieux compris la nature de nos problèmes et que cette collaboration sur les aspects d'implémentation des conditions aux limites et de stabilité numérique et convergence pourra se réaliser dans un proche futur. Je tiens aussi à remercier Pascal Chabert d'avoir accepté l'invitation et de donner son avis d'expert en «plasma froids ». Je tiens également à le remercier d'avoir assumé au pied levé le rôle de président du jury qui aurait sinon été assumé par Xavier, selon mon opinion et d'après la composition du jury. Mais du fait des péripéties météorologiques (neige), l'avion du Xavier n'a pas vu passer Lyon. Il a donc été contraint de rebrousser chemin. Il a quand même pu assister à une rediffusion de ma soutenance lors de ma visite à Cadarache quelques semaines plus tard.

Pour terminer le tour du jury, je tiens à exprimer ma plus grande gratitude et mes plus sincères remerciements à mon directeur de thèse, Stéphane Heuraux (ou $€ pour les intimes) et mon co-directeur de thèse Laurent Colas. Laurent m'a suivi au quotidien. Son bureau du 513 était juste à côté du mien. Il a maintenant déménagé au 508 pour rejoindre le reste du GCHF. Nous avons eu de très nombreux après-midi (et matinées) de discussions sur la théorie, sur l'implémentation dans Comsol, sur la philosophie du code, sur les résultats et leur interprétation physique. Son encadrement a été très réussi. Il a su faire preuve d'une grande pédagogie afin de m'expliquer les choses que je ne comprenais pas. J'ai pu ensuite au fil de temps prendre plus d'initiatives. Je suis amené à continuer notre collaboration (avec un éloignement géographique) durant mon Post-Doc. Les discussions téléphoniques avec Stéphane ainsi que mes quelques visites (occasions de rentrer dans ma région natale) m'ont beaucoup aidé. Je le remercie beaucoup d'avoir fait l'interface avec l'Université de Lorraine et l'école doctorale du fait de l'éloignement géographique. Je le remercie aussi pour l'UE de physique stellaire en licence qui fut pour moi le cours le plus intéressant que j'ai suivi durant ma licence de physique aussi bien par le contenu que par l'évaluation par un travail personnel sur un sujet au choix. J'avais choisi l'évaluation de la datation du rayonnement cosmologique avec un modèle newtonien. Cela demandait des notions de cosmologie, de thermodynamique, de mécanique quantique.

Je remercie également les Professeurs Michel Fabry et Gérard Bonhomme de m'avoir convaincu de proposer ma candidature au master Erasmus Mundus Fusion Engineering Physics lors d'une porte ouverte. Je remercie de plus Gérard Bonhomme de s'être occupé de toutes les démarches administratives concernant les bourses Erasmus-Socrates puisque à l'époque les étudiants européens du master n'étaient pas financés par le master. De plus, le choix définitif de Madrid pour le troisième semestre s'était fait après la limite de dépôt des dossiers. Nous avons malgré tout pu obtenir ces bourses. J'en profite également pour saluer mes 3 autres comparses français et lorrains de la promotion 2010 : Guillaume Bousselin, Jordan Cavalier et Grégoire Hornung qui ont aussi terminé leur thèse. Je remercie également tous les enseignants du master pour la qualité de leurs cours.

Mes plus sincère remerciements à Marc Goniche qui a choisi de me suivre d'assez près à Cadarache afin de me donner quelqu'un d'autre à qui parler de mes travaux. Sa spécialité est plutôt les ondes dans le domaine hybride, mais il a su me donner des remarques pertinentes et me faire bénéficier de toute son expérience.

Mes résultats de simulations numériques n'auraient pas grande valeurs dans le travail en amont des expérimentateurs : Martin Kubič, Yann Corre, Jamie Gunn, Frédéric Clairet, Gilles Lombard, Arnaud Argouarch et les autres. Je les remercie pour la qualité de leurs

mesures même si je leur demande en conclusion de mon manuscrit à l'avenir de repousser encore les limites.

Un grand merci à Daniele Milanesio et Riccardo Maggiora pour leur collaboration afin d'interfacer SSWICH avec TOPICA. J'ai beaucoup apprécié travailler principalement avec Daniele.

Je tiens également à remercier les utilisateurs de Comsol à l'IRFM : Julien Hillairet, Mélanie Preynas et Laurent. Nous avons partagé les mêmes galères avec le logiciel afin de lui faire accomplir ce que l'on désirait avec beaucoup de souffrances. Comsol peut simplifier la vie en épargnant le lourd développement numérique mais n'est «plug and play ».

Je remercie également mes camarades du bureau 123 au bâtiment 513 : Feng Liu et Mervat Madi. J'ai beaucoup apprécié nos discussions sur la chine en anglais puis en français en Feng. La même chose s'est produite avec Mervat pour le Liban. J'ai également pu enseigner Comsol à Mervat. Je la remercie de m'avoir donné l'opportunité «d'enseigner»pendant ma thèse. Je suis désolé que les PMLs ne fonctionnent pas encore pour l'hybride. Un grand merci aussi à Walid Helou pour nos discussions sur les antennes.

Merci également à tous les membres du groupe GCHF que j'ai pu revoir récemment au cours du repas de groupe lors de ma visite en décembre. J'ai beaucoup aimé ces petits cadeaux sympathiques made in GCHF qui me sont très utiles ici à Garching.

Je remercie mes amis doctorants de l'IRFM qui ont soutenu comme moi (Grégoire, Didier, Stéphanie, Pierre, Farah, Timothée)... ou qui n'ont pas encore terminé (Thomas, François, Damien, Fabien, Hugo, Mervat, Claudia, Emely, Maxim, Dmitry, Billal, Walid, Alexandre, Jean-Baptiste, ...). Courage. Nos conversations souvent loufoques durant le déjeuner permettaient de se vider l'esprit et de décompresser durant quelques minutes durant la journée. Les parties de basketball étaient également un grand moment de détente. Mais je dois dire que je ne regretterai pas le fait de me faire marcher sur les pieds, notamment par François. Vous allez beaucoup me manquer. P.S. : J'espère trouver quelques volontaires à Garching pour faire du basket.

Je remercie également au passage tous les enseignants que j'ai eu au cours de ma scolarité. Notamment Henri Marion, enseignant en technologie et sciences physiques au collège Saint-Laurent de La Bresse. Je lui avais posé pas mal de questions scientifiques à l'époque. J'ai également beaucoup apprécié l'invitation à parler aux élèves de $3^{\text{ème}}$ de leur possible futur, de leur choix d'orientation, de la recherche, de science et de la fusion en particulier. Je salue également mon ancienne directrice d'école primaire, à la retraite maintenant, Thérèse Gehin, que j'avais croisée avant le début de ma thèse. Elle m'avait dit : «J'ai toujours su depuis que tu es tout petit que tu passerais un doctorat et que tu ferais de la recherche».

Une page de remerciement ne serait pas complète sans les remerciements à la famille. Évidemment je remercie mes parents pour tout ce qu'ils ont fait pour moi, pour m'avoir aidé et soutenu tout au long de ma scolarité. Un grand merci aussi à mes deux sœurs, Aurélie et Mélanie, ainsi qu'à mon frère, Jérémy. Cela n'a pas toujours été facile de vous aider à distance par skype pour vos devoirs. Je tiens aussi à remercier mon grand-père qui m'a donné l'envie de voyager. Je remercie aussi la grande famille au sens large : oncles, tantes, cousins, cousines. Ils sont trop nombreux pour être énumérés. Certains ont pu venir à ma soutenance. Je les remercie d'avoir pris en charge l'organisation du pot de soutenance afin de me laisser me concentrer sur ladite soutenance.

Pour terminer, je tiens énormément à remercier Fanny de m'avoir soutenu moralement et pour ses encouragements ces derniers mois pendant que je rédigeais ce manuscrit (et la préparation de la conférence) avec l'échéance s'approchant de plus en plus. Les Doctoriales de l'Université de Lorraine, au cours desquelles je l'ai rencontrée, n'auront donc pas servi

à rien, en dehors du fait de l'occasion de voir la famille et de l'obligation de participer. L'année 2013 fut extrêmement chargée. J'ai beaucoup apprécié pouvoir me détendre en fin de journée en lui parlant.

Cette thèse de doctorat est à présent finie. Le bateau lève l'ancre et vogue vers de nouvelles aventures. Première escale à Garching. La suite..., l'avenir le dira aux grés des courants (politiques, économiques et scientifiques).

List of notations

This is a non-exhaustive list of the variables used in this thesis. Bold variables, like $\mathbf{B}$, indicate vector whereas double bar, like $\bar{\bar{\varepsilon}}$ indicates tensor quantities. Plain variables, like T, indicate scalar quantities. Extensive use of the subscript s will be made indicating that the quantity is specific to the species of type s. Extensive use of the symbols $\parallel$ and $\perp$ is made to denote respectively the direction along the static magnetic field $\mathbf{B}$ and the two others dimensions which are perpendicular to the magnetic field.

Latin notations:

Symbol	Name	Units
a	horizontal minor radius	m
$\mathbf{B}$	magnetic field	T)
B	magnetic field amplitude	T)
B_0	magnetic field amplitude on axis	T
B_p	poloidal magnetic field amplitude	T
B_t	toroidal magnetic field amplitude	T
$\mathbf{D}$	electric displacement	$\mathrm{C.m^{-2}}$
e_{strap}	distance between the center of two straps	m
$\mathbf{E}$	electric field	$\mathrm{V.m^{-1}}$
$\mathbf{E}_\parallel$	parallel electric field	$\mathrm{V.m^{-1}}$
f_0	launched wave frequency	Hz
h_{max_i}	maximum element size allowed in the i direction	m
$\mathbf{H}$	magnetic induction	$\mathrm{A.m^{-1}}$
I_p	plasma current	A
$\mathbf{j_{ant}}$	antenna current	A
$k_\perp$	vacuum wavenumber	$\mathrm{rad.m^{-1}}$
$k_\parallel$	parallel wavenumber	$\mathrm{rad.m^{-1}}$
$k_\perp$	perpendicular wavenumber	$\mathrm{rad.m^{-1}}$
$L_\perp$	radial size of the plasma	m
L_{strap}	height of the strap	m
L_{PML_i}	PML depth in the i direction	m
m_s	particle mass of species s	kg
n	density	$\mathrm{m^{-3}}$
$n_\parallel$	parallel refractive index	
$n_\perp$	perpendicular refractive index	
p_i	PML order in the i direction	
P_i	component of the Poynting vector in the i direction	$\mathrm{W.m^2}$
P_t	strap power transmitted to the plasma	W
q_s	electric charge of the species s	C

Symbol	Name	Units
$Q_{\parallel,e}$	ion heat fluxes	$\mathrm{MW.m^{-2}}$
$Q_{\parallel,i}$	electron heat fluxes	$\mathrm{MW.m^{-2}}$
$Q_{\parallel,tot}$	total parallel heat fluxes	$\mathrm{MW.m^{-2}}$
R	major radius	m
R_c	strap coupling resistance	$\Omega.\mathrm{m^{-1}}$
R_{strap}	position of the fast wave cutoff of the antenna on major radius axis	m
R_{strap}	position of the leading edge of the antenna on major radius axis	m
S_i	complex stretching function for the i direction	
$S_i^{'}$	real stretch of the stretching function is the i direction	
$S_i^{''}$	imaginary stretch of the stretching function is the i direction	
t_i	stretched coordinate in the i direction	
SWR	standing wave ratio	
T	plasma temperature	eV
T_i	ion temperature	eV
T_{IR}	surface temperature measured by the infrared camera	K
T_e	electron temperature	eV
T_s	temperature of the species s	eV
v_p	phase velocity of the wave	
V_{DC}	DC plasma potential	V
V_{float}	probe floating potential	V
V_{RF}	oscillating sheath voltage	V
V_{strap}	strap voltage	V
w_{strap}	width of the strap	m
Z_s	atomic number of the species s	
x	radial direction	m
y	poloidal direction	m
z	parallel direction to the magnetic field	m

Greek notations

Symbol	Name	Units
Γ	complex reflection coefficient	
δ	average local sheath width	m
$\bar{\bar{\varepsilon}}$	permittivity/dielectric/Stix tensor	
$\varepsilon_{\parallel}$	parallel component with respect to the static magnetic field of the dielectric tensor	
$\varepsilon_{\perp}$	perpendicular component with respect to the static magnetic field of the dielectric tensor	
$\bar{\bar{\varepsilon}}_{PML}$	dielectric tensor in the PML	
ε_X	off diagonal term in the dielectric tensor	
η	reflection coefficient amplitude	
η_{pred}	predicted reflection coefficient amplitude	
η_{sim}	reflection coefficient amplitude in the simulation	
λ_0	wavelength in vacuum	m
λ_{De}	Debye length	m
$\bar{\bar{\mu}}$	permeability tensor	
ρ_{ant}	antenna space charge	
ρ_s	Larmor radius of species s	m
$\bar{\bar{\sigma}}_{RF}$	oscillating conductivity tensor	
$\bar{\bar{\sigma}}_{DC}$	DC conductivity tensor	$\mathrm{S.m^{-1}}$
$\sigma_{\parallel}$	Spitzer parallel conductivity	$\mathrm{S.m^{-1}}$
$\sigma_{\perp}$	DC perpendicular conductivity	$\mathrm{S.m^{-1}}$
τ_E	energy confinement time	s
φ	phase between incident and reflected wave	rad
ω	wave pulsation	$\mathrm{rad.s^{-1}}$
ω_{ps}	plasma frequency of species s	$\mathrm{rad.s^{-1}}$
Ω_s	cyclotron frequency of species s	$\mathrm{rad.s^{-1}}$

List of Physical Constants

Constant Name	Symbol	=	Constant Value	Units (SI)
Speed of Light in vacuum	c	=	$2.997\ 924\ 58 \times 10^{8}$	$\mathrm{m.s^{-1}}$
Elementary charge	e	=	$1.602\ 176\ 46 \times 10^{-19}$	C
Boltzmann's constant	k_B	=	1.380650310^{-23}	$\mathrm{m^2.kg.s^{-2}.K^{-1}}$
Vacuum permittivity	ε_0	=	8.854187821010^{-12}	$\mathrm{m^{-3}.kg^{-1}.s^{4}.A^{2}}$
Vacuum permeability	μ_0	=	1.256637061010^{-6}	$\mathrm{m.kg.s^{-2}.A^{-2}}$

Glossary

APL: **A**ntenna **P**rotection **L**imiter
DC: **D**irect **C**urrent
ECRH: **E**lectron **C**yclotron **R**esonant **H**eating
HFS: **H**igh **F**ield **S**ide
FDTD: **F**inite **D**ifference **T**ime **D**omain
FEM: **F**inite Element **M**ethod
ICRH: **I**on **C**yclotron **R**esonant **H**eating
ITER: **I**nternational **T**hermonuclear **E**xperimental **R**eactor
FS: **F**araday **S**creen
ILP: **I**TER **L**ike **P**rototype
JET: **J**oint **E**uropean **T**okamak
LH: **L**ower **H**ybrid
LCFS: **L**ast **C**losed **F**lux **S**urface
LFS: **L**ow **F**ield **S**ide
LPT: **L**imiteur **Pompé** **T**oroidal, french acronym standing for **T**oroidal **P**umped **L**imiter (TPL)
LPA: **L**imiteur de **P**rotection d'**A**ntenne, french acronym standing for **A**ntenna **P**rotection **L**imiter (APL)
MHD: **M**agneto**h**ydro**d**ynamic
NBI: **N**eutral **B**eam **I**njection
PEC: **P**erfect **E**lectric **C**onductor
PMC: **P**erfect **M**agnetic **C**onductor
PFCs: **P**lasma **F**acing **C**omponents
PML: **P**erfectly **M**atched **L**ayer
RDL: **R**esonant **D**ouble **L**oop
RF: **R**adio-**F**requency
SBC: **S**heath **B**oundary **C**ondition
SOL: **S**crape **O**ff **L**ayer
SSWICH: **S**elf-consistent **S**heaths & **W**aves for **I**on **C**yclotron **H**eating
TE: **T**ransverse **E**lectric
TM: **T**ransverse **M**agnetic
TOPICA: **TO**rino **P**olytechnic **I**on **C**yclotron **A**ntenna
WEST: **W** **E**nvironment in **S**teady-state **T**okamak

Contents

Chapter 1

Introduction

1.1 Thermonuclear fusion

Our current civilization consumes every day large and increasing amount of energy coming from non-sustainable sources that are dangerous for the Earth environment and will wear off in the future [1]. Achieving sustainable energy is a monumental challenge that Mankind must pass. Thermonuclear fusion, the energy powering the stars, is one possible candidate to provide abundant, clean and sustainable energy if it can be harnessed for civil applications.

The energy released in the nuclear fusion reactions of nuclei with lower masses than iron comes from the difference in the nuclear binding energy ΔE. The masses of nuclei are actually always smaller than the sum of the nucleon masses constituting them. Einstein's energy-mass relation tells us that $\Delta E = \Delta m\, c^2$ ($\approx$ MeV, i.e. 6 orders of magnitude larger than the energy released in chemical reactions of burning fossil fuels).

Nuclear fusion reactions are governed by the strong nuclear force binding the protons and the neutrons in the nucleus and acting over a distance of the order of the nucleon radius. Above this distance the repulsive Coulomb force between the positively charged nuclei dominates. To approach a pair of nuclei close enough so that the fusion reaction can occur, the Coulomb repulsion between the fusing nuclei must be overcome with high kinetic energies.

From the possible nuclear fusion reactions, the deuterium-tritium (${}^2_1D - {}^3_1T$) reaction has by far the largest cross-section with the maximum at relatively low kinetic energies and temperature and is therefore the most promising candidate for future fusion reactors, as it is the easiest to achieve as a potential energy source [2]:

$$ {}^2_1D + {}^3_1T \rightarrow {}^4_2He(3.56\text{ MeV}) + {}^1_0n(14.03\text{ MeV}) \tag{1.1} $$

The distribution of $\Delta E \approx 17.6$ MeV of the reaction between the ${}^4He$ (α particle) and the neutron is inversely proportional to their masses $m_n/m_\alpha = E_\alpha/E_n$.

In order to maximize the cross-section of the D-T reaction, the optimal temperature range is $T_i \geq 20$ keV. At such high temperatures, matter exists in a state of ionized gas. In the case when it is quasi-neutral, it is called plasma [3]. Quasi-neutrality is given by the following expression:

$$ \sum_{k=1}^{N} Z_k \cdot n_k + n_e = 0, \tag{1.2} $$

where N is the number of ion species, n_k is the ion density of species k with electric charge Z_k and n_e is the electron density. Each species in the plasma is associated with a plasma

frequency:

$$\omega_{ps}^2 = \frac{q_s^2 n_s}{\epsilon_0 m_s}, \tag{1.3}$$

with ε_0 the permittivity of vacuum, n_s and q_s the density and electric charge of the species s (ions of species k + electrons) respectively. The quantity q_s is taken to be algebraic, so that for the electrons $q_s = -e$ and $q_s = Z_s e$ for the ions.

The level of performance of the plasma can be measured by introducing the enhancement factor Q [3] which corresponds to the ratio of the power released into the plasma by fusion reactions P_{fus} and the level of power injected into the plasma P_{inj} . The $Q = 1$ limit is called the break-even, it corresponds to the state where the plasma is sustained to equal parts by the fusion energy power and by the external power input, while the $Q = +\infty$ limit is called ignition where the plasma is self-sustained without any external means. The ignition condition [4] given by the Lawson criterion can be derived from a simple energy balance in the fusion reactor:

$$n\tau_E T \geq 3.10^{21} \text{ keVs}^{-1}. \tag{1.4}$$

In plasma physics, it is convenient to write temperatures in electronvolt (eV) that defines the amount of energy gained by a single electron moving across an electric potential difference of 1 V. The conversion between K and eV is done with the formula: $T\,(\text{eV}) = T\,(\text{K})\,k_B/e$ with k_B the Boltzmann constant and e the electric charge. Several possibilities can be considered in order to reach the Lawson criterion. With $T_i \geq 20$ keV, two parameters remain in the triple product. Two main directions can be explored on Earth to satisfy the Lawson criterion [5], as the huge gravitation force existing in the core of stars cannot be reproduced on Earth:

- *Inertial confinement* aims at obtaining very dense plasmas ($n \sim 10^{31}$ m^{-3}) for very short time ($\tau_E \sim 10^{-11}$ s). These conditions are reached with focused high energy lasers beams heating and compressing the fuel target consisting of a deuterium-tritium pellet. Large scale experiments exploring this option are the NIF in the US and the Laser Mégajoule in France.

- *Magnetic confinement* consists in using strong magnetic fields (several teslas) to generate a magnetic "bottle" confining the plasma [3]. The aim is thus to increase significantly the energy confinement time ($\tau_E \sim 1$ s) without any direct contact with the material of the bottle vessel (that would cool down the plasma) of a "low" density plasma ($n \sim 10^{20}$ m^{-3}).

1.2 Magnetic confinement fusion

1.2.1 Magnetic confinement

Charged particles in a magnetic field have helical trajectories around the magnetic field lines [5]. Movement along the field lines is free. The extent ρ_s of the helix perpendicular to the magnetic field line is called Larmor radius. Perpendicularly to the magnetic field of amplitude B, each particle s of mass m_s and charge q_s has a cyclotron motion at the pulsation:

$$\Omega_s = \frac{q_s B}{m_s}, \tag{1.5}$$

The cyclotron frequency Ω_s for a species s is one of the natural frequencies of a plasma. With a perpendicular velocity $v_\perp$ it gives for the Larmor radius:

$$\rho_s = \frac{v_\perp}{\Omega_s} = \frac{m_s v_\perp}{q_s B}. \tag{1.6}$$

As the Larmor radius is inversely proportional to the amplitude of the magnetic field, a stronger magnetic field will provide better confinement properties. In devices relying on magnetic confinement, the amplitude of the magnetic field is typically of several teslas (T), compared to Earth magnetic field amplitude of 3.1 10^{-5} T at the equator. In the following of this thesis, $\parallel$ index will denote the direction along the static magnetic field $\mathbf{B}$ while the $\perp$ index will denote the two others dimensions which are perpendicular to the magnetic field.

1.2.2 Short history

Several magnetic configurations (magnetic mirrors, stellerators) have been studied since the beginning of nuclear fusion research in the 1950's. The confinement properties also depend on the geometry of the magnetic field. Historically the first devices confining magnetically the plasma with open field lines were linear. However the important particle and energy losses at the extremities of the field lines are not compatible with the requirement on the energy confinement time for sustainable energy production. Avoiding these losses led to creating the simplest magnetic configuration in which the magnetic field lines are closed by closing the device on itself to form a torus. This is unfortunately not enough to achieve confinement since with a purely toroidal magnetic field particles still experience an outward drift due to the curvature and the gradient of the magnetic field. The solution is to add a poloidal component to the magnetic field to twist the field lines helically around the torus. The field lines thus wind up around nested magnetic surfaces, cancelling on average the outward drift of the particles: particles derive outward then inward along a field line. The particle orbits are thus periodic and confined inside the vessel.

Two main approaches exist to generate this poloidal magnetic field. In devices called stellarator [6], the poloidal magnetic field is produced externally by field coils placed around the torus. In devices called tokamaks, the poloidal magnetic field is produced indirectly through a toroidal electric current in the plasma. The tokamak concept [3], invented by Soviet physicists in the 1960's, is currently the most successful magnetic configuration. It has been besides widely promoted by many research institutes (a couple hundred of devices in the world) and has obtained the best results in terms of fusion power.

1.2.3 The tokamak magnetic configuration

A diagram of the tokamak concept [5] is shown in Figure 1.1. The toroidal magnetic field B_t is produced by toroidal field coils surrounding the torus. The poloidal magnetic field B_p in a tokamak is generated indirectly through the transformer effect. The resulting helical magnetic field $\mathbf{B}$ is thus the superposition of both components. In tokamaks the poloidal field is typically smaller by one order of magnitude than the toroidal field. The magnetic configuration is thus completely defined only in the presence of a plasma. This makes of tokamaks intrinsic pulsed devices since the transformer cannot be maintain continuously, unless additional methods produces non-inductive current drive. Poloidal field coils are added to the design for additional positioning and shaping of the plasma as well as for stability by active feedback.

The essential geometrical parameters in a tokamak are the aspect ratio $A = R/a$ where R is the major radius of the torus and a the horizontal minor radius. The ellipticity κ is the ratio of vertical minor radius b over the horizontal minor radius a. Vertically elongated plasmas offer better confinement properties, as well as high toroidal magnetic field B_t. The magnetic field B_t evolves as $1/R$ with the maximum at the inner side of the coil called high field side (HFS) and the minimum at the outer side of the coil called low field side (LFS). For stability, essential parameters are the plasma current I_p, β defined by the ratio of the plasma pressure over the magnetic pressure that measures the efficiency of the magnetic confinement and the safety factor q indicating how the field lines are twisted around the flux surfaces: $q = rB_t/RB_p$. It is connected to MHD stability.

As a tokamak is axisymmetric, all the toroidal cross sections are identical in the confined region (plasma core). Nested magnetic surfaces, where the magnetic field is everywhere tangent to the surfaces, can thus be represented by their cross section in the radial/poloidal plane, as shown in Figure 1.2. Some quantities have a constant value on magnetic surfaces only changing from surface to surface. Among them are the temperature T, the density n, the safety factor q and the current density J. Assuming a circular cross section ($b = a$), each magnetic surface is indexed by its minor radius r and each surface quantity is only function of r.

Control of the plasma-wall interaction [7] is crucial for the performance of the device, as it determines the damage of the plasma facing components (PFCs) that reduces the lifetime of the machine and its reliability and the plasma contamination by impurities inducing radiation which reduces the energy confinement time τ_E. The limit of the confined plasma is determined by the last closed flux surface (LCFS): the separatrix. The region beyond the separatrix, where magnetic field lines are open (i.e. connected to the wall), is called Scrape Off Layer (SOL). The two main existing configurations in tokamaks are shown on Figure 1.2. The first one is the limiter (left) that keeps away the plasma from the PFCs by a carefully designed piece of material. Consequently the interaction takes place at the

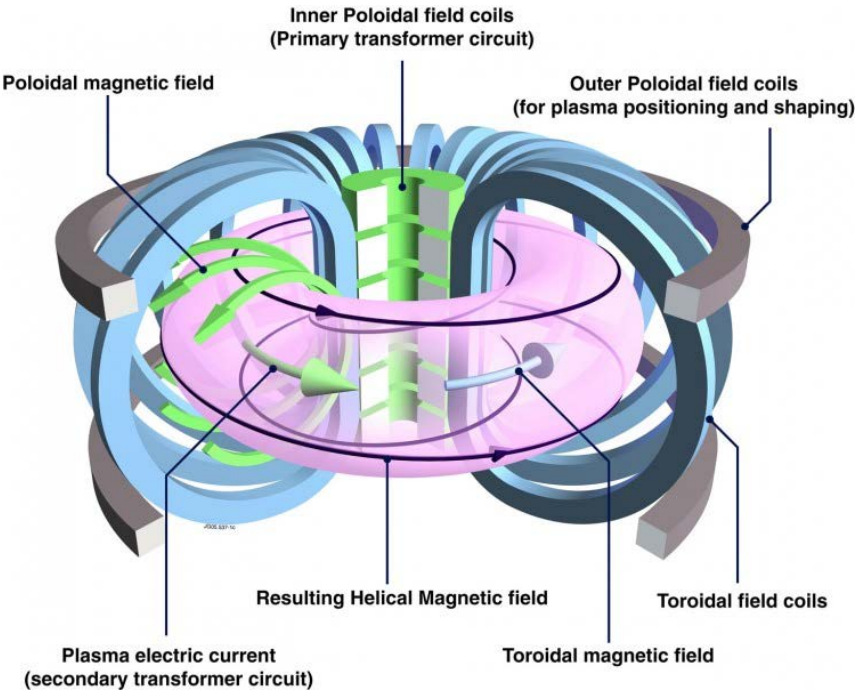

Figure 1.1: Schematic view of the tokamak concept.

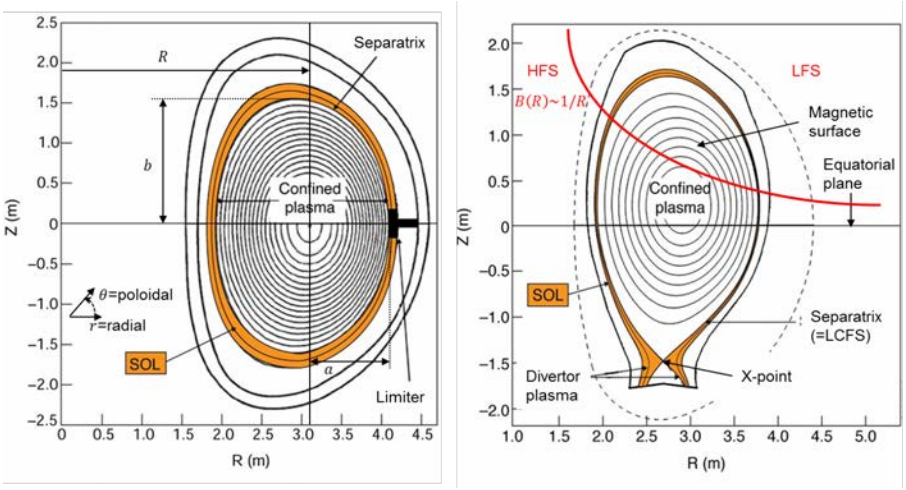

Figure 1.2: Magnetic configuration of the JET tokamak with a limiter (left) and with a divertor (right).

limiter. The second configuration is the divertor (right) that consists in modifying the magnetic field at the separatrix: an X-point is formed where the poloidal field is zero. It is more flexible since the position of the X-point can be moved in a controlled manner. The plasma-wall interaction occurs here far away from the confined plasma, providing better performances since fewer impurities can enter the core plasma to radiate.

1.3 Heating and current drive methods in a fusion plasma

In a future operating fusion reactor, part of the energy generated through nuclear fusion reactions (α particles) will serve to maintain the plasma temperature as fresh fuel is introduced. However, in the start-up phase of a reactor, the plasma still have to be heated by external means to its operating temperature (>10 keV). Furthermore, external heating presents a way to keep operational control over the burning plasma, thus keeping it in the sub-ignition state. Moreover in current magnetic fusion experiments, the fusion power is insufficient to maintain the burning plasma. Different methods to heat a plasma to fusion relevant conditions, shown on Figure 1.3, exist and will be presented in this section.

1.3.1 Ohmic heating

Since the plasma is an electrical conductor, it is possible to heat the plasma by inducing a current through it. In fact, the induced current to provide the poloidal magnetic field also heats through the Joule effect. The heating caused by the induced current is called ohmic (or resistive) heating. As the transformer effect is inherently a pulsed process due to the limit in magnetic flux (there are also other limitations on long pulses), tokamaks must therefore either operate for short periods or rely on other means of heating and non-inductive current drive by external means or by optimizing naturally occurring currents in the plasma (bootstrap current associated to pressure gradient). A steady state operation of a tokamak requires at least 20% of the plasma current provided non-inductively.

Furthermore the heat generated depends on the resistivity of the plasma η and the amount of electric current running through it. But as the temperature T of heated plasma rises, the resistivity decreases as $T^{-3/2}$ by the nature of Coulomb collisions and ohmic

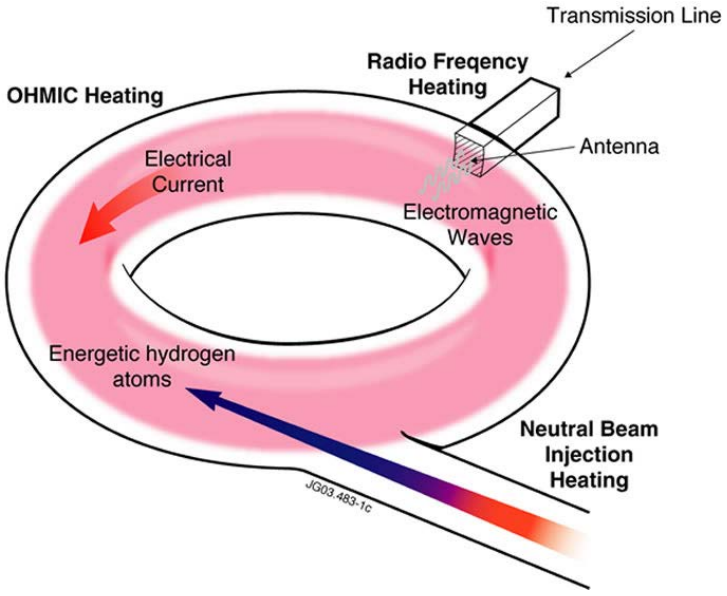

Figure 1.3: Diagram showing the existing ways to heat a fusion plasma in a tokamak.

heating becomes less effective. The parallel Spitzer conductivity is the inverse of the resistivity [3]:

$$\sigma_{\parallel,S} = \frac{(0.001T_e)^{3/2}}{1.65\ 10^{-9}\ln\Lambda}, \tag{1.7}$$

where T_e is in eV, $\ln\Lambda$ is the Coulomb logarithm whose typical values are between 15 and 20. It appears that the maximum plasma temperature attainable by ohmic heating in a tokamak is $3-4$ keV. Furthermore too important plasma current induces MHD instabilities. To obtain relevant fusion temperatures (>10 keV), additional heating methods must be used, that can also be used to drive non inductive current. The basics idea is to target in the plasma some populations of particles with additional heating. The energy is then distributed to the entire plasma through turbulent processes.

1.3.2 Neutral beams injection

All charged particles injected into a magnetic field have a helical motion, so they cannot penetrate deeply in the plasma excepted at very high energy. Thus it is better to use neutrals to deposit energy in the core plasma [8]. To generate energetic neutrals, the atoms or molecules are in the neutral beam injector first ionized, then accelerated to an energy of several hundred of keV, and after neutralized to become again neutrals before going, following a straight line, into the plasma. These fast atoms propagate through the plasma until they are ionized again by the charged particles of the plasma, and when they are stripped from their electron, they are trapped by the magnetic field and have time to deposit their energy into the plasma. By choosing to inject the neutral beam with an oblique angle, toroidal momentum parallel to the direction of injection can be produced, providing a way to obtain non inductive current drive: co-current or counter current according to the direction of the beam compared to the plasma current.

1.3.3 Radio-Frequency (RF) waves heating in general

Radio-frequency electromagnetic waves are generated by oscillators outside the torus. As hot plasmas are weakly collisional, RF wave damping has to rely on collisionless wave-particle mechanisms. If the waves have a frequency (and wavelength) corresponding to a natural frequency of the plasma and the correct polarization, energy or momentum can be transferred to the charged particles in the plasma. The wave energy is then distributed from the resonant particle population to the bulk plasma trough collisions. Assuming a plane wave with harmonic oscillations in $\exp(-i\omega t + i\mathbf{k}\cdot\mathbf{r})$, the resonance condition for the resonant particles population reads:

$$\omega - p\Omega_s - k_{\parallel} v_{\parallel_s} = 0, \tag{1.8}$$

where p is the cyclotron harmonic number, $k_{\parallel}$ the parallel component of the wave vector and $v_{\parallel_s}$ the component of the s particle velocity parallel to the static magnetic field.

Different frequency bandwidths with the typical magnetic fields of present tokamaks, shown in Figure 1.4, can be envisaged according to which resonant population is targeted. They carry the name Electron Cyclotron Resonance Heating (ECRH), Lower Hybrid (LH) and Ion Cyclotron Resonance Heating (ICRH) in the framework on fusion plasmas whereas they are more commonly known as VHF, SHF and EHF respectively. Each bandwidth will be briefly described.

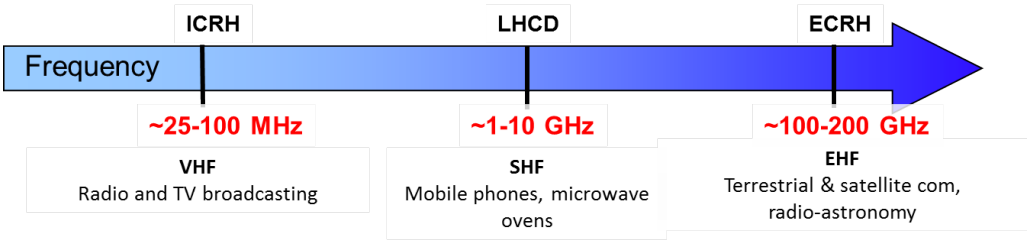

Figure 1.4: Diagram showing the bandwidths to heat and/or drive current in a tokamak.

1.3.4 Electron Cyclotron Resonance Heating (ECRH)

The concept of Electron Cyclotron Resonant Heating relies on one property of the movement of charged particle in magnetic fields. They have a cyclotron motion around field lines. By coupling to the plasma a wave whose frequency coincides with the cyclotron frequency of the electrons Ω_e, one can obtain a transfer of the wave electromagnetic energy to electrons kinetic energy. The corresponding frequency bandwidth is $100 - 200$ GHz. As B_t varies as $1/R$ in the tokamak cross section, the location of the power deposition due to cyclotron resonance can easily be controlled by tuning either the magnetic field or the wave frequency.

Two possible modes of propagation exist: the ordinary or O-mode and the extraordinary or X-mode. Due to the radial magnetic field gradient, accessibility conditions must be satisfied for the electron waves to propagate. Fundamental X-mode heating is only possible from the HFS. Second harmonic X-mode and fundamental O-mode have similar accessibility conditions from any direction. A review about electron cyclotron waves heating and current drive can be found in [9].

Moreover the wave can be tightly focused resulting in an absorption layer of only a few centimeters. With an oblique injection with respect to the perpendicular plane of the torus,

current drive can also be produced with efficiency close to lower hybrid. Experiments have also demonstrated that the ECRH method is useful for the plasma start-up, the control of MHD instabilities such as stabilizing the Neoclassical Tearing Mode [10, 11] or the sawtooth oscillation [12], which requires a very localized and peaked current density profile. Electron cyclotron waves can be launched in vacuum and propagate directly into the plasma without attenuation or interaction with the edge, before being locally absorbed in the resonance region. Reviews on ECRH and ECCD can be found in the following references [13, 14]

1.3.5 Lower Hybrid (LH)

Another frequency method in the gigahertz range is the Lower Hybrid Heating and Current Drive. The large parallel electric field carried by LH waves propagating along the magnetic field was shown to lead to strong electron Landau damping ($p = 0$ in (1.8)) and consequently to electron heating and non-inductive current drive (LHCD). The capability to also produce off-axis current allows the development of advanced tokamak scenarios by controlling the current profile to create internal transport barrier in the plasma in addition with the bootstrap current.

For the lower hybrid waves to have access to the plasma in this frequency range, the parallel refractive index $n_{\|}$ must satisfy an accessibility condition [15]. The LH waves are consequently evanescent at the plasma edge and efficient coupling of the waves requires the LH waves antenna at proximity to the plasma. Furthermore the current drive efficiency is inversely proportional to the square of $n_{\|}$ index: small $n_{\|}$ are favoured. To generate the required spectrum necessary to satisfy to the accessibility condition, antennas composed of multiple phased waveguides are used [15].

Moreover, the high current drive efficiency makes of Lower Hybrid Current Drive (LHCD) system a crucial actuator to save inductive flux and to generate additional plasma current in present day tokamak experiments [16]. Several superconducting tokamaks (Tore Supra, TRIAM-1M, HT-7, EAST) have demonstrated the feasibility of long pulse operation using LHCD. For example, a discharge on Tore Supra of 6 min was performed in 2003 at a plasma current of $I_p = 0.5$ MA, a magnetic field $B_t = 3.4$ T and 3 MW of LH power [16]. More recently higher LH power 5 MW have been coupled in combination with 3 MW of ICRH power during a 18 s pulse on Tore Supra. In ITER, steady-state operation with a mix of D-T fuel is foreseen to be with 100% of non-inductive current drive.

1.3.6 Typical parameters of a few tokamaks

The characteristics of the Tore Supra tokamak, the upgrade of Tore Supra defined as the WEST (**W** **E**nvironment in **S**teady-state **T**okamak) project and the ITER machine can be found in Table 1.1. Numbers in between brackets signify proposal for upgrade and as such not included in the baseline.

Tore Supra is considered as a large tokamak with a circular plasma cross-section (major radius $R = 2.4$ m and minor radius $a = 0.7$ m) whose last closed flux surface (LCFS) is defined by the intersection of the magnetic field lines with the bottom toroidal pumped limiter or with the outboard antenna protection limiter (APL). The maximal plasma current and toroidal magnetic field are $I_p < 1.5$ MA and $B = 3.8$ T, respectively. Its main features are the superconducting toroidal field coils and the actively cooled first wall and components, which make actually the Tore Supra tokamak an ideal machine for the study of long plasma discharges [17]. Tore Supra exclusively relies on RF heating systems, especially ICRH and can drive large amount of non-inductive current with LH.

The ITER tokamak, currently in construction, is designed to operate routinely at $Q = 10$ when operating with D-T fuel. When finished, it will be the largest tokamak ever built with a major radius $R = 6.2$ m and minor radius $a = 2.0$ m giving a plasma volume of 830 m^3. The predicted fusion power output is of the order of 500 MW well above the present record of 16 MW and $Q \approx 0.6$ with the JET tokamak, this level should be maintained for as long as 400 s. A commercial fusion reactor should operate around $Q = 40$ continuously. It will be massively equipped with all types of heating/current drive systems to dispose of large amount of power to be injected.

The WEST project [18] is a major upgrade of Tore Supra, scheduled to be completed in the end of 2015, proposing to transform it into a technological and physics testbed for ITER. In particular, the technologies behind the actively cooled tungsten divertor have never been tested in realistic conditions over long pulses with high heat fluxes in a full metallic environment. Since Tore Supra has superconducting coils and can be sustained through very long pulses with non-inductive current, it represents an excellent opportunity to test crucial technologies for ITER and thus minimize the risks and the future costs. For that, a divertor structure in W will be installed in Tore Supra. Furthermore three new ICRH antennas will be built [19]. The ICRH antennas are at the core of this thesis. Consequently ICRH waves are granted with more significance.

	Tore Supra	WEST	ITER
Major radius R (m)	2.5	2.5	6.2
Minor radius a (m)	0.7	0.5	2.0
Ellipticity κ	1	1.3-1.8	1.85
Plasma volume (m^3)	25	15	830
Plasma current I_p (MA)	1.5	0.5-0.8	15
Magnetic field amplitude B_t (T)	3.8	3.7	5.3
Configuration	circular toroidal pumped limiter	divertor	D shape divertor
Fuel mix	D-D	D-D	D-D/D-T
Pulse duration (s)	100	1000	400(3000)
ICRH power (MW)	12	9	20(40)
ECRH power (MW)	0.8	0.8	20(40)
LH power (MW)	7	7	0(40)
NBI power (MW)	0.5	0	33(50)
Fusion power P_{fus} (MW)	10^{-3}	10^{-3}	500
Amplification factor Q	«1	«1	>10

Table 1.1: Principle parameters for Tore Supra, WEST and ITER tokamaks.

1.4 Ion Cyclotron Resonance Heating (ICRH)

The main additional heating/current drive systems on tokamaks have been briefly presented above. The last auxiliary heating system to be presented is the one at the center of this thesis: Ion cyclotron Resonance Heating.

1.4.1 Principle

Heating at the ion cyclotron resonance is based on the same principles as electron cyclotron heating, except that electrons are replaced by ions to establish the wave-particles resonance. The frequency domain is between 25 MHz and 100 MHz. Since its also relies on cyclotron resonance, the power deposition is also localized and mainly on ions. By launching asymmetric $k_{\|}$ spectra, current drive can also be obtained.

ICRH proves to be very effective for heating the ions inside the plasma. Presently most large and medium size tokamaks use ICRH to couple large amount (several MW) of power to the plasma using different scenarios. A review of ICRH heating and current drive scenarios was made in Ref.[20]. One of the advantages is that the frequencies currently in operation are essentially the same necessary for future reactors. This limits the necessary technological development. The ICRH system on Tore Supra will be presented in Section 2.4.

ICRH mainly heat ions in the plasma, on the contrary to others systems that only heat ions indirectly by collisions with electrons during thermalization. ICRH antennas emit two kinds of waves: the fast magnetosonic wave (FW) useful for heating and the slow magnetosonic wave (SW) generated parasitically whose properties will be detailed in Chapter 2. Propagation of the fast wave is strongly perpendicular to the static magnetic field, with no accessibility issue to the plasma center.

1.4.2 Main ICRH wave absorption scenarios

There are a priori several possible heating scenarios with the fast magnetosonic ion wave. Some of them are presented here. It is useful to look at the wave absorption mechanisms in the plasma [21]. Although radio-frequency heating is similar to a microwave oven, the absorption mechanism is different. For a plasma the absorption at the resonance occurs by collisionless damping. The first scenario is absorption at the fundamental ion cyclotron resonance ($\omega = \Omega_i$ and $p = 1$ in (1.8)). This is the simplest mechanism. The perpendicular component of the polarized wave rotates in the same direction as the cyclotron motion of the ions around magnetic field lines. The wave is thus absorbed by the ions whose cyclotron motion is in resonance with the wave pulsation ($\omega = \Omega_i$). The ions are consequently accelerated in the perpendicular direction. It is can be shown that for a single ion species plasma the wave polarization around the resonance rotates exactly in the opposite direction of the gyration motion of the ions. This solution is therefore not a viable option for heating a plasma as the screening of the wave electric field on the ion gyro-motion prevents the transfer of power from the wave to the single ion species plasma.

The second possibility is harmonic absorption. This happens when the wave pulsation is a multiple of the ion cyclotron frequency ($\omega = p\Omega_i$, with p an integer). Let us take an example with $p = 2$. The ion is thus accelerated during half the cyclotron period and decelerated during the other half. If the wave electric field is homogeneous, there is no net transfer of energy between wave and ion. On the contrary, with an inhomogeneous electric field, the field will be larger one side of the revolution. There is thus a net transfer of energy. The efficiency of the transfer depends on the inhomogeneity of the electric field (linked to the plasma parameters) and on the Larmor radius of the ion (linked to the perpendicular velocity) [22]. The efficiency is also decreasing with increasing harmonic number.

The third possibility is minority heating. It consists in adding in the plasma a small quantity ($\approx 5\%$) of another species where the resonant species is largely in minority. The wave frequency is chosen to produce wave-resonance at the fundamental of the minority. The damping zone is localized at the ion-ion hybrid resonance located between the individ-

ual cyclotron resonance of the two species. With the minority ion population, it turns out that the wave polarization yields a component in the direction of the minority ions rotation. It is desirable for the minority species to have a higher cyclotron frequency than the majority species. In practice, hydrogen (^1_1H) or helium-3 (^3_2He) are chosen in deuterium plasma. The efficiency is independent of the temperature and weakly dependent on the density. The wave energy is then distributed to the majority ions through collisions [21].

1.5 ICRH challenges

ICRH is an effective method to transfer to the plasma large amount of power to the ions. There is however still some issues to be solved. The main challenges from the generator to the central plasma that the ICRH community still has to achieve to obtain a reliable high power steady state system are introduced here. Only some of them are among the objectives of this thesis work.

In the core plasma of a reactor, α particles created by nuclear fusion reactions could lead to parasitic absorption of ICRH power, increasing the losses and decreasing heating efficiency [23].

As it will be further explained in Section 2.2.1, an ICRH antenna consists in a phased network of poloidal straps of current. The imperfect coupling limits the amount of power that can be effectively transferred to the plasma for a given strap current. A significant fraction of the power maintaining the current distribution on the straps can thus be reflected towards the generator. To avoid this, an impedance matching network has to be inserted in the straps network to isolate the generator from the antenna [24]. This matching network is getting more complex with the number of straps. Another complication arises from rapid time-scales of the changes of the conditions at the edge of the plasma that require fast matching systems [25].

In a reactor, an ICRH antenna should be able to provide external high level of power in steady state. This is nowadays unachievable. Progresses on thermal exhaust on the antenna, the transmission lines and the generators still have to done.

The challenges concerning this thesis were at the interface between the antenna and the plasma, crucial for the antenna integrity and performance: fast wave power coupling to the plasma and radio-frequency sheaths in the vicinity of the antenna.

1.5.1 Wave power coupling to the plasma

Wave absorption in the ICRH range of frequencies is nowadays well understood. Good theoretical models exist are available to predict wave absorption in the core [26–29]. Conditions for strong absorption of the fast magnetosonic wave are known and can be realized and controlled experimentally. However, before reaching the absorption layer in the plasma core, the fast wave must be launched effectively from the antenna structure. This will be detailed in Section 2.2.1. As it will be described in Section 2.1.4, the FW must cross an evanescent layer at the edge of the plasma, where the plasma density is lower than the wave cutoff density. The simplest solution would be to place the antenna at a position where the plasma density is higher than the cutoff density, so that the power carried by the fast wave can be transmitted to the plasma region without losses.

In reality, the antenna cannot however be placed that close to the plasma since damages of the antenna could become critical due to the high heat fluxes in the plasma (high temperature and high density). Moreover that would facilitate antenna erosion and the subsequent plasma pollution by metallic impurities would radiate the plasma energy. The

antenna must therefore be isolated from the plasma. As a result, the antenna is placed in the SOL and the fast wave must tunnel through the evanescent region, as thin as possible, before reaching a sufficiently dense plasma where the wave can propagate towards the plasma core. The position of the antenna is thus a balance between the integrity of the antenna and the power loss during the tunnelling.

The complexity of the antennas geometries requires numerical treatment, but there is good confidence that the underlying physics is mostly understood at least in the linear case. Several wave coupling codes for ICRF waves already exist: TOPICA [30, 31] ICANT [32]) or ANTITER2 [30]. Chapter 4 introduces a novel way to simulate wave coupling for Tore Supra ICRH antennas that relies on a method commonly used for classical media in order to handle outgoing propagative waves but not for magnetized plasmas that is presented in Chapter 3.

Even if the antenna is placed far away in the SOL where the plasma has low density and low temperature, the antenna and its neighbouring objects can still be damaged by the consequences of RF sheaths that is the other challenge raised in this thesis.

1.5.2 Radio-frequency sheaths

Heating of the plasma using Ion Cyclotron Resonant Heating (ICRH) is essential to achieve the high temperatures required to reach fusion relevant conditions. However, in addition to the desired heating in the core plasma, spurious interactions with the plasma edge of magnetic fusion devices and material boundary have been documented by many experimental and theoretical studies and have been known to occur due to non-linear mechanisms [33].

Among them, one of the most important mechanism is the RF sheath formation [34] in which ICRH waves is enhancing the sheath potential on objects in the vicinity of the antenna, often setting the operational limits of the radio-frequency (RF) systems.

As a result of the increased sheath potential by RF-sheath rectification due to the presence of the slow wave, ions are significantly accelerated in the close vicinity of wall material causing enhanced sputtering releasing impurities [35], increased heat fluxes [36] (up to several $\mathrm{MW/m^2}$) on the antennas themselves during pulses and convection cells in the SOL inducing density re-distribution [37–39] modifying the coupling properties of the antenna. RF sheaths were observed in various experiments on several machines such Alcator C-Mod [40], Tore Supra [41], ASDEX-Upgrade [42] and TEXTOR [37]. Perturbations with other active ICRH antennae were reported on JET in mixed phasing scenarios [43]. On JET, Tore Supra, Alcator C-Mod and EAST, lower hybrid wave coupling was locally perturbed on particular launching waveguides, connected magnetically to powered ICRF antennas [44]. One other inherent effect of RF sheath formation is the appearance of DC currents in the SOL in the vicinity of the antenna [37, 42] and on probes far from the antenna [45, 46].

RF-sheaths spatial topology and magnitude are a priori influenced by the active RF strap currents and by the image currents induced on the surrounding passive structures. For reliable ICRH operation at high power over long pulses, spurious interactions due to RF sheaths must be minimized. The usual ways to act on these RF sheaths experimentally is to modify the operational scenario (i.e. changing the phase between current straps) [47] or the launcher design [48, 49]. The quantities measured in the experiments are (1) RF-generated impurities (measurement of the increased impurity influx to the core plasma), (2) missing power and reduced heating efficiency (e.g. due to sheath power dissipation), (3) hot spots on the antenna and surrounding limiters (also due to sheath power dissipation) and (4) effects of RF sheath-driven convection cells.

Finally other interesting phenomena related to RF sheath-plasma interactions could potentially yield significant effects on tokamak operations: sheath-plasma wave [50] and sheath-plasma resonances [51, 52].

If one seeks a truly accurate description of RF-sheath interactions with first principles, a kinetic description with the detailed sheath structures must be done. However the RF sheaths are so complex that it is better to start with low order analytic approaches. Moreover if the aim is to evaluate effects such as the impact of sheaths on waves in the SOL and sheath potentials in the worst case scenario, it is then possible to fix the engineering limits of the antenna and thus guide the design of antennas. Furthermore, in that case these details may be considered as high-order effects. The results have then to be confronted to experimental observations and higher order effects implemented if necessary. For detailed understanding and predictive capability useful for quantitative evaluation, numerical simulation of sheath-plasma interactions with realistic geometry and plasma profiles is required. This is the philosophy that this thesis will follow.

A novel self-consistent model of the interplay of the slow wave propagation and of DC biasing of the SOL in a magnetized plasma due to RF near-fields sheaths has been developed during this thesis. The model, that will be exhaustively presented in Chapter 5, most notably include a sheath boundary condition [53] essentially assuming that sheath effects on a SOL plasma are captured through the boundary condition for plasma analysis without using the field quantities in the sheaths. Another novel feature is a finite effective DC conductivity tensor to produce DC currents in addition to asymmetric voltage [54]. As it will be shown in Chapter 6, the model has been successfully applied for comparison with unexpected results on Tore Supra [55] when one antenna was equipped with a prototype Faraday screen [56], whose purpose will be explained in Section 2.4.5, supposed to minimize RF sheaths [48].

1.6 Thesis outline

This thesis is at the beginning stage of a wider project whose ultimate objective is to simulate an ICRH antenna facing a plasma as a whole. In a near future the objective is to able to model simultaneously fast wave coupling with RF sheaths due to the slow wave rectification in a self-consistent manner. This thesis presents the embryos of two separate codes - one for wave coupling and one for RF sheaths - that in principle could be merged together to form a single code. The thesis thus mainly focuses on the fast wave coupling issue and on RF sheaths issue. In order to analyse and bring some insight to the previously mentioned issues, the present thesis is organised as follows:

- **Chapter 2** introduces the necessary theoretical background about ICRH physics to understand this thesis. The first section recalls briefly the waves existing in a cold magnetized plasma in the ICRH frequency range. The second section is a review of the state of the art about ICRH waves generation, coupling and propagation is presented. In the third section, the same is done for RF sheaths physics. Their purpose is to show what has already been done and understood but also to point out some limits. The last section shows a brief description of the technological elements that constitutes an ICRH antenna with a specific focus on Tore Supra.

- **Chapter 3** presents the Perfectly Matched Layer method [57] commonly used for classical dielectric media to absorb outgoing waves without reflection. The formalism is applied here for magnetized plasmas. The specificities of this medium with respect to the PML method are outlined. Numerical benchmarks are performed with plane

waves in homogeneous magnetized plasmas by quantifying the efficiency of the PML with a reflection coefficient compared with analytical predictions. Limits of the PML are identified and solutions to go around for fusion tokamaks plasmas are presented.

- **Chapter 4** is devoted to fast wave coupling simulations of ICRH antennas where radiating outgoing waves are dealt with the Perfectly Matched Layer method presented in Chapter 3. 2D and 3D models of simplified Tore Supra ICRH antennas have been implemented in the code. The coupling efficiency of ICRH waves evaluated from simulation results is compared with experimental data. The necessary level of complexity of the antenna geometry to reproduce the experiments is investigated. An immediate prospect for the coupling code is shown with some elements of a preliminary study for the design of the new ICRH antennas for WEST. The end of this chapter presents some long term prospects for the fast wave coupling code and for the improvements of the PML method.

- **Chapter 5** shows the development of a novel model, called **S**elf-consistent **S**heaths & **W**aves for **I**on **C**yclotron **H**eating (SSWICH), to model self-consistently the interplay between the slow magnetosonic wave and DC biasing of the edge plasma by the intermediate of RF sheaths. In the first section, the physics behind the SSWICH code is presented, coupling together in a self-consistent manner elements presented in Chapter 2. The implementation of the model in the multiphysics software Comsol is detailed in the second section. Benchmark tests of SSWICH are shown in the third section. Finally the fourth section identifies some prospects for SSWICH as well as the possible improvements that could be realized.

- **Chapter 6** is an application of the SSWICH code for Tore Supra ICRH antennas coupled with the antenna code TOPICA [31]. The simulation results are compared to the main experimental observations summarized in the first section. The second section is devoted to the simulation results and their interpretation. SSWICH has been able to reproduce key observations and justify the theoretical model in Chapter 5. A non-linear analytical model of the DC biasing is used for benchmarking SSWICH and for extrapolation to realistic Tore Supra geometry parameters. In the third section, some predictions for the blanket shielding module around the ICRH antenna in ITER are presented. The fourth section gives a brief summary of this chapter.

- The **Conclusion** recalls the thesis objectives with its motivations. A synthesis on the two main parts of this thesis is performed and some prospects are discussed in conjunction with the thesis objectives. The difficulties are also mentioned. Finally the advancement of the project to simulate an ICRH antenna is examined.

Chapter 2

Theoretical and experimental background required for the thesis

This chapter is devoted to give an overview of the theory of plasma waves, wave coupling to the plasma and RF sheaths physics observed in the Scrape Off Layer of a tokamak during ICRH operations, as it is understood until now. The goal here is to derive the equations that govern the behaviour of plasma waves in the SOL and the interaction between waves and sheaths forming on every material surface.

The plan in this chapter is as follows. In the first part, a description of the electromagnetic waves existing within the cold plasma approximation is presented for the ICRH frequency domain. Then wave excitation and coupling to the plasma will be summarized. The different ways to model wave coupling in the ICRH and LH bandwidths will be recalled and special attention will be given to radiating boundary condition. The second part is focused of RF sheaths physics. A brief summary of the past theoretical and experimental works is presented is presented. The different mechanisms and properties behind RF sheaths physics are presented. The concept of "sheath boundary condition" is introduced as well as a DC biasing model with finite DC conductivity. The last part is dedicated, as an illustration, to a brief description of the ICRH system technology with the example of Tore Supra ICRH system.

2.1 Theory of ICRH waves

2.1.1 The Maxwell's equations

We start from the widely known macroscopic Maxwell's equations:

$$\begin{cases} \nabla \times \mathbf{E} &= -\partial_t \mathbf{B}, \\ \nabla \times \mathbf{H} &= \mathbf{j_{ant}} + \partial_t \mathbf{D}, \\ \nabla \cdot \mathbf{D} &= \rho_{ant}, \\ \nabla \cdot \mathbf{B} &= 0, \end{cases} \tag{2.1}$$

where c is the speed of light, $\mathbf{E}$ is the electric field, $\mathbf{H}$ the magnetic induction, $\mathbf{D}$ the electric displacement and $\mathbf{B}$ the magnetic field. These RF fields are excited by antenna currents $\mathbf{j_{ant}}$ and space charge ρ_{ant}.

The first two equations in the system (2.1) are a set of two first order partial differential equations connecting $\mathbf{E}$ and $\mathbf{H}$ fields to some partial space derivatives of their components. The other two equations are gauge relationships.

Maxwell's equations describe how the fields react to the presence of charges and currents. The wave problem thus needs to be complemented with constitutive relations to be self-consistent. The constitutive relations aim at describing how the fields produce charges and currents in the medium.

Assuming small amplitude perturbation, $\mathbf{E}$, $\mathbf{B}$, $\mathbf{H}$, $\mathbf{D}$ and $\mathbf{j_{ant}}$ in (2.1) can be expended as follows:

$$\mathbf{A}\left(\mathbf{r},t\right)=\mathbf{A_0}+\mathbf{A_1}\left(\mathbf{r},t\right), \tag{2.2}$$

where the subscripts 0 and 1 denote the zero order equilibrium quantity (static field) and the first order perturbed (RF fields) quantities ($\mathbf{A_1} << \mathbf{A_0}$). Linearising, the constitutive relations take the form: $\mathbf{D}=\bar{\bar{\varepsilon}}\mathbf{E}$ and $\mathbf{B}=\bar{\bar{\mu}}\mathbf{H}$, where for the sake of generality the dielectric tensor $\bar{\bar{\varepsilon}}$ and magnetic permeability tensor $\bar{\bar{\mu}}$ are full due to the anisotropy of magnetized plasmas. All information about the properties of the considered medium are contained in $\bar{\bar{\varepsilon}}$ and $\bar{\bar{\mu}}$. Throughout this thesis, RF quantities are assumed to oscillate in time as $e^{-i\omega t}$ where ω is the wave pulsation and the contribution of the slow-time variations of the RF field stay negligible. Assuming thus a monochromatic wave, the time derivative ∂_t can be replaced by $-i\omega$. The general vectorial time-harmonic wave propagation problem in a medium reads:

$$\left\{\begin{array}{rcl}\nabla\times\mathbf{E_1} &=& i\omega\mathbf{B_1},\\ \nabla\times\mathbf{H_1} &=& -i\omega\mathbf{D_1}+\mathbf{j_{ant_1}},\\ \nabla\cdot\mathbf{D_1} &=& \rho_{ant_1},\\ \nabla\cdot\mathbf{B_1} &=& 0.\end{array}\right. \tag{2.3}$$

In the system (2.3), substituting the first equation into the second equation and using the constitutive relations lead to the Helmholtz equation:

$$\nabla\times\bar{\bar{\mu}}^{-1}\left(\nabla\times\mathbf{E_1}\right)+\frac{\omega^2}{c^2}\bar{\bar{\varepsilon}}\cdot\mathbf{E_1}=+i\omega\mu_0\mathbf{j_{ant_1}}, \tag{2.4}$$

where μ_0 is the vacuum permeability. In the following, the equivalent dielectric description is used. The permeability tensor becomes $\bar{\bar{\mu}}=\mu_0\bar{\bar{\mathbf{1}}}$.

2.1.2 Dielectric tensor within the cold plasma approximation in the SOL

Plane waves oscillating spatially as $e^{i\mathbf{k}\cdot\mathbf{r}}$ are assumed, with $\mathbf{k}$ the wavenumber. With the condition $k_\perp\rho_{L_s} << 1$ satisfied with $k_\perp$ the perpendicular wavenumber and ρ_s the Larmor radius for a particle of species s defined in (1.6), it can be shown that the plasma can be modelled with fluid equations neglecting the thermal effects. This thesis is focused on waves in the SOL where temperature for electrons and ions are less than 100 eV, which fulfils the cold plasma conditions [58]. Being also far away from resonances permits to integrate over the velocity space and to use fluid equations to describe the wave propagation.

The density n_s and mean fluid velocity $\mathbf{u_s}$ must satisfy the moment's conservation: particle conservation without sources and momentum conservation without collisions.

$$\begin{array}{rcl}\partial_t n_s+\nabla\cdot\left(n_s\mathbf{u_s}\right) &=& 0,\\ n_s m_s\left(\partial_t\mathbf{u_s}+\left(\mathbf{u_s}\cdot\nabla\right)\mathbf{u_s}\right) &=& -\nabla\cdot\bar{\bar{P}}_s+n_s q_s\left(\mathbf{E}+\mathbf{u_s}\times\mathbf{B}\right),\end{array} \tag{2.5}$$

where $\bar{\bar{P}}_s$ is the pressure tensor of the species s. Within the cold plasma approximation, the first term in the right hand side (RHS) about pressure can be neglected. Taking into account only the first order terms in the momentum equation for each species (2.5) to describe the wave propagation without non-linear effects and focusing of monochromatic plane wave mode yields:

$$-i\omega\mathbf{u_{s_1}} = \frac{q_s\mathbf{E_1}}{m_s} + \frac{q_s}{m_s}\mathbf{u_{s_1}} \times \mathbf{B_0}. \tag{2.6}$$

It is convenient to multiply (2.6) by $n_0 q_s/\varepsilon_0$ to introduce the plasma frequency (1.3) and cyclotron frequency (1.5) for each species:

$$-i\omega\frac{n_0 q_s}{\varepsilon_0}\mathbf{u_{s_1}} + \frac{n_0 q_s}{\varepsilon_0}\Omega_s\mathbf{b} \times \mathbf{u_{s_1}} = \omega_{ps}^2\mathbf{E_1}, \tag{2.7}$$

where $\mathbf{b} = \mathbf{B_0}/B$ is the unit vector along the magnetic field direction. The solution for the mean fluid velocity $\mathbf{u_s}$ thus gives:

$$\frac{n_0 q_s}{\varepsilon_0}\mathbf{u_s} = -i\left(\frac{\omega\omega_{ps}^2}{\Omega_s^2 - \omega^2}\right)\mathbf{E_1} - \frac{\omega_{ps}^2}{\Omega_s^2 - \omega^2}\Omega_s\mathbf{b} \times \mathbf{E_1} + \frac{i\omega_{ps}^2}{(\Omega_s^2 - \omega^2)\,\omega}\Omega_s\,(\mathbf{b}\cdot\mathbf{E_1})\,\mathbf{b}. \tag{2.8}$$

This fluid velocity directly yields the current ($j_1 = \sum_s n_s q_s \mathbf{u_{s_1}}$) as a linear function of $\mathbf{E_1}$. By comparing with Ohm's law ($\mathbf{j_1} = \bar{\bar{\sigma}}_{RF}\mathbf{E_1}$), the RF conductivity tensor $\bar{\bar{\sigma}}_{RF}$ is obtained which is inserted into $\bar{\bar{\varepsilon}} = \bar{\bar{1}} + i\bar{\bar{\sigma}}_{RF}/\omega\varepsilon_0$ to get the expression for the cold dielectric tensor. It is enough to define the dielectric properties of the medium. Labelling z the direction of anisotropy (i.e. that of the confinement magnetic field $\mathbf{B}$) the dielectric tensor $\bar{\bar{\varepsilon}}$ takes the form given by Stix in [58]:

$$\bar{\bar{\varepsilon}} = \begin{pmatrix} \varepsilon_\perp & -i\varepsilon_X & 0 \\ i\varepsilon_X & \varepsilon_\perp & 0 \\ 0 & 0 & \varepsilon_\parallel \end{pmatrix}, \tag{2.9}$$

where $\varepsilon_\parallel$, $\varepsilon_\perp$ and ε_X are called usually the Stix parameters written as:

$$\varepsilon_\parallel = 1 - \sum_s \frac{\omega_{ps}^2}{\omega^2}, \tag{2.10}$$

$$\varepsilon_\perp = \frac{1}{2}\left(\varepsilon_R + \varepsilon_L\right), \tag{2.11}$$

$$\varepsilon_X = \frac{1}{2}\left(\varepsilon_R - \varepsilon_L\right), \tag{2.12}$$

$$\varepsilon_R = 1 - \sum_s \frac{\omega_{ps}^2}{\omega\left(\omega + \Omega_s\right)}, \tag{2.13}$$

$$\varepsilon_L = 1 - \sum_s \frac{\omega_{ps}^2}{\omega\left(\omega - \Omega_s\right)}, \tag{2.14}$$

in which ω_{ps} and Ω_s were defined in Section 1.1 and Section 1.2.1. The medium response is thus frequency dependent, resulting in dispersion. Also note that $\bar{\bar{\varepsilon}}$ is gyrotropic (i.e. non-null non diagonal terms in the tensor due to the presence of the static magnetic field).

Plane wave with harmonic oscillations in $\exp\left(-i\omega t + i\mathbf{k}\cdot\mathbf{r}\right)$ are now assumed. In such medium, different kind of plane waves can propagate at different speeds. This property is at the origin of the Faraday effect or the Hall effect, since it breaks the tensor symmetry. Charge ambipolarity in the plasma is assumed to be retained: $n_{e0} = n_{i0} = n_0$. The components of the dielectric tensor $\bar{\bar{\varepsilon}}$ are however independent of the wave vector components on the contrary to the hot plasma dielectric tensor [59]. Hereafter, the subscript 1 will be omitted.

2.1.3 General dispersion relation for plane waves

Having obtained the dielectric tensor $\bar{\bar{\varepsilon}}$, the wave equation has simple analytic solutions for plane waves. An exhaustive review of waves in plasmas can be found in major textbooks such as [22], [58] and [60]. Assuming a plane wave, ∇ can be replaced by $i\mathbf{k}$. It implicitly implies that a homogeneous plasma with constant density and a constant magnetic field in space at equilibrium is considered. The Helmholtz equation given by (2.4) thus reads in the region where $\mathbf{j_{ant}} = 0$:

$$\mathbf{k} \times (\mathbf{k} \times \mathbf{E}) + \frac{\omega^2}{c^2} \bar{\bar{\varepsilon}} \cdot \mathbf{E} = 0. \tag{2.15}$$

At this point it is convenient to introduce the dimensionless vector $\mathbf{n}$ which has the magnitude of the refractive index and is parallel to $\mathbf{k}$:

$$\mathbf{n} = \frac{\mathbf{k}c}{\omega}. \tag{2.16}$$

with c the speed of light in vacuum. The wave equation (2.15) is rewritten:

$$\mathbf{n} \times (\mathbf{n} \times \mathbf{E}) + \bar{\bar{\varepsilon}} \cdot \mathbf{E} = 0. \tag{2.17}$$

The Stix coordinate system is defined with:

$$\zeta = \frac{\mathbf{k}_\perp}{|\mathbf{k}_\perp|},\ \mathbf{b} = \frac{\mathbf{B}}{|\mathbf{B}|},\ \varpi = \frac{\mathbf{b} \times \mathbf{k}_\perp}{|\mathbf{k}_\perp|}. \tag{2.18}$$

In a homogeneous plasma, the two perpendicular direction have equivalent roles. If $k_\perp$ does not have a poloidal component, then the Stix frame coincides with the tokamak frame ($\mathbf{x}$,$\mathbf{y}$,$\mathbf{z}$=$\mathbf{b}$). (2.15) becomes in the Stix frame with $\mathbf{n} = n_\perp \zeta + n_\parallel \mathbf{b}$:

$$\begin{pmatrix} \varepsilon_\perp - n_\parallel^2 & -i\varepsilon_X & n_\parallel n_\perp \\ i\varepsilon_X & \varepsilon_\perp - n^2 & 0 \\ n_\parallel n_\perp & 0 & \varepsilon_\parallel - n_\perp^2 \end{pmatrix} \begin{pmatrix} E_\zeta \\ E_\varpi \\ E_\parallel \end{pmatrix} = 0 \tag{2.19}$$

Evaluating the determinant of (2.19) yields the fourth order in $n_\perp$ dispersion relation:

$$\left(n_\parallel^2 - \varepsilon_\perp\right)\left(n^2 - \varepsilon_\perp\right)\left(n_\perp^2 - \varepsilon_\parallel\right) - n_\parallel^2 n_\perp^2 \left(n^2 - \varepsilon_\perp\right) - \left(n_\perp^2 - \varepsilon_\perp\right) = 0. \tag{2.20}$$

2.1.4 Fast and slow waves in the ICRH frequency domain

2.1.4.1 Dispersion relation

In the ICRH frequency domain ($30 - 100$ MHz), two eigenmodes, called slow wave (SW) and fast wave (FW), exists in the cold plasma approximation. They appear coupled in (2.20). Within two limiting case, (2.20) can be reduced to two second order dispersion relations. They both obey the ordering $|\varepsilon_\parallel| >> \left|n_\parallel^2\right|, |\varepsilon_\perp|, |\varepsilon_\times|$. Their respective dispersion relation reads away from the coupling region ($\varepsilon_\perp \neq n_\parallel^2$):

$$n_{\perp_{FW}}^2 = \frac{\left(\varepsilon_R - n_\parallel^2\right)^2 \left(\varepsilon_L - n_\parallel^2\right)^2}{\left(\varepsilon_\perp - n_\parallel^2\right)} \qquad \text{with } \left|\varepsilon_\parallel\right| >> \left|n_{\perp_{FW}}^2\right|, \tag{2.21}$$

$$n_{\perp_{SW}}^2 = \varepsilon_\parallel \left(1 - \frac{n_\parallel^2}{\varepsilon_\perp}\right) \qquad \text{with } \left|\varepsilon_\parallel\right| \approx \left|n_{\perp_{FW}}^2\right|. \tag{2.22}$$

When $\varepsilon_\perp \approx n_\parallel^2$ the value of $n_\perp^2$ for the FW becomes very large, whereas its value becomes very small for the SW. In this case the orderings that were used to decouple the fast and slow waves are no longer valid.

The wave phase velocity v_p and the wave group velocity v_g are described by the following expressions [60]:

$$v_p = \frac{\omega}{k}, \qquad v_g = \frac{\partial \omega}{\partial k}. \tag{2.23}$$

A wave is considered a forward (backward) wave if the directions of its phase and group velocities are the same (opposite) for collinear velocities [60]. In the case of non-collinear velocities this definition is generalized in a natural manner using the scalar product. The scalar product of the phase and group velocities is positive for a forward wave and negative for a backward wave. The fast wave is consequently from this definition a forward wave whereas the slow wave is a backward wave [58].

2.1.4.2 Electric field polarization

The polarization is defined as the eigenvector associated with one eigenvalue of the matrix given in (2.19). The polarizations for the fast and slow waves are determined from the appropriate sub-matrices of (2.19). Taking the third component of the vector given by (2.19) yields for the FW:

$$\left|\frac{E_\parallel}{E_\zeta}\right| = \left|\frac{n_\parallel n_\perp}{\varepsilon_\parallel}\right| << 1. \tag{2.24}$$

The parallel component of the electric field $E_\parallel$ can thus be neglected when talking about the fast wave. The fast wave is thus a transverse electric (TE) wave. It reduces (2.19) to:

$$\begin{pmatrix} \varepsilon_\perp - n_\parallel^2 & -i\varepsilon_X \\ i\varepsilon_X & \varepsilon_\perp - n^2 \end{pmatrix} \begin{pmatrix} E_\zeta \\ E_\varpi \end{pmatrix} \approx 0. \tag{2.25}$$

It yields for the fast wave polarization:

$$\frac{E_\varpi}{E_\zeta} = i\frac{\varepsilon_X}{\varepsilon_\perp - n^2}. \tag{2.26}$$

Similarly, the slow wave ordering gives:

$$\frac{E_\zeta}{E_\varpi} = -i\frac{n_\perp^2}{\varepsilon_\perp} >> 1. \tag{2.27}$$

The poloidal component of the electric field E_ϖ can thus be neglected when talking about the slow wave. Using the Maxwell's-Faraday law, it induces $B_\parallel = 0$, whatever the value of the poloidal wavenumber k_y. The slow wave can then be called a magnetic transverse wave. It reduces (2.19) to the sub-matrix:

$$\begin{pmatrix} \varepsilon_\perp - n_\parallel^2 & n_\parallel n_\perp \\ n_\parallel n_\perp & \varepsilon_\parallel - n_\perp^2 \end{pmatrix} \begin{pmatrix} E_\zeta \\ E_\parallel \end{pmatrix} \approx 0, \tag{2.28}$$

yielding for the slow wave polarization:

$$\frac{E_\zeta}{E_\parallel} = \frac{n_\perp n_\parallel}{n_\parallel^2 - \varepsilon_\perp}. \tag{2.29}$$

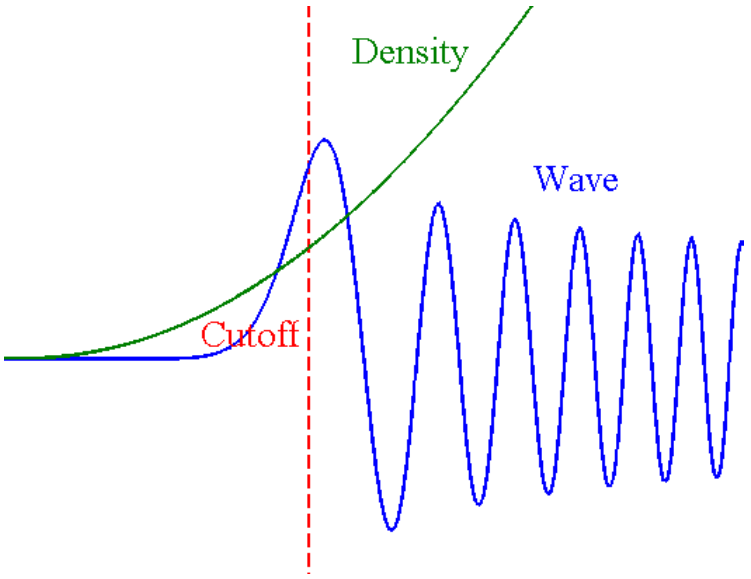

Figure 2.1: Example of the wave behaviour near a cutoff.

Note that the dispersion relations given by (2.22) can be also be found with the sub-matrices given by (2.25) and (2.28).

When $|\varepsilon_\parallel|$ is high the FW and the SW are totally decoupled. In that case the parallel electric field $E_\parallel$ is mainly due to the SW. The fast wave is a compressional Alfvén wave and can be seen, in the low frequency limit ($\omega << \Omega_i$), as a compressional oscillations of the magnetic field lines whereas the slow wave is the torsional or shear Alfvén wave, at the origin of a vast phenomenology in space and laboratory plasmas [61]. The transverse electric polarization of the fast wave make it a very good candidate for cyclotron heating since it is possible to reach a resonance to synchronize the particle cyclotron motion with the wave polarization. At this point strictly speaking, a kinetic description should be used. This means that the fast wave will carry the RF power to the central plasma.

2.1.4.3 Resonance and cut-off

Here $n_\parallel$ (or $k_\parallel$) is assumed to be determined by the antenna. A resonance condition for a wave appears when $n_\perp$ becomes infinite (i.e. phase velocity v_p and wavelength λ tend to zero). From (2.21), the FW resonance occurs at $\varepsilon_\perp = n_\parallel^2$. From (2.22), the SW resonance occurs at $\varepsilon_\perp = 0$, which corresponds to the lower hybrid resonance. A cutoff condition materializes a change from propagating (i.e. real $n_\perp$) to evanescent (i.e. imaginary $n_\perp$) wave when $n_\perp^2$ goes through zero. For a chosen wave frequency, cutoffs define the plasma density and the static magnetic field above or below which the wave ceases to propagate (phase velocity v_p and wavelength λ tend to infinity). In the example shown in Figure 2.1, the wave ceases to propagate above a critical density. Before that the wavelength has been increasing due to the plasma. At a cutoff region, the wave is reflected. Beyond the cutoff is the evanescent region where the wave will decay exponentially. From (2.21), the FW exhibits two cutoffs - called right cutoff and left cutoff - whose expressions are given by:

$$n_\parallel^2 = \varepsilon_R, \tag{2.30}$$

$$n_\parallel^2 = \varepsilon_L. \tag{2.31}$$

From (2.22), the SW also a priori exhibits two cutoffs: $n_\parallel^2 = \varepsilon_\perp$ and $\varepsilon_\parallel = 0$. However

within typical fusion plasmas, the density is such that for waves in the ICRH frequency domain $\varepsilon_\parallel << 0$. Therefore $\varepsilon_\parallel = 0$ is never encountered.

Determining the two cutoff density expressions for the fast wave and the slow wave cutoff yields for a single ion species plasma:

$$n_{c,SW} = \frac{\varepsilon_0 m_e}{e^2} \frac{g_i g_e \left(1-n_\parallel^2\right)}{g_i + g_e \frac{m_e}{m_i}}, \tag{2.32}$$

$$n_{c,R} = \frac{\varepsilon_0}{e^2} \left(\frac{1}{m_i} \frac{1}{(\omega+\Omega_i)\omega} + \frac{1}{m_e} \frac{1}{(\omega+\Omega_e)\omega} \right)^{-1} \left(n_\parallel^2 - 1\right), \tag{2.33}$$

$$n_{c,L} = \frac{\varepsilon_0}{e^2} \left(\frac{1}{m_i} \frac{1}{(\omega-\Omega_i)\omega} + \frac{1}{m_e} \frac{1}{(\omega-\Omega_e)\omega} \right)^{-1} \left(n_\parallel^2 - 1\right), \tag{2.34}$$

with $g_i = \frac{\omega-\Omega_i}{\omega+\Omega_i}$ and $g_e = \frac{\omega-\Omega_e}{\omega+\Omega_e}$.

Now that we have seen the properties of the existing waves in a cold plasma for the ICRH range of frequencies, we will see how can waves can be generated and sent into the plasma for heating or current drive purposes. The wave generation is constrained by the properties detailed in this present section.

2.2 Theory of fast wave coupling to the plasma

2.2.1 Wave excitation by a phased array of straps

In the ICRH frequency domain, the wavelength of electromagnetic waves in vacuum λ_0 is typically of the order of a few meters ($\lambda_0 = c/f_0 \sim 6$ m at $f_0 = 50$ MHz). This is of the same order as the reactor size. ICRH waves therefore cannot be propagated as quasi-optical beams from a generator to the target plasma. The antenna would hardly fit into the vacuum vessel of the tokamak. They rather have to be transmitted along coaxial lines and excited inside the vacuum vessel filled by the plasma.

The aim is to generate a fast wave that will propagate transversely to the magnetic field for injecting power into the plasma. As the fast wave is primarily a TE wave, it can be generated, as shown on Figure 2.2(a), by an inductive loop fed with an poloidal oscillating current $j_{ant,RF,y}$, the source of RF currents in Maxwell's equations (2.3) which has to be determined in a self-consistent manner. Due to accessibility constraints and voltage stand-off considerations the poloidal current straps are small compared to the size of the machine and are localized in horizontal ports at the low field side of the machine. As the cold plasma is an anisotropic dielectric medium, the launched RF electric field is commonly decomposed into individual plane waves for which well-defined propagation properties were established above.

The wavenumber spectrum in the toroidal direction $k_\parallel$ and poloidal direction k_y are imposed by the geometry of the launcher, while wave-numbers (generally complex) in the radial direction are deduced from a dispersion relation of the form $k_\perp^2 = f(\omega_0, k_\parallel^2, \bar{\bar{\varepsilon}})$, such as the ones shown in (2.21) and (2.22). In order to tailor the launched $k_\parallel$ spectrum, the current straps are frequently arranged in 1D (toroidal) or 2D (toroidal/poloidal) phased arrays. An illustration is shown in Figure 2.2(b) for a two straps array. The main parameters are the strap width w_{strap}, the strap spacing e_{strap}, the strap height L_{strap} and the current distribution on the strap that change the propagation constant [32, 62]. Neglecting the finite extension of the straps in the poloidal direction ($L_{strap} \to \infty$) and the finite thickness of the strap ($d_{strap} \to 0$), an analytical expression for the $k_\parallel$ spectrum of the

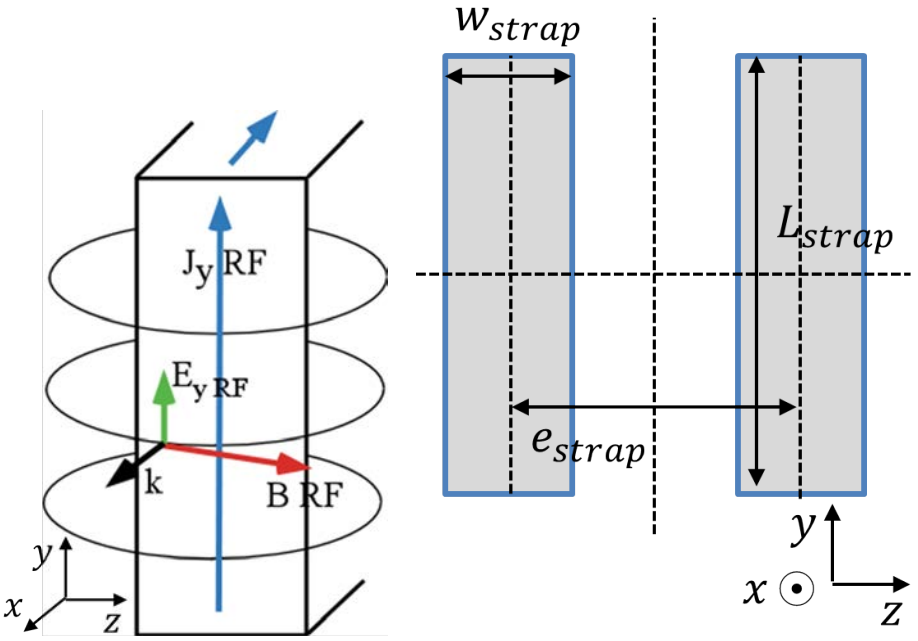

(a) (b)

Figure 2.2: (a) Principle of fast wave excitation by a radiating strap on which is circulating a poloidal oscillating current. (b) Schematic of a two straps array launcher with characteristic parameters.

excited currents:

$$j_y\left(k_{\|}\right) = 2i\pi j_0 w_{strap} \exp\left(i\Delta\phi\right) \cos\left(\frac{k_{\|} e_{strap} + \Delta\phi}{2}\right) \frac{\sin\left(\frac{k_{\|} w_{strap}}{2\pi}\right)}{\frac{k_{\|} w_{strap}}{2\pi}}, \tag{2.35}$$

where j_0 the current density of the strap, $\Delta\phi$ is the phasing between the two straps. The current density on the strap is assumed here constant. It is not the case in reality. The current density spatial variation in the toroidal direction is due to magnetic shielding [63]. Simulation results in Chapter **??** will show the importance of the finite strap thickness and of the finite poloidal size.An example of $k_{\|}$ spectrum is given in Figure 2.3 for different toroidal phasings $\Delta\phi$ between straps (monopole $[0, 0]$, dipole $[0, \pi]$, current drive + $[0, \pi/2]$ and current drive $[0, -\pi/2]$) with $j_0 = 1$ A/m, $e_{strap} = 0.224$ meter and $w_{strap} = 0.109$ meter corresponding to Tore Supra strap parameters. For monopole and dipole toroidal phasing, the spectrum is symmetric with respect to $k_{\|} = 0$ whereas it is asymmetric for current drive phasing.

The real radiated electric field is actually more complex than this ideal picture due to the finite strap length, slight RF current variations along the straps and image currents induced by the straps on surrounding passive metallic parts on the launcher.

2.2.2 Wave coupling to the plasma

The ICRH wave launcher has a characteristic size ($\lesssim 1$ m) far smaller than the wavelength in vacuum (~ 6 m at 50 MHz). Most of the RF power is thus radiated on spectral components with $\left|n_{\|}\right| > 1$ that are evanescent transversely to the magnetic field in vacuum

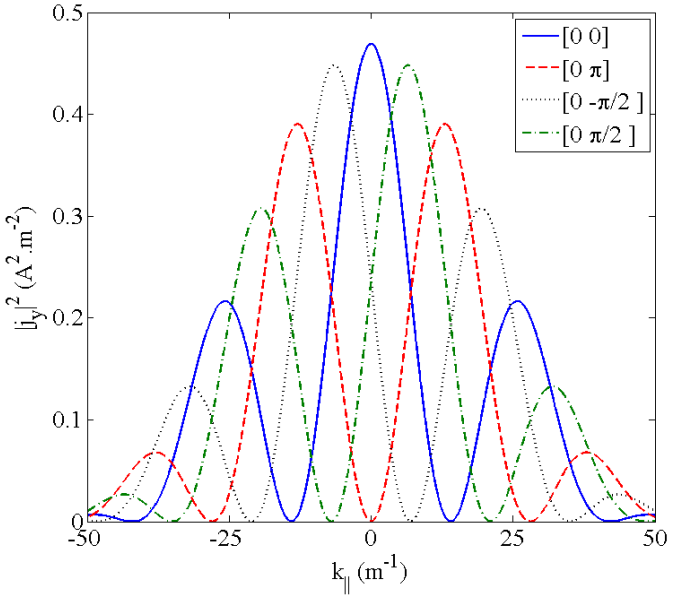

Figure 2.3: $k_{||}$ spectrum of RF currents excited by a "classical" Tore Supra antenna composed of two straps for different toroidal phasings with (2.35). Homogeneous current distribution is assumed on the strap and only the straps are taken into account: $j_0 = 1$ A/m, $e_{strap} = 0.224$ meter and $w_{strap} = 0.109$ meter.

and for densities below the R-cutoff corresponding to $\varepsilon_R = n_{||}^2$. This constrain imposes to excite the fast wave in the vicinity of the plasma. Reproducing this peripheral evanescence is essential to evaluate the fast wave coupling [64]. A didactic paper by Koch [8] offers more insights about the coupling of electromagnetic power to plasmas.

It can be seen from the slow wave cut-off density expression, given by (2.33), that the wave is propagating below some critical density $n_{c,SW}$ and is evanescent above. However its polarization is unfavoured for cyclotron heating. Furthermore the slow wave is associated with spurious phenomena that will be described later in Section 2.3 due to parallel polarization able to accelerate particles in the parallel direction. However the high parallel RF conductivity of the plasma provides, even in the SOL, an excellent natural screening of the slow wave. Consequently the slow wave is rapidly evanescent with a typical skin depth $\lambda_{skin,SW} = c/\omega_{pe}$ with a typical size in the centimeter order.

If the region below the R-cutoff is sufficiently thin, the fast wave can tunnel through the cutoff region to the main plasma. However, part of the wave will still be reflected. This is illustrated in Figure 2.4(a). The R-cutoff density is also intrinsically linked to the dimensions of the strap array through the launched $k_{||}$ spectrum. From (2.34), of which a graphical representation is shown in Figure 2.4(b), it is easily seen that the R cut-off density increases as $k_{||}$ increases. High $k_{||}$ in the launched spectrum thus have to tunnel further away than low $k_{||}$ and consequently tend to be filtered from the spectrum.

From (2.31), it can be seen that ε_R is roughly proportional to the local density n that is increasing when going from the edge towards the center of the plasma. Consequently the distance between the strap where the fast wave is excited and the R-cutoff will influence greatly the tunnelling of the fast wave. The reflection of the fast wave increases (i.e. the efficiency at which the wave is coupled to the plasma is decreasing) as the tunnelling distance increases [65].

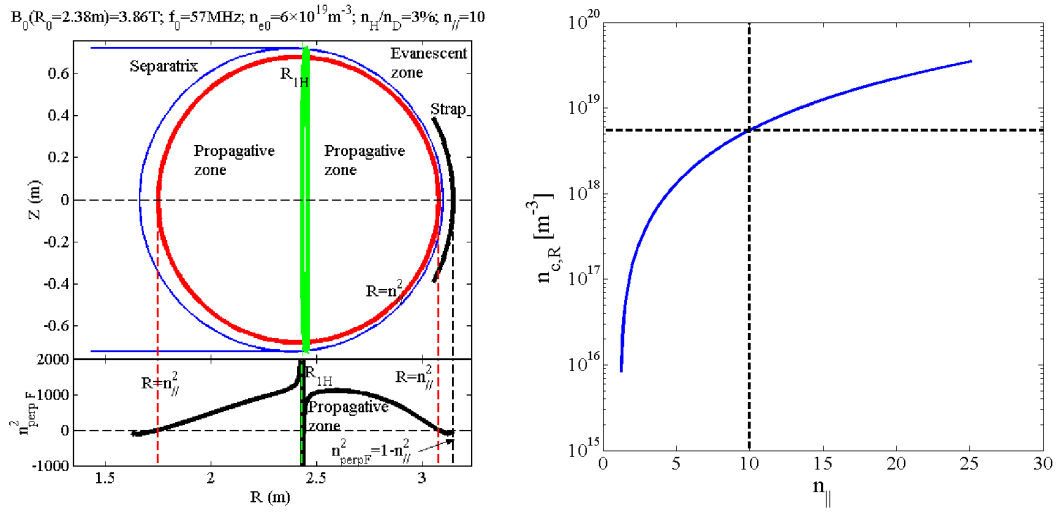

(a) (b)

Figure 2.4: (a) Fast wave behaviour in D(H) minority heating scenario on Tore Supra, for $n_{\parallel} = 10$. Above: 2D mapping of propagative and evanescent zones in a poloidal cross section. The green curve show the location of the cyclotron resonance layer for ${}^1_1H$. Below: radial profile of $n^2_{\perp,FW}$ in plane $Z = 0$. (b) Right cut-off density $n_{c,R}$ versus parallel index $n_{\parallel}$. The black dashed line shows the cut-off density for $n_{\parallel} = 10$.

2.2.3 Coupling resistance definition

The quality of wave coupling to the plasma is quantified via the distributed loading or coupling resistance R_c(in $\Omega.m^{-1}$) of each current strap defined through Ohm's law as:

$$P_t = \frac{1}{2} R_c L_{strap} J^2_{y,RF}, \tag{2.36}$$

where P_t is the transmitted power. Once the evanescent fast wave has crossed the R-cutoff, the fast wave can propagate towards the plasma core to be extremely well damped when the wave-particle resonance is met according to the plasma heating scenario defined in Section 1.4.2. Alternatively the fast wave can be converted into others extremely well damped waves [20]. The single pass absorption measures the absorbed fraction of the incident power on the absorption region for one pass only, before subsequent reflections of the unabsorbed wave on the cutoff layers or on the vessel walls. In case of high single-pass absorption, the wave is totally absorbed and never reaches the HFS. In case of low single-pass absorption, the wave however bounces several times between both R-cutoffs at LFS and HFS, forming a standing wave or cavity modes inside the plasma. It was shown in [66] that it influences the wave coupling process. This difference impacts the modelling of wave coupling.

2.2.4 Review of the different historical ways to model wave coupling

To summarize the above section, wave coupling is mainly determined by the interaction of the near radio frequency (RF) field with the plasma edge surrounding the antenna structure. Reproducing this interaction in numerical simulations requires at least a detailed description of the launcher geometry and of the edge plasma. How detailed should this description be is still a matter of debate.

Due to limited computational resources, the wave propagation away from the antenna as well as its absorption in the hot core plasma are generally included only as boundary phenomena in wave coupling codes. Only the vicinity of the antenna is modelled. So instead of a volume enclosed by the metallic wall of the tokamak, we have only a fraction of the volume in the vicinity of the antenna with some metallic boundaries and some open boundaries on the computational domain. A similar approach is adopted for Lower Hybrid waves. An exception is presented in ref. [49], where the whole plasma cross-section is modelled within the cold plasma approximation with artificial collisions. Furthermore, as only the edge plasma is simulated due to computational resources, no mechanism is naturally included to simulate wave single pass absorption that normally happens in the central hot plasma by cyclotron resonance. Some trick has to be included to emulate wave absorption. Finally in low single-pass regimes of power absorption, cavity modes [66] can be formed, characterized by partial wave reflection in the boundary condition.

Summarizing waves coupling to the plasma and waves propagation towards the core magnetized plasma is made difficult due to the strong anisotropy, gyrotropy and inhomogeneity of the plasma. Therefore the typical wavelengths strongly depend on the direction of the wave propagation with respect to the static magnetic field. The elements in the dielectric tensor $\bar{\bar{\varepsilon}}$ can have opposite sign. Gyrotropic media are also birefringent. Besides, the hot core plasma can become spatially dispersive. Within the cold plasma approximation, the medium is dispersive in time but not in space.

In the literature several strategies were followed to implement this plasma side boundary condition. The standard tool is the spectral surface admittance/impedance matrix formalism [66, 67] according to what is the easiest quantity to manipulate in a given situation. Advanced wave coupling codes relying on this method are TOPICA [30, 31] ICANT [32]) or ANTITER2 [30] for ICRH waves, as well as TOPLHA [68] and ALOHA [69] for LH waves. The method is quite general: it can handle spatially dispersive media and cavity modes [66]. However, strictly speaking the interface where the boundary condition is applied should be a slab approximation of the whole tokamak toroidal/poloidal extension, whereas the emitted near field is intense only in a limited portion of this surface. Besides, the spectral character of the boundary condition is generally not well adapted to the numerical methods applied in the main simulation domain near the antenna structure. All this translates in a heavy numerical cost as Fourier transforms and multiple integrals are required to match the plane waves of the plasma to the vacuum modes. Furthermore, such codes model the antenna in vacuum, whereas in reality the antenna is surrounded by a low density plasma that has been neglected until now.

While many heating scenarios have low single pass absorption, antennas are usually designed assuming high single pass absorption. One easy solution to emulate this situation is to implement a lossy radiation medium featuring artificial collisions [70]. But using this method, the wave reflection is marginally controlled. In order to use commercial RF simulation softwares (HFSS [71], MWS [72]), the plasma is even sometimes replaced with an equivalent lossy isotropic dielectric [73–75]. It simplifies the situation as the gyrotropy and the anisotropy both disappear. However, since the birefringence is also suppressed, only one eigenmode of the plasma is correctly reproduced. Therefore mode conversion between slow wave and fast wave cannot be reproduced. Furthermore only positive dielectric constants can be handled in most commercial softwares. In these cases the inner boundary condition to apply is similar to radiating or transparent boundary conditions.

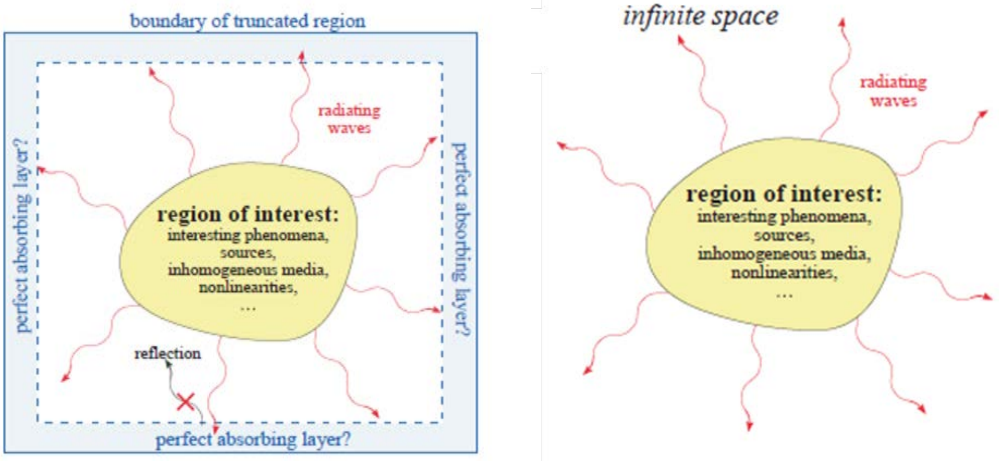

(a) (b)

Figure 2.5: A finite region of interest where sources, inhomogeneous media, non-linearities are being investigated. (a) Sketch of a typical bounded wave-equation problem. An absorbing layer is placed adjacent to the edges of the computational region to absorb outgoing waves without reflection coming from the edge of the absorber. (b) Sketch of a typical unbounded wave-equation problem that we want to solve as exactly as possible to reality. *Courtesy of Steven J. Johnson [79]*

2.2.5 Why emulating radiating boundary conditions?

Since in most cases it is impossible to find an analytical solution to Maxwell's equations (especially in realistic geometries), numerous computational methods have been developed to solve them in a discretized space (finite difference [76], finite element (FEM) [77], finite volume, transmission line matrix [78]). In all these techniques, the physical space is split into elementary cells, elements, volumes that must be smaller than the shortest wavelength of interest and the smallest details of the geometry of the objects placed within the region of interest. Nevertheless, computers do not - and never will - have the computational resources to handle an infinite number of elementary cells. It means that Maxwell's equations can only be solved for a finite region of space (see Fig. 2.5(a)) and finite spatial resolution.

This is however inconsistent with unbounded problems in electromagnetisms, illustrated by Fig. 2.5(b). In other words, the physical boundary conditions should be placed at infinity. On the other hand the unbounded physical space is replaced by a finite computational domain due to finite resources. If the problem is solved within this bounded medium, the obtained solution is erroneous. This is the case here since the enclosed torus with metallic walls cannot be entirely simulated and thus the computational domain is only the immediate vicinity of the antenna. There are thus some open boundary conditions in the reduced volume. Finding a way to correctly treat open boundaries in radiation problems is thus one of the accepted challenges in numerical modelling and in particular for finite element modelling in order to overcome such contradictory requirements. The answer is the so-called absorbing boundary conditions (ABCs).

While keeping in mind that the substitution is not perfect, they emulate the infinite space that surrounds a finite computational domain. Satisfying some requirements, the computed solution is then a good estimation of what would be computed, if it was feasible,

within a infinite domain. Nevertheless, these ABCs only absorb fields and cannot in any case replace the sources of the electromagnetic fields. The sources cannot therefore be placed outside of the ABCs.

The requirements that a ABCs should fulfil depends on its location with respect to the source of the field. If the ABC is only able to handle homogeneous plane waves, it must then be placed far from any sources. If the ABC is however able to handle evanescent fields, it can then be placed close to the source, thus reducing the overall computational domain cost.

2.2.6 Short history of radiating boundary conditions

Several local ABCs solutions have been developed over the years. To summarize, there exist two categories of ABCs:

- *global ABCs*[80]: the field at any point on the enclosing boundary of a given volume can be expressed as retarded-time integral of the field upon a surface enclosing all the sources,

- *local ABCs*: the field on the boundary is expressed as a function of the field in the vicinity (closest points of the mesh) of the considered point.

As global ABCs are computationally expensive, all widely used ABCs in the past are local ABCs. The first technique was extrapolation [81]. It was then followed by "radiating boundary" [82]. Another one was the matched layer which consisted in surrounding the domain with an absorbing medium whose impedance matches the impedance of the main simulation domain. The most popular one was the one-way approximation of the wave equation initially described by Engquist-Majda ABC [83] for acoustic waves. It was then applied to electromagnetism by Mur [84] and generalized later by Trefethen and Halpern [85]. Higdon ABC [86] is also based on the one-way approximation.

However, all of the previously cited ABC techniques share the same Achilles heel. A wave is only absorbed without reflection in particular cases: a plane wave propagating perpendicularly to the boundary. Since realistic problems in electromagnetism involve both travelling and evanescent waves, it is not well suited. In the 1990's new techniques have thus been developed to emulate radiating boundary conditions inside a bounded computational domain while overcoming the limitations of the standard ABCs: Perfectly Matched Layer [57] and complementary operators method (COM)[87]. The PML technique will be further developed in Chapter 3. The aim here is to use the PML to handle outgoing waves without reflections in a plasma filled domain where both the slow wave and fast wave exist. On the antenna structure, the boundary conditions could be different from metallic boundary conditions that are commonly applied in order to account for the non-linear wave-plasma interactions at the wall due to RF sheaths that will be presented in the next section.

2.3 Generation of radio-frequency sheaths by waves

Spurious interactions [35–37] due to RF sheaths [34] between the peripheral plasma of magnetic fusion devices and powered ICRH antennas are often setting the operational limits of the radio-frequency systems and can even perturb other antennas [44]. Investigation on plasma sheath formation by RF waves has established that the most likely origin of this physical mechanism is RF rectification [88, 89]. However, in a tokamak device with ICRH power, RF sheaths are associated with plasma waves, which have quite-complicated

structures, and they are often classified into the following two broad categories: far-field sheaths and near-field sheaths.

First, RF sheaths, referred to as far-field sheaths, are generated on material surfaces when a launched FW propagates to a wall due to SOL propagation or poor central absorption [90] and the magnetic flux surfaces do not match the wall shape. In this case the incident FW typically generates a reflected FW and an evanescent SW by mode conversion at the wall together with the rectified sheath potential. Robust analytical models to understand the mechanisms behind far-field sheath formation have been developed [51, 91, 92]. The sheath potentials resulting from far-field sheaths are considered to be less important than near-field sheaths from the standpoint of local damage to material structures. However, if far-field sheaths cover a substantial portion of the wall, it could lead to reduced heating efficiency by sheath power dissipation in the entire sheath volume.

Second, sheaths on the antenna surface and nearby material boundaries, such as limiters, are referred to as near-field sheaths. The physical mechanisms behind RF near-fields sheaths will be explained in Chapter 2. Near-field sheaths are ascribed to the generation of the parasitic slow wave by the current straps on the ICRH antenna. The slow wave has a large $E_{\|}$ component (electric field component parallel to the background magnetic field), that can be generated by either antenna currents with a component parallel to the magnetic field line or by spatial variation of the distribution of charge of the straps. The slow wave then propagates until it reaches a material surface.

Before going in details in the current understanding of the physical ingredients in RF sheath formation, let us introduce some basics concept about sheath with the thermal or Debye sheath.

2.3.1 Recall of the Debye sheath physics

A volume, as illustrated by Figure 2.6, occupied by charged particles consists of two separate regions:

- The first is the plasma itself which usually fills the majority of the available space. The plasma is by definition electrically neutral or at least quasi-neutral at scale larger than the Debye length.
- The second is the sheath surrounding all the plasma in the chamber, usually thin and adjacent to a solid surface, which has a greater density of positive ions, and hence an overall excess positive charge, that balances an opposite negative charge on the surface of a material with which it is in contact.

Poisson's equation allows determining the characteristic length over which any perturbation of potential inside the plasma is screened. The sheath typical size is of the order of a few electronic Debye length given by [93]:

$$\lambda_{De} = \left(\frac{\varepsilon_0 k_B T_e}{n_e e^2} \right)^{1/2}. \tag{2.37}$$

Taking typical SOL conditions with $T_e = 20$ eV and $n_e = 10^{18}$ m^3 yields a sheath size of the order of 10^{-4} m. This length is much smaller than the typical size of the open magnetic field lines in the SOL. Furthermore, it is also smaller than the typical particles mean free path in the SOL [3]. This sheath can thus be assumed collisionless.

Due to their higher mobility more electrons reach the wall than ions. As more electrons than ions leave the plasma, a separation of charge is occurring and positive charge density

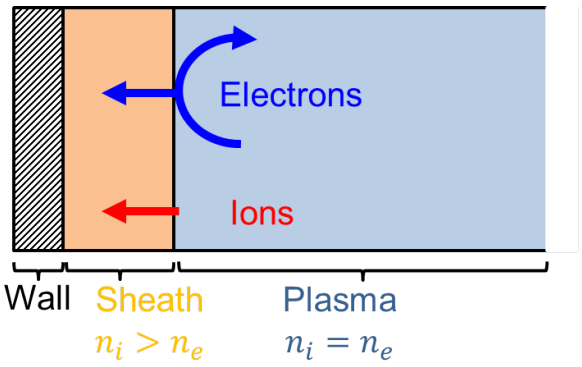

Figure 2.6: Sketch of the Debye sheath formation at the walls and of transport of particles towards the walls.

appears in a thin region corresponding to the sheath. The negative potential of the wall in respect to the plasma generated a self-consistent electric field which repels the electrons and speed up the ions. In the beginning this electric field is not sufficient to repel significantly the electrons flux. As more electrons leave the plasma, this electric field increases until an equilibrium dynamical state is reached where the ions and electrons fluxes in absolute value are equal on the wall. At this moment the loss of ions and electrons on the wall are equal. Ions gain energy in the sheath at the expense of the electrons which are cooled down because only the high velocity electrons can leave the plasma while the other ones are repelled by the sheath potential.

By analysing the sheath side of the plasma-sheath interface, we will find the Bohm criterion. Assuming steady state, no collisions, inertia free electrons and a Maxwellian distribution function of the electrons, the Bohm criterion giving the speed of the ions at the sheath entrance v_{se} can be obtained. Using quasi-neutrality in the plasma, the Poisson's equation in the sheath, momentum conservation and energy conservation, it gives at the end [93, 94]:

$$v_{se} \geq c_s = \left[\frac{k_B\left(T_e + \gamma T_i\right)}{m_i}\right]^{1/2}, \tag{2.38}$$

where $\gamma = 1$ for isothermal flow, 5/3 for adiabatic flow with isotropic pressure or 3 for 1D adiabatic flow, the subscript se denotes the sheath edge with the plasma and c_s the sound speed. In the following, isothermal flow will be assumed. It thus yields $\gamma = 1$. The ion velocity at the sheath entrance must be equal or higher than the sound speed in order to reach the wall. A generalized Bohm criterion has been found within a kinetic approach [95].

Since the ion mean velocity in the plasma is null, the Bohm criterion justifies the existence of an intermediate quasi-neutral region between the sheath and the plasma whose main purpose is to transfer energy from the electrons to the ions in order to accelerate them to the sound speed at the sheath entrance. It can alternatively be seen as an "imperfection" in the Debye shielding [93]. As a consequence, a small but non-zero electric field exists in this region called presheath whose size is much larger than the sheath size. The density at the sheath edge, due to the pre-sheath existence, is only half of the plasma density at the stagnation point [93]:

$$n_{se} = \frac{n_i}{2}. \tag{2.39}$$

It also gives a condition on the ion speed in the presheath-sheath interface: $v_{se} \leq c_s$. The ion velocity at the sheath entrance is thus $v_{se} = c_s$.

Equalling electrons and ions fluxes at the sheath entrance gives the potential drop in the sheath compared to the plasma [93]:

$$V_f = \frac{k_B T_e}{2e} \ln \left[2\pi \frac{m_e}{m_i} \left(1 + \frac{T_i}{T_e} \right) \right]. \tag{2.40}$$

This potential is also called floating potential since no other force, except the one created by the plasma, acts on the wall. Note that the density does not intervene. Since the electron mass is much smaller than the ion mass, V_f is negative. The T_i dependence is easily explained. The higher the ion temperature is, the higher the ion flux of the wall is and the lower the electric field necessary to accelerate them to the Bohm speed is. The floating potential is this smaller. The $1/T_e$ dependence is explained by the inverse reasoning. For an electrically insulated wall, the wall will be negatively biased at V_f. For a wall connected to ground, the plasma will be positively biased to $-V_f$. The I-V characteristic of a 1D non-magnetized sheath has the following form [93]:

$$I = j^+ \left[1 - \exp \left(\frac{e\,(V_f - V)}{k_B T_e} \right) \right] \tag{2.41}$$

where

$$j^+ = 0.5 e n_i c_s \tag{2.42}$$

is the local ion saturation current, V_f the local floating potential given by (2.40) and $V_f - V$ is the potential difference between the plasma and the collecting plate. It has a ionic term contribution (first term on the left hand side) and a electronic contribution (second term in the left hand side). This expression holds true as long as $V_f - V > 0$ (i.e. as long as a sheath exists at the plasma-wall interface).

When there is no magnetic field or when the magnetic field is normal of the wall in an ideal situation, it has no influence on the sheath description [93]. In reality however, surfaces are tilted to spread the power onto the target. The tilt of the magnetic field will change the sheath description [96]. For the sheath to form, the incident angle of the magnetic field compared to the wall should not be too small. Otherwise, if case of grazing incidence, the electron loss to the wall is negligible due to the gyromotion of the electrons. The criterion for the sheath formation takes the following form:

$$\sin \alpha = \frac{B_n}{B} > \left(\frac{m_e}{m_i} \right)^{1/2}, \tag{2.43}$$

where B_n is the perpendicular component of the static magnetic field with respect the wall. Below that limit the present sheath theory becomes questionable since ions can be lost faster than electrons. When the magnetic field is not perpendicular to the wall, another region called magnetic presheath appears [96–98]. It mainly affects the ion velocity condition at the sheath edge that must be along the magnetic field direction.

Until now, no RF electric fields were assumed. When they exist, the electrons are further accelerated and the electron density in the sheath oscillates at the wave frequency while the ions are considered immobile. It results that more electrons are lost and the plasma becomes positively charged to compensate this additional losses induced by the RF electric field component, as it will be shown in Section 2.3.2.

2.3.2 Properties derived from principles driving oscillating sheaths for self-consistent modelling

Self-consistent modelling of RF sheaths towards first principles have just started a few years ago to take into account the fact that the RF sheath itself modifies the boundary

conditions for the slow wave and for the fast wave, as it will be shown in Section 2.3.3, which depends on the near field in front of the antenna. Thus a proper modelling should be done to describe simultaneously the RF sheath effects on the boundary conditions and on rectification processes, which influence each other. The problem consequently becomes non-linear. Until now, it has relied on a few key properties: RF sheath rectification and RF sheath capacitance. In this thesis, the model also assumes that the RF and DC effects can be split and treated individually. The DC plasma potential comes from average value over the period of the launched wave and the sheath boundary condition accounts for the instantaneous response in the sheath zone at the frequency of the launched wave.

2.3.2.1 Splitting of RF and DC quantities

In the immediate vicinity of the ICRH launcher in the SOL, the "open" magnetic field lines are bounded by lateral metallic walls, as sketched in Figure 2.7. Between the bulk plasma (in purple) and the metallic wall (in grey), a thin transition layer or sheath (in orange) is established. An equivalent dielectric circuit of the sheath is also shown on Figure 2.7. The following assumptions are considered [94]:

- The ions respond only to the time-averaged potentials whereas the electrons respond to the instantaneous potentials and carry the RF discharge current.
- The electron density is zero within the sheath regions while the ion density is uniform and constant in time everywhere in the plasma and sheath region.
- There is no transverse variation.

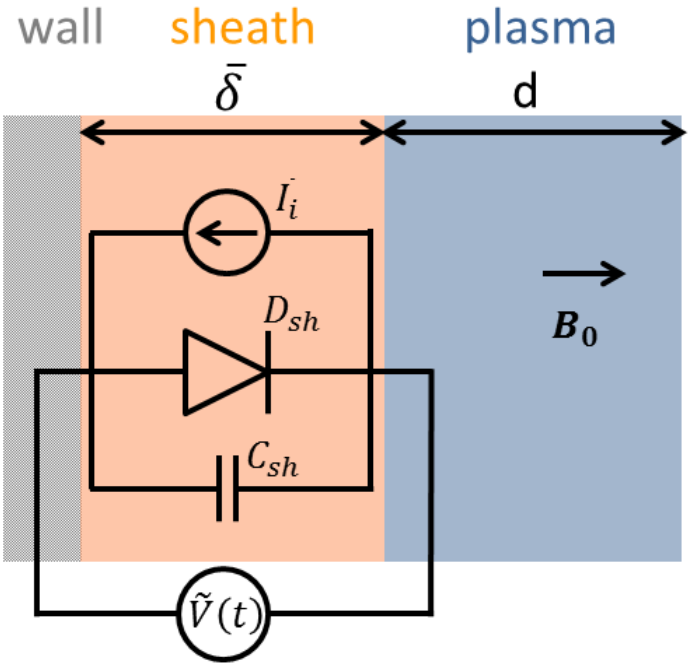

Figure 2.7: Equivalent electric circuit of the RF sheath appearing between the wall and the plasma where RF waves are propagating.

From (2.10), the admittance of a bulk plasma slab of thickness d and cross-sectional area A gives in the absence of magnetic field and with electron–neutral collisions [94]:

$$Y_p = j\omega C_0 + \frac{1}{j\omega L_p + R_p}, \tag{2.44}$$

where $C_0 = \varepsilon_0 A/d$ is the vacuum capacitance, $L_p = \omega_{pe}^{-2} C_0^{-1}$ is the plasma inductance and $R_p = \nu_m L_p$ is the plasma resistance. ν_m is the electron–neutral collision frequency for momentum transfer. This form for Y_p represents the series combination of L_p and R_p in parallel with C_0. The displacement current that flows through C_0 is much smaller than the conduction current that flows through L_p and R_p. Assuming that the sheath capacitance has a similar form than the plasma capacitance $C_{sh} = \varepsilon_0 A/\overline{\delta}$ gives when compared a factor $d/\overline{\delta}$. The sheath capacitance is thus much greater than the plasma capacitance since $d \gg \overline{\delta}$.

In the same way comparing C_{sh} with L_p gives a ratio $\omega_{pe}^{-2} C_0^{-2} \overline{\delta}/d$. With the typical electron density in the SOL of a tokamak being $\approx 10^{18}$ m^{-3}, it results in $L_p \ll C_{sh}$. The inductive impedance of the bulk plasma is small compared to the capacitive impedance of the sheaths, such that almost all the applied RF voltage due to RF waves appears across the sheath. The electrostatic approximation is assumed in the sheath region. The resistive part of the sheath is neglected. It is assumed that the RF current is mainly a displacement going through the capacitor branch of the circuit. When dealing with DC currents, the conduction currents through the sheaths go entirely through the diode [94]. Consequently a clear separation can be made between RF and DC effects. Association of DC currents with the diode and RF current with the capacitor is the simplest model. More complex models would assume otherwise.

The instantaneous sheath potential $\tilde{V}(t)$ is supposed to be composed of a DC part V_{DC} and of an RF part oscillating at the RF generator frequency ω_0 and with amplitude V_{RF}. No other frequency is considered, contrary to [99]. It yields:

$$\tilde{V}(t) = V_{DC} + V_{RF} \cos(\omega_0 t), \tag{2.45}$$

where V_{RF} is function of the RF electric field $\mathbf{E_{RF}}$ whose field distribution is supposed known. V_{RF} is the oscillating sheath voltage generated by RF waves. The wall is assumed electrically grounded, so that the DC sheath potential V_{DC} is also the local DC plasma potential. The instantaneous sheath voltage $\tilde{V}(t)$ associated with the instantaneous conduction current into the sheath $\tilde{I}(t)$ gives the ideal sheath I-V characteristic:

$$\tilde{I}(t) = j^+ \left[1 - \exp\left(\frac{e\left(V_f - \tilde{V}(t)\right)}{k_B T_e} \right) \right] \tag{2.46}$$

where j^+ is the local ion saturation current (2.42), V_f the local floating potential in the absence of RF waves given by (2.40). The factor 0.5 in j^+ accounts for the density drop in the presheath according to (2.39). c_s is the ion sound speed at the sheath entrance ((2.38)) and n_i is the plasma density. This I-V electrical characteristic was rigorously established for DC sheaths with a wall normal to $\mathbf{B}$. No equivalent presently exists with tilted $\mathbf{B_0}$, like the Chodura model for DC sheaths [96].

2.3.2.2 Sheath rectification

Since the sheath exhibits a non-linear I-V characteristic, a rectification process occurs that provide the RF to DC coupling. The sheath I-V characteristic established for DC behaviour

is extended to a dynamical regime. More elaborate treatments of the conduction current going through the diode branch of the sheath exist in the literature [100]. Averaging the instantaneous conduction current over an RF period $T_0 = 2\pi/\omega_0$ and combining (2.45) with (2.46) yields:

$$\langle \tilde{I}(t) \rangle = j^+ \Big\langle 1 - \exp\left(\frac{e\left(V_f - V_{DC} - V_{RF}\cos(\omega_0 t)\right)}{k_B T_e} \right) \Big\rangle, \tag{2.47}$$

where $\langle\rangle$ denotes the time average of a quantity over a RF period. Writing explicitly the average in time with the integral form reads:

$$\langle \tilde{I}(t) \rangle = j^+ \left[1 - \frac{1}{T_0} \int_t^{t+T_0} \exp\left(\frac{e\left(V_f - V_{DC}\right)}{k_B T_e} \right) \exp\left(\frac{-eV_{RF}\cos(\omega_0 t)}{k_B T_e} \right) \right] \tag{2.48}$$

The modified Bessel function of order 0 I_0 is defined as:

$$I_0(z) = \frac{1}{\pi} \int_0^{\pi} \exp\left[z\cos(\varphi) \right] d\varphi. \tag{2.49}$$

Using the definition of the modified Bessel function, (2.48) can be rewritten:

$$\langle \tilde{I}(t) \rangle = j^+ \left[1 - \exp\left(\frac{e\left(V_f - V_{DC}\right)}{k_B T_e} \right) I_0\left(\frac{eV_{RF}}{k_B T_e} \right) \right]. \tag{2.50}$$

A biasing voltage V_b is introduced through the following definition:

$$V_b = \frac{k_B T_e}{e} \ln\left[I_0\left(\frac{eV_{RF}}{k_B T_e} \right) \right], \tag{2.51}$$

where I_0 is the modified Bessel function of order 0 defined in (2.49) and V_{RF} the oscillating part of the sheath voltage in (2.45). With this definition, the biasing voltage can be added in the argument of the exponential of the average conduction current through the sheath. It yields:

$$\bar{I} \equiv \langle \tilde{I}(t) \rangle = j^+ \left[1 - \exp\left(\frac{e\left(V_f + V_b - V_{DC}\right)}{k_B T_e} \right) \right]. \tag{2.52}$$

(2.52) is similar to (2.46) with the addition of an additional term in the argument of the exponential. Everything happens as if the RF waves were positively biasing the wall to the DC voltage V_b. RF waves whose average amplitude over a period is null can thus generate a positive bias. This biasing will force the plasma to increase its potential V_{DC} significantly to keep quasi-neutrality in the plasma [89]. The rectified sheath potential in the vicinity of ICRH antennas can reach the order of kVwhen a large source of current is available. An analogy can be found with a diodes bridge that rectifies oscillating current into DC current. No rectification model presently exist in the case of tilted magnetic field such as the Chodura sheath [96] for DC sheaths.

2.3.2.3 Sheath capacitance

RF fields can significantly change the DC plasma potential through RF sheath rectification. Inversely DC potentials act non-linearly on RF fields through the RF sheath capacitance.

For the RF waves, the sheaths are assimilated to parallel-plate capacitors filled with a dielectric material having a dielectric constant ε_{sh}. Since the resistive part of the sheath

is neglected, ε_{sh} does not include an imaginary term representing power dissipation in the sheath. This description is motivated since the sheath is a region depleted of electrons similar to vacuum. In-line with this view, the distance between the capacitor plate is of the order of the local, time average sheath width δ. It is implicitly assumed that the RF current through the sheaths is predominantly a linear displacement current that goes exclusively through the capacitor. Despite the high RF oscillations amplitude, the sheath width δ follows the Child-Langmuir law for plane electrodes [101, 102]:

$$\delta\left(x,y\right)=\lambda_{De}\left(\frac{eV_{DC}\left(x,y\right)}{k_BT_e}\right)^{3/4}, \tag{2.53}$$

where λ_{De} is the electron Debye length whose expression is given by (2.37).

The Child-Langmuir law was established for DC sheaths. In the context of capacitive RF discharges, more refined models were developed in [100, 103]. In presence of high power waves, the instantaneous sheath width may be subject to large RF oscillations at frequency ω_0 around its mean value, which may affect the sheath capacitance. They indicate that the Child-Langmuir law should be modified by multiplying it by a factor $\sqrt{50/27}\approx 1.36$ to take into account oscillating effects whereas the effective sheath dielectric constant should be $\varepsilon_{sh}\sim 1.226$ instead of $\varepsilon_{sh}\sim 1$. The dimensionality of the ratio ε_{sh}/δ is equivalent to a capacitance per surface unit:

$$C^*_{sh}=\frac{\varepsilon_{sh}}{\delta}. \tag{2.54}$$

2.3.3 Sheath boundary conditions

The sheath capacitance C^*_{sh} will modify the behaviour of the sheaths in presence of RF waves. Since the sheath width δ usually is much thinner by several orders of magnitude than the typical toroidal extension $L_\parallel$ of the simulation domain, its consequence on the RF electric field propagation is accounted for via a RF sheath boundary condition (SBC) that replaces the classical metallic boundary condition, as it will be shown later during numerical tests in Chapter 5. Myra and D'Ippolito developed the sheath boundary conditions formalism to account for this effect [53]. Although they rigorously prevail only at the sheath/plasma interface, the RF-SBC is applied directly at the wall. Then it would be virtually impossible at this time to calculate detailed wave phenomena over the entire volume of the SOL and in the sheaths simultaneously. As the typical spatial scales are very different, a prohibitive number of grid points would be required in the mesh if the typical grid size is adjusted to the size needed to get a fine enough spatial resolution of the physics in the sheath region. Thus huge amount of computational resources would be required and consumed. Some adjustments could be however made with multi-scales grids but the grids should not be vastly different at the interfaces for a numerically stable calculation.

An arbitrary tilt of the static magnetic field is envisaged as shown in Figure 2.8. The complete derivation can be found in [53, 104]. Two coordinate systems are defined. The first one is defined with respect to the magnetic field whereas the second one is defined with respect to the wall surface or the sheath surface. The RF electric field $\mathbf{E}$ relative to both the sheath surface and the magnetic field thus reads:

$$\mathbf{E}=\left(E_n\mathbf{e_n}+\mathbf{E_t}\right)\exp\left(i\mathbf{k}\cdot\mathbf{r}-i\omega t\right)=\left(E_\parallel\mathbf{b}+\mathbf{E}_\perp\right)\exp\left(i\mathbf{k}\cdot\mathbf{r}-i\omega t\right). \tag{2.55}$$

In ICRH, the value of k_0 is usually much smaller compared to k_t. The sheath is also assumes to be thin. Then the electrostatic approximation is valid in the sheath region.

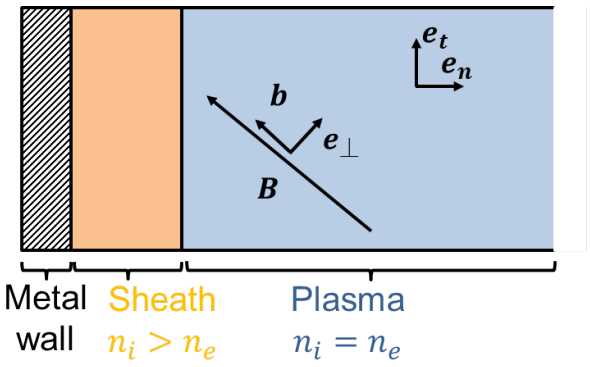

Figure 2.8: Schematic representation of the sheath and the two coordinate systems defined when the magnetic field is tilted. The first system is with respect to the magnetic field $(\mathbf{b}, \mathbf{e}_\perp)$. The second system is with respect to the wall $(\mathbf{e_t}, \mathbf{e_n})$. The normal $\mathbf{e_n}$ is defined to point from the wall to the plasma.

This requires:

$$|\mathbf{k_t}|\,\delta \ll 1, \tag{2.56}$$

where δ is till the local time averaged sheath width. In the electrostatic limit, the electric field in the sheath is expressed only with the electric potential Φ^{sh} as follows:

$$\mathbf{E^{(sh)}} = -\nabla V_{RF}^{(sh)}. \tag{2.57}$$

Since the interest is only on the sheath effect on the fundamental wave component at frequency ω, the oscillating motion of the sheath at frequency ω can be neglected. The boundary condition is thus applied at the location of the time averaged sheath width. Electromagnetism theory imposes the continuity of $D_n = \mathbf{e_n} \cdot \mathbf{D} = \mathbf{e_n} \cdot \bar{\bar{\varepsilon}} \cdot \mathbf{E}$ across an arbitrary interface. Here the interface separates the plasma region from the sheath region. Superscripts (pl) and (sh) denote quantities on the plasma side and on the sheath side respectively. A discontinuity in the mean density is assumed between the plasma and sheath. Consequently a discontinuity is also present in the dielectric tensor. ε_{sh} is the sheath dielectric constant defined in Section 2.3.2.3. At the plasma-sheath interface, continuity of D_n reads:

$$D_n^{(sh)} \equiv \varepsilon_{sh} E_n^{(sh)} = D_n^{(pl)}. \tag{2.58}$$

In the electrostatic limit, (2.57) is combined with (2.58) to give:

$$-\varepsilon_{sh} \nabla V_{RF}^{sh} = D_n^{(pl)}. \tag{2.59}$$

Integrating (2.59) from the metallic wall through the sheath in the direction of the normal vector $\mathbf{e_n}$ yields:

$$-\varepsilon_{sh} \Phi^{(sh)} = \delta D_n^{(pl)}, \tag{2.60}$$

with the conditions $V_{RF}^{(sh)} = 0$ on the wall and $V_{RF}^{(sh)} = V_{RF}$ at the sheath-plasma interface. Taking the tangential gradient $\mathbf{E_t} = -\nabla_t \phi$ of (2.60) and imposing the continuity of the tangential electric field $\mathbf{E_t}$ across an interface according to classical macroscopic electromagnetism theory yields:

$$\mathbf{E_t}^{(sh)} = \nabla_t \left(\frac{\delta}{\varepsilon_{sh}} D_n^{(pl)} \right). \tag{2.61}$$

which gives the constraint only involving the RF fields on the plasma side of the sheath-plasma interface. Note that in the limit when the sheath vanishes ($\delta \to 0$), (2.61) reduces to the usual metallic BC. Remembering (2.54), (2.61) can be re-written:

$$\mathbf{E_t}^{(pl)} = \nabla_t \left(\frac{1}{C^*_{sh}} D_n^{(pl)} \right). \tag{2.62}$$

The superscript (sh) in (2.61) is replaced by (pl) in (2.62) on the left hand side. From (2.62), the right hand side represents the effect of the sheath capacitance on the parallel electric field structure. It will thus influence the slow wave propagation in the plasma.

In the case where $\mathbf{B}$ is perpendicular to the wall, $\mathbf{e_n} = \mathbf{b}$ and $\mathbf{e_t} = \mathbf{e}_\perp$. Dropping also the (pl) superscript, (2.62) consequently reads:

$$\mathbf{E}_\perp = \nabla_\perp \left(\frac{1}{C^*_{sh}} D_\parallel \right). \tag{2.63}$$

The sheath capacitance expression in (2.54) allows us to define an expression for the oscillating sheath voltage V_{RF} in (2.45) that reads:

$$V_{RF} = \oint E_{RF} \cdot dl = \frac{D_n}{C^*_{sh}}. \tag{2.64}$$

It may be noteworthy to recall that when $|\varepsilon_\parallel|$ is high that the FW and the SW are totally decoupled. Moreover if the wall is perpendicular to $\mathbf{B}$ than $D_n = \varepsilon_\parallel E_\parallel$. In that case the parallel electric field $E_\parallel$ is mainly due to the SW.

A new class of modes, called Sheath-Plasma Waves (SPW) [53], arises from the SBCs as they do not exist with metallic BCs.

The form of (2.62) results of course from the approximation that the current carried through the sheath is a displacement current in the immobile ion limit. What would become the SBC if a part of conduction current was also accounted for? The electrostatic approximation is justified in the thin sheath limit. As the sheath width δ was averaged over time, the SBC moreover assumed the static sheath approximation that neglect the effects of the wave harmonics and of the sheath dynamical oscillations. The density is assumed as the time average density in the present model. The impact of the fast time scale physics on slow time scale physics only started to be considered due to its complexity [105].

The derivation of the sheath boundary condition assumes that the sheath is effectively a vacuum region for the RF waves, which corresponds to the zero-th order in the sheath description [92].

The resistive part of the sheath was neglected and only its capacitive nature was accounted for. Calculations in ref [53] however suggest that the validity of this assumption is better for larger amplitude of $E_\parallel$.

Finally kinetic effects must be considered to investigate the correct physics inside the sheath, at least to verify that the present assumptions made to derive the sheath boundary condition are enough to capture the essential physics. It thus raises the question on how to connect a kinetic sheath with a cold plasma and how to handle the additional cost of kinetic equations where integrals must be evaluated numerically instead of analytical expressions.

2.3.4 DC biasing model of the SOL plasma with DC conductivity tensor

A constant homogeneous electric field applied perpendicularly to the static magnetic field $\mathbf{B}$ in fully ionized plasmas causes $\mathbf{E} \times \mathbf{B}$ drift for both ions and electrons with a common

velocity in amplitude and in direction. Thus, no separation of charges occurs, no friction occurs and hence no particles flux and no DC currents along the electric field direction are generated. The transverse DC conductivity in steady state is zero. In partially ionized plasmas, DC current are simply proportional to the applied electric field with the relation $\mathbf{j} = \sigma_{DC}\mathbf{E}$ where σ_{DC} is the DC conductivity determined by collisions between charged particles and neutrals.

Several observations indicating the presence of perpendicular DC currents have nevertheless been reported in many experiments such as ASDEX Upgrade [106]. One example is provided by biasing experiments where an electrode is installed into the plasma inside the separatrix and a voltage is applied between the electrode and the limiter (or divertor). It results first in a bias of the whole flux surface due to the huge Spitzer parallel conductivity (1.7). Second, radial DC current flows from the core through the separatrix towards another electrode (limiter) was measured [107]. A flux average transverse DC conductivity has thus been deduced.

Moreover DC currents, ascribed to RF sheaths, have been observed in several experiments on TEXTOR [37], ASDEX Upgrade [108] and Tore Supra [46] in the vicinity of active ICRH antennas. Negative currents have been measured near the antenna structure and positive current far from it [42] on magnetic field lines connected to the powered ICRH antenna. Probes are measuring significant floating potential on the outer side of the active antenna [45]. However the path between the probe and the antenna follow the magnetic field line that is intersected by the antenna side limiter, as it will be shown in Section 2.4. Then how can the probe measure floating potential on the outer side of the limiter when it is not supposed to be connected magnetically to the active part of the antenna? During the last experimental campaign on Tore Supra in 2011, larger radial structures of the floating potential with larger amplitude was measured on the prototype Faraday screen (see Section 2.4.5) compared to the classical Faraday screen. Is there a link between both that can explained the larger structures? Is the antenna status and geometry modifying the transport parameters of the SOL.

It is noteworthy to mention that the DC perpendicular conductivity can only be a small fraction of the parallel Spitzer conductivity (1.7), since huge gradient of DC plasma potential will appear in the radial direction [45, 109].

Several theoretical modelling of RF sheaths proposed explanations for DC currents [54, 110]. Different mechanisms for the formation of radial electric field in a tokamak have been proposed [111, 112]: ions-neutrals collisions, viscosity and inertia. DC currents in fully ionized plasmas arise only in presence of inhomogeneous electric fields (polarization current is neglected since there is no temporal derivative of the electric field). As a result, the DC current density is not proportional to the electric field but to its spatial derivatives. Ions-neutrals collisions are associated with the first order derivative whereas viscosity and inertia are associated with second and third derivatives, respectively. This indicates that, generally speaking, it is incorrect to introduce the DC conductivity tensor as it is commonly defined. Instead one can introduce with analogy an "effective" DC conductivity tensor using dimensionality arguments.

Writing the particle and momentum balance equations for electrons and ions gives access to the expressions of the different terms for the perpendicular DC current [112]. Each term is associated to one possible mechanism of radial DC currents formation written with the DC plasma potential V_{DC}:

- **Friction ion-neutrals**: In the case of ion collisions with neutrals, the transverse

DC plasma conductivity $\sigma_{\perp DC}$ is a scalar quantity and $\mathbf{j_{\perp i-N}}$ reads [112]:

$$\mathbf{j_{\perp i-N}} = -\sigma_{\perp DC}\nabla_{\perp}V_{DC}, \tag{2.65}$$

with

$$\sigma_{\perp DC} = -\frac{n_i q_i^2 \nu_{iN}}{M_i \Omega_i^2}, \tag{2.66}$$

where n_i is the ion density, q_i the ion charge, Ω_i the ion cyclotron frequency and $\nu_{iN} << \Omega_{ci}$ the ion neutral collision frequency. In this case, the DC conductivity is not only an effective conductivity but is the real conductivity. Then a characteristic transverse length can be defined as follows by writing $\nabla \cdot \mathbf{j} = 0$:

$$\lambda_{j,i-N}^2 = \frac{L_{\parallel}\sigma_{\perp DC}k_B T_e}{2ej^+}, \tag{2.67}$$

where $L_{\parallel}$ is the parallel connexion length and the ion saturation current.

- **Ion viscosity**: In a fully ionised plasma the only linear effective conductivity mechanism is associated with the ion viscosity η. The transverse DC current takes the form [112]:

$$\mathbf{j_{\perp vis}} = \frac{\eta}{B^2}\nabla_{\perp}\Delta_{\perp}V_{DC} \tag{2.68}$$

The classical viscosity is due to ion-ion collisions [111] where $\nu_{ii} << \Omega_{ci}$ is the ion-ion collision frequency:

$$\eta_B = \frac{0.3 n T_i \nu_{ii}}{\Omega_i^2} \tag{2.69}$$

Another possibility is to introduce the anomalous viscosity η_A since anomalous transport, whose origin is ascribed to turbulence [113], has been observed in many experiments:

$$\eta_A = n_i M_i \mu, \tag{2.70}$$

where μ is a mobility assumed to be of the order of the anomalous diffusion coefficient D. A characteristic transverse scale is associated:

$$\lambda_{vis}^2 = \rho_{ci}^2 \left(\frac{M_i}{m_e}\right)^{1/4} \left(\frac{\mu}{\rho_{ci}^2 \nu_{ii}}\right)^{1/2}. \tag{2.71}$$

- **Inertia currents** might arise due to the ion inertia when a convective flux across the magnetic field exist inside the plasma with transverse velocity $\mathbf{u_d}$. The expression for the transverse DC current in that case reads [112]:

$$\mathbf{j_{\perp inertia}} = -\frac{n_i M_i}{B^2}\left(\mathbf{u}_{\perp}\cdot\nabla_{\perp}\right)\nabla_{\perp}V_{DC}. \tag{2.72}$$

The characteristic transverse scale in that case is defined by:

$$\lambda_{inertia}^2 = \rho_{ci}^2 \left(\frac{u_d}{c_s}\frac{\lambda_{mfp}}{\rho_{ci}}\right)^{2/3} \left(\frac{M_i}{m_e}\right)^{1/3} \tag{2.73}$$

with m_e the electron mass, ν_{ii} the ion ion collision frequency, ρ_{ci} the ion Larmor radius, η the viscosity, μ the anomalous viscosity coefficient, u_d a plasma velocity responsible for the transverse current and λ_{mfp} the mean free path between two collisions.

2.3.5 Previous RF sheath modelling

We have seen that sheaths are thin positively charged regions in between the plasma and a wall whose existence maintains quasi-neutrality in the plasma. When sheaths are subjected to a RF potential in discharges or to RF waves in tokamaks, they oscillate and induce strong DC rectified potentials in the plasma [114]. An exhaustive description of RF sheaths would be fairly complex as different time scales and length scales would have to be accounted for with a kinetic description of a magnetized plasma containing several species where RF oscillations exist over a complex geometry such as a antenna. Such a description is presently impossible (and may always be). Instead partial advancements have been made by focusing individually on one aspect of the general problem with tools (theoretical and numerical) getting more and more complex. A few of these major advancements, in my opinion, will be briefly stated here.

The cold plasma approximation is usually adopted in the description. The most common way to treat RF sheaths has been by evaluating a rectified potential due to RF waves penetrating the sheaths. A voltage difference thus appears between two 1D capacitor plates along the magnetic field line calculated with $\int |\mathbf{E} \cdot \mathbf{dl}|$. This approach has been able to predict the poloidal location of high sheath regions on "long field lines" and strap phasing effects. A Faraday screen prototype on Tore Supra was designed following this approach by minimizing the integrated parallel electric field along long field lines. But recent unexpected results during experiments with the ICRH system on [56] show that this Faraday screen failed to minimize RF sheaths. On Alcator C-Mod, a field aligned antenna did not minimize RF sheaths [49, 109] but it did reduce sputtering and impurity contamination. The main issues likely come from the dimensionality reduction from 2D to 1D by integrating along field lines and the lack of the reverse feedback of the influence of the plasma DC biasing on the RF wave propagation. Linking only the fast time scale to the slow time scale is not enough. The reverse feedback of the slow time scale on the fast time scale is also necessary. In addition this approach seems to favour the far electric field whereas the near electric fields are more likely to play a role in RF formation on the antenna structure. A better description of the magnetic field lines topology is also necessary.

One main issue if the numerical simulation covers a significant volume is the prohibitive numerical cost of meshing the sheaths and the plasma due to their very different scale lengths whether with the finite difference or the finite elements methods. A truly accurate description of RF-sheath interactions needs also to consider kinetic effects and detailed sheath structures. However to capture the essential impact of sheaths on waves in the SOL and sheath potentials, the concept of RF sheaths boundary condition was developed by Myra and D'Ippolito [53, 91]. It is now able to handle the fast wave in addition to the slow wave. The sheaths at the material boundaries are treated as a thin vacuum layer for the RF waves. A similar approach was pursued for modelling sheath formation in plasma processing [115, 116].

Kohno [92] adopted the sheath boundary conditions formalism in a new finite element numerical scheme for analysing self-consistent radio-frequency (RF) sheath-plasma interaction problems in the ion cyclotron range of frequencies in simplified models for the SOL of a tokamak. He performed numerical analyses in one and two-dimensional domains several important physical properties (e.g. existence of multiple roots, hysteresis effects, sheath-plasma waves). However, even if the description is self-consistent, the description of the slow time-scale remains simple. No DC conductivity tensor is considered. No DC currents exchange are thus allowed. The antenna description is also simple. However the finite element scheme allows a better description of the antenna geometry in the future.

An attempt by Van Compernolle to implement the sheath boundary condition into

TOPICA antenna code [31, 117] using a realistic ICRH antenna model was made [118]. However, this work stopped at a primitive level. First, the sheath boundary condition is introduced to a vacuum RF model. This corresponds to a vacuum sheath. The boundary condition is thus not coupled with the plasma dielectric tensor, yielding unphysical consequences.

Smithe [119, 120] has been modelling on large scale computers with the time domain software package VORPAL [121] the behaviour of 3D imported drawings of the antenna facing a cold plasma with non linear sheath boundary conditions. He also investigated the numerical stability of finite difference time domain scheme mixing together implicit and explicit terms in the context of non-linear phenomena involving radio-frequency waves [122].

Electromagnetism PIC (Particle in Cell) simulations for sufficiently small volumes can grasp relevant sheaths physics [123]. However PIC methods cannot be used for large volumes such as simulating the behaviour of an ICRH antenna in the SOL of a tokamak due to the prohibitive numerical cost and time.

An asymmetric double probe model can lead to the generation of parallel DC currents [54]. Comparison of the fluid model with a PIC code gave similar results. A more accurate fluid description of the density with the DC potential is performed in [124]. However the double probe rectification model is simple. Circulation of DC currents decreases the DC plasma potential. The transverse transport is enhanced by convective fluxes and DC currents able to bring density around the biased flux tube.

A recent work tried to account for the wave dynamic in the sheaths and the density in the sheaths with respect to the orientation of the magnetic field [105]. It proposed to go even further to first principles and simultaneously solving Maxwell equations together with the equation of motion and the continuity equation (possibly augmented with the energy equation) rather than solving the equation of motion is an approximate way for a cold plasma. In addition, a detailed description of the ion and electron behaviour in the sheath layer itself is possible in order to understand the power losses in the sheath. The SBC approach cannot take these effects into account. Only the fast time-scale is accounted for. Such sophisticated description is however even more costly and numerical convergence is not ensured.

2.4 Overview of the ICRH system on Tore Supra

During RF heating and current drive, electromagnetic waves are launched from the outer edge of the plasma usually at low field side due to technical accessibility and propagate to a desired location inside the plasma where absorption must take place. This section will give a brief overview on the inner working if an ICRH system focusing on Tore Supra. The system is designed to couple high power waves to the plasma with the maximum achievable efficiency while keeping at an acceptable level the spurious interactions due to the presence of the RF sheaths that often impose the operational limits of the system as local overheated zone (i.e. hot spots) and impurity release into the plasma.

2.4.1 Synopsis of the excitation on high power waves in tokamaks

Whatever the frequency domain, the schematic diagram of the RF system, shown on Figure 2.9, is the same. The RF source is driven by a high voltage power supply which, in turn, is connected to the standard electrical grid at 50 Hz. The electromagnetic energy carried by the waves is transmitted from the source to the launcher through a transmission

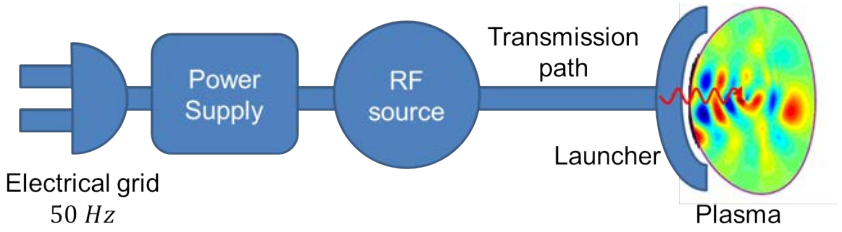

Figure 2.9: Schematic diagram of a RF system on a tokamak.

line network. The launcher is a structure that acts as an interface between the transmission circuit and the edge of the plasma.

The type of source depends upon the operating frequency. For ICRH typical frequencies, the source is called tetrode [125] or triode, whereas for LH and ECRH they are called respectively klystron [126] and gyrotron [127]. They usually deliver power between 100 kW and 1 MW CW.

The type of transmission circuit also depends of the frequency domain. For LH and ECRH typical frequencies, waveguides are used. They are rectangular gas pressurized for LH whereas they are circular vacuum pumped for ECRH. For ICRH, the transmission lines are coaxial waveguides pressurized with nitrogen.

The launcher form is also frequency dependent. The ECRH system uses mirrors [128] whereas the LH system uses an array of waveguides [129]. For the frequency domain evoked in this thesis, it was shown in Section 2.2.1 that the launcher must be an array of radiating straps. Only the ICRH system will be further described in the context of Tore Supra.

2.4.2 ICRH system on Tore Supra

As the main additional heating system and the only means to heat the ions, in the absence of high-power neutral beam injection, the ICRH system [41, 130] plays a central role in plasma scenario developments on Tore Supra.

As said above, a RF system on a tokamak is composed on RF source, a transmission line for the waves transmission to the launcher and a launcher. On Tore Supra, three horizontal ports are dedicated to ICRH antennas. These ports are fed by six transmission lines connected to the RF power plant composed of three modules of two generators each, one per launcher. The six identical RF power lines each features a synthesizer, a modulator, a solid-state wideband amplifier and a three-stage THALES tetrode amplifier. The high power stage is based on a TH525 tube [131]. The pulse duration is limited to 30 s at nominal power (2.2 MW per generator) and 500 kW in steady-state operation.

Because of the launcher electrical circuit, the six 80 m long coaxial transmission lines installed from the generator to the torus hall operate in nearly matched conditions in most situations. They are pressurized by 3 bar of nitrogen to raise the arcing threshold (i.e. lower the sensitivity to arcs). In terms of operation and development, the most critical part of the transmission line is the vacuum window, located just behind the vessel port plate for easy maintenance and replacement. The present thermal limitation of the RF lines is 2.5 MW for 30 s or 800 kW in steady state.

2.4.3 Two electrical layouts for the Tore Supra ICRH antennas

A Tore Supra ICRH antenna is a sizable object with typical dimensions about 8 m $\times$ 60 cm $\times$ 60 cm that weights about 5 tons. It is designed to operate in the frequency range

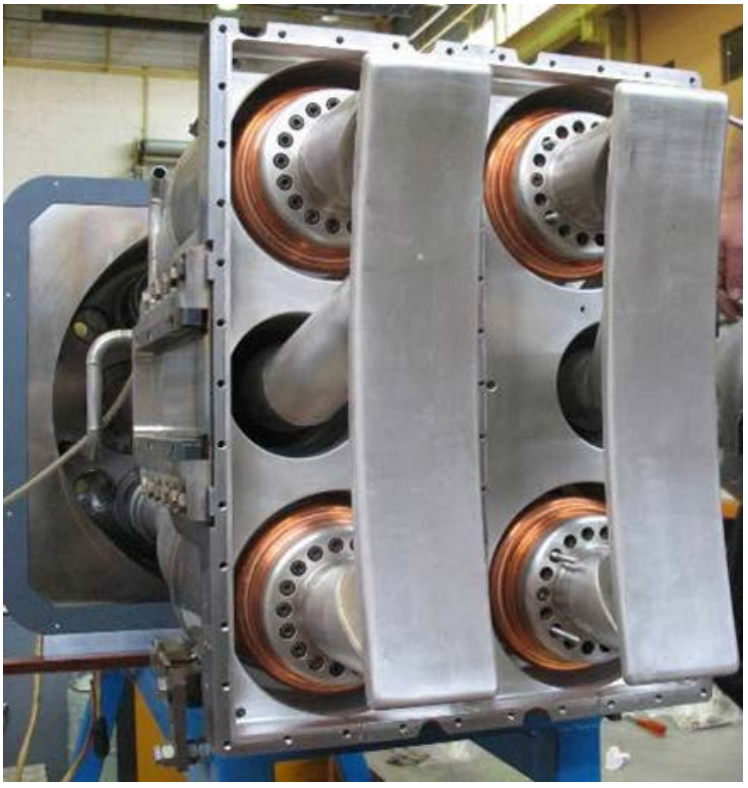

Figure 2.10: Classical two straps double resonant loops ICRH antenna on Tore Supra without its Faraday screen.

$40 - 60$ MHz. A first specificity of the launchers is their unique plug-in structure, easing the maintenance of the antenna. Tore Supra ICRH antennas are thus compact antennas, giving a high $k_{\|}$ spectrum. Hydraulic jacks can move the antennas radially inside the vacuum chamber, with a stroke of 300 mm. A second specificity of the launchers is the active cooling of the antenna front parts, required by the Tore Supra operational conditions. Even though the antennas are not CW, they are partially cooled by high-temperature pressurized water. Two electrical layouts are been tested on Tore Supra. This thesis only focuses on the part of the antennas facing the plasma, that can operate in steady-state.

2.4.3.1 The classical Tore Supra ICRH antenna

Figure 2.10 is a photograph of the TS antenna front face inside the vacuum vessel. The active elements are two poloidal straps fed near their midpoint by coaxial transmission lines. The straps are internally matched electrically to their transmission line via a resonant double loop (RDL) circuit featuring two variable capacitors at both strap extremities [132]. Each radiating strap is connected to one generator. The straps are 500 mm long, 109 mm wide and 25 mm thick. The 18 mm thick vertical septum is centered in the box.

All these original features result in high performance of the ICRH system launchers but also imply a high level of complexity in comparison with more classical antennas. The technical specifications of the system were initially to inject up to 4 MW per launcher for 30 second pulses.

Figure 2.11: Front face of the ILP antenna with the massive poloidal septum and its Faraday screen.

2.4.3.2 The load resilient ITER like prototype (ILP) ICRH antenna

ICRH antennas adaptation is one of the critical issues in the H-mode environment in the ITER baseline scenarios. In H-mode plasmas, the electrical circuit must compensate sudden increases in antenna coupling due to fast density modifications during edge localized modes (ELMs) [133] in order to prevent a mismatch in the circuit tripping the generators. This led to the development of several techniques to provide load-resilient electrical layouts under fast perturbations of the edge plasma density facing the antenna [134]. The development of an ITER-like prototype (ILP) ICRH antenna for Tore Supra was initiated in 2003 [135]. This project aimed at testing and understanding the behaviour of the ITER-like electric relevant scheme during plasma operation. The design of this prototype is based on the conjugate-T concept proposed for ITER [24] to deal with fast loading perturbations due to ELM activities or pellet injection and provided the first indications on the load tolerant properties of the electrical circuit [136].

The ILP antenna is illustrated by Figure 2.11. It features two toroidally adjacent ITER-like resonant double loops (RDL) with poloidal symmetry. Each RDL is composed of two poloidal current straps short-circuited on top or bottom of the antenna box and connected in series to a variable tuning capacitor at the other one. Each RDL is fed from a conjugate-T layout connected to the main coaxial line. Compared with the "conventional" RDL circuit, this RF circuit has lower sensitivity to a high variation of the resistive part of the load [25, 137]. The thinner (15 mm) and shorter (236 mm), but wider (131 mm) straps are further away from the plasma compared to the classical antenna by 18 mm.

As toroidal mutual coupling between straps and asymmetries greatly influence on the performance of the load resilience conjugate-T and render complicated the task of finding a match point, due to a high sensitivity to the power and phase balance between the two resonant circuits, the antenna was equipped with a Faraday screen displaying massive poloidal and toroidal septa with a thick protrusion on the antenna front to reduce inter straps coupling. The 18 mm thick vertical septum, centered in the box, present a 80 mm large protrusion. "Sharp" edges were smoothed off to improve the voltage standoff capability without arcing.

2.4.4 The lateral antenna limiters

Each ICRH and LH antenna side limiter [138] consists of two completely identical lateral protections, bolted on the left and right side of the antenna mouth (see Figure 2.12). Their purpose is to protect the delicate components of the antennas from heat fluxes coming from the plasma. The latest generation of actively cooled guard limiter must allow Tore Supra operation at high power (15 MW convective + 10 MW radiative) for long pulses. They are mainly composed of three parts: the active part, which is facing the plasma, the side plates and the header for the water supply.

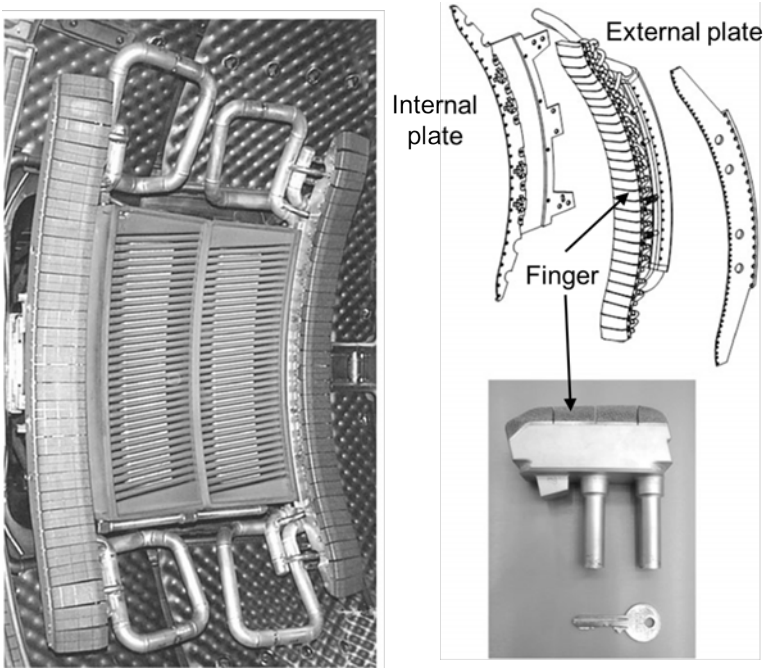

Figure 2.12: Guard limiter of Tore Supra antennas.

The active part is made out of 30 100 mm long elementary components made of CuCrZr alloy, called fingers shown on Figure 2.12. Like all the other PFCs of Tore Supra, the finger is actively cooled by pressurized water at 150 °C and feature a 10 MW m^{-2} exhaust capability. The stainless steel header, located just behind the protection, allows water to feed the 30 fingers in parallel by groups of ten, each group composed of three fingers connected in series. A thin film of boron carbide (B_4C) is applied by plasma spraying technique to surfaces not covered by CFC which receive a flux below 1 MW m^{-2}. The large toroidal extension of the limiter dimension allows by geometrical effect, to spread out the deposited power density. The toroidal surface of the limiter is indeed built in such a

way that it is almost tangent to the LCFS. The perpendicular flux seen by the finger is thus minimised.

2.4.5 Two Faraday screen designs on Tore Supra

Section 2.3 has shown that RF sheaths are generally attributed to SW rectification. Although poloidal strap arrays are meant to excite the FW, as shown in Section 2.2.1, the SW is still excited parasitically. The sources of the SW are parallel RF currents and oscillating space charges on the antenna metallic structure. In an ideal situation, the straps are always aligned with the static magnetic field. In reality it is however not the case. In presence of field line pitch a small $j_{\parallel_{RF}}$ appears along the vertical strap. This, in principle, should however not happen if the antenna structure is perfectly aligned with the static magnetic field [49]. Moreover non-homogeneous surface charge along the vertical direction of the straps can also generate a parallel electric field, i.e. SW. In order to filter-out specifically the SW [139], an object, called Faraday Screen (FS), is interposed between the straps and the plasma, consisting of metallic rods roughly aligned with the tilted field lines. It additionally protects the straps from heat fluxes coming from the plasma [40]. As illustrated on Figure 2.13(a) and (b), the Faraday screen acts in principle as a polarizing mirror letting through only the FW and filtering out the SW. When it sees a RF electric field parallel to its rods (SW), the FS induces image parallel RF currents in the opposite direction. The incident electric field is thus reflected, as shown on Figure 2.13(a). On the contrary, in presence of transverse electric fields (FW), the FS only develops limited RF currents ("magnetic shielding" [32, 139]), letting the RF wave through, as shown on Figure 2.13(b), nearly unperturbed. Experiments have shown "thermal advantage" for protecting the antenna from the fluxes coming from the plasma. The "electrical advantage" is still under debate.

On Tore Supra ICRH present antennas, the antenna box is closed on its plasma side by an actively cooled Faraday screen made of steel, copper-plated to reduce RF losses and its plasma-facing part is coated with boron carbide (B_4C) to limit high Z impurity contamination of the plasma.

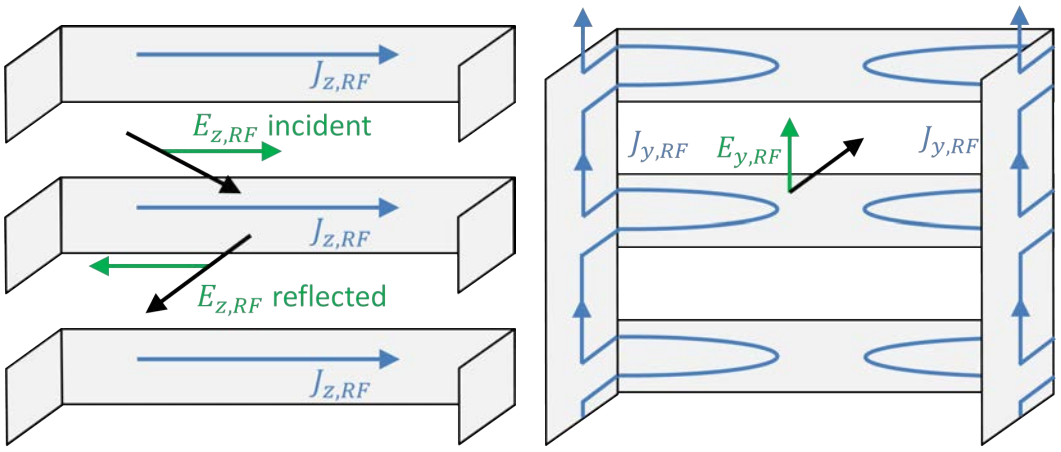

(a) (b)

Figure 2.13: Principle of the Faraday screen (FS) concept as seen from inside the antenna box. Reaction of the FS to incident RF electric field (a) parallelly and (b) transversely to the metallic FS rods.

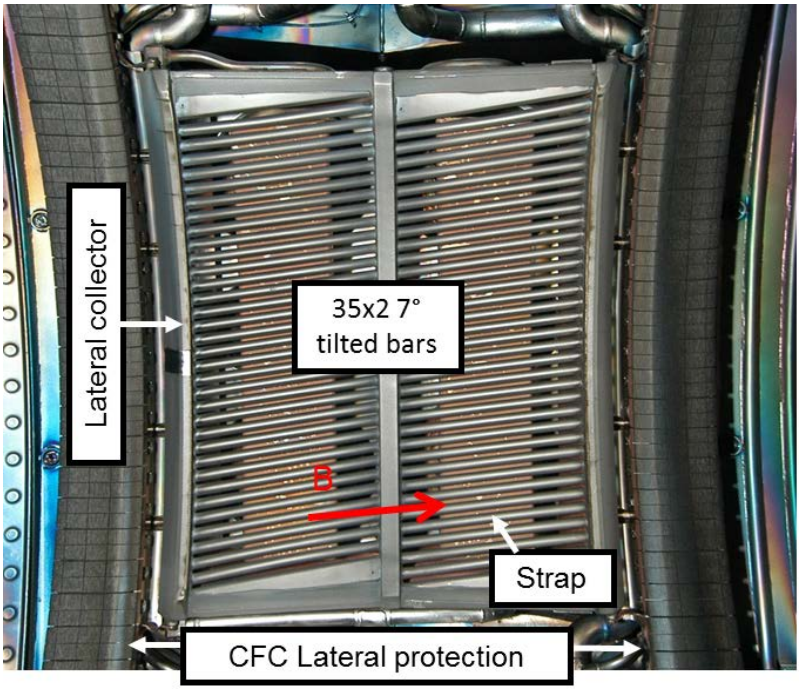

(a)

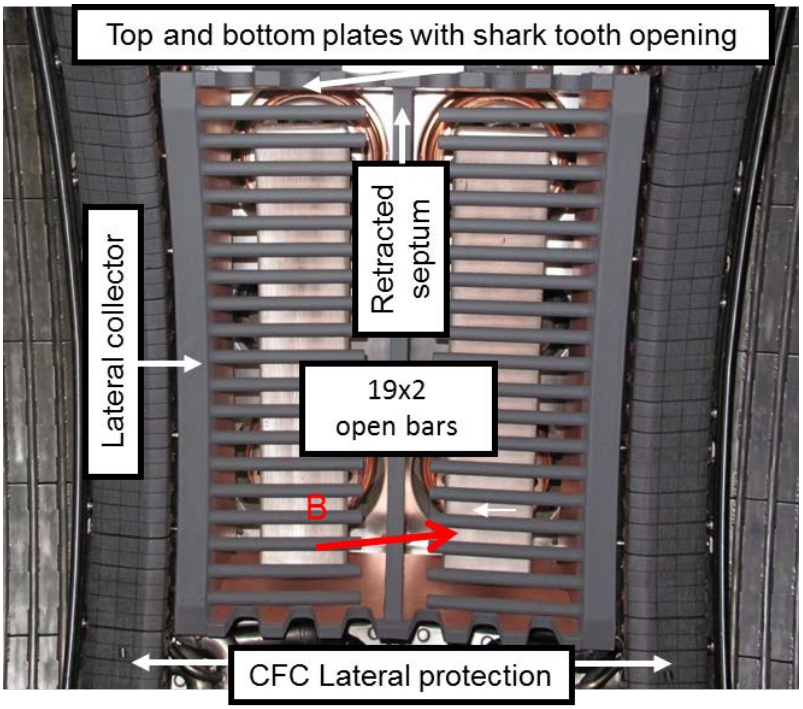

(b)

Figure 2.14: Front face of the ICRH antenna hosting for (a) the conventional and (a) the CBSB Faraday screen prototype. View inside the vacuum vessel.

Two types of FS have been tested on Tore Supra: a classical FS and a prototype FS illustrated respectively by Figure 2.14(a) and Figure 2.14(b). The prototype ICRH FS aimed at answering the questions related to thermal, mechanical and electrical upgrades for Tore Supra and ITER high-power long-discharge operations. The thermomechanical design aimed at increasing the heat exhaust capability [140] in order to reduce the thermal limitation and increase the fatigue cycle within the scope of the high-power long-discharge operation. The electrical design aimed at minimizing spurious phenomena due to RF sheaths.

Using the standard modelling approach to mitigate RF sheaths until now by minimizing the line-integrated parallel electric field led to cut paths for parallel RF currents on the antenna structure on long open field lines passing in front of the antenna [48].

Therefore the prototype FS is characterized electrically, by a slotted frame with "shark teeth" and cantilevered horizontal rods, as opposed to tilted bars (by 7°) attached on their two sides on the classical FS [36]. Cantilevered FS bars from the vertical septum additionally lower the mechanical stress level. The FS bars are also thicker (15 mm vs 12 mm) and their number was reduced from 34 to 19 to conserve transparency defined as the amount of the Faraday screen surface not covered by metal. The central septum was retracted radially. It is also called cantilevered bars and slotted box (CBSB) Faraday screen.

In view of long pulse operation at high power the new FS is actively cooled on its bars, septum and lateral collectors. Its cooling scheme was revised to accommodate the new front face design. Each FS bar features a coaxial inner return pipe, such that water inlet and outlet are located on the same side. The lateral collector have been enlarged (3.7 cm) to receive fast ion losses and with reduced welds in critical areas [140]. This improves the heat exhaust up to 1 MW/m^2 CW (and transiently 2 MW/m^2), versus 0.5 MW/m^2 (respectively 1 MW/m^2) for the classical screen. Only one of three antennas was equipped with CBSB Faraday screen, while the other two antennae were equipped with classical Faraday screens on Figure 2.14(a).

2.4.6 Diagnostics on the Tore Supra ICRH antenna

It was seen in this chapter that the properties of the SOL on a tokamak in the immediate environment of the ICRH antennas is crucial for their proper operations (wave coupling, spurious interaction due to RF sheaths). Tore Supra is a tokamak equipped with numerous diagnostics. Some of them are dedicated to monitor the ICRH antennas and measure physical quantities for later analysis. During Tore Supra plasma operation, the protection of PFCs (i.e. antenna can be considered as PFCs) relies basically on the surface temperature T_{IR} (measured by infrared thermography [141]) and metallic impurity (measured with a high-resolution vacuum ultraviolet spectrometer) monitoring systems. Furthermore ICRH antennas are not only PFCs in the sense that they not only have to keep the structural properties but also their electrical properties.

When hot spots are detected on the antenna during RF pulses by infrared monitoring system, the IR real-time control (IR-RTC) safety system [142] is triggered if T_{IR} exceeds a threshold fixed by regulations. It results in a decrease in the injected power level. However hot spots can be due to either intense heat loads that the actively cooled system of the antenna cannot moderate resulting in the rise of T_{IR} or either to flaking of the the B_4C coating. In that case the region identified as flaking is excluded from the real-time control monitoring system.

RF measurements through capacitive probes at the top and bottom of each strap allow

voltage control of the straps (in left/right strap magnitude and phase). Line RF power (forward/reflected amplitude and phase) are also measured in the feed line at generator output and at antenna input. In complement of RF measurements diagnostics, several arc safety systems [143] have been implemented to prevent any destructive damage due to arcs in the antenna and transmission lines. The safety systems stop the generator for typically 50 ms, the estimated time to kill an arc. Concerning the matching capability, a feedback matching system was implemented to allow assessment every 2 ms. Fast servomotors adjust the capacitor at the desired position [41]. A real time automatic matching monitoring system allows following loading variations on a 100 ms time scale.

Direct measurements with reciprocating Langmuir probes allow quantifying quantify the SOL perturbations in the vicinity of an active ICRH antenna. Two-dimensional (2D) mappings by reciprocating Langmuir probes [38, 144] are possible on Tore Supra. The Langmuir probes are magnetically connected to the ICRH antennas. The connection points are labelled by their altitude and their radial position with respect to the leading edge of the side limiters with an 0.5 cm accuracy. Radial resolution is provided by the probe reciprocation (i.e. the depth of the probe plunge). The probe is immersed into the SOL during the discharge several times. Between the plunges the edge safety factor $q\,(a)$ is changed in little steps. As a consequence the magnetic connections of the probe to the antenna move up poloidally providing poloidal resolution.

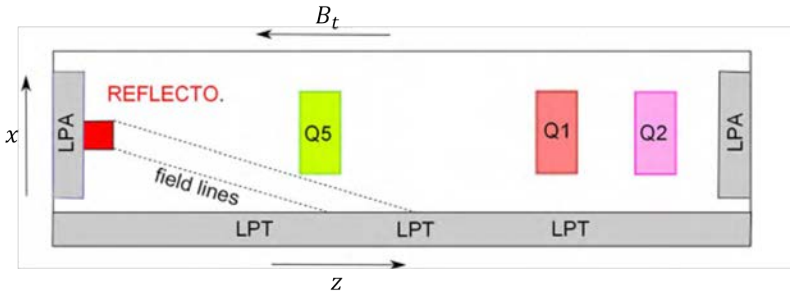

Figure 2.15: Schematics of the ICRH antennas toroidal locations in Tore Supra, with respect to the reflectometer. Q5, Q1 and Q2 label the ICRH antennas. LPA and LPT refer to the antenna limiter and toroidal limiter, respectively. The magnetic connections of the reflectometer are also shown. The figure is adapted from [145].

The density is measured with a reflectometer [146]. It is noteworthy to show the locations of the ICRH antennas with respect to the reflectometer port. Figure 2.15 shows an illustration of the torus wall unwrapped along the toroidal direction z. The reflectometer is located in the same port that the antenna protection (LPA). As the LPA is radially closer to the LCFS than the ICRH antennas, the LPA acts as a solid boundary. The $z = 0$ reference position is the LPA toroidal position. While moving along the toroidal direction, the antenna placed in the port plug Q5 is the closest antenna with respect to the reflectometer, followed by Q1 and finally Q2. The reflectometer is generally magnetically connected to the toroidal limiter (LPT). The field lines intersect the LPT below the ICRH antenna Q5. The density measurements in this thesis are averaged to smooth the fluctuations. The density profile measured in front of the reflectometer will be assumed to be also the one in front of the antenna. Thus the density n is a profile depending along on the radial coordinate x.

Other diagnostics on Tore Supra that were not used during this thesis, are available to monitor and measure the impact of ICRH antennas.

2.5 Summary

In conclusion of this chapter, we have seen that in the ICRH frequency domain ($30 - 100$ MHz) two kind of cold plasma waves can exist with very different properties: the slow wave and the fast wave. The fast wave due to its polarization will be useful for plasma heating and current drive. It is however evanescent at low density and cannot be perfectly coupled to the plasma. The slow wave, by exciting RF sheaths, is deemed at the origin of spurious interactions in the edge plasma that fix the operational limits of the antenna. Until now these two effects have been studied independently. On the contrary, they should be simulated simultaneously in a self-consistent manner. One of the consequences of RF sheaths is the modification of the density distribution in front of the ICRH antenna due to convection cells. Since the density is modified, the evanescence length that the fast wave has to tunnel through is also modified. The efficiency of the coupling of the FW is thus also changed. Typically antennas are programmed to couple a constant amount of power. The antenna thus adapt its voltage to couple the required amount of power. The amount of power that can be coupled depends on the evanescence length which in turn depends on the density. The density is modified by RF sheaths whose magnitude depends on the voltage on the antenna. The amplitude of RF sheaths has also been seen to depend on the fine details in the design of the antenna.

The model that has to be developed and implemented in numerical simulations should thus:

- be self-consistent,
- emulate single pass absorption,
- reproduce accurately FW coupling,
- be versatile in terms of geometry to handle complex ICRH antenna geometries,
- allow the full definition of a cold plasma with anisotropy, gyrotropy and inhomogeneity,
- be compatible with the implementation RF sheaths through SBCs,
- be compatible with the finite element method,
- accept realistic tokamak plasma parameters,
- correctly reproduce past and present observations to guide the design of future ICRH antennas and predict their behaviour on typical plasma scenarios.

Chapter 3

Perfectly Matched Layer to emulate radiating boundary conditions for waves in magnetized plasmas

The first part of the thesis consisted in finding a novel manner to model the outgoing propagative FW without reflection as the simulation domain is only the edge plasma. This constitutes one the two essential pieces for the code modelling wave coupling and RF sheaths simultaneously in a self-consistent manner.

Perfectly **M**atched **L**ayers (PMLs)[57] are nowadays a common tool to emulate radiating boundary conditions at infinity. They are commonly used in classical dielectric material. However they have never been used in fusion plasmas. As explained in Section 2.1, there already exist several methods to model antenna wave coupling to the plasma with their own strengths and weaknesses. Another objective is to find a wave coupling modelling method compatible with the presence of realistically modelled plasma around the antenna to account at the same time and self-consistently for wave-edge plasma interactions such as RF sheaths.

This chapter is devoted to provide a synthetic view of the PML technique as it is known in order to understand how to use it later for tokamak magnetized plasmas. The first section introduces the method in general and focuses then on PMLs requirements in cases of magnetized plasmas. The aim is to handle outgoing waves in an open boundaries domain filled with plasma without reflection. The second section gives a mathematical description of the PML technique as well as how it works. The last section is devoted to compute the analytical reflection coefficient occurring for a 1D PML with plane waves. The resulting expression gives some hints on the manner to parametrise the PML for optimal use. A number of tests are then performed numerically with monochromatic plane waves. The reflection coefficient calculated from the simulations is then compared to the analytical predictions. Finally an alternative to the reflection coefficient only defined for plane waves is presented when dealing with a spectrum of plane waves emitted by an antenna.

3.1 The Perfectly Matched Layer method

The Perfectly Matched Layer (PML) concept was originally formulated by Bérenger in 1994 [147] for use with Maxwell's equations in Cartesian coordinates, and since that time there have been several related reformulations of PML for both Maxwell's equations and for other wave equations.

In order to provide the non-reflecting boundary condition for an open-domain problem, an absorbing layer as thin as possible, called a PML, is added at the boundaries of the main calculation domain to simulate problems with open boundaries, especially in the Finite Difference Time Domain (FDTD)[148] and Finite Elements Method (FEM). The PML itself is generally ended by a perfect conductor. But in a properly tuned PML this latter boundary condition should play only a minor role. Therefore, a PML is not strictly speaking a boundary condition but an additional domain absorbing incident radiations without producing reflections ideally. It acts like a buffer area between the medium and the boundary condition. It provides good performances for a wide range of incident angles or eigenvector number while being as insensitive as possible to the shape of the waves fronts.

The key property of a PML that distinguishes it from an ordinary absorbing material is that it is designed so that waves incident upon the PML from a non-PML medium do not reflect at the interface. This property allows the PML to strongly absorb outgoing waves from the interior of a computational region without reflecting them back into the interior.

From a mathematics viewpoint, a perfectly matched layer is an analytic continuation of the wave equation into complex coordinates under the requirement that the wave impedance should remain unaffected as in ref.[149]. It means that one (or more) of the coordinates is mapped into complex numbers. The effect is to replace inside this particular region propagating (oscillating) waves by exponentially decaying ones. The PML principle works in time domain and in frequency domain for any kind of discretization of an arbitrary wave equation. The mathematical form are however different in time domain and in frequency domain. The focus here is on frequency domain PML. Applications on PML in time domain are shown in references [147, 148].

This approach is known as **stretched-coordinate PML**. This complex coordinate approach, while not the original one, is elegant and general in the sense that it allows to extend this technique to other wave equations and other coordinate systems "easily". The transformation can be defined for others coordinate systems and for an arbitrary "wave equation".

Different PML formulations were done, but they have all been unified under the same formalism in [150]. The different interpretations of the PML have also been shown to be equivalent: complex stretched coordinates perpendicular the medium-PML interface, physical lossy medium with dependent electric and magnetic currents densities.

An exhaustive literature exists for classical dielectric such as air but it is scarce for complex dielectric media such as cold magnetized plasmas. Recently this technique started being used in inhomogeneous ionospheric plasmas [151].

A cold magnetized plasma is equivalent to a birefringent gyrotropic medium as shown by the tensor given by (2.9). For example PMLs already exist for the propagation of one eigenmode of magnetized plasmas, generally in 2D transverse to the confinement magnetic field, described by a scalar Helmholtz equation [152]. We would like to extend this result in 3D for the two eigenmodes, described by a vectorial wave equation, in view of many applications in lots of contents.

Specific radiation conditions thus need to be emulated simultaneously for two eigenmodes. But, these two eigenmodes present a great disparities of scale lengths (i.e. very different wave vector radial component n_x) resulting in very different properties for the slow wave and the fast wave.

Moreover, in our case the antenna used to excite the waves launches a wide spectrum of $n_{\parallel}$. Both propagative and evanescent waves can exist. Furthermore, in this spectrum, a $n_{\parallel}$ window will give rise to $n_{\perp}$ close to zero (i.e. very long wavelengths). Management

of this region around the cutoff is of serious concern. Finally forward and backward waves can coexist if $\varepsilon_{\parallel} < 0$ and $\varepsilon_{\perp} > 0$. The PML will select one of the two. We have therefore to make sure that the one selected is the one carrying the power towards the plasma.

Is it possible to obtain a PML for such a medium? How to control the reflection? Is it possible to construct a PML working for both polarizations at the same time? How to obtain a PML for a spectrum of $n_{\parallel}$ offering the best compromise? How to cope with the cutoffs? How to minimize the numerical cost while keeping an acceptable accuracy? How to measure the reflections for both travelling and evanescent waves? What are the limits that we cannot go beyond? Those are a few questions to which we have to find answers to.

3.2 Mathematical description of the Perfectly Matched Layer

3.2.1 Introduction

The aim is to define the PML as an artificial anisotropic absorbing medium, where the standard equations of electrodynamics can be applied in their usual form. A complete formulation of general closed-form PML in bi-anisotropic and dispersive media can be found in [150] and is briefly summarized below. The case treated here considered the constitutive relations $\mathbf{D} = \bar{\bar{\varepsilon}}\mathbf{E}$ and $\mathbf{B} = \bar{\bar{\mu}}\mathbf{H}$, where for the sake of generality the dielectric tensor $\bar{\bar{\varepsilon}}$ and magnetic permeability tensor $\bar{\bar{\mu}}$ are full. In the constitutive relations $\mathbf{B}$ only depends on $\mathbf{H}$ and $\mathbf{D}$ on $\mathbf{E}$ on the contrary to the general case treated in [150].

In the following development, the system of equations (2.3) is replaced with a modified wave propagation problem solved over the whole computation domain including the PML layer and radiation conditions at the boundaries of the main simulation domain. For that purpose we envisage the most general PML in the three directions. Following [150], the Cartesian space coordinates in (2.3) are transformed by an analytic continuation to a complex variable spatial domain [153, 154]. This mathematical transformation, central to the PML theory, is written with stretching function deforming the Cartesian space. The effect of this transformation is to alter propagative modes into exponentially decaying modes in the PML layer, allowing reflectionless absorption of the electromagnetic waves within a finite length assumed to be smaller than the studied spatial zone.

3.2.2 Wave damping via artificial coordinate stretching in the complex plane: qualitative introduction via a simple example in 1D

Let us take first a simple example to pedagogically illustrate the principle on which the PML relies on: a PML designed to absorb travelling waves propagating in the x direction.

Let's also assume that the stretching function takes the form $S_x(x) = 1 + \frac{i\sigma(x)}{\omega_0}$ with ω_0 the wave pulsation and σ some function of x. The transformation of the real coordinate to complex stretched coordinate in that case reads:

$$x \to x + \frac{i}{\omega_0}\int^x \sigma(x')dx', \tag{3.1}$$

where $\sigma(x)$ is a damping function following:

$$\begin{cases} \sigma(x) &= 0 \text{ if } x < 0, \\ \sigma(x) &> 0 \text{ if } x > 0. \end{cases} \tag{3.2}$$

If $\sigma > 0$, the integral in (3.1) reads:

$$\sigma > 0 \quad \Rightarrow \quad \int^{x} \sigma(x')dx' > 0 \tag{3.3}$$

$$\Rightarrow \quad \lim_{x\to+\infty} \int^{x} \sigma(x')dx' \to +\infty \tag{3.4}$$

For a wave of dependence in e^{ikx} travelling in $+x$ direction ($k > 0$), it thus gives:

$$ikx \quad \Rightarrow \quad ik\left(x + \frac{i}{\omega_0}\int^{x} \sigma(x')dx'\right) \tag{3.5}$$

$$\Rightarrow \quad ikx - \frac{k}{\omega_0}\int^{x} \sigma(x')dx'. \tag{3.6}$$

As $\lim_{x\to+\infty} e^{-\frac{k}{\omega_0}\int^{x}\sigma(x')dx'} = 0$, the wave is thus attenuated as shown in:

$$\lim_{x\to+\infty} e^{i(kx-\omega_0 t)} e^{-\frac{k}{\omega_0}\int^{x}\sigma(x')dx'} = 0. \tag{3.7}$$

In that case, each time an x derivative appears in the wave equation, it is replaced by:

$$\partial_x \to \frac{1}{1+\frac{i\sigma(x)}{\omega_0}}\partial_x. \tag{3.8}$$

The typical length associated by the gradient is thus proportional to σ/ω_0. If this ratio is larger than one, the propagating wave is damped faster over a shorter distance.

3.2.3 Formulation of the spatial coordinates stretching problem in 3D Cartesian geometry with full permittivity and permeability tensors

After this qualitative example, let us go to a general 3D case. The solution of the problem in 3D Cartesian geometry should remain unchanged in the main computational domain where the stretched coordinates coincide with the normal ones. The analytic continuation is formally expressed by the following transformation:

$$u \to t_u = \int_0^{u} S_u(u')du', \tag{3.9}$$

where S_u are the complex stretching functions [155] and u stands for any of the Cartesian coordinates x, y, z. S_u can be chosen with great flexibility, but should depend exclusively on coordinate u. The imaginary part will damp the incoming propagative waves whereas the real part will take care of the evanescent ones.

In the stretched complex space, the Maxwell's equations read:

$$\begin{cases} \nabla_S \times \mathbf{E} &= +i\omega_0\bar{\bar{\mu}}\mathbf{H}, \\ \nabla_S \times \mathbf{H} &= -i\omega_0\bar{\bar{\varepsilon}}\mathbf{E} + \mathbf{j_{ant}}, \\ \nabla_S \cdot [\bar{\bar{\varepsilon}}\mathbf{E}] &= \rho_{ant}, \\ \nabla_S \cdot [\bar{\bar{\mu}}\mathbf{H}] &= 0. \end{cases} \tag{3.10}$$

Within the new formulation, the wave problem in the PML takes the same form as (2.3), but the differential operator ∇ in Cartesian coordinates is replaced by the modified operator ∇_S in stretched coordinates, defined as:

$$\nabla_S \equiv \begin{pmatrix} \frac{\partial_x}{S_x(x)} \\ \frac{\partial_y}{S_y(y)} \\ \frac{\partial_z}{S_z(z)} \end{pmatrix} = \bar{\bar{S}}^{-1} \cdot \nabla \ , \tag{3.11}$$

where

$$\bar{\bar{S}} \equiv \begin{bmatrix} S_x(x) & 0 & 0 \\ 0 & S_y(y) & 0 \\ 0 & 0 & S_z(z) \end{bmatrix} . \tag{3.12}$$

3.2.4 Interpretation of the PML as an artificial lossy medium

Since $\partial/\partial x$ commutes with $S_y(y)$ and $S_z(z)$, and $\bar{\bar{S}}$ is a diagonal tensor, the two differential operators ∇ and ∇_S are related for any vector field $\mathbf{a}(x,y,z)$ by the following properties:

$$\bar{\bar{\Lambda}} \cdot [\nabla_S \times \mathbf{a}] \quad = \nabla \times \left(\bar{\bar{S}} \cdot \mathbf{a} \right), \tag{3.13}$$

$$\det\left(\bar{\bar{S}}\right) \nabla_S \cdot \mathbf{a} \quad = \nabla \cdot (\bar{\bar{\Lambda}} \cdot \mathbf{a}), \tag{3.14}$$

where $\bar{\bar{\Lambda}} = \det\left(\bar{\bar{S}}\right) \bar{\bar{S}}^{-1}$ and $\det \bar{\bar{S}} = S_x S_y S_z$.

A simple mnemonic trick for $\bar{\bar{\Lambda}}$ is to remember that the S_i function does not appear for the i direction.

Combining (3.11), (3.13) and (3.14), the modified wave propagation problem in the PML can be reformulated using the standard differential operators as:

$$\begin{cases} \nabla \times \left(\bar{\bar{S}} \cdot \mathbf{E} \right) & = & +i\omega_0 \left(\bar{\bar{\Lambda}} \cdot \bar{\bar{\mu}} \cdot \bar{\bar{S}}^{-1} \right) \left(\bar{\bar{S}} \cdot \mathbf{H} \right) \\ \nabla \times \left(\bar{\bar{S}} \cdot \mathbf{H} \right) & = & -i\omega_0 \left(\bar{\bar{\Lambda}} \cdot \bar{\bar{\varepsilon}} \cdot \bar{\bar{S}}^{-1} \right) \left(\bar{\bar{S}} \cdot \mathbf{E} \right) + \bar{\bar{\Lambda}} \cdot \mathbf{j_{ant}}, \\ \nabla \cdot \left[\left(\bar{\bar{\Lambda}} \cdot \bar{\bar{\varepsilon}} \cdot \bar{\bar{S}}^{-1} \right) \left(\bar{\bar{S}} \cdot \mathbf{E} \right) \right] & = & \det\left(\bar{\bar{S}}\right) \rho_{ant}, \\ \nabla \cdot \left[\left(\bar{\bar{\Lambda}} \cdot \bar{\bar{\mu}} \cdot \bar{\bar{S}}^{-1} \right) \left(\bar{\bar{S}} \cdot \mathbf{H} \right) \right] & = & 0. \end{cases} \tag{3.15}$$

The new set of equations (3.15) can have the following interpretation. They can be seen formally as the standard equations of electrodynamics in system (2.3). However, the original RF fields $\mathbf{E}$ and $\mathbf{H}$ are replaced respectively by artificial RF fields $\bar{\bar{S}}\mathbf{E}$ and $\bar{\bar{S}}\mathbf{H}$. The original and artificial RF fields coincide inside the main simulation domain, where the stretching tensor is the identity tensor ($\bar{\bar{S}} = \bar{\bar{1}}$).

The artificial RF fields propagate in an artificial absorbing medium with modified dielectric and magnetic properties [156, 157]. The original tensors $\bar{\bar{\varepsilon}}$ and $\bar{\bar{\mu}}$ are replaced respectively with the artificial tensors $\bar{\bar{\varepsilon}}_{PML}$ and $\bar{\bar{\mu}}_{PML}$. From a general dielectric tensor $\bar{\bar{\varepsilon}}$, one obtains the perfectly matched tensor $\bar{\bar{\varepsilon}}_{PML}$:

$$\bar{\bar{\varepsilon}}_{PML} \equiv \bar{\bar{\Lambda}} \cdot \bar{\bar{\varepsilon}} \cdot \bar{\bar{S}}^{-1} = \begin{bmatrix} \varepsilon_{xx} \frac{S_y(y) S_z(z)}{S_x(x)} & \varepsilon_{xy} S_z(z) & \varepsilon_{xz} S_y(y) \\ \varepsilon_{yx} S_z(z) & \varepsilon_{yy} \frac{S_z(z) S_x(x)}{S_y(y)} & \varepsilon_{yz} S_x(x) \\ \varepsilon_{zx} S_y(y) & \varepsilon_{zy} S_x(x) & \varepsilon_{zz} \frac{S_x(x) S_y(y)}{S_z(z)} \end{bmatrix} . \tag{3.16}$$

This is the most general tensor one can find. Then according to the situation, the tensor can be simplified by considering the zeros ε_{ij} elements. Considering in which directions the stretching occurs can also simplify the tensor by putting to 1 some of the $S_u(u)$.

The same stretching needs to be applied to the magnetic permeability tensor. Original and artificial tensors again coincide in the main simulation domain. These two properties characterize the artificial medium called perfectly matched layer. Also note that the three tensors $\bar{\bar{\Lambda}}$, $\bar{\bar{S}}^{-1}$ and $\bar{\bar{\mu}}$ commute if the tensor $\bar{\bar{\mu}}$ is diagonal.

The present formulation is valid for any permittivity and permeability tensors $\bar{\bar{\varepsilon}}$ and $\bar{\bar{\mu}}$ and can be implemented indifferently in 1D, 2D and 3D. As all the needed information is contained in the modified constitutive tensor properties $\bar{\bar{\varepsilon}}_{PML}$ and $\bar{\bar{\mu}}_{PML}$ and only the **E** and **H** fields are required the formulation is aesthetic and straightforward to implement, especially in commercial software which authorize the definitions of exotic media.

To minimize reflections for inhomogeneous media, the constitutive parameters $\bar{\bar{\varepsilon}}$ and $\bar{\bar{\mu}}$ at any transverse plane inside the PML are equal to those at the plasma-PML interface, and invariant along the normal direction to the interface. Inhomogeneities present in the transverse directions will eventually produce reflections inside the PML. However, such reflections contribute only along the transverse directions to the interface [158]. Reflections can get in the continuous case arbitrary small, until a reflectionless PML is achieved. The next section will show how for a 1D PML by solving analytically the wave equation in a domain plasma+PML.

3.3 Reflection of plane waves by a 1D PML

In order to get insight into the main properties of the PML, we exhibit general rules to tune the PML and assess its implementation in numerical codes. A simple test case is first considered, for which analytical results are available: plane wave propagation in half space filled with homogeneous medium with radiation at infinity. Since the original wave problem is linear, many realistic RF fields of physical interest can be decomposed into a characteristic spectrum of plane waves. This test problem, although academic, is useful to guide PML implementation. For the sake of generality Cartesian coordinates (r, l, h) are temporarily defined. RF field oscillation as $e^{+ik_l l + ik_h h}$ is assumed parallel to the half space border and propagation is solved along the coordinate r (see figure Figure 3.1). In flattened tokamak geometry, depending on the PML, r can represent any of the principal directions parallel or normal to the confinement magnetic field. In presence of radiation conditions the wave equation (1) in the half-plane ($r > 0$) has solutions of the form:

$$\hat{E}_{exact}(r, k_h, k_l) = \hat{E}_0(k_h, k_l) e^{+ik_r r} e^{+ik_l l} e^{+ik_h h}. \tag{3.17}$$

In this expression, the wave vector **k** and wave polarization $\hat{E}_0(k_h, k_l)$ are respectively eigenvalue and eigenvector of the wave equation:

$$\mathbf{n} \times (\mathbf{n} \times \mathbf{E}) + \bar{\bar{\varepsilon}} \cdot \mathbf{E} = 0, \tag{3.18}$$

where $\bar{\bar{\mu}} = \mu_0 \bar{\bar{1}}$, $\mathbf{n} = \mathbf{k}/k_0$ is the index vector and $k_0 = \omega/c$ the modulus of the wave vector in vacuum. In birefringent media like magnetized plasmas, several eigenmodes can coexist. Only one of them is considered in our test problem. The dispersion relation, given by the determinant of (3.18), is then generally expressed as:

$$k_r^2 = f\left(\omega, k_l^2, k_h^2, \bar{\bar{\varepsilon}}\right). \tag{3.19}$$

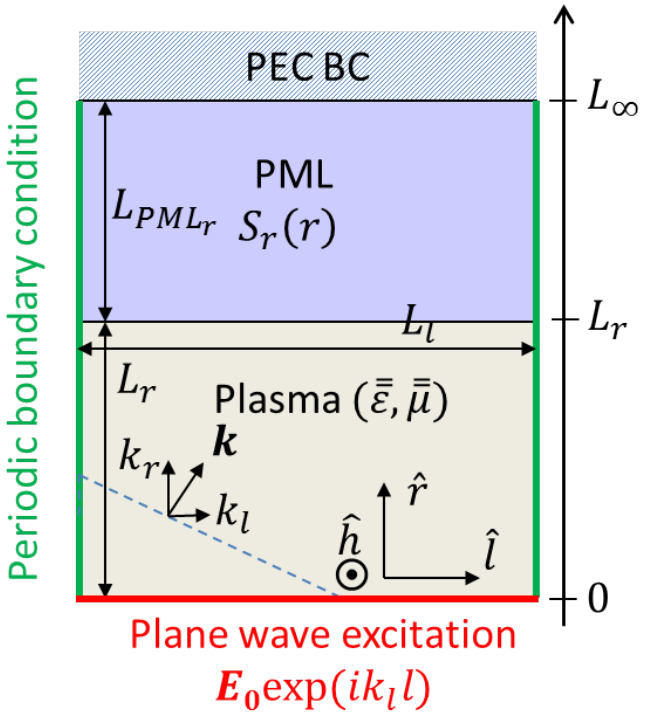

Figure 3.1: Sketch of the geometry used for the tests of a PML in one direction with plane waves.

3.3.1 Analytical reflection coefficient in presence of a PML

Being semi-infinite in space, our test problem cannot be solved numerically in its present form. Instead it is replaced by a modified problem in a bounded simulation domain $0 < r < L_r$ (see Figure 3.1). A PML domain is added in the r direction between $L_r < r < L_r + L_{PML_r}$ to emulate the proper radiation conditions at the boundary of the main domain. The PML is ended by a Perfect Electric Conductor (PEC) that should ideally play no role in the modified problem. Finally the RF field $\hat{E}_0(k_h, k_l)$ is imposed in $r = 0$. Having boundary conditions at $r = 0$ and $r = L_\infty \equiv L_r + L_{PML_r}$ and continuity at $r = L_r$, a unique solution can be found for the second-order wave equation of the modified problem. This solution can be easily obtained as follows: the modified problem is first solved as if the plasma occupied the whole simulation domain $0 < r < L_r + L_{PML_r}$. Then, the radial coordinate r is replaced by the stretched coordinate t_r defined in (3.9). A general form of the solution is therefore the sum of an incident wave (identified by $+$) and a reflected wave (identified by $-$):

$$\hat{E}_{PML}\left(t_r, k_h, k_l\right) = \hat{E}^+(k_h, k_l)e^{+ik_r t_r} + \hat{E}^-(k_h, k_l)e^{-ik_r t_r}, \tag{3.20}$$

where k_r is solution of the same dispersion relation (3.19).

The two coefficients $\hat{E}^+(k_h, k_l)$ and $\hat{E}^-(k_h, k_l)$ are determined from the boundary conditions in $t_r = 0$ ($\hat{E}_{PML} = \hat{E}_0$) and in $t_r = t_\infty = t_r(L_\infty)$ ($\hat{E}_{PML} = 0$). This leads to:

$$\hat{E}^+(k_h, k_l) = \frac{i}{2}\frac{e^{-ik_r t_\infty}}{\sin(k_r t_\infty)}\hat{E}_0\left(k_h, k_l\right), \tag{3.21}$$

$$\hat{E}^-(k_h, k_l) = \Gamma_{pred}\hat{E}^+(k_h, k_l), \tag{3.22}$$

with

$$\Gamma_{pred} = -\exp\left(2ik_r t_\infty\right) \tag{3.23}$$

a complex reflection coefficient. Comparing $\hat{E}_{PML}$ with $\hat{E}_{exact}$ the ideal situation would be to reach $\hat{E}^+ = \hat{E}_0$ and $\hat{E}^- = 0$ for all physically useful values of (k_h, k_l) excited in the wave propagation problem. These conditions are fulfilled if $|\Gamma_{pred}| << 1$. Therefore the amplitude of the reflection coefficient is a figure of merit of the efficiency of the PML.

Several conclusions can already be drawn independently of any particular choice for $S_r(r)$. First, to achieve $|\Gamma_{pred}| << 1$ the stretching function $S_r(r)$ needs to incorporate a complex part in order to damp the incoming propagative waves in the bounded PML, so that the modified spatial path is necessarily stretched in the complex plane: $t_\infty = t'_\infty + it''_\infty$. The PML becomes effectively perfectly reflectionless as t'_∞ and t''_∞ tend to infinity. For finite values of t_∞ the PML will fail in the vicinity of a cutoff layer, for which $|k_r|$ assumes very small values. The spectral width of the unfavourable region in k_r depends on the values t'_∞ and t''_∞ and can be made arbitrarily small, at the expense of larger PML size to handle the larger wavelength.

Secondly, in an anisotropic medium the applied stretching is the same for all the eigenmodes despite possibly very disparate wavelengths in direction r. The PML therefore needs to be adapted to the largest wavelength while being able to resolve properly the wave structure and ensure a smooth stretching to avoid spurious numerical reflections.

Stretching the space coordinates allows contracting the space, thus bringing what can be considered as infinity at a finite value.

3.3.2 Criteria for choosing the stretching function properties to minimize the analytical reflection coefficient

Each direction of our anisotropic medium needs its own perfectly matched layer characterized by its stretching tensor $\bar{\bar{S}}$ as shown in Figure 3.1.

Perfectly matched layers are usually designed to only attenuate propagating waves without reflection by definition. Purely evanescent waves are transformed into oscillating waves in the PML but do not decay more quickly. Attenuation of evanescent waves can however be accelerated by adding a real coordinate stretch in the PML.

A large range of stretching functions $S_u(u)$ can be envisaged for the PML. The main criteria are:

- $S_r(r)$ should be continuous across the interface $r = L_r$ (medium/PML interface).
- $S_r(r)$ should also be sufficiently smooth within the PML.
- The damping should have the appropriate sign to get power sent to the plasma.
- The stretching function parameters (L_{PML_r}, S'_r, S''_r, p_r) should be chosen with the constraint that the fields must vanish before reaching the end of the PML. As long as the truncation is done after a long enough distance (where the exponential tails are small), the boundary condition used will not matter. If that condition is realized, then the perfect electric conductor (PEC) boundary condition is automatically satisfied.

As a consequence of these assumptions, no discontinuity should be present in the PML. Therefore the PML cannot replace sources of electromagnetic fields. They only absorb fields produced by sources located inside the surrounded domain. Since PMLS are designed for the absorption of travelling waves, this means implicitly that they must be placed some distance from the sources and outside the possible evanescent region that can numerically

costly to handle. As a corollary to the discontinuity, each point in a volume space bounded with a PML must be in direct visibility from any other point of this volume, i.e., the interface between the inner medium and the PML must be either plane (in the Cartesian case) or concave, in the general case [159].

3.3.3 Application to polynomial stretching function

A common choice, but not unique, for the PML is a stretching function having a polynomial form:

$$S_r(r) = \begin{cases} 1 & \text{for } 0 \leq r \leq L_r, \\ 1 + (S'_r + iS''_r)\left(\frac{r-L_r}{L_{PML_r}}\right)^{p_r} & \text{for } L_r \leq r \leq L_\infty, \end{cases} \tag{3.24}$$

where L_r, L_{PML_r}, p_r, S'_r S''_r are respectively the position of the medium/PML interface, the PML depth, the order of the stretching function, the real stretch and the imaginary stretch. This leads to: $t_\infty = L_\infty + (S'_r + iS''_r)\left(\frac{L_{PML_r}}{p_r+1}\right)$. The analytical reflection coefficient for forward waves (real positive k_r) yields:

$$\eta_{pred} \equiv |\Gamma_{pred}| = \exp\left(-2k_r L_{PML_r} \frac{S''_r}{p_r+1}\right) \tag{3.25}$$

Similar calculation can be done for backward waves (real negative k_r). For evanescent waves (pure imaginary k_r), it reads:

$$\eta_{pred} = \exp\left[-2\,|k_r|\left(L_r + L_{PML_r}\frac{1+S'_r}{p_r+1}\right)\right]. \tag{3.26}$$

3.3.4 Qualitative reflections on the choice of the PML parameters and on numerical errors due to discretization

Formula (3.25) provides some hints to minimize the wave reflection in the simulation domain and the associated numerical cost. A deep PML always improves the accuracy of the result, at the expense of larger CPU and memory requirements, since the PML also needs to be meshed. It might seem desirable to take large S'' as well as low p up to some value where the resulting gradient in the stretched direction cannot be computed by the mesh without local mesh refinement to avoid additional errors. If local refinement is necessary, then the gain in numerical cost is limited and ultimately cancelled. Formula (3.25) also confirms that grazing incident angles or cutoffs ($k_r \to 0$ greatly affect the effectiveness of the PML in its reflectionless properties. For formula (3.26), the same hints still apply replacing S'' by $1 + S'$. These qualitative hints will have to be checked numerically.

These analytical results only quantify the error introduced when switching from the original Maxwell's equations to the modified ones. The PML is a mathematical object defined to remove perfectly all the reflected waves at the boundary. However its formulation was done for continuous media. All the defaults of the PML come from the discretization of a continuous medium into a finite number of points. From a numerical viewpoint the total error should also incorporate extra wave reflection due to space discretization or round-off errors in numerical schemes. The boundary between the PML and the medium is no longer reflectionless, but the reflection are small because the discretization is presumably a "good approximation" of the exact wave equation. They are discussed in ref.[160] in the context of finite differences.

Reflections can be made arbitrary small, even without a PML, by slowly varying the medium properties. It results for the PML in the absorption coefficient σ gradually turned on from zero over a short distance of the scale of the wavelength of the wave. As absorption gradually increases, reflections goes to zero due to an adiabatic theorem [161]. With a non-PML absorber, getting acceptable reflections requires very thick absorbing layer as absorption is very slowly turned on [162]. Increasing the resolution also increases the effectiveness of the PML, as it approaches the exact wave equation. The required effectiveness is then function on the application. It means that the σ profile in the PML is not uniform. The profile is however uniform in the direction perpendicular to the medium/PML interface. The PML is thus not uniform and as such can be seen as a stratified medium with the typical size of one stratum having the typical element size.

Thinking on the increase of the stretching coefficient leads to think that always keeping the same slope between two adjacent grid points would be beneficial for the minimization of the numerical spurious reflection. Indeed the gradient length would stay constant. This is not the case for polynomial function whose slope is always increasing except for order one. Geometrical functions however satisfy this property. Geometrical functions are nevertheless more difficult to implement, especially with finite elements in non-regular grids. Moreover regular grids are incompatible with multi-scale grids as they will encounter joining issues at the interfaces of the different grids.

After this discussion on the effect of discretization of the efficiency of the PML, let us turn to numerical simulations for plane waves to verify that the PML is indeed working but has numerical limits.

3.4 Numerical tests with plane waves in an homogeneous magnetized plasma compared to analytical predictions of the reflection coefficient

The PML method has been introduced for a possible usage for magnetized plasmas that are anisotropic, gyrotropic and inhomogeneous media. The presence of cutoffs is also a concern as well as the possible coexistence of forward and backward waves. To start with, it is important to know if the current PML formulation works well for homogeneous magnetized plasmas. Both the slow and fast waves were tested for various conditions. A 2D homogeneous plasma with a radial PML with a polynomial profile of $S_x(x)$ is simulated by FEM using the Comsol Multiphysics software. Then the reflection coefficient for monochromatic plane waves was computed and compared to the expected value found in 3.25.

3.4.1 Assessment of the reflection coefficient in numerical simulations with the standing wave ratio

To assess the PML performance in numerical simulations, the amplitude reflection coefficient $\Gamma \equiv E_-/E_+$ should be quantified for a given set of PML parameters. It is written as $\Gamma_{sim} \equiv \eta_{sim} \exp(i\varphi)$ with amplitude $\eta_{sim} = |\Gamma_{sim}| \leq 1$ and phase φ. Only the magnitude of Γ_{sim} is of interest. In order to extract η_{sim}, one can evaluate the modulus of the RF electric field $E(r, l)$ over all plasma domain:

$$|E|^2 = \left|E^+\right|^2 \left[1 + \eta_{sim}^2 + 2\eta_{sim} \cos(2k_r r + \varphi)\right]. \tag{3.27}$$

In the ideal case of a perfect PML ($\eta_{sim} = 0$), $|E|^2$ is constant over the domain. In presence of wave reflection ($\eta_{sim} > 0$), the field amplitude pattern exhibits periodic

modulations along direction r, whereas wave fronts may have oblique incidence. This is clearly visible on Figure 3.2(a) with $l = z$ and $r = x$. The wavelength of the amplitude modulations can be used to test the dispersion relation in the main plasma. The position of the maxima and minima can be used to calculate the phase φ (modulo 2π). The amplitude of the spatial modulations are representative of the quantitative value of η_{sim}.

In telecommunications, the standing wave ratio (SWR) of a partial standing wave in an electrical transmission line [163] is defined as the ratio of its amplitude at an antinode (maximum) to the amplitude at an adjacent node (minimum). By analogy, a SWR is here

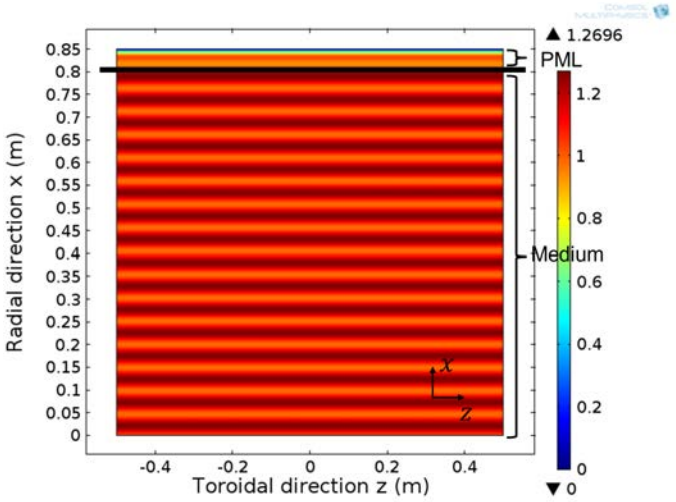

(a)

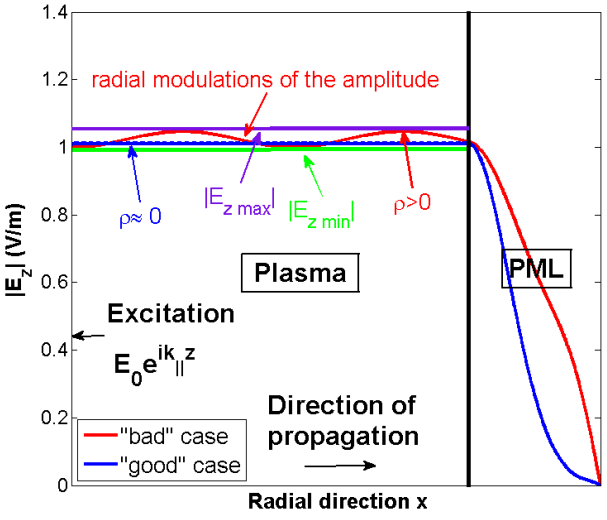

(b)

Figure 3.2: Illustration of radial modulations of the field amplitude. A harmonic excitation is prescribed at the location $x = 0$. The wave then travels through the plasma and is attenuated when reaching the PML. (a) Map of the norm of the electric field $|E|$ where reflection is visible by the presence of radial modulations of $|E|$ in vacuum. $l = z$, $r = x$, $h = y$. (b) A "good" case in blue and a "bad" case in red are represented.

defined for the electric field amplitude. Noting:

$$SWR \equiv \frac{\max|E|}{\min|E|} = \frac{1+\eta_{sim}}{1-\eta_{sim}}. \tag{3.28}$$

Combining (3.27) and (3.28), the SWR gives access to the reflection coefficient via:

$$\eta_{sim} = \frac{SWR-1}{SWR+1}. \tag{3.29}$$

Figure 3.2(a) shows how a not well suited PML can generate radial modulation in the electric field pattern. It creates oscillations in the normally flat front wave. Figure 3.2(b) gives qualitatively an illustration of the method used to quantify the reflection coefficient due to the PML in the radial direction for propagative waves. It is obtained from Figure 3.2(a) by plotting the norm of the main component of the electric field along the radial cut line in white on the figures. Two cases are represented here: a "good" one in blue and a "bad" one in red.

The radial modulations are clearly visible for the "bad" case and that case obviously has a non negligible reflection coefficient while the "good" one presents almost no modulations (at least none that are visible to the naked eye).

This technique can be implemented provided that at least one minimum and one maximum are present in the radial modulations. This is ensured if the radial width of the main plasma represents at least half a wavelength for the launched eigenmode. The method also assumes that the minima and maxima can be quantified precisely. For that purpose the radial resolution of the simulation mesh should be well below the simulated wavelength. This technique is well adapted for propagative waves if the mentioned requirements are satisfied. However, it is not suited for evanescent waves.

3.4.2 Test for PML in perpendicular direction and in parallel direction

To test the PML numerically, a vectorial full-wave version of our modified problem described in Section 3.2.4 was solved with the commercial software Comsol [164] computing RF fields through the Finite Element Method [77]. This solver allows implementing very versatile materials via their full dielectric and permeability tensors, including magnetized plasmas and their associated PML. The dielectric tensor, while homogeneous, can contain positive and negative components of very different values giving a strong anisotropy and gyrotropy.

The simulation domain was meshed very finely in order to validate the computations in the parameter ranges of our application. Nevertheless these values have to be chosen in order to correctly resolve the wavelengths in all directions. The first thing that can be done to optimize the numerical cost is to remember the scale lengths in the parallel direction and in the radial direction are different due to the strong anisotropy in the dielectric tensor (2.9). It justifies the use of a heterogeneous numerical grid. It brings out two value of the maximum size of the mesh element h_{max}: $h_{max_{\parallel}}$ in the parallel direction and $h_{max_{\perp}}$ in the perpendicular direction. To get reliable results, the wavelength in one direction should contain ≈ 10 grid elements. At first, numerical performances is not taken into account.

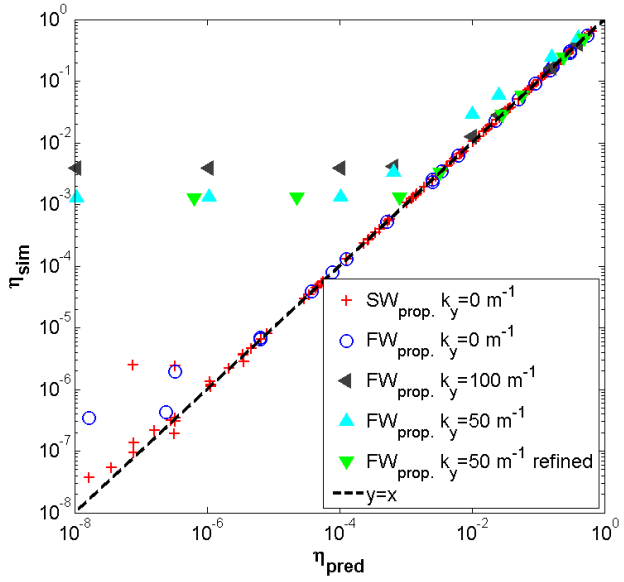

(a)

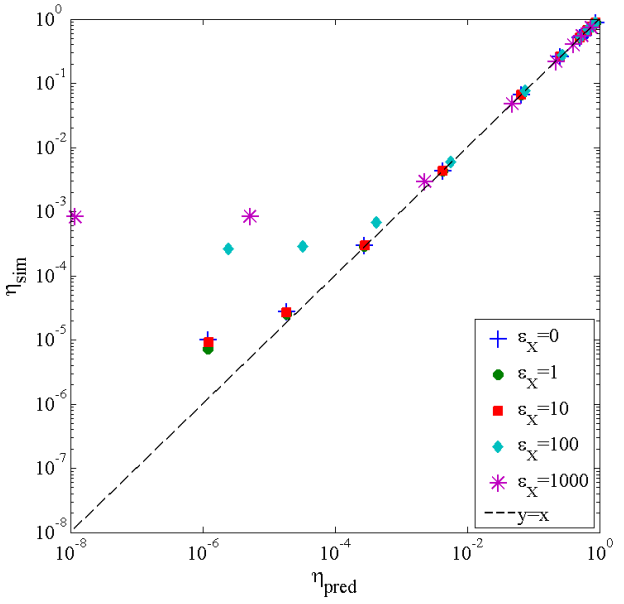

(b)

Figure 3.3: Reflection coefficient from simulations versus analytical predictions obtained with (3.25) for: (a) the SW and the FW considered separately with a PML in the transverse direction and (b) the FW excited in the second configuration with a PML in the parallel direction. Scans in ε_X and L_{PML} are performed. Each dot represents one simulation.

The PML was tested in 2D in two configurations representative of a magnetic fusion plasma: PML in the radial direction x and PML in the parallel direction z, while periodic boundary conditions were applied in the other directions. All the work has been performed with pulsation $\omega_0 = 2\pi f_0$ where $f_0 = 57$ MHz.

The first configuration corresponds to $l = z$, $r = x$ and $h = y$ in Figure 3.1. The plane wave is excited by providing at $x = 0$ an electric field of the form $e^{-ik_z z}$ with $k_z = 2N\pi/L_z$ where N is the mode number and L_z the parallel width of the simulation domain. For the FW this electric field is oriented along the y direction whereas it is along the z direction for the SW. The plasma eigenmodes were studied independently. Several $\varepsilon_\parallel$, $\varepsilon_\perp$, N, L_{PML}, S_r'', p, k_y and mesh size have been tried.

To include $k_y \neq 0$ in 2D simulations, the k_y terms in the wave equation were added to the dielectric tensor $\bar{\bar{\varepsilon}}$. The stretching in the PML must also be included for these k_y terms. The tensor $\bar{\bar{n}}_y$ containing all the elements depending on $n_y = k_y/k_0$ with their respective stretching reads with $\bar{\bar{\mu}} = \bar{\bar{1}}$:

$$\bar{\bar{n}}_y \equiv \begin{bmatrix} -\frac{S_z(z)}{S_x(x)S_y(y)} n_y^2 & \frac{S_z(z)}{S_x(x)S_y(y)} n_y n_x & 0 \\ \frac{S_z(z)}{S_x(x)S_y(y)} n_x n_y & 0 & \frac{S_x(x)}{S_y(z)S_z(z)} n_y n_z \\ 0 & \frac{S_x(x)}{S_y(z)S_z(z)} n_z n_y & -\frac{S_x(x)}{S_y(z)S_z(z)} n_y^2 \end{bmatrix}. \tag{3.30}$$

The second configuration corresponds to $l = x$, $r = z$ and $h = y$ in Figure 3.1. The plane wave is excited by providing at $z = 0$ an electric field of the form $e^{-ik_x x}$ with $k_x = 2N\pi/L_x$ where N is the mode number and L_x the radial width of the simulation domain. Instead of applying input conditions along the parallel direction, they are applied on the radial direction. The dispersion relation given by (2.21) is also reversed: $k_\parallel = f(k_\perp)$. Prior knowledge of k_z^2 is nevertheless necessary as the FW wave polarization depends on it when the Stix tensor given by (2.9) is not diagonal.

The reflection coefficient η_{sim} was then computed with the method presented in Section 3.4.1 for propagative modes and compared with the prediction given by (3.25) η_{pred}. The results are shown on Figure 3.3(a) for the first configuration.

An excellent agreement can be observed between predictions and simulations as long as $\eta_{sim} > 10^{-5}$ with $k_y = 0\,\mathrm{m}^{-1}$. Below that limit the simulated reflection coefficient saturates, which is attributed to numerical effects. This saturation occurs when $2k_x L_{PML} S_r'' (p+1)^{-1} > 10$.

With $k_y \neq 0\,\mathrm{m}^{-1}$ prior knowledge of the dispersion relation is required to compute k_x from k_y and k_z that are imposed. The effective dielectric tensor $\bar{\bar{\varepsilon}}_{PML}$ becomes $\bar{\bar{\varepsilon}}_{PML} + \bar{\bar{n}}_y$. With $k_y \neq 0\,\mathrm{m}^{-1}$ the reflection coefficients are more sensitive to the mesh. Nevertheless $\eta_{sim} < 10^{-2}$ have been reached. Some sensitivity to the mesh resolution can be observed.

For evanescent modes, the radial profile of E_z and E_y were fitted by an exponentially decaying function for the slow wave and the wave respectively and compared to the analytical prediction for k_x. The PML was placed in the decay of the wave to get finite wave amplitude at the PML entrance. Excellent fits were found while the PML depth is larger than half the typical wavelength associated to k_x. Larger value of S_r' (here $S_r' = 1$) would even diminish further the PML depth.

The results for the second configuration are shown in Figure 3.3(b). Only the FW is considered. A scan in ε_X was performed while varying the PML depth L_{PML_t} to observe the effect of the gyrotropy in $\bar{\bar{\varepsilon}}$. Similar behaviour is observed. The saturation is however occurring at higher η_{sim} values and is dependent on the gyrotropy of the dielectric tensor. Increasing the mesh resolution in the radial direction did not allow reaching a smaller saturation level.

3.4.3 Numerical optimization of the PML for a given plane wave

Now that it has been seen that it is possible to obtain a working PML for one plane wave eigenmode, it is crucial to know the influence of the different PML and mesh parameters (h_{max}, p, S'' and L_{PML}) in order to optimize it and therefore reduce its computational cost that causes an additional strain on the available resources. The "desired" domain is thus not only the plasma but the "needed" the union plasma+PML. The observed influence of a parameter can then be compared to what is predicted analytically from (3.25). This relatively academic test for plane waves will bring guidelines for the more complex situation with realistic antenna geometries in Chapter 4.

The following part is done only for the Fast Wave with a radial PML ($r = x$ and $l = z$) and $k_y = 0\ \mathrm{m}^{-1}$. The parametric dependence should not depend anyway of the choice of the wave. The stretching coefficient S'' is chosen to be negative to get a positive group velocity and thus an antenna emitting power that is sent into the plasma.

The simulations were defined with the following parameters: $\varepsilon_\parallel = -10000$, $\varepsilon_\perp = 1000$, $\varepsilon_X = 100$ for the Stix parameters, the parallel dimension of the domain $L_\parallel = 1$ m and the perpendicular dimension of the medium $L_\perp = 0.4$ m. With the parallel mode number $N = 2$, it gives $k_\parallel = 2N\pi/L_\parallel = 4\pi\ \mathrm{m}^{-1}$ corresponding to a parallel wavelength $\lambda_\parallel = 0.5$ m. With Stix parameters defined above, it gives using the dispersion relation for the fast wave, given by (2.21), $k_x = 35.4\ \mathrm{m}^{-1}$ corresponding to a radial wavelength $\lambda_\perp \approx 0.18$ m.

The optimization procedure consists in finding the best set of PML parameters and grid parameters giving a reflection coefficient η_{choice} that is thought to be acceptable for accuracy and numerical cost.

3.4.3.1 Influence of the PML depth L_{PML} on η

The test consisted in verifying that (3.25) was correct in saying that the reflection is decreasing as the PML depth L_{PML} is increasing for all other PML parameters fixed: $S' = 1$, $S'' = -1$ and $p = 2$. The test should also compare the PML depth L_{PML} to the radial wavelength since the PML is placed in the radial direction. $h_{max_\parallel} = 0.02$ m was chosen giving 25 elements per wavelength. The same procedure has to be done for the radial wavevector. With $h_{max_\perp} = 0.01$ m, it gives about 18 elements per wavelength. The results of this scan are shown on Figure 3.4. The reflection coefficient is decreasing when L_{PML} is increasing up to some limit that could be due to the mesh parameters. It will be tested in the next parametric scan. More importantly the simulations results follow the prediction given by (3.25). It can also be seen that the worse reflection coefficient are obtain for $L_{PML}k_x < 1$ meaning that the PML depth is smaller than the typical radial wavelength. This effect can easily be observed in (3.25). With a small product $L_{PML}k_x$ it is more difficult to obtain a high value for the exponent. It will unfortunately be the case in the region near the cutoffs where $k_x \approx 0$, meaning high wavelength. The best thing to do would be then to place the plasma/PML interface far away from the cutoffs region in order to avoid any incoming problem.

3.4.3.2 Influence of the elements size $h_{max_\perp}$ and type on η

The first parametric scan has shown a limit in the agreement between simulations and predictions for η possibly due to the mesh parameters. In order to correct it, several values of $h_{max_\perp}$ have been tested. For all of them, there were at least two elements per wavelength giving a minimum resolution of the wavelength. The grid resolution is kept the same in both the medium and the PML. The other PML parameters are: $S' = 1$, $S'' = -1$ and

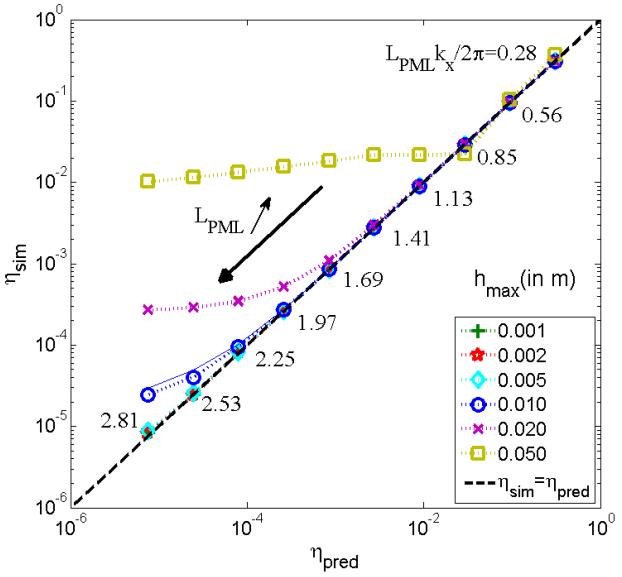

Figure 3.4: Comparison of the reflection coefficient obtained in the simulations with the expected analytical reflection coefficient during a scan of the PML depth L_{PML} for several maximum element size parameters $h_{max_\perp}$ with a mapped regular mesh. The curve $\eta_{sim} = \eta_{pred}$ is also plotted as a reference. Each dot represents one simulation. An example with a triangular mesh is also shown with cyan circles.

$p = 2$.

Figure 3.4 shows again that there is a correlation between the simulations result and the expectations for the reflection coefficient. Moreover it also shows a link between the minimum reflection coefficient η_{sim} that can be reached and the numerical limitations imposed by the discretization in the radial direction. A dense grid (with small elements) enables to reach a smaller reflection coefficient for a given PML depth. Where a regular mapped grid created with $h_{max_\perp} = 0.05$ m reaches reflection as low as $\eta = 10^{-2}$, a grid using $h_{max_\perp} = 0.005$ m reaches the region where $\eta = 10^{-5}$. Below the value $h_{max_\perp} = 0.005$ m there is not much improvement for the reflection coefficient at all while costing precious computational resources. The ratio cost/improvements is thus bad. The minimum reflection coefficient that can be reached is therefore $\eta = 10^{-5}$. On the contrary, there is a huge improvement by using $h_{max_\perp} = 0.005$ m instead of $h_{max_\perp} = 0.05$ m. The computational cost is multiplied by 10, but the reflection coefficient is decreasing by 1000 for large PML. The ratio cost/improvements is in that case very interesting. It is also observed that the best that can be achieved is $\eta_{NL} \approx 10^{-5}$. It is imposed by numerical limits.

A link also can be made between the PML depth L_{PML} and the resulting reflection coefficient for different grids. Increasing PML depth is emphasizing the numerical limit due to discretization. For example, if one is only interested in reflection coefficient around 10^{-2}, taking a grid with $h_{max_\perp} \approx 0.05$ m and $L_{PML}kx \approx 1$ is enough and will save a lot of computational resources. On the contrary, if one is interested in having reflection coefficient as low as possible, it is strongly advised to use smaller $h_{max_\perp}$, such as $h_{max_\perp} \approx 0.005$ m and a deeper PML, such as $L_{PML}k_x \approx 2$.

It is also interesting to see if the results are dependent on the type of elements. To check this two grids with the same max element size in both direction are used: $h_{max_\parallel} = 0.02$ m and $h_{max_\perp} = 0.005$ m. The elements nature is however different: triangular element and

mapped square elements. The other PML parameters were kept still the same as before: $S' = 1$, $S'' = -1$ and $p = 2$. For small PMLs no difference on the reflection coefficient has been seen on Figure 3.4. However, a discrepancy appears for $L_{PML}k_x > 2$ and $\eta < 10^{-4}$. Numerical grids effects are the root cause of this discrepancy. It means that the results are sensitive to the grid elements nature below this threshold. This is of course not physical. It thus gives the limit reachable for the reflection coefficient measurements as the result should not be grid dependent. The minimum reflection coefficient achievable is then reassessed: $\eta = 10^{-5} \rightarrow \eta = 10^{-4}$. Reaching more accurate results would require a finer refinement of the mesh especially in the parallel direction and a finer sampling in the data set used for data exportation.

3.4.3.3 Influence of the stretching function order p on η

Another PML parameter appearing in the analytical reflection coefficient is the PML order p. The influence of this parameter will be highlighted here. Stretching order $p = 2, 3, 4$ have been tested. The other parameters are: triangular element with $h_{max_\perp} = 0.01$ m, $S' = 1$ and $S'' = -1$. It is intuitive from (3.25) that low order is preferable. Nevertheless $p = 1$ is avoided in order to retain the continuity of the first derivative of the stretching function S in (3.24) at the medium/PML interface ($r = L_r$ in Figure 3.1). Simulation results are showed in Figure 3.5. The reflection coefficients resulting from the simulations behave as expected from the analytical formula. It is also clear that (3.25) is correct when saying that low order give smaller reflection coefficient for a given PML depth. It also confirms that large PML depth give better results. However, a PML depth as small as possible is aimed at in order to minimize the computational cost. As a consequence, from now on, $p = 2$ will be used as the stretching function order.

Figure 3.5 shows again that for the considered mesh the minimum value of the reflection coefficient that can be reached is $\sim 10^{-5}$. That level is reached faster with low PML order as expected from (3.25). η decreases faster with a low PML order and consequently reach

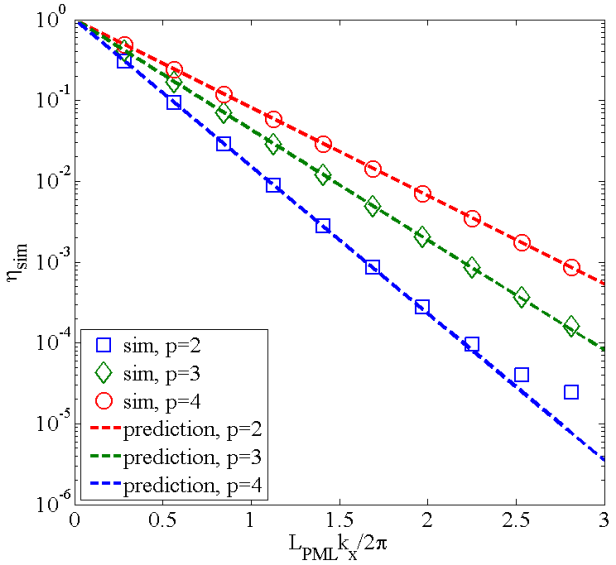

Figure 3.5: Reflection coefficient from the simulations versus the PML depth normalized to the radial wave vector component for several order value. $S' = 1$, $S'' = -1$, $h_{max_\perp} = 0.01$ m. The dashed lines are the predicted reflection coefficient.

the numerical saturation level faster.

3.4.3.4 Influence of the stretching function coefficient S'' on η

It has been seen that the reflection coefficient that can be reasonably achieved is $\eta = 10^{-4}$. Looking at Figure 3.4, it can be deduced that to achieve this condition, it is enough to take $h_{max_\perp} = 0.005$ m, thus limiting the computational cost to what is necessary.

In (3.25) it can easily be seen that increasing S'' will decrease the reflection coefficient until the saturation level near $\eta \approx 10^{-5}$ where the simulation dots stop following the predictions. This is true, but it does not take into account neither the discretization due to the grid, nor the fact that a spatial stretching function can be interpreted as a complex density gradient. Increasing S'' will then also produce a steeper gradient in the stretching function used to transform the coordinate. If the grid is not dense enough to correctly resolve the gradient, some spurious reflection will appear.

This is what happens in Figure 3.6 for high value of S''. For example, in the case $S'' = 50$ or $S'' = 20$ a non monotonous behaviour is seen. η_{sim} also are far from the predictions. It is interpreted as the presence of numerical artefacts. The results are otherwise in accordance with the expectations. If the acceptability for the reflection coefficient is fixed at $\eta = 10^{-4}$, there is a great improvement in term of computational resources when increasing $|S''|$ from 1 to 8. The necessary PML depth goes from $L_{PML} \approx 0.4$ m to $L_{PML} \approx 0.05$ m. When speaking in radial wavelength unit, it corresponds to a transition from $L_{PML}k_x \approx 2.3$ to $L_{PML}k_x \approx 0.3$.

Figure 3.6 shows that being too careful with L_{PML} and S'' brings out a serious overcost. At the other extremity, it is not necessary to use extreme S'' value. It is important to notice that for high S'' the sensibility on L_{PML} causes huge variations on the reflection coefficient η. The variation in ρ due the variation of one element or 1 cm is more important for high S'' than for low S''. Taking a moderate value, such as $|S''| = 4$, already allow to obtain a PML of about half the wavelength of the considered wave while not be too sensible.

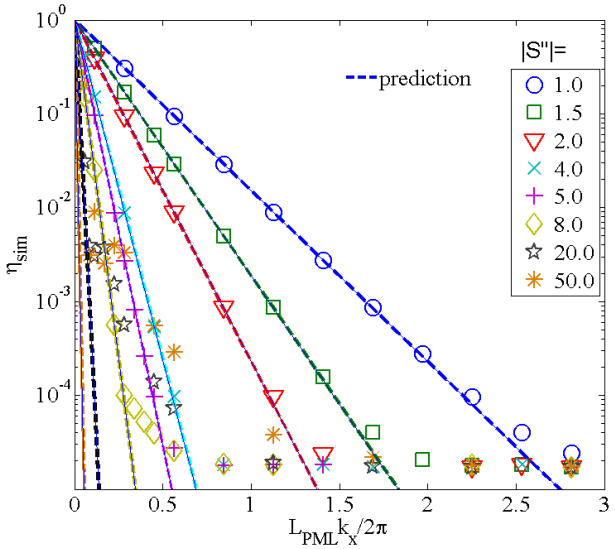

Figure 3.6: Plot of the reflection coefficient obtained in the simulations in function of the PML depth for several stretching value. $S' = 1$, $p = 2$, $h_{max_\perp} = 0.005$ m. The dashed lines are the predicted reflection coefficient.

Looking now at the κ factor ($\kappa = L_{PML}/h_{max}$) corresponding to the number of elements in the radial dimension of the PML, it goes from 40 in the conservative case to 5 in the extreme case. Concerning the moderate case, κ is equal to 10.

To conclude Section 3.4.3, let us summarize the main results. Numerical simulations with plane waves in homogeneous plasmas has confirmed analytical predictions given by (3.25). It has also confirmed the existence of numerical limits explained in Section 3.3.4. A common advice in textbook [147] is to take a PML depth of the order of the considered wavelength which has been confirmed here. This advice will be followed in Chapter 4. The order $p = 2$ is favoured as it obtain lower reflection for a smaller PML than higher order as expected from (3.25). The imaginary stretching coefficient can be tuned, but should not go beyond $S^{''} = 10$. The grid resolution has also shown to be an important parameter. The wave, of course, should correctly be resolved with around 10 grid points inside a wavelength. It is advised to take at least 5 grid points in the PML [147]. To avoid huge numerical cost, a cutoff should be avoided since the wavelength is large. Let us focus now of a more fundamental issue with PML formulation when forward and backward waves coexist simultaneously in a medium.

3.4.4 Simultaneous handling of two polarizations in gyrotropic medium

Remembering that the stretched space coordinate is written as $t_\infty = t'_\infty + it''_\infty$, fulfilling the condition $\eta_{pred} << 1$ means:

$$\exp\left(|k_r|\, t'_\infty\right) >> 1 \text{ with } \quad k_r = i\,|k_r|\,, \tag{3.31}$$

$$\exp\left(|k_r|\, t''_\infty\right) >> 1 \text{ with } \quad k_r = |k_r|\,, \tag{3.32}$$

$$\exp\left(|k_r|\, t''_\infty\right) << 1 \text{ with } \quad k_r = -\,|k_r|\,. \tag{3.33}$$

Conditions (3.32) and (3.33) are incompatible. In practice choosing the sign of t''_∞ via the sign of S''_r will "select" the sign of the phase velocity in direction r for the propagating plane wave that will "emerge" from the numerical simulations. While PMLs can be devised to emulate correct radiations conditions at infinity for both [forward+evanescent] or [backward+evanescent] waves, the PML in its present formulation is not suitable for handling [forward+backward] waves simultaneously.

This issue is of practical importance when modelling radiation from antennas. In such problems the physically relevant plane waves are those that carry RF power away from the antenna, i.e. those with a group velocity directed towards the PML in direction r. In isotropic media, for symmetry reasons the group velocity is always parallel to the phase velocity. In anisotropic plasmas it can happen that the physically relevant components correspond to forward waves for one eigenmode and backward waves for the alternative polarisation, leading to incompatibility when both propagative eigenmodes need to be handled simultaneously. A similar situation was also met for wave propagation in flowing fluids or orthotropic solids [165]. This is an area where significant progress still has to be performed.

It is illustrated in Figure 3.7(a) and in Figure 3.7(b) with $r = x$ and $l = z$ for respectively the FW and the SW. The same sign for imaginary stretch was taken for propagative plane waves. The main component of the Poynting vector for the FW wave is radial. The Poynting vector lies mainly in the parallel direction for the SW. The power is transmitted to the plasma for the FW while with the same stretch the power flows from the plasma to the wall in the case of SW.

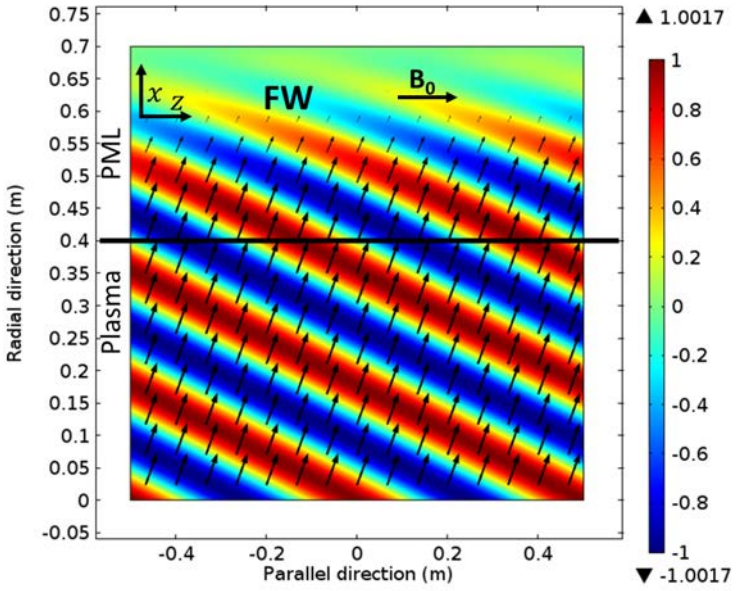

(a)

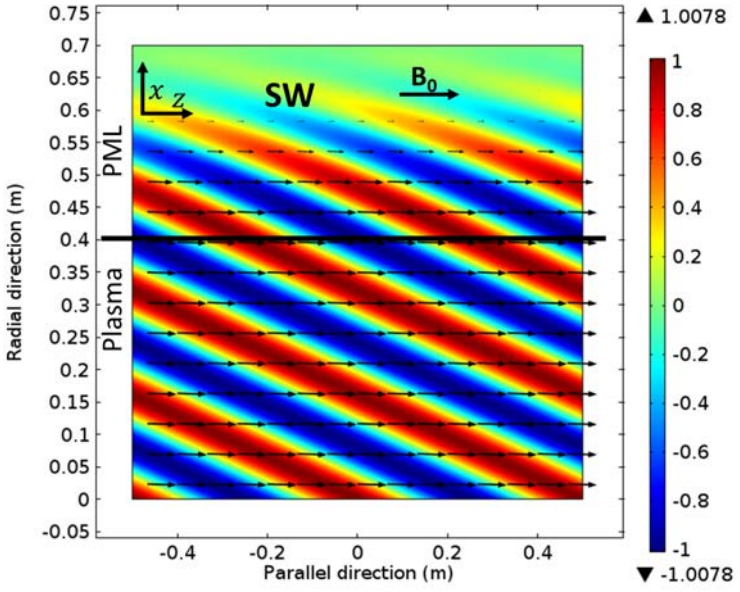

(b)

Figure 3.7: 2D map of the real part of the electric field for: (a) the Fast Wave (forward wave) and (b) the Slow Wave (backward wave). The magnetic field is along the toroidal direction. $\varepsilon_{\parallel} < 0$, $\varepsilon_{\perp} > 0$ and $S'' < 0$ in order to "select" forward waves. The black arrows correspond to the Poynting vector. In (a) $\varepsilon_{\parallel} = -10^5$, $\varepsilon_{\perp} = 10^3$, $\varepsilon_{\times} = 10^2$. In (b) $\varepsilon_{\parallel} = -10^5$, $\varepsilon_{\perp} = 10^2$, $\varepsilon_{\times} = 1$. In both cases $N = 2$, $p_r = 2$, $S''_r = -1$ and $S'_r = 1$.

3.4.5 From reflection coefficient to Poynting vector flux

It was extensively verified that the modulus of the amplitude reflection coefficient observed in plane waves simulations agrees with the analytical predictions. Looking for radial modulations of the RF field amplitude is only possible for plane waves, as the notion of reflection coefficient can only be defined for plane waves. This ideal case is far from reality where a broadband spectrum of wave-numbers, such as excited by realistic ion cyclotron antennas in magnetic Fusion devices, exists. As the system is linear, a reflection coefficient can still be evaluated for each plane wave assuming that plane waves can easily be distinguished even in the presence of several kinds of PMLs replacing the periodic boundary condition used previously. Defining a spectrum of plane waves from the simulations is only possible with some transverse boundary conditions. This process, if possible, will moreover be long and fastidious. In more realistic simulations, another quantity can be monitored: the RF power transferred through the PML interface, i.e. the flux of the Poynting vector. Since PMLs are meant to emulate radiation at infinity, this transmitted power should be insensitive to variations of the PML parameters in the successful simulations. For the case of a plane wave, an explicit analytic expression linking Poynting vector and reflection coefficient can be derived. The complete derivation is shown in Appendix B. Scalar expressions are now replaced by vectorial ones for one eigenmode. The electric field reads:

$$\mathbf{E}\left(x, k_{\|}, k_y\right) = \left[\mathbf{E}^{+} \exp\left(ik_x x\right) + \mathbf{E}^{-} \exp\left(-ik_x x\right)\right] e^{ik_z z + ik_y y}. \tag{3.34}$$

Section 3.4.4 showed that a PML cannot be adapted simultaneously for propagating fast and slow wave. As in the ICRH applications, the fast wave carries the RF power to be deposited in the plasma, it will be the one treated. Moreover the slow wave is evanescent in the considered range of densities and therefore it never reaches the PML. The fast wave electric field reads: $\mathbf{E} = E_y\left(i\alpha\hat{x} + 1\hat{y}\right)$ with $\alpha = \frac{\varepsilon_X}{\varepsilon_\perp - n_\|^2}$.

Since plane waves are considered, $\mathbf{H} = \frac{c}{\mu_0}\mathbf{n} \times \mathbf{E}$. With the incident (index +) and reflected wave (index −) propagating in opposite radial directions, the total induction $\mathbf{H}$ reads:

$$\mathbf{H} = \mathbf{H}^{+} + \mathbf{H}^{-} = \frac{c}{\mu_0}\mathbf{n}^{+} \times \mathbf{E}^{+} + \frac{c}{\mu_0}\mathbf{n}^{-} \times \mathbf{E}^{-}. \tag{3.35}$$

The incident and reflected poloidal field amplitudes are related by the complex reflection coefficient $\Gamma \equiv \eta \exp\left(i\varphi\right)$. The radial component of the time average Poynting vector P_x thus yields:

$$P_x = \frac{1}{2}\Re\left(\mathbf{E} \times \mathbf{H}^{*}\right)_x = \varepsilon_0 c \frac{\left|E_{y0}^{+}\right|^2}{2} n_x \left(1 - \eta^2\right). \tag{3.36}$$

The poloidal electric field E_{y0} imposed at the position $x = 0$ is:

$$E_{y_0} = E_{y0}^{+}\left(1 + \eta e^{i\varphi}\right). \tag{3.37}$$

Multiplying (3.37) by its complex conjugate and combining it with (3.36), yields:

$$P_x = \varepsilon_0 c \frac{\left|E_{y_0}\right|^2}{2} n_x \frac{1 - \eta^2}{1 + 2\eta\cos\left(\varphi\right) + \eta^2}. \tag{3.38}$$

The cosine can change sign in the denominator, thus giving a damped oscillatory behaviour of the coupled power as the reflection coefficient η approaches unity.

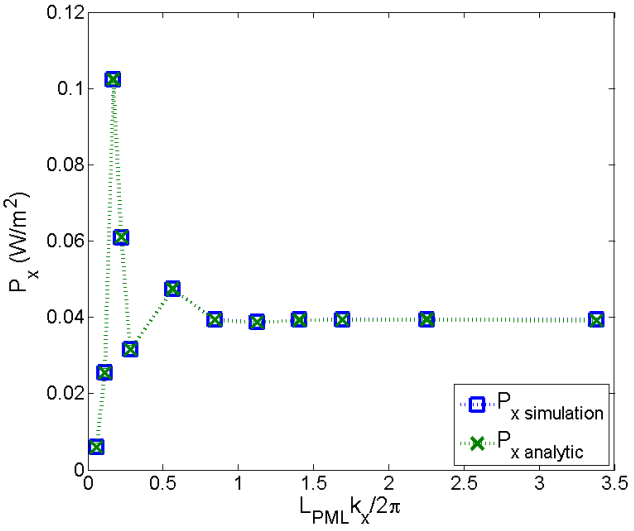

(a)

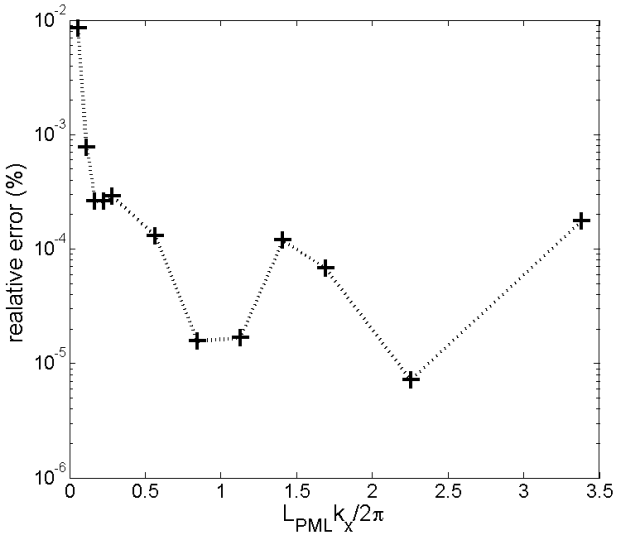

(b)

Figure 3.8: (a) Comparison of the radial Poynting vector value obtained in the simulations with that predicted from (3.38) vs the PML depth normalized to the radial wavelength. (b) Relative error of the Poynting vector shows an excellent agreement between plane wave theory and simulations.

A confirmation of this feature has been performed. The results are shown in Figure 3.8(a). The PML depth was progressively reduced while keeping the plasma domain identical. The parameters of the scan are: $N = 2$, $\varepsilon_{\parallel} = -10^5$, $\varepsilon_{\perp} = 10^3$ and $\varepsilon_{\times} = 10^2$, $S'_r = 1$, $S''_r = -1$, $p_r = 2$, $L_{\parallel} = 1\,\mathrm{m}$ and $L_{\perp} = 0.4\,\mathrm{m}$. Triangular finite elements of size 2 cm were used with a 10 scale factor in the mesh in the radial direction. The scale factor is the ratio of the typical element size in both directions. The value of the radial component of the Poynting vector is then compared to its prediction from (3.38). The agreement between predictions and simulations is excellent as the relative error is small. It also confirmed that taking a PML depth larger than the radial wavelength does not allow much improvement on the Poynting vector. The transmitted power is therefore another possible qualitative indicator to monitor the quality of the PML in realistic simulations, faster than evaluating a reflection coefficient for each plane wave in the excited spectrum of wave-numbers.

3.5 Summary

An original use of PML method has been successfully performed in homogeneous magnetized plasmas. Within this approach, the PML technique is used to emulate radiating boundary conditions at infinity. Magnetized plasmas contain several specificities that could be a priori of concern for the application of PMLs for vectorial simulation of time-harmonic wave propagation in magnetized plasmas.

The first issue concerns its formulation for gyrotropic dielectric tensors with off-diagonal elements. A versatile formulation was found in the literature and was interpreted as standard wave propagation in an artificial medium with damping properties. Its implementation is quite general, aesthetic and easy to accomplish.

PMLs have been at first tested on homogeneous magnetized plasmas for plane waves using the finite element method in the Comsol software. For plane waves, the PML efficiency has been evaluated both analytically and numerically by a reflection coefficient. Agreement with simulations is excellent as long as a threshold due to numerical effects is not reached. This assessment provides useful guidelines for PML implementation in more realistic simulations, where a compromise between low reflection and numerical cost needs to be found over a broadband spectrum of plane waves. For given PML parameters, the reflection is enhanced near a cutoff layer. For propagative plane waves in vacuum, this corresponds to the case of grazing incidence, where the PML behaviour is known to degrade. The spectral domain of low PML reflection can be reduced by enlarging the PML size, at the expense of increased memory requirements and computational time. A better solution is therefore to avoid placing a PML in the neighbourhood of a cutoff for all relevant modes in the radiated power spectrum.

A second specificity is related to the birefringence of magnetized plasmas, implying the coexistence of plane-wave eigenmodes with very different properties. The incompatibility of the present PML formulation to handle simultaneously forward and backward propagative waves has been demonstrated analytically and illustrated numerically. Similar situation was also met for wave propagation in flowing fluids or orthotropic solids [165]. This is an area where significant progress still has to be performed. A way to overcome this critical issue in a tokamak simulation is to exploit the plasma spatial inhomogeneity and let it reflect one of the polarizations, the slow wave in our application. The PML is thus only adapted for the other polarization, the FW here. The situation here however considered an homogeneous plasma. The PML behaviour in presence of an inhomogeneous medium would nevertheless have to be first checked in Chapter 4.

Finite values of k_y have also been considered. It does not indicate any particular issue. However interplay between k_y and the discretization of the grids has been observed. Furthermore the accuracy reached for finite k_y values is less than with $k_y = 0$ for identical mesh parameters. Reflection coefficient of 10^{-3} has nevertheless been obtained. This indicates that for finite size antenna where k_y spectrum exist, PML can be used and that the limits of the PML technique comes from the discretization. It should however be conceded that an exhaustive scan of the impact of finite k_y has not been performed by lack of time and other priorities. This could be envisaged as a prospect. Instead a rapid check with a couple of values has been done.

Numerical optimization for plane waves in homogeneous plasmas of PML and mesh parameters brought some guidelines that will be useful for the application of PMLs for antenna geometries. The PML depth should be of the order of the corresponding wavelength in the PML direction. The PML order $p = 2$ will be used. Increasing the value of the imaginary stretch can reduce significantly the PML depth and thus the numerical cost, but can also cause spurious effects since the gradient in the PML will not be resolved by the mesh any more. That brings some conditions of the mesh parameters. It should of course resolve the wave accurately. For that, a common advice is to have around 10 grid points per wavelength. The same mesh parameters will be also used in the PML. It is noteworthy to recall that the PML can be rendered perfectly reflection less only in the continuous wave equation. But finer mesh resolution in the discretization get us closer to that ideal situation. Polynomial stretching function have been used here and will be used in Section 4, but a possible prospect to reduce and control furthermore the numerical spurious reflection could be to use geometrical stretching function that always keep a constant gradient between adjacent grid points.

An formal equivalence for plane waves between normal component to the medium-PML interface of the Poynting vector and reflection coefficient have been demonstrated. The former quantity will be easier to use with ICRH antennas that emit a spectrum of plane waves. The next step is thus to apply the PML technique in a code calculating FW coupling for ICRH antenna in a tokamak plasma environment.

Chapter 4

Fast wave coupling code for ICRH antennas facing a fusion magnetized plasma in Comsol relying on the Perfectly Matched Layer technique: Application on Tore Supra

The formalism outlined in Section 3.2 is very versatile and can be adapted to a large set of configurations. We would like to include the PML technique for the first time in tokamak plasmas (to our knowledge) in a fast wave coupling code having a full cold plasma description and an ICRH antenna geometry in high single-pass absorption scenarios.

As the goal here is to simulate and predict the behaviour of the ICRH antenna in a given experiment, which does not radiate a plane wave, we have to test and improve the implementation proposed in the previous part. This PML layers have been designed to be use in 3D configurations and for sure there are limitations that we describe in the case of simulations of Tore Supra antennas. Similar studies using PMLs have been done in the case of wave propagation and mode conversion in inhomogeneous ionospheric magnetized plasmas [151]. Some limitations of the PML have been encountered in the study of the PML properties for plane waves in Section 3.4 and in this chapter we will show how, in the simulations of Tore Supra ICRH antennas, to overcome these limitations.

Moreover the proposed solution is applicable only in a given domain, which is described in detail as all the numerical requirements and all the tools needed to reconnect the simulation to experimental parameters to validate the code. Depending on the degree of sophistication of the antenna modelling, we deduce what should be a good description of the antenna to reach its correct behaviour in experiments. However as usual in simulations we have to determine a good compromise between computer limitations and desired degree of accuracy, for which some indications are provided. As a result, the full-wave near field is simulated in two or three dimensions to interpret fast wave coupling experiments carried out on the Tore Supra tokamak.

This exercise provides the opportunity to discuss concrete PML implementation issues in realistic cases, with emphasis on specificities due to anisotropy and birefringence:

- PML adapted to a broadband spectrum of plane waves, how to estimate its quality a priori and check it a posteriori.

- PML adapted to different directions in tokamak.
- Where to place the PML with respect to the antenna structure in order to capture the relevant fast wave physics.
- Avoid the eigenmode incompatibility issues discussed in Section 3.4.4.

The first part of this chapter introduces the experimental parameters and the experimental observations that the fast wave coupling code should be able to reproduce. Then the antenna and plasma modelling is discussed. Finally the implementation and the tests of the PML technique with an antenna geometry in the context of tokamak magnetized plasmas is performed. In the second part, simulations in 2D and in 3D are compared to experimental values of the coupling resistance. Also addressed is the accuracy level needed in the antenna geometry to produce quantitative wave coupling results compatible with the measurements. A comparison with simulations performed with the reference code in this domain is also performed. The last part is devoted to some prospects on the short term for WEST antennas coupling studies and in the longer term.

4.1 Modelling, implementation and numerical tests

4.1.1 Link between Poynting vector and coupling resistance

As it was shown formally for plane waves in Section 3.4.5, the Poynting vector can be a figure of merit of the reflection instead of the reflection coefficient. More specifically the evolution with changes of PML parameters of the component of the Poynting vector perpendicular to the interface plasma-PML can be of interest. The figure of merit still holds true for an antenna, as it is exciting a spectrum of plane waves.

In the simulations, integrating over the contour separating the plasma from the PML region the normal component to the contour of the Poynting vector gives the power carried by the wave leaving the plasma. This also corresponds to the power that is coupled/transmitted to the plasma from the antenna. This is performed by computing the cross product of the electric field $\mathbf{E}$ and of the conjugate of the magnetic induction $\mathbf{H}^*$:

$$P_t = \int_{\text{contour}} \left(\mathbf{E} \times \mathbf{H}^*\right)_n ds, \tag{4.1}$$

where s denotes the coordinate along the contour. The transmitted power is explicitly linked to the coupling resistance R_c defined in (2.36).

On Tore Supra, this linear coupling resistance R_c in Ω/m is obtained from standing antenna voltage and capacitor measurements through a commonly used transmission line model of the antenna [41]:

$$R_c = 2P_t \left(L_{\text{strap}} \int_{\text{strap}} |I_{RF}(s)|^2 \, ds \right)^{-1}, \tag{4.2}$$

where $I_{RF}(s)$ denotes the RF peak current profile along the strap (assumed sinusoidal in 2D), P_t the net time averaged transmitted power in the feeding line and L_{strap} the length of the strap. The resistance per length unit is adjusted over a large band of frequencies to reproduce experimental matching values on vacuum taking into account geometrical parameters of the line in the characteristic line impedance. On plasmas, it gives coherent results with expectations [65].

4.1.2 Description of the wave coupling experiment

Wave coupling was assessed in dedicated RF pulses conducted in dipole phasing, using the D(H) minority heating scenario at 57 MHz, with minority fraction 5% and with magnetic field $B_0 = 3.87$ T at $R = 2.37$ m (see Figure 2.4(a)). The classical antenna, introduced in Section 2.4, was located at $R_{ant} = 3.13$ m, which denotes the radial position of the leading edge of the antenna limiter, the innermost part of the antenna. For these experiments the FW single pass absorption was effective, which motivates using PMLs to emulate FW radiation to the main plasma. During the RF pulse #43026 the plasma separatrix was pushed back progressively from the antenna. Over this radial scan the density profile was measured by reflectometry with an estimated ± 1 cm uncertainty in the radial position of each density point [65, 146]. The time average density profiles over 0.5 sec intervals are shown in Figure 4.1(a). The radial positions of the separatrix R_{sep}, known with a 0.5 cm accuracy, are also averaged over time.

In Tore Supra it was found that R_c is well characterized by a parameter representative of the wave tunnelling through the edge plasma: the radial distance between the radiating straps and a characteristic cut-off layer for the fast wave, evaluated for $k_{\|} = 13\ \mathrm{m}^{-1}$ the maximum in the RF current spectrum in dipole strap phasing [65]. The cut-off density is: $n_{cutoff,FW} = 9.3 \times 10^{18}\ \mathrm{m}^{-3}$. In Figure 4.1(b) R_c was plotted against the measured strap-cutoff distance, that was moved from about 5 cm to 10 cm (see Figure 4.1(a)). Exponential variation of R_c with $R_{strap} - R_{cutoff}$ is evidenced, consistent with an evanescence process. R_{strap} and R_{cutoff} denote respectively the position of the front face of the strap and the position of the cutoff layer. The coupling resistance is assumed to behave as [65]:

$$R_c \sim \exp\left(-2 < k_x > [R_{strap} - R_{cutoff}]\right), \tag{4.3}$$

where $< k_x >$ can be seen as an average value of k_x over the radial path strap/cutoff [65]. $< k_x >$ is indicative of the slope of the curve in Figure 4.1(b).

The same procedure was followed in the pulse #40574 where several antennas were available: two classical antennas and the ILP antenna, also introduced in Section 2.4. In this pulse, the antennas were at 48 MHz and the central magnetic field was accordingly changed to 3.1 T to keep the cyclotron resonance position invariant. One classical antenna, named here classical (2), and the ILP antenna were placed at $R_{ant} = 3.13$ m while the other classical antenna, named classical (1), was located 2 cm behind of the two others radially at $R_{ant} = 3.15$ m. The antennas were active one by one with the same power. The plasma environment around the antennas is assumed to be equivalent.

The radial position of the separatrix was moved horizontally over 5 cm to modify the distance between the strap and the considered cut-off layer (see Figure 4.1(c)). It gets to similar results for R_c, as shown in Figure 4.1(d). The two classical antennas coupled similar amount of power taking into account the 2 cm difference in their radial position. The ILP antenna coupling efficiency was however only 40% of the one for the classical antenna for the same distance. It was attributed to the 1.8 cm shift outwards for the straps position in the ILP antenna (represented by the horizontal shift between the blue and red curve in Figure 4.1(d)). It does not explain however the vertical shift between the red and green curves, since the distance strap-cutoff is equivalent for both antennas. The explanation is most probably in the antenna design. We will come back later on this issue (see Section 4.3.2) once the fast wave coupling code for ICRH antennas in tokamak plasmas relying on the PML technique has been checked.

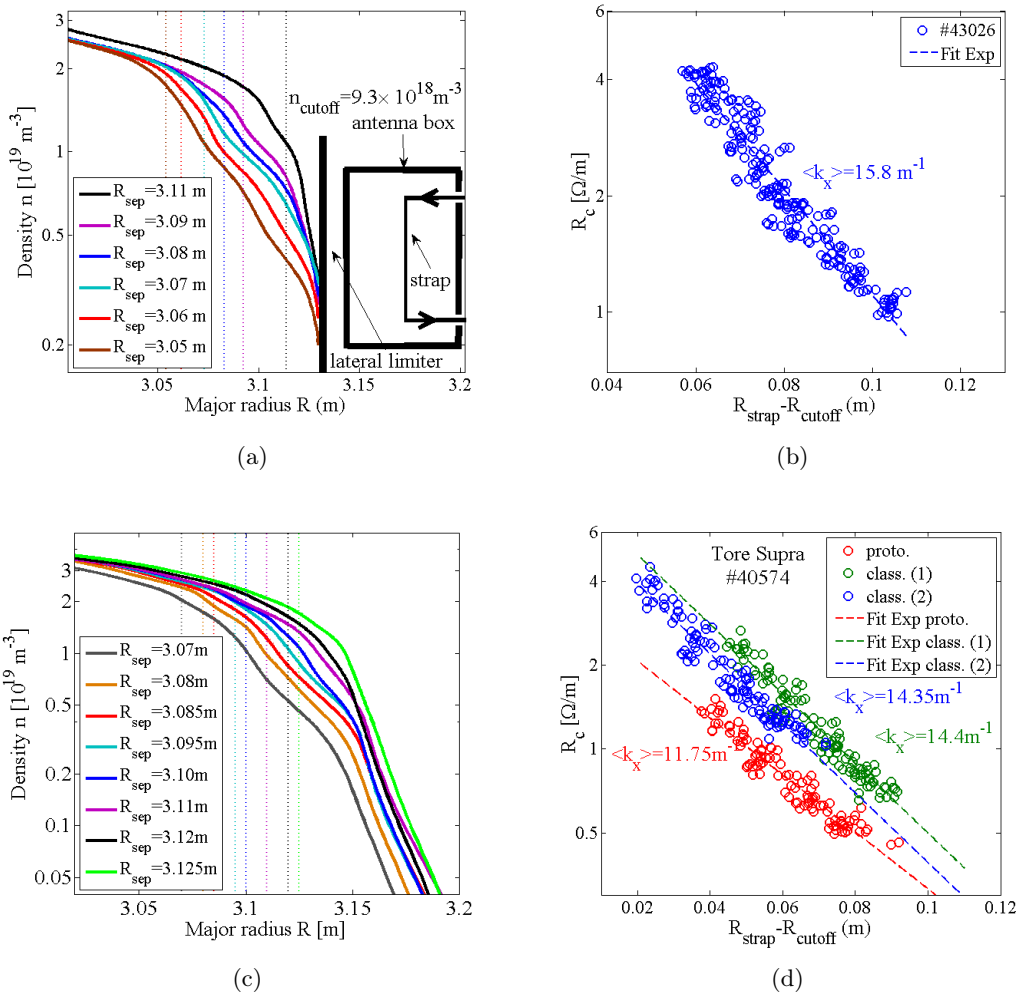

Figure 4.1: Density profiles versus major radius R for the pulses (a) #43026 and (c) #43026. The density profile is modified by moving the separatrix R_{sep} (vertical dashed lines). The sketch of an antenna (not to scale) is drawn to give an idea of the radial distances involved. Experimental coupling resistance values versus distance strap/cutoff for the pulses (b) #43026 and (d) #40574. Each circle represents one measurement of R_c. Three antennas with the same power were used in #40574. Two antennas (blue and green) are of the classical type and one was the ILP antenna (red).

4.1.3 Modelling of the Tore Supra ICRH antennas and of the edge plasma

To reproduce numerically the experimental observations, the full-wave time-harmonic vectorial Maxwell's equations given by the system (2.3) were solved in two dimensions (radial/toroidal) and three dimensions in the edge plasma domain surrounding the wave launcher geometry, using the FEM method with the Comsol Multiphysics commercial software [166].

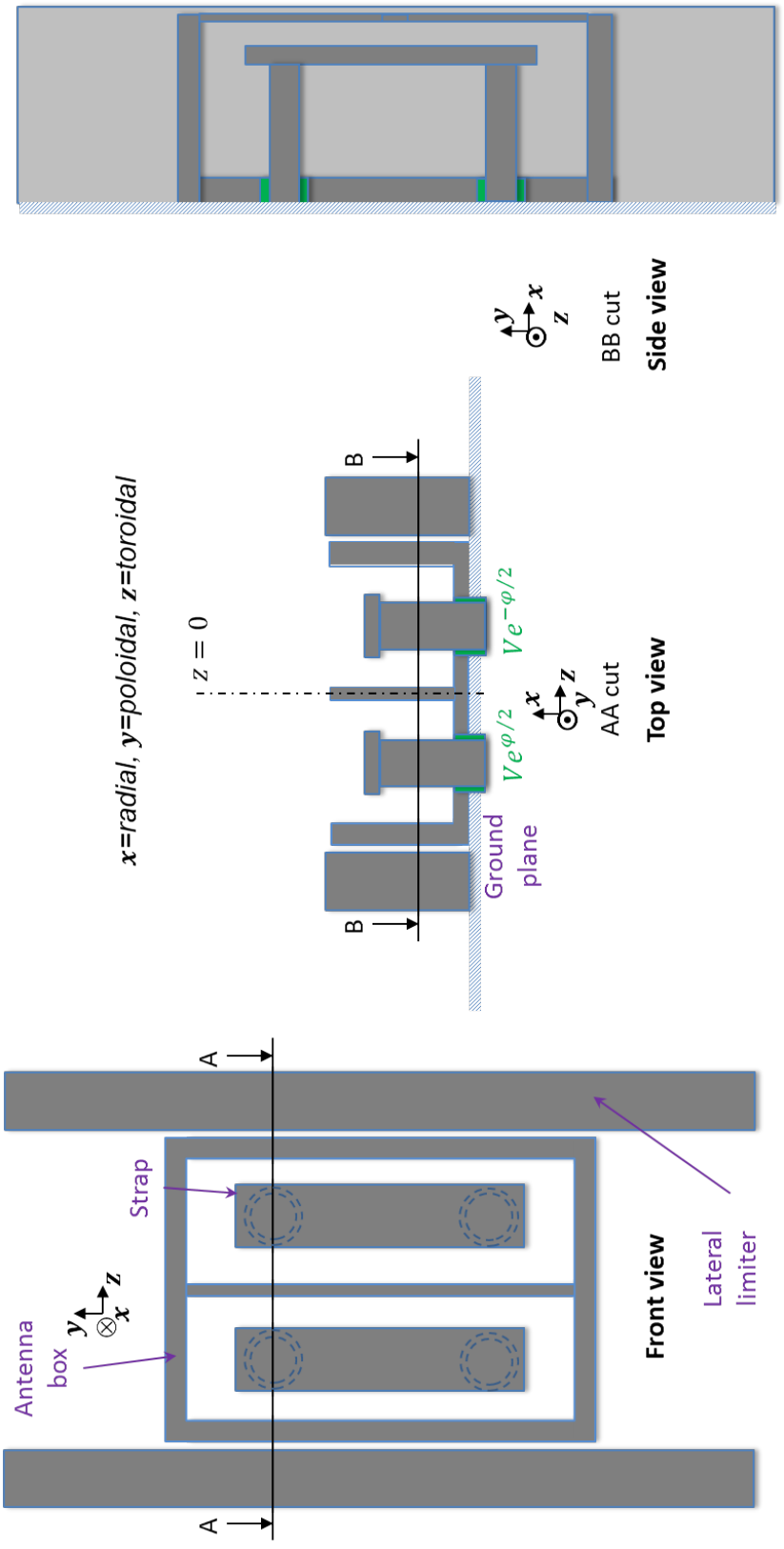

Figure 4.2: Simplified Tore Supra ICRH classical antenna geometry viewed from the front, the top and the side.

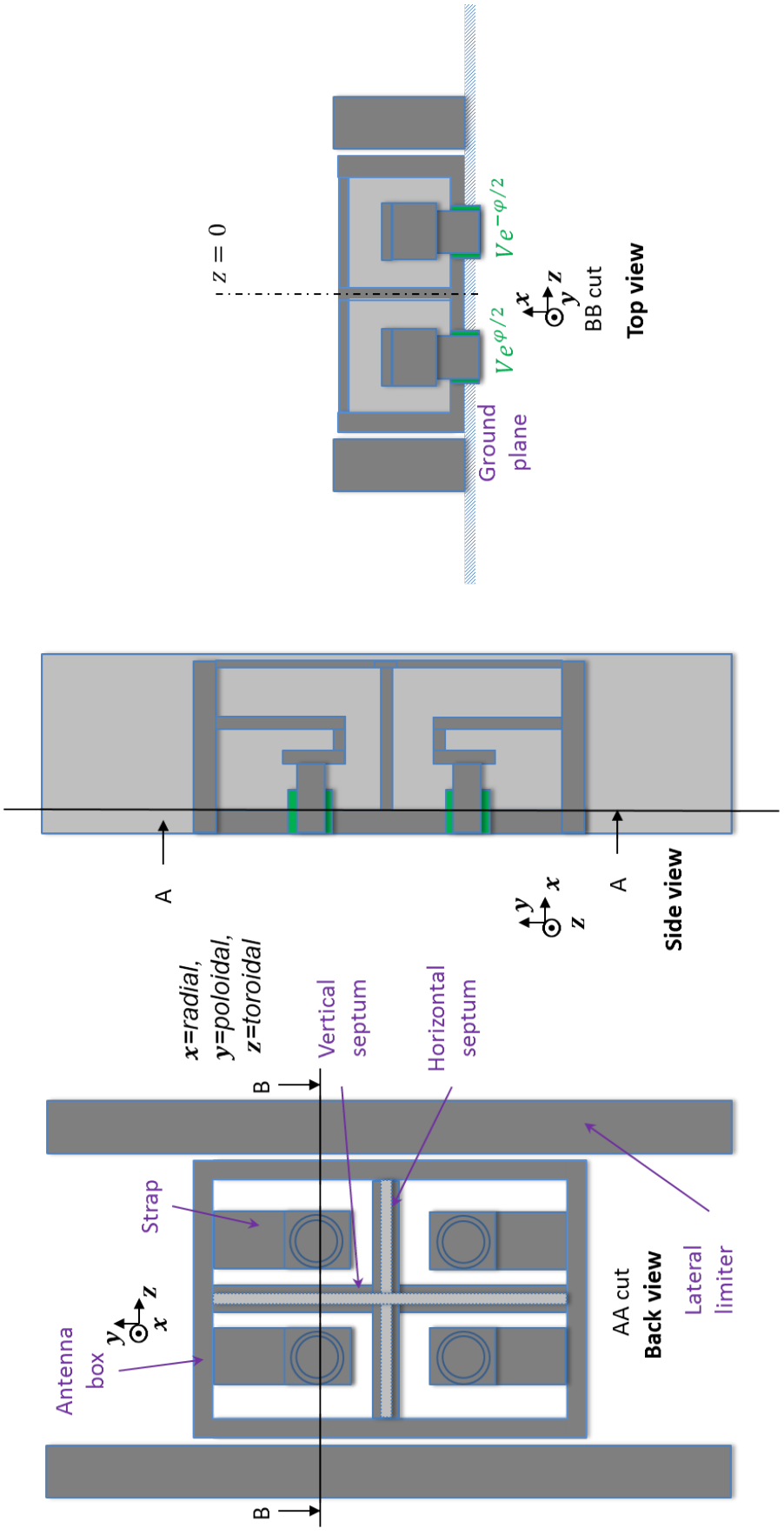

Figure 4.3: Simplified Tore Supra ICRH ITER-like prototype antenna geometry viewed from the back, the side and the top.

Full designs of the antennas with CAD draws are available for TOPICA simulations. However such details are resources consuming. A simplified version of the classical Tore Supra ICRH antenna geometry, shown in Figure 2.10, is here included in the model. For the sake of simplicity the plasma and the antenna structure were flattened in the toroidal and poloidal directions. The shape of the different objects composing the design is as simple as possible with as few objects as possible. Both the active straps and their surrounding passive elements contribute a priori to the fast wave coupling and need to be included in the antenna description. The objects that are kept are both active radiating straps, the antenna box, the central septum and the lateral limiters. An investigation of the necessary description of these objects will be presented later in Section 4.2.2. The Faraday screen is not included. After simplification, the classical antenna looks like in Figure 4.1.3.

All boundaries of the passive components are treated as perfect electric conductors in the simulation domain. Tore Supra ITER-like prototype antenna [137], shown in Figure 2.11 has also been modelled with a flattened geometry, shown in Figure 4.1.3. The same considerations are also assumed to be true.

In 2D geometry in the toroidal/radial plane, both antennas appear to have similar in the design. The difference is in the strap width and the massive protruding part of the poloidal septum. The straps are also further away from the plasma in the ILP antenna. This 2D top view of the antenna is misleading as 3D drawings show that they are quite different. A massive horizontal septum is present on the ILP antenna. The straps are also quite different. The classical antenna has two long straps while the ILP antenna has four short straps with the short-circuit on the top and bottom of the antenna box.

As including a feeding line is impossible for a 2D infinite strap, the fast wave is excited in 2D simulations by imposing a surface current density on each strap face independently, with the condition that the total current on the strap is 1 A. It is noteworthy to mention that this situation is not self-consistent but an ad hoc choice. Self-consistency can only be achieved in 3D. It is also possible to change the current balance between front face and back face, thus imposing more current on one face than on the other (see Figure 4.1.3). The surface current density is assumed homogeneous in the toroidal direction. In reality due to magnetic shielding, the current distribution is peaked on the sides of the strap [63]. Magnetic shielding also occurs due to current loop of the Faraday screen rods [32], that are not included here. The current densities on the sides are linearly ramped up from the value at the back to the value on the front to keep continuity of the current density along the strap contour, as shown in Figure 4.1.3.

In the ideal 3D model the complete resonant double loop (RDL) scheme should be reproduced and its match point should be found before simulating the antenna [167]. Here a simpler procedure is followed to simulate the perfectly matched RDL. The coaxial line and the capacitors are not modelled. Instead RF voltages are imposed at the RF ports connected to the capacitors (see Figure 4.1.3), with an imposed phase between the top and bottom of the straps. The RF current then develops self-consistently along the straps, treated as perfect metallic conductors.

The simulated magnetic field is assumed horizontal (i.e. no poloidal component), whereas its actual pitch angle is estimated to be 3.5° in the reported experiment. Furthermore since the Faraday screen is not included or at least tilted FS rods are not included, left/right antenna symmetry can be assumed. Only half of the antenna can therefore be simulated, with a symmetry condition on the plane $z = 0$ (see Figure 4.1.3), to reduce by half the numerical cost in 3D. Tilted FS rods and tilted $\mathbf{B}$ would however break the symmetry. The full antenna would thus have to be included.

With a dipole ($[0, \pi]$) toroidal phasing between straps, this symmetry condition is ac-

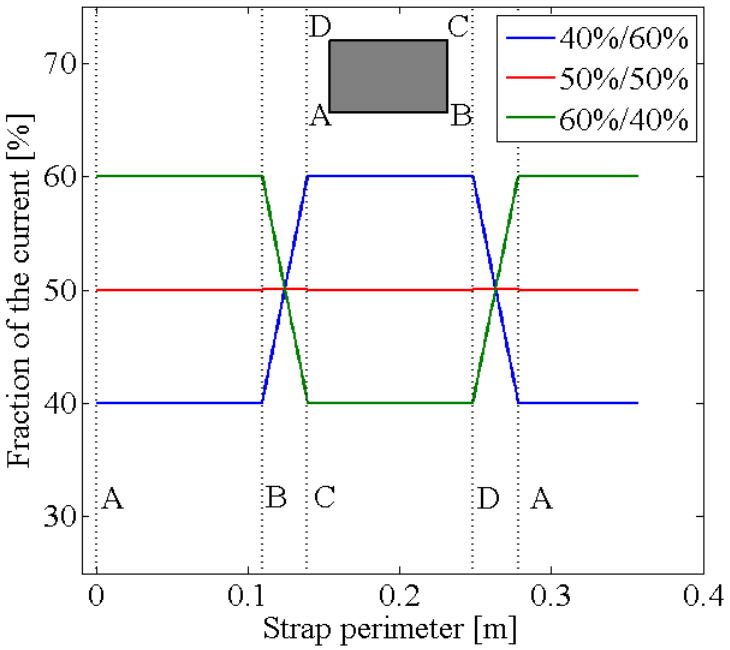

Figure 4.4: Surface current density along the strap perimeter ABCD in 2D simulations. Different current balance front/back faces are displayed.

tually an anti-symmetry for the RF electric field between left and right straps. This is performed in practice by enforcing a metallic condition on the plane $z = 0$. Test simulations with full and half antenna have been performed in 2D and give the same results for the coupling resistance R_c. Monopole phasing can also be considered. In that case, a symmetry for the electric field is observed between left and right straps. In practice, it is realized by enforcing a perfect magnetic conductor condition.

The antenna is placed in vacuum facing a plasma, as shown by Figure 4.5. Only one ion species is considered: no ion-ion hybrid resonance is envisaged in the plasma edge, only majority ions are supposed to play a role there. In the Stix dielectric tensor, the plasma is considered here as pure deuterium (D). Simulations with 5% H produce a discrepancy of less than 1% on the coupling resistance.

The time-averaged radial density profiles from reflectometry, as well as a radial magnetic field profile varying as R^{-1} are included in the simulated plasma domain, to be as close as possible to the experimental conditions. In the radial PML, the density and the magnetic field strength are constant and their values are those in the main plasma at the PML entrance. In the toroidal PML the plasma is inhomogeneous parallel to the PML boundary. The same kind of stretching functions are used in all PMLs. It is not fully clear how this affects the PML behaviour since it was observed that most of the wave power is entering the radial PML. Only a small fraction on the wave power is entering the lateral PMLs. No effect was observed in these conditions.

4.1.4 Requirement on the PMLs

The plasma-vacuum domain is surrounded by PMLs, as shown by Figure 4.5 in the 2D case. The PMLs have to satisfy to several requirements. First, as the plural of PML is

used, several PMLs need to be considered. Each direction needs its own PML as shown in section 3.2.3. As the general situation is three-dimensional, there are the radial, toroidal and poloidal PMLs. There are additionally PMLs with combination of two of the possible three directions: radial-poloidal, radial-toroidal and poloidal-toroidal. At last in the corners, there are PMLs combining all three directions. The same kind of stretching function has been used, following the rules expressed in Chapter 3. That gives in total seven types of PMLs to be defined. The coordinate stretching must maintain continuity at PML-PML interfaces. In 2D simulations, the situation is simpler since the poloidal direction vanishes. Three types of PMLs were implemented, where either the radial coordinate or the toroidal one or both were stretched (see Figure 4.5).

The second requirement is on the mode to be damped since the incompatibility for PML requirements between forward and backward waves has been shown in Section 3.4.4. Although ICRH antennas are meant to produce the FW, they also excite the SW parasitically. When propagative (generally in the immediate antenna vicinity) the SW is a backward mode in the ICRH frequency range, while the FW is forward. In the case of a fusion plasma, there is a way to overcome this critical issue: take benefit from the inhomogeneity of the density profile. In the far Scrape-Off-Layer (SOL), corresponding to the region denoted 1 in Figure 4.5, most FW modes are evanescent whereas the SW modes are propagative. There exists however a critical density $n_{c,SW}$ above which the SW is evanes-

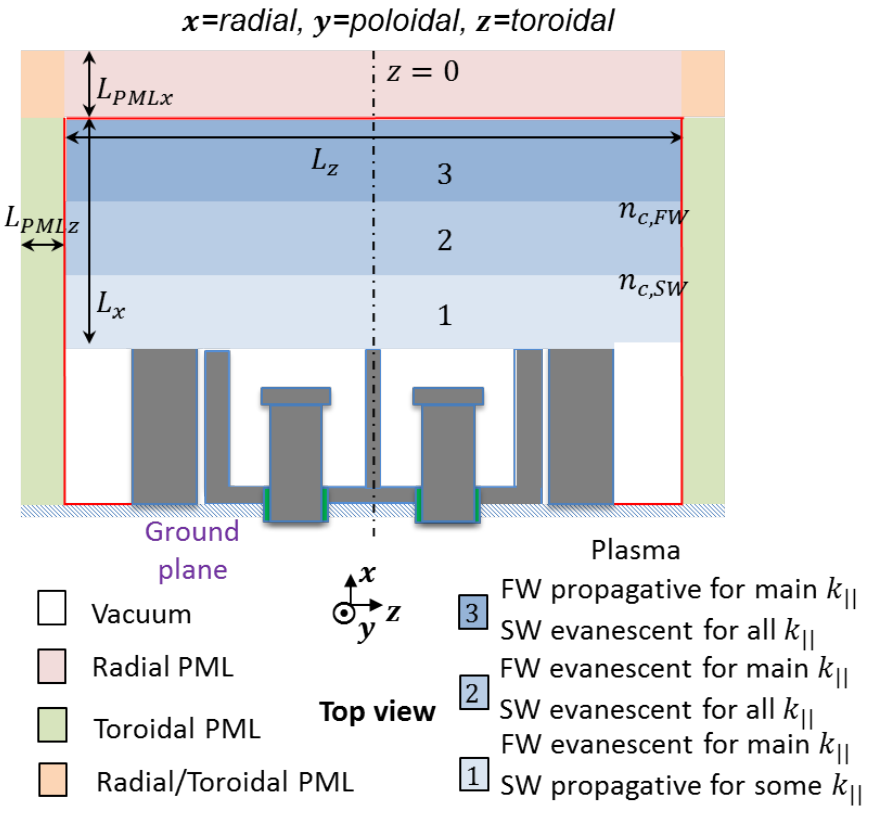

Figure 4.5: Diagram of the complete computational domain in 2D for simplicity. Different regions are considered: vacuum, plasma and three PML types around the antenna structure. The red contour defines the plasma-PML interface where the flux of the Poynting vector is evaluated. In the plasma, subregions exist according to the behaviour of the waves.

cent whatever $k_{\|}$. This occurs when $\varepsilon_{\perp} = 0$, corresponding to $n_{c,SW} \approx 1.3 \cdot 10^{17}$ m^{-3} in our simulations. Above the SW cutoff the wave becomes evanescent, it is naturally reflected by the plasma and penetrates only for density below the cutoff density. Above, an exponential decay is present which avoids the use of PML for SW at densities above the cutoff density (natural screen of SW). As no power associated to SW goes at high density and even if the PML does not work for SW, no spurious effects of the computation are induced. The solution is thus to place the radial PML beyond the location of the SW cutoff. The PML thus only has to be adapted for the FW.

As the antenna structure is placed in vacuum and the density at the antenna limiter leading edge is 10^{18} m^{-3}, the SW is here always evanescent. This condition is presently incompatible with the study of RF sheaths [34] requiring also the density profile up to the antenna radial position. For these additional radial positions the slow wave can possibly be propagative (see Section 2.1.4). Issue with lower hybrid resonance ($\varepsilon_{\perp} = 0$) is avoided in this thesis by a sharp transition between vacuum and plasma at density above this resonance. But the countered part is a reflection associated to the index jump. Moreover a shallow density profile crossing the layer $\varepsilon_{\perp} = 0$ could produce resonance cones [168–170]. It becomes in that situation impossible to adapt the PML due to the singularity introduced by the resonance cone by remembering that a singularity is associated with discontinuity incompatible with the use of PML (see Section 3.3.2). A comparison in 2D with an exponentially decaying density profile between the side limiters (where the minimum density still gives $\varepsilon_{\perp} < 0$) but vacuum in the antenna box has not shown a significant difference on R_c (second decimal).

Other requirements related to the FW physics exist for the PML position. In region 2 on Figure 4.5, the SW is evanescent, as is the FW below the cutoff density $n_{c,FW} \approx 9.3 \cdot 10^{18}$ m^{-3} for the main mode. To reproduce ICRH wave coupling, it is important to reproduce the peripheral tunnelling of all the important plane wave components in the launched $k_{\|}$ spectrum. The plasma-PML interface should be placed radially beyond the position of the highest $n_{c,FW}$ for the considered modes. Knowing the FW dispersion relation (2.21), $n_{c,FW}$ can be easily found. The FW in the region denoted as 3 is now propagative for the main $k_{\|}$ in the spectrum.

Moreover further caution should be taken in order to avoid any problem because of these cut-off layers ($k_x \to 0$), which would be requiring huge PML depth. This should be avoided to minimize the numerical cost of the PML. The PML entrance should thus be placed even further, at a radial position where the radial wavelength is much smaller. This is illustrated by Figure 4.6 where the radial wavelength is computed with the fast wave dispersion relation (2.21) for the first density profile in Figure 4.1(a). Characteristic values of $k_{\|}$ in the antenna spectrum were taken. They indicate several informations. First, the PML interface should be placed after the cutoff indicated on Figure 4.6 by the peaks in the radial wavelength. Second, they indicate that the radial wavelength is rather large just after the cutoff. It is therefore necessary to place the PML interface at the location where the wavelength is smaller in order to limit the computational cost. Less importance is given to high value in the $k_{\|}$ spectrum since they are preferentially reflected by the plasma. In practise the position of the radial PML interface is chosen by looking at $k_{\|} = 13$ m^{-1} corresponding to the maximum in the spectrum. The PML interface was placed in the following around $x \approx 0.4$ m where the radial wavelength for $k_{\|} = 13$ m^{-1} is approximately 0.2 m. A scan around this position has shown a small variation of R_c. This process was done here manually, but it could in principle be automated, if the antenna $k_{\|}$ spectrum, the density profile and the dispersion relation are known.

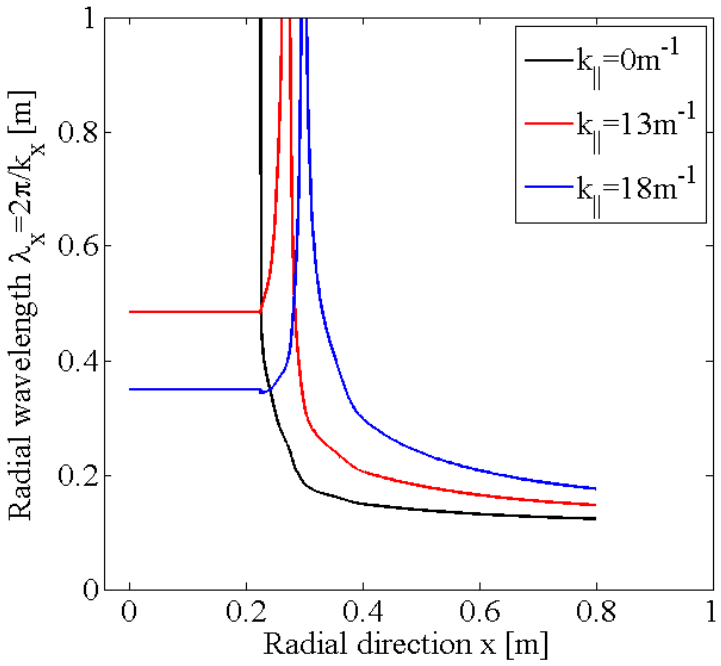

Figure 4.6: Radial wavelength λ_x (in m) versus the radial direction x (in m) pointing towards the plasma center for different characteristic values in the antenna $k_{||}$ spectrum: minimum value, optimal value and maximum value.

4.1.5 Simulation setup and resources requirements

Simulations were performed on a dedicated computer equipped with two Intel Xeon E560 processors and up to 24 Go of RAM memory. The domain is meshed by triangular finite elements in 2D and tetrahedral elements in 3D. The 2D simulations were performed with a maximum element size of 0.01 m and a scaling in the mesh $(2,1)_{(x,z)}$ whereas it was 0.04 m and a scaling $(3,1,2)_{(x,y,z)}$ in 3D. The plasma domain is about 0.5 m $\times$ 0.15 m $\times$ 1 m in the parallel, radial and poloidal direction respectively. It gives for the effective simulation domain (i.e. without the PMLs) a 0.12 m^2 surface with $\approx 80,000$ triangle elements in 2D and a 0.12 m^3 volume with $\approx 190,000$ tetrahedral elements in 3D. Comparing a simulation with PML to the entire volume in Tore Supra $\left(25\ \mathrm{m}^3\right)$ gives at least a factor 200 for the plasma volume (not counting the PML volume and vacuum) for the memory and CPU usage and even more if hot plasma effects have to be included. It consumes about 3 Go of RAM memory in 2D and about 18 Go in 3D. Gyrotropy in the dielectric tensor consumes significantly more memory than the non gyrotropic case. The main limitation to simulate finer geometry in 3D is the RAM memory. To reduce the numerical cost in 3D, only half of the antenna is simulated with an anti-symmetry condition on the plane $z = 0$ as explained in Section 4.1.3. The PMLs domains are meshed in the same way as the plasma. These meshes are not fine enough to accurately resolve the slow wave dynamic spatially that is anyway reflected by the plasma. With these settings a typical simulations in 2D is done in less than one minute while the simulation time in 3D is greatly dependent on the required accuracy and on the presence or not of gyrotropy in the dielectric tensor. 3D results without gyrotropy and a precision of 10^{-3} can be obtained within 2 hours whereas with gyrotropy it can take 1 day. As a comparison, to produce each surface impedance matrix [8], TOPICA [31] needs approximately 4 hours with 576 cores on a supercomputer.

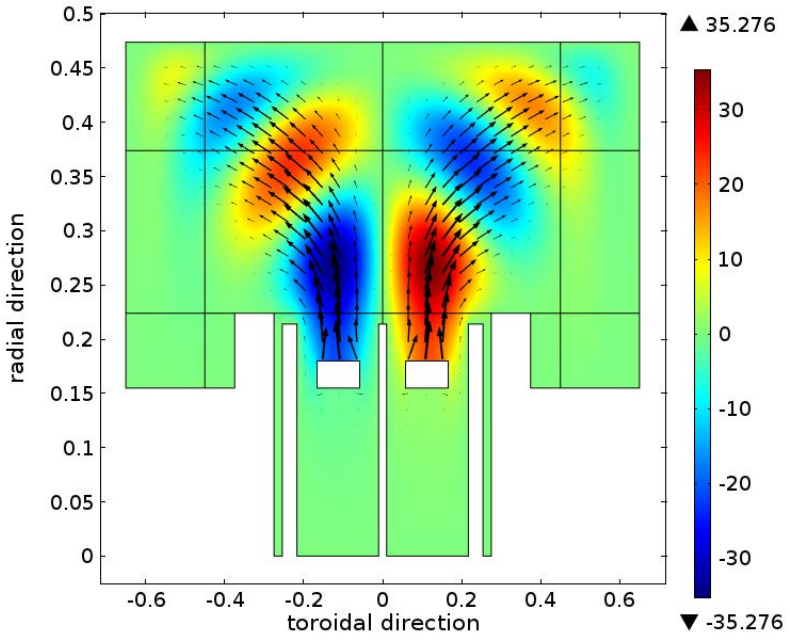

(a)

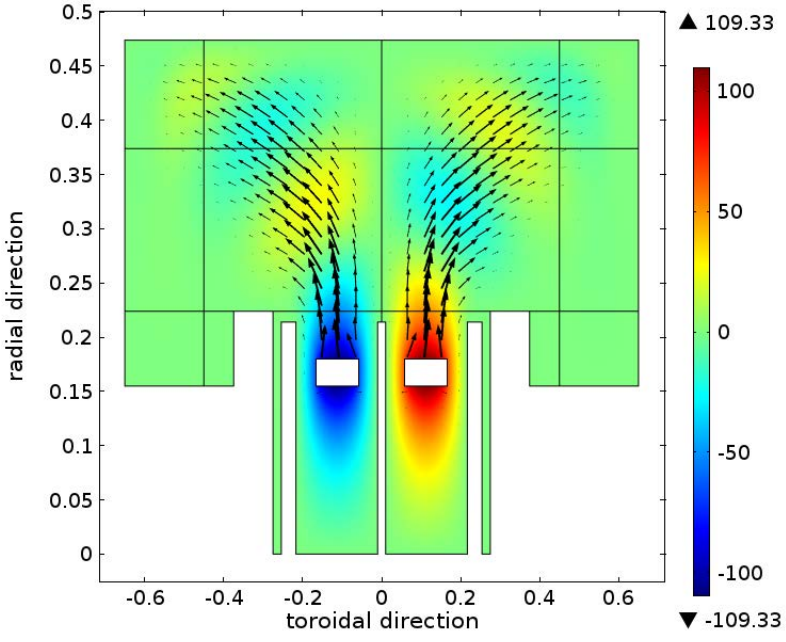

(b)

Figure 4.7: 2D map of (a) $\Re(E_y)$ and (b) $\Im(E_y)$ in V/m radiated by the antenna in the toroidal/radial plane (dimensions in meter) with the first density profile. The black arrows represent the Poynting vector. The abscissa axis represents the toroidal direction while the ordinate axis denotes the radial direction written under the form $x = R_{ref} - R$ where R is the major radius and R_{ref} the position of the back of the antenna box.

4.1.6 Test of the PMLs with a 2D antenna in a fusion plasma environment

In this section, only the classical antenna with the pulse 43026 was used. Figure 4.7(a) and (b) shows an example of the obtained map for the real and imaginary parts, respectively, of the poloidal component of the wave electric field. The FW wave is excited by the straps and tunnels towards the plasma. It then propagates freely until it reaches the PMLs surrounding the domain and is damped without sign of reflection. The direction of the Poynting vector is also indicated with black arrows, showing that the RF power is sent into the plasma. The wave is mainly absorbed in the radial PML. The radial density and magnetic field gradient does not seem to cause any issue for the lateral PMLs.

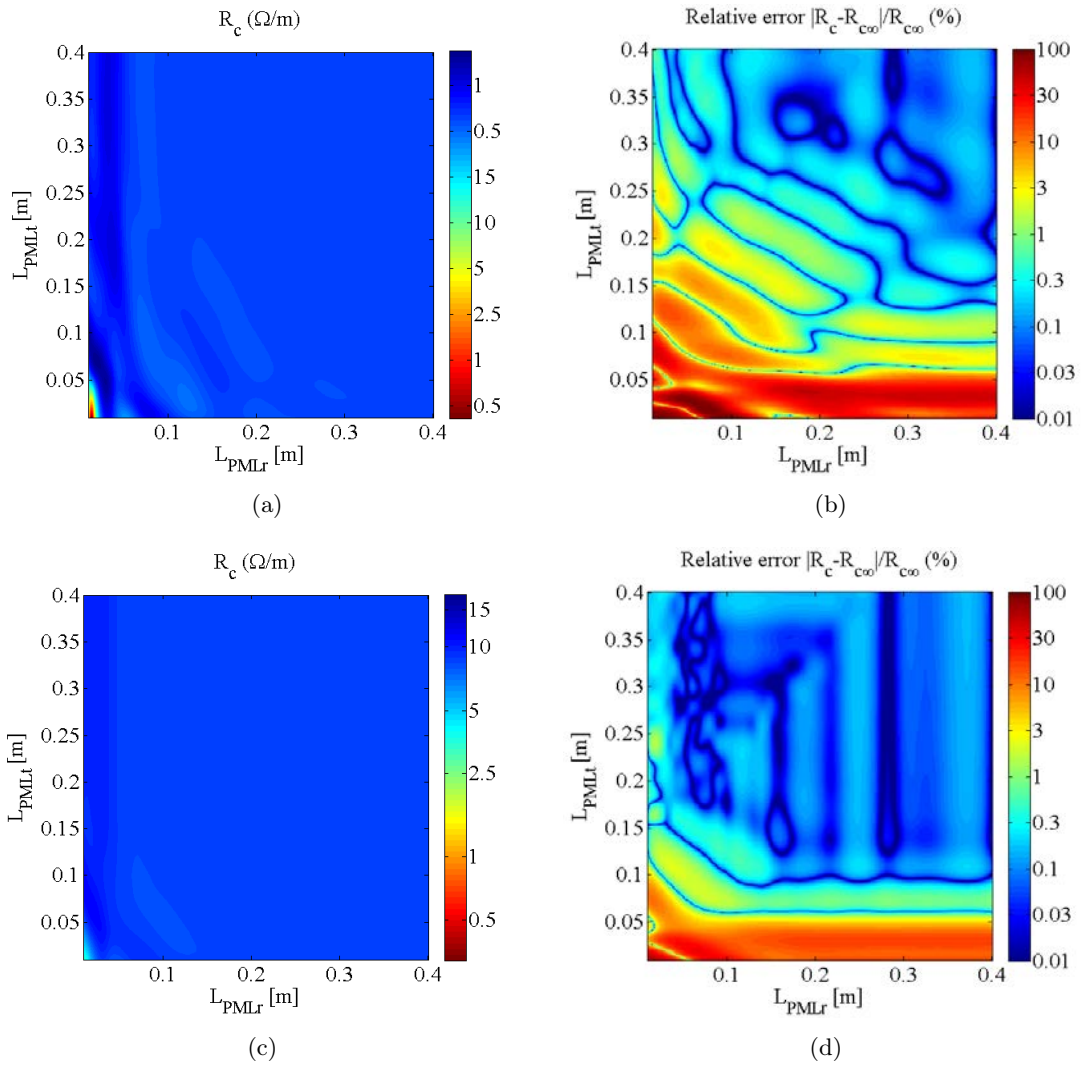

Figure 4.8: (a) Sensitivity of the coupling resistance to the PML depth in both radial and toroidal directions with $S_r'' = S_t'' = -1$ with the first density profile. (b) Relative error in $\log_{10}$ scale of the coupling resistance in function of the PML depth with $S_r'' = S_t'' = -1$. (c) and (d) Same as (a) and (b) with $S_r'' = S_t'' = -2$.

Monitoring the coupling resistance while varying the PML depth or stretch can be used to check the PML validity. However it does not quantify the efficiency unlike in the plane

wave case.

Figure 4.8(a) and Figure 4.8(c) show that the R_c is not PML dependent if the PML is large enough. Both the radial PML and the toroidal PML have to be taken into account. Scans were performed by varying the PML depth *cm* by *cm*. In these scans, the following parameters have been used: $L_{\|} = 0.5$ m, $L_{\perp} = 0.15$ m. The same current density was enforced on the front and the back of the strap. The first density profile (the closest to the antenna) in Figure 4.1(a) was taken. The results were then smoothed. When the PML is not large enough, the oscillatory behaviour seen for plane waves is recovered. Increasing the PML depth suppresses the oscillations. The results are then no more PML dependent. The size of the PML can be compared to the radial wavelength at the plasma-radial PML interface (≈ 0.2 m) for the maximum in the $n_{||}$ spectrum given by FW dispersion relation (2.21). The relative error is calculated by comparing the R_c values to the case with $L_{PML_r} = L_{PML_t} = 0.4$ m. Figure 4.8(b) and Figure 4.8(d) show that less 1% discrepancy can be achieved for a cheaper numerical cost and for the same mesh by increasing the imaginary stretching factor as expected from (3.25).

In the following, $L_{PML_r} = L_{PML_t} = L_{PML_p} = 0.1$ m and $S_r'' = S_t'' = S_p'' = -2$ are taken. An arbitrary choice has fixed a good accuracy at less than 1% error on R_c. A conservative choice is done for the value of the imaginary stretch. Indeed, Section 3.4 has shown that the optimal value for a plane wave is $S'' = -8$. However here, a spectrum of plane waves is present. Taking $S'' = -2$ seems a good compromise to reduce the numerical cost due to the mesh size while keeping an acceptable accuracy and saving working time to verify the impact of S'' on the numerical cost and accuracy of R_c. It allows, according to Figure 4.8(d), to obtain less than 1% error for R_c with a PML that has roughly a size of half the wavelength. With these parameters, implementing the PMLs roughly increases by 60% the domain surface in 2D and it roughly doubles the domain volume in 3D, also increasing by the same amount the total number of elements. Further optimization is still possible for either numerical cost or accuracy.

4.2 Comparison of Fast wave coupling properties obtained from the simulations with 2D and 3D simplified Tore Supra ICRH antennas geometries with experiments

Being tested, the model can now be used to study the FW coupling properties and compare the results with the experimental observations. The study quantities are the results of the knowledge of the previous studies done with the existing codes ICANT [32], TOPICA [31]. We also study the role and impact of modelling sophistication on the simulation results.

4.2.1 Launched and coupled spectrum

The first thing to be done is to obtain the power spectrum of the FW wave. The coupled power spectrum is computed by performing the product of the Fourier transform of **E** and **B** on the radial plasma-PML interface giving the flux of the radial component of the Poynting vector. The power spectrum was evaluated by taking an overly large domain in the toroidal direction in order to get most of the absorption in the radial PML. The lateral sides of the red contour defined in Figure 4.1.3 can therefore be neglected.

The maximum of the RF current spectrum in dipole strap phasing is actually obtained at $n_{\|} = 10.9$, corresponding to $k_{\|} = 13$ m^{-1}, by looking at Figure 4.9. Negative $n_{\|}$ are not shown since the profile is symmetrical with dipole toroidal phasing.

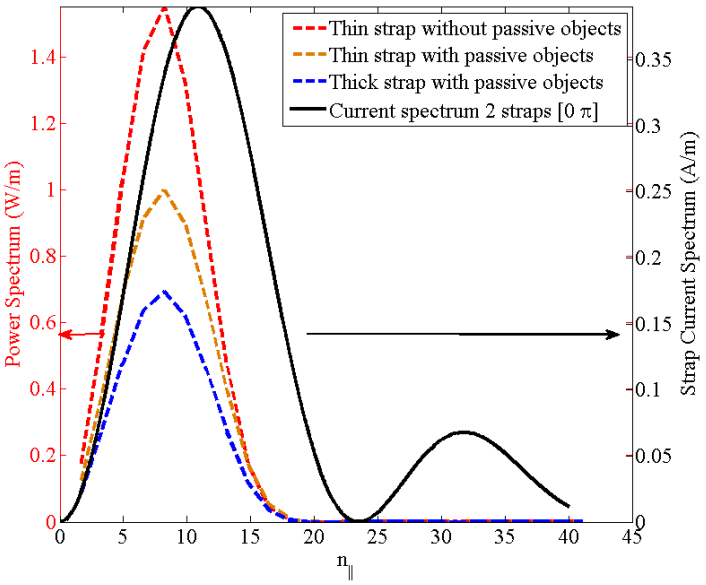

Figure 4.9: Squared amplitude of analytical Fourier spectrum for the RF current on the straps (black straight curve) and coupled power (colour dashed curves) spectrum at plasma/PML interface for the different configurations vs $n_{||}$ for $R_{strap} - R_{cutoff} = 0.045$ m. Negative $n_{||}$ are not shown since the profile is symmetrical with $[0\,\pi]$ phasing.

The maximum of the power spectrum is however situated at $n_{||} = 8.2$, corresponding to $k_{||} = 9.7\,\mathrm{m}^{-1}$and consistent with the results obtained with ICANT in [65], and the secondary lobe vanishes. This is explained since the plasma actually reflects preferentially the high $k_{||}$ waves. Integrating the power spectrum also allows to recover the coupling resistance R_c.

4.2.2 Influence of the antenna geometry elements of the coupling resistance

Only the first profile in Figure 4.1(a) has been used to study the impact of the antenna geometry in 2D. It is shifted radially to modify the distance between the strap and the cut-off layer. This is not strictly speaking equivalent to shifting the position of the separatrix as the shape (gradient) of the profile is not modified while moving the separatrix necessarily modified the radial gradients. But this procedure allows to reproduce the exponential decay of the FW coupling with only $R_{strap} - R_{cutoff}$ as shown in Figure 4.10. Some discrepancy can however be seen by observing the blue dots and the cyan stars, obtained with the real profiles, at high $R_{strap} - R_{cutoff}$.

Several features were progressively added in the antenna geometry: the presence of passive objects and the strap thickness. The trend provided by including these features go towards the experimental coupling resistance values. This shows that these elements are important to recover a fair agreement between simulations and measured coupling resistances. The strap thickness changes the amplitude of R_c while the passive objects change both the amplitude of R_c and the slope. This is consistent with Figure 4.9. Changing the geometry of the antenna modifies the amplitude of the main lobe in the power spectrum. An oversimplified geometry overestimates the amplitude. The thickness of the strap

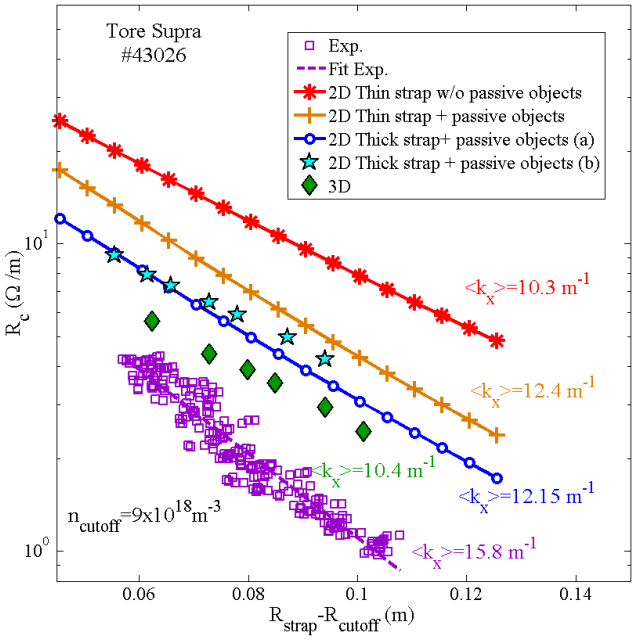

Figure 4.10: Coupling resistance R_c vs the distance strap/cutoff for $k_{\|} = 13$ m^{-1} in dipole toroidal strap phasing. The experimental values are shown again in purple squares for comparison. Simulations results in 2D with different antenna configurations by shifting the first density profile are shown. The 3D results have been obtained using the density profiles in Figure 4.1(a)

(2.5 cm) is not negligible compared to the typical evanescence length for the fast wave (R_c loses 20% every cm). The current flowing on the back of the strap actually sees a larger distance to the cut-off layer than the current on the front. The passive objects induce image currents changing the current map on the antenna.

The coupling resistances with a 3D antenna geometry in Figure 4.10, with the density profiles shown in Figure 4.1(a), are below the ones in 2D with a factor ≈ 1.4. It could be a priori explained by several effects: the presence of a k_y spectrum in 3D due to the finite strap size, the non-consistently computed surface current in the strap in 2D. Despite these 3D refinements, the coupling resistance is always overestimated by an almost factor 2.

The slope of the curve is fairly reproduced. It confirms the evanescent decay of R_c with the distance strap-cutoff. It is however slightly shallower than expected in both 2D and 3D simulations. This could be due to the curvature of the objects composing the antenna geometry not taken into account. The distance strap/cutoff layer is not homogeneous over the entire antenna. Another reason could be the average procedure performed to produce the density profile that is smoothing the fluctuations. The influence of the Faraday screen has also been neglected as well as the pitch angle of the magnetic field. The Faraday screen would lower R_c. Finally, the detailed geometry structures could be added. The reproduction of the decay, plus the fact that only the edge plasma is simulated, suggests however that in our case the coupling resistance is essentially governed by the wave tunnelling through the under-dense SOL.

4.2.3 Influence of the current distribution on the strap of the coupling resistance

Since the current distribution on the strap is not self-consistently computed in 2D, it is interesting to know the sensitivity of the coupling resistance R_c when the current ratio I_f/I_b in % between the front and the back of the strap changes while keeping continuity on the strap sides with a linear function. Again in 2D, only the first density profile in Figure 4.1(a) is used. The profile is shifted radially to modify the distance $R_{strap} - R_{cutoff}$.The ratio I_f/I_b is varied from 40%/60% to 55%/45% in Figure 4.11. It can be observed that R_c is sensitive to the current balance between the front and the back of the strap. Changing the current distribution by 20% changes the coupling resistance by 40-50%.

R_c is higher when more current is on the front of the strap closer to the cutoff. More current is closer to the plasma, the coupling efficiency is therefore better. The current on the back and on the front of the 3D strap have been computed and compared. They give values around 45%/55%, which corresponds to results in 2D where a current distribution between $40-45\%/60-55\%$ is used.

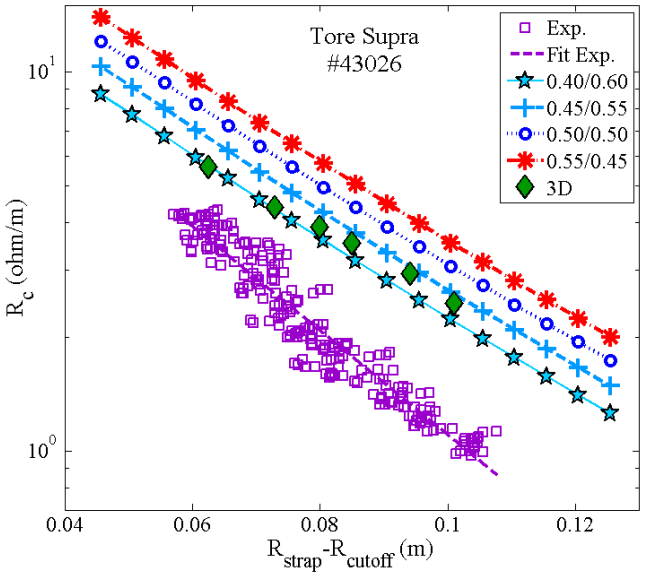

Figure 4.11: Coupling resistance R_c vs the distance strap/cutoff for different current balance front/back in 2D compared to 3D simulations and experiments.

4.2.4 Comparison of the classical antenna with the ILP antenna

To invalidate the possibility that the overestimation of R_c could be due to an error in the code, another pulse (#40574) has been studied where several antennas were available: 2 classical antennas and the ITER-like antenna. As the wave frequency ($f_0 = 48$ MHz) for this pulse is only slightly changed, the other parameters (especially the PML parameters) are kept identical. The coupling resistance R_c is evaluated for each antenna with the density profiles shown in Figure 4.1(c) with a 2D geometry and a 3D geometry.

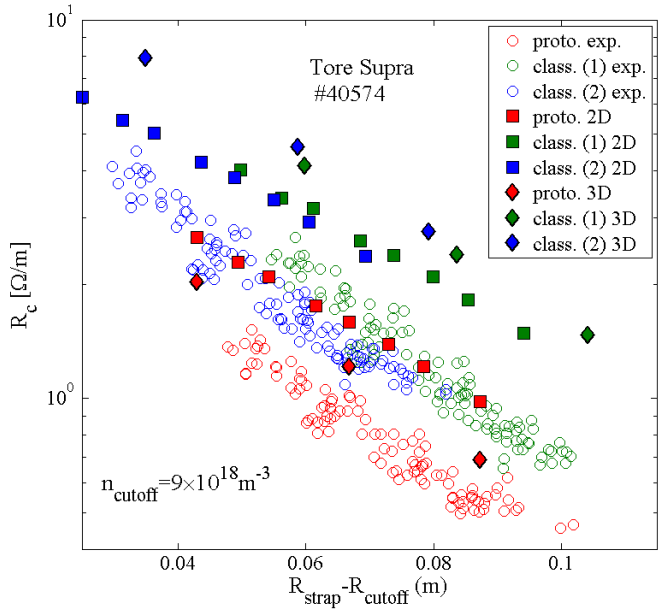

(a)

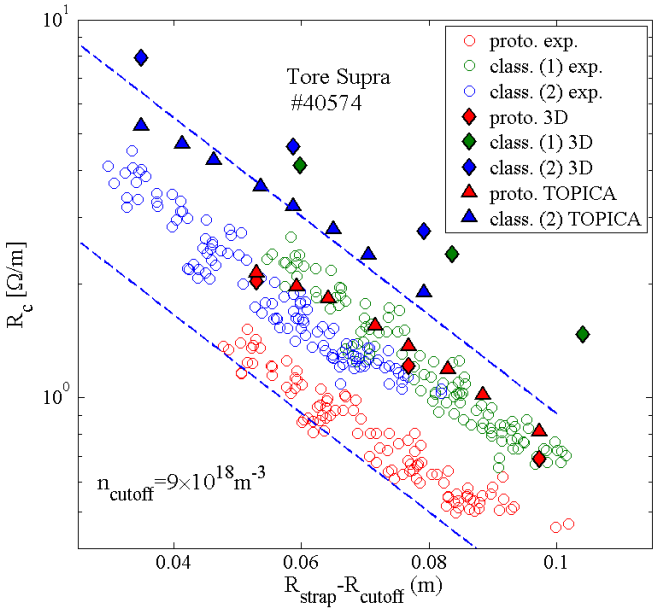

(b)

Figure 4.12: Coupling resistance R_c versus $R_{strap} - R_{cutoff}$ for pulse 40574. Experimental values (circles). The colours represent the 3 active antennas. Comparison with (a) Comsol in 2D (squares) and 3D (diamonds) (b) Comsol in 3D (diamonds) and TOPICA (triangles). Two dashed blue lines shows the sensitivity of R_c from a ± 2 cm change in the distance strap-cutoff for the experimental results.

Figure 4.12(a) shows that both classical antennas, shifted radially by ≈ 2 cm, follow the same curve, strengthening the affirmation that R_c depends mainly here upon the distance strap/cutoff. It also shows that the ITER-like antenna coupling resistance is about 40% of the classical antenna one, despite thinner straps that should in principle increase the coupling efficiency. This ratio is also well recovered with Comsol in 2D and in 3D and also corresponds to the experimental observations on R_c. Moreover, the exponential decay with the distance to the cutoff is also fairly reproduced.

Comparing the pulse #40574 at $f_0 = 48$ MHz with the pulse #43026 at $f_0 = 57$ MHz shows that R_c is overall smaller for the pulse #40574. The amount of power that can be carried by a wave is frequency dependent and increasing with the frequency. From this consideration, it is expected that coupling is better at a higher frequency.

However, R_c is still overestimated by a factor ≈ 2. A 3D geometry taking into account the finite length of the strap allows us to get closer to reality, but it is still not enough. A comparison of the model in Comsol with TOPICA was also performed for this pulse. TOPICA model included a more detailed geometrical description of the antennas with a Faraday screen. The coupling resistance R_c on this pulse is also overestimated with simulations, but by a smaller factor between $1.4 - 1.6$ depending on the profile looked upon. Despite this, the relative factors of comparison between antennas are been well recovered in 2D and in 3D with Comsol and with TOPICA. If an error is present in the code, this error is systematic and exists in both codes.

4.2.5 Possible origins for the overestimation of the coupling resistance

Section 4.2.4 has shown that a comprehensive description of the antenna geometry explains partially the overestimation of R_c. The most probable explanation is the magnetic shielding and the filtering of the electrostatic component of the electric field due to the presence of the Faraday screen changing the wave propagation constant β [32]. Modification of the propagation constant has in turn an influence on the radiated power and thus of the coupling resistance R_c. Including the Faraday screen in the Comsol model geometry would therefore provide estimations closer to TOPICA.

Another possible explanation for at least part of the overestimation of coupling resistance in simulations compared to experiments could be due to a difference in the convention between both evaluations. In the Tore Supra database, the coupling resistance represents a coupled power for 1A on the straps (on average over the strap length). TOPICA calculate coupled powers for 1A at the feeders. In Comsol 1V is imposed at the feeders. It turns out that there could be a substantial difference between these conventions: 1A on the feeders would not necessarily results in 1A on the strap and the coupling resistance would be possibly be overestimated. More quantitative assessment of this effect is needed.

Part of the overestimation can also be interpreted as an uncertainty on the radial distance between the strap and the cutoff by adding $\approx$ 2 cm to the evaluation based on experiment. There are several uncertainties that can cumulate: ± 1 cm for the radial position given by the reflectometer, $\pm 0.5 - 1$ cm for the position of the objects in situ under vacuum conditions. 1 cm variation change R_c by $\sim 20\%$. There is also an uncertainty on the capacitance values to evaluate the experimental coupling efficiency. The capacitance is evaluated for a batch of capacitors. The retained value is an average value over this batch. The real value for a given capacitor can vary of $\pm 10\%$ around this average value.

Influence of the slow wave dynamic, which is removed here through a vacuum antenna box and a mesh not fine enough in the antenna box, cannot be eliminated. The slow wave can, through RF sheath rectification [89], create a convection cell in front of the

antenna [38]. The distance strap-cutoff and the density gradient of the profile would thus be modified. Consequently the efficiency at which the fast wave is coupled to the plasma would also be modified. In that case the density profile in front of the antenna is not the same as the one measured in front of the reflectometer due to the convection cells [38]. Moreover this convection cell does not modify uniformly the density in front of the antenna. The distance to the cutoff would thus be the same poloidally along the strap. Convection could also explain the slope is steeper in the experiments than in the simulations. Furthermore both polarization can get coupled by depolarisation processes when the wall is tilted with respect to the static magnetic field B [171]. The overestimation does not however seem to be related to an issue with the PML technique.

4.3 Conclusions & Prospects for the Fast Wave coupling code with the Perfectly Matched Layer technique

4.3.1 Summary on FW coupling computations relying on the PML technique

An original way to compute fast wave coupling in a tokamak plasma environment is to rely on the PML technique to emulate radiating boundary conditions at infinity, in situations of good wave single-pass absorption. After having checked that the PML works for plane waves in homogeneous plasmas, simulations were performed with an ICRH antenna to study FW coupling properties.

The position of the PML interface has been discussed. The incompatibility of simultaneous forward and backward propagative waves is solved by exploiting the tokamak plasma spatial inhomogeneity. The plasma thus reflects one of the polarizations, the slow wave in our application. The PML is thus only adapted for the other polarization, the FW here. The PML interface must be at a location where the SW is evanescent and the FW is propagative. Moreover to avoid any issue with the FW cutoff, the PML interface should be far away.

The resulting FW coupling model has been implemented and solved using the finite element method in the Comsol software. The model includes a simplified flattened 2D or 3D geometry of a Tore Supra ICRH antenna, as well as the detailed profiles of the edge density, up to a radial position slightly beyond a critical cutoff layer for the FW. The coupling resistance R_c has been showed to be a figure of merits easier to use for antennas than the reflection coefficient.

The measured coupling resistances R_c of the Tore Supra antenna have been reproduced over a radial displacement of the target plasma, in heating scenarios with good single pass absorption. The absolute values of R_c are always overestimated. Evaluations with TOPICA overestimate R_c but by a smaller factor (≈ 1.5), equivalent to the factor between 2D and 3D. This could be related to uncertainty of the actual distance strap-cutoff. The overestimation is not however related to an issue with the PML technique. An exponential decay of R_c with the distance strap-cutoff has been recovered. The decay is slightly shallower than the experimental decay. This property, plus the fact that only the edge plasma is simulated, suggests that in our case the coupling resistance is essentially governed by the wave tunnelling through the under-dense SOL. The placement of the antenna in vacuum in the present model misses the slow wave field influence on coupling. This feature should be modified to check the importance of the slow wave on coupling directly or indirectly with RF sheaths and the generation of convective cells [172].

The necessary level of antenna geometrical description was also investigated. A fair

picture of the coupling resistance can already be achieved within a few minutes by simulating a simple 2D (toroidal/radial) cross-section of the launcher. The results get closer to reality as the geometry is refined. However more and more computational resources are needed, which is incompatible with fine antenna design optimization. As it is fast, a wide range of geometries can be explored. It was found that the strap thickness, as well as some electrically passive elements as the septum and the antenna box have to be included in the antenna design to reproduce faithfully FW coupling. A more detailed geometry, such as the ones used in TOPICA, would certainly give results closer to reality.

Compared to alternative approaches for modelling ICRH wave propagation, our proposed model presents some advantages as well as drawbacks. As the PML technique is used, there is no need for spectral surface admittance matrices and Fast Fourier tranform (FFT). The computational cost is lower. However, using PMLs is limited to heating scenarios with high single pass absorption. As for the surface admittance matrix formalism, the present PML formulation needs to be implemented at a flat interface. Using the FEM method is convenient to handle simultaneously complex wave launcher geometry and an inhomogeneous-anisotropic radiation medium. However this direct method (as opposed to spectral ones) is limited to spatially non-dispersive media, such as cold plasmas. This is not really a problem as only the cold edge has to be modelled in high coupling scenarios. Moreover PMLs in low coupling scenarios serve no purposes. Including a density profile and handling the full dielectric tensor is more realistic than propagation in an equivalent isotropic lossy dielectric. In particular both eigenmodes of the gyrotropic plasma are retained in the radiated near RF field, which could be important e.g. for simulating radio-frequency sheaths in the vicinity of the antenna [173, 174]. But using the cold plasma dielectric tensor makes the numerical resolution more difficult and its subsequent convergence slower, at least in 3D.

Several prospects exist for this code with different timelines. In the short term, it will be used in combination with others codes (TOPICA, HFSS) for the design studies on the new ICRH antennas for WEST. The present code in Comsol can provide fast calculations for FW coupling with a full cold plasma description for parametric scans of fine geometrical parameters scans. Antenna adaptation is not achievable with the present version of the code. With HFSS, FW coupling and antenna adaptation are possible but only with diagonal media, on the contrary to Comsol that accept arbitrary tensors. Finally with TOPICA, both FW coupling and antenna adaptation are possible but require very detailed geometries. However the high level of computation resources needed for one case excludes fine parametric scans. Several others prospects with in mind a longer timeline can be foreseen.

4.3.2 Preliminary optimizations of FW coupling with a improved antenna design based on the ILP antenna for WEST

For the major upgrade of Tore Supra into the WEST platform, three new ICRH antennas are needed. Their design will be an improved version of the ILP that shows insensitivity to load variations compared to the classical antennas with an internal matching system. The improvements must also be compatible with an active cooling system for long pulses. However, as illustrated by Figure 4.12(b), the coupling properties of the ILP were not at the level of the classical antennas. It has thus to be improved for the new antennas to couple larger amount of power to WEST plasmas.

Refining the geometry provide results closer to reality as the cost of computational, hardly compatible with fine antenna optimization. A fair picture of the coupling re-

sistance can already be achieved however within a minute by simulating a simple 2D (toroidal/radial) cross-section of the launcher. Qualitative trends can be obtained by exploring a wide range of geometries and parameters. They can provide useful guidelines for the improvement of the ILP antenna.

During the preliminary studies to improve R_c, hybrid designs of the ILP antenna have been created where parametric scans could be performed. These studies are made with a Tore Supra typical plasma on the pulse 40574. The 2D model is illustrated by Figure 4.13. Several scanned parameters are shown: the strap position with respect to the plasma d_{sp}, the strap thickness d_{strap} and the thickness of the protrusion of the vertical septum Δz.

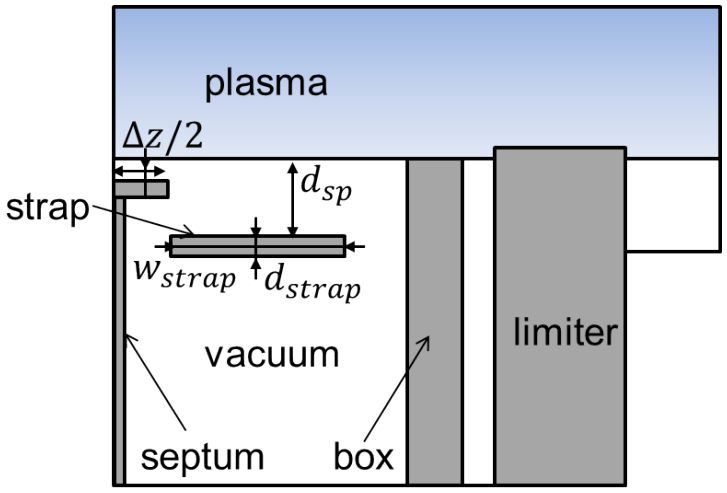

Figure 4.13: Sketch of the 2D antenna geometry for the parametric scans performed in order to find trends to improve coupling of the ILP.

One candidate to explain the poor coupling of the ILP antenna is the strap position with respect to the plasma d_{sp}. The waves have to tunnel through another 18 mm layer of vacuum before reaching the plasma, as illustrated on Figure 4.13. As a shift by 1 cm changes R_c by 20%, it can easily be deduced that after a 18 mm shift, R_c is only 65% of its value.

A confirmation of this feature has been performed with an hybrid antenna design where the straps of the ILP antenna have been placed closer to the plasma by 18 mm. The septum did not have any protruding part ($\Delta z = 18$ mm). This consideration gives a 35% reduction of R_c, but still does not explain the 60% reduction between the antennas classical (2) and ILP. It neither explains the 30% difference between the antennas classical (1) and ILP.

Another candidate is the thick protrusion of the septa on the ILP whose aim is to reduce mutual inductance between adjacent straps. Figure 4.14 shows a scan of the thickness of the protruding part of the vertical septum Δz in 2D.

The decreasing R_c with increasing Δz can be explained by the induction of larger image currents in the antenna box due to the presence of this thick protrusion in the box. The comparison between thin septum of the classical antenna and thick septum of the ILP antenna recover a 30% difference. This corresponds to the factor remaining, unexplained until now, after taking into account the strap position with respect to the plasma. This effect is enhanced as the strap is more toroidally extended and not centered in the box. In fact the inner edge of the strap is almost at the vertical of the protrusion of the septum. It favours the induction of image currents of the antenna structure. The issue still in waiting is to know up to which level the protrusion thickness can be reduced without compromising

matching.

The ILP antenna had thinner strap than the classical antenna. This will not be the case for WEST antennas, as the straps will be actively cooled. The straps thus need to be thicker to incorporate water pipes. A thicker strap will decrease R_c. The reason is simple and is exactly the same as the difference between infinitely thin strap and finite thickness strap. Part of the current radiates from the front face of the strap and part from the part of the strap. With a thicker strap, the distance from the back of the strap is larger, thus the tunnelling length is larger for part of the current. Consequently R_c is smaller. Additional small gains can be expected by optimizing the strap width, the strap position in the box. Moreover more parameters are available in 3D. The Faraday screen will be included at least with not tilted bars to evaluate the impact of the Faraday screen on coupling and on the strap electric length for antenna adaptation. The next step will be then to calculate the coupling properties on WEST typical plasmas scenarios.

4.3.3 In the long term

The present model either in 2D or in 3D only gives access to the coupling resistance. To simulate more detailed electrical properties, e.g. the full input impedance matrix necessary [67] to match the antenna, a more comprehensive 3D geometry including the antenna feeders is necessary. This extension is possible at the expense of a computational cost in resources and time and the addition of matching module as an equivalent electric circuit.

While including a density profile and handling the full dielectric tensor is more realistic than propagation on an equivalent isotropic lossy dielectric, it also renders the numerical resolution of the cold plasma dielectric tensor more difficult and its subsequent convergence slower, at least in 3D, due to the gyrotropy and inhomogeneity. More robust algorithm would be a nice feature.

Extending the density profile up to the antenna radial position would also allow to

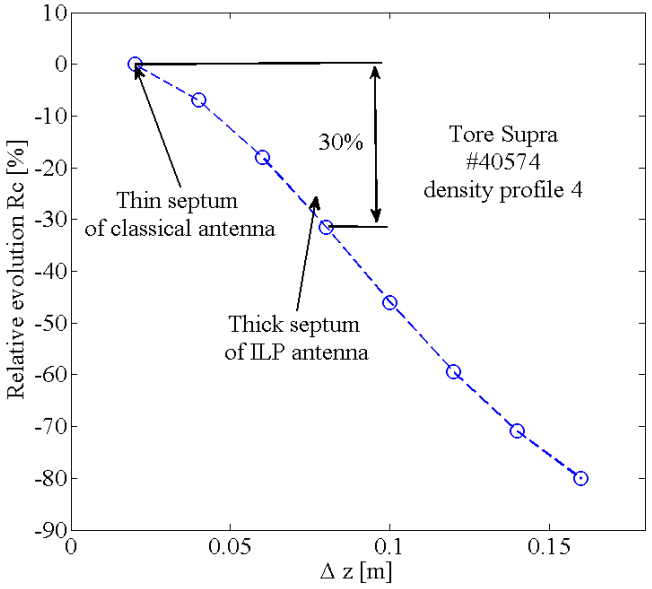

Figure 4.14: Parametric scan in 2D of the thickness of the protrusion of the vertical septum with a density profile for the pulse 40574. All other antenna parameters correspond to the ILP antenna.

include the slow wave physics in the model. A finer mesh would also be required to accurately resolve the slow wave typical scale. It also raise the problem of whether or not put a finite density on the strap itself.

Some improvements on the PML itself can be envisaged. The impossibility of coexisting backward and forward waves is a major issue. As for the surface admittance matrix formalism, the present PML formulation needs to be implemented at a flat interface. But in reality, the static magnetic field is curved imposing plasma curvature in both poloidal and toroidal directions. Checking the PML behaviour with curvature should be done. In such geometries, the PML formulation should be written in a different coordinates system than the Cartesian system. In my opinion, the medium-PML interface should be kept on iso-density lines to conserve the impedance continuity along the interface instead of having a flat interface crossed by several iso-density surfaces. Extending this formulation to curvilinear interface [154] is necessary to be able to couple this wave coupling model with an absorption model [175]. This could provide a solution to get around the issue with multi-pass absorption. A generalisation of the PML technique to convex domain of arbitrary shape and not only rectangular is presented in Ref [176] with prismoidale coordinates.

The implemented PML is versatile and its application to Fusion plasmas is not limited to the FW coupling simulations discussed here. Numerous prospects can be imagined. Future prospects include implementing the PML technique for Lower Hybrid waves coupling [70]. In this case the PML would have to be adapted for the slow wave, which is a backward mode. The most challenging issue in that case is the presence of the lower hybrid resonance that will be in my opinion of concern for the lateral PMLs where the resonance is encountered at some point perpendicularly to the interface. If no trick can be found to circumvent this issue, then only classic ABCs manually adapted to account for the inhomogeneity can be of use.

This model relying on the PML technique can in principle handle a finite density in the antenna box. Another possible application is thus describing self-consistently RF sheaths that arise in the vicinity of ICRH antennas [49, 108, 140, 177] that give often the operational limits of the antenna. A comprehensive explanation of the underlying mechanism is yet forthcoming. This application requires a very detailed description of the antenna environment, so that simulating the full plasma is excluded. In particular both eigenmodes of the gyrotropic plasma are retained in the radiated near RF field. Our present RF sheaths model (SSWICH) [173, 174] only accounts for the slow wave, which is naturally evanescent above a critical density. Including the fast wave in the near field description requires implementing radiation conditions at the inner boundary of the simulation model to handle the propagative outgoing waves. Moreover having a full self-consistent description of the waves coupling with RF sheaths would present a great interest for the reliability of the predictions. For that to happen, the slow wave, that is the coupling code correctly meshed, would need to be meshed really finely, especially in the radial direction. Furthermore symmetry could not be assumed. Thus the entire antenna would have to be modelled. This would require much more memory that was is presently available. The behaviour of the PML technique in the presence of sheath-plasma waves [33] is also not clear yet.

Chapter 5

Development of an antenna-plasma code SSWICH-SW with a self-consistent description of RF sheaths effects

Until now, this thesis was focused on FW coupling to the plasma. RF sheaths can modify the local density in front of the antenna and thus influence the coupling properties on the antenna. In the past, RF sheaths have been treated mostly sequentially through a post-treatment of the output of the antenna codes relying of a simple rectification model. The goal was then to minimize the integrated parallel electric field along field lines. This approach was also used to design a new generation Faraday screen on Tore Supra [56] in order to minimize the magnitude RF sheaths. On Alcator C-Mod, symmetry considerations led to design a field aligned antenna [49] to reduce SOL interactions. It also naturally results into minimizing $\int E_{\|} dl$. In reality, the observations were not conformed to the predictions. On Alcator C-Mod, the impurity contamination and the impurity sources at the antenna decrease while the plasma potential remains unchanged. On Tore Supra, the impurity content was similar whereas the magnitude of the plasma potential was much higher. More advanced modelling of RF sheaths is thus needed. The relation between impurities production and the plasma potential also needs to be understood. The sheaths feedback impact of RF wave propagation has been until now neglected. The observations of DC currents in the SOL with active antennas were unexplained.

Experiments have thus highlighted some shortcomings of classical sheaths models. The feedback effect of the plasma of the wave propagation should be accounted for. The field line topology in the vicinity of the antenna should be better described in order to account for long field lines passing in front of the antenna and short field lines connected to the side limiters. A mechanism to generate significant DC currents is also necessary.

This chapter is devoted to the description of a novel model of RF sheaths. In the first part the equations of the model are presented with the boundary conditions needed to solve the model. In the second part the numerical implementation in Comsol and its coupling to the TOPICA antenna code is discussed. In the third part, some numerical tests of part of the model are performed to verify some of the assumptions made initially in the model development. The model is also compared in simple situations to analytic solutions. Finally in the fourth section, the status and prospects for this code are presented.

5.1 Physics in SSWICH-SW

Although no consensus presently exists over an alternative approach, RF-sheath physics needs improvement towards the first principles mechanisms driving the non-linear interactions between the RF waves and the edge plasma. Our proposed approach, SSWICH (**S**elf-**C**onsistent **S**heaths and **W**aves for **I**on **C**yclotron **H**eating) includes in its current form the minimum required physics package to model self-consistently RF wave propagation in the bounded SOL plasma and the resulting DC biasing of the SOL from both ends of open magnetic field lines.

The model involves DC quantities as well as harmonic RF waves oscillating at the ICRH fundamental wave frequency ω_0. No other frequency is included on the contrary to the model in ref.[99] that includes harmonic frequency of ω_0 . Our model also assumes that RF and DC quantities can be split as explained in Section 2.3.2.1. It assumes that the RF current exclusively goes through the capacitance and the DC current through the diode on the sheath equivalent circuit in Figure 2.7. The resistance part of the sheath is neglected.

A three-fluid approach is followed, inspired by earlier work on RF plasma discharges [100, 103] and recently applied to tokamaks [53, 118]. Three fields are solved for: the RF parallel field $E_\parallel$, oscillating sheath voltages V_{RF} (both varying as $exp(-i\omega t)$ at the RF pulsation ω_0) and the DC plasma potential V_{DC}. Furthermore some transport coefficients remain phenomenological. The RF and DC parts of the model are coupled by non-linear RF and DC sheath boundary conditions at both ends of open magnetic field lines. As fluid fields are treated here, the concept of flux tubes [93] is not as important as in previous modelling.

The following model is valid for high amplitude collisionless RF sheaths parallel to **B** in flat geometry, with immobile ions and inertia-less electrons. The following description is a priori valid in 2D and in 3D, but is shown in 2D for simplicity.

5.1.1 Tore Supra geometry in the vicinity of the ICRH antenna in SSWICH

The geometry actually considered in Tore Supra simulations is already rather complex, as illustrated by Figure 5.1(b). The geometry is shown here with Tore Supra geometry in mind, but could be applied to other devices with the condition that wall boundaries are either parallel or perpendicular to **B**.

The simulation domain in the parallel/radial 2D plane, sketched on Figure 5.7, is a set of bounded straight magnetic field lines aligned along z in the SOL of a magnetized plasma in the vicinity of an IC antenna located on the low field side of a flattened tokamak. The computational domain considered here is a cut at one vertical position in the parallel/radial 2D plane of the full 3D antenna geometry, illustrated by Figure 5.1(a). The geometry of the objects is simplified to satisfy the condition on the orientation of the static magnetic field **B**. They thus have a rectangular form instead of a domed form to enlarge the surface wetted by the plasma.

The domain contains protruding material objects able to intercept magnetic field lines, e.g. antenna side limiters, developing sheaths. Sheath boundary conditions, introduced in Section 2.3, are enforced on the lateral boundaries for both the RF part and the DC part of the problem, as illustrated on Figure 5.1(b) where the sheaths width are overly exaggerated to be visible. Even more complex geometries will be progressively implemented when the condition on the orientation of the magnetic field will have been overcome.

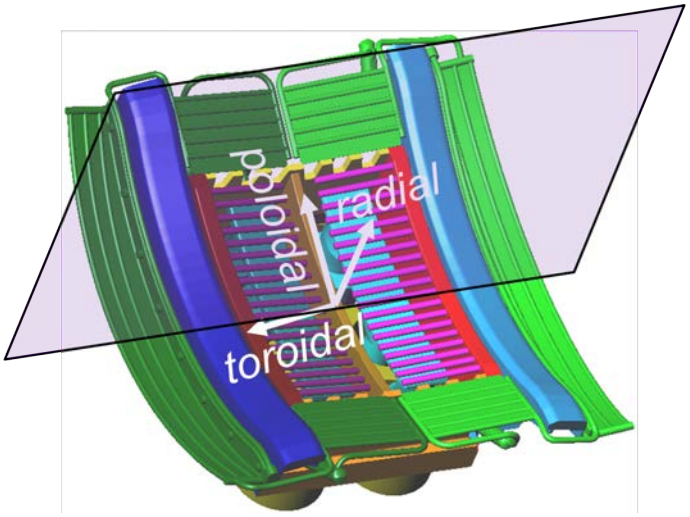

(a)

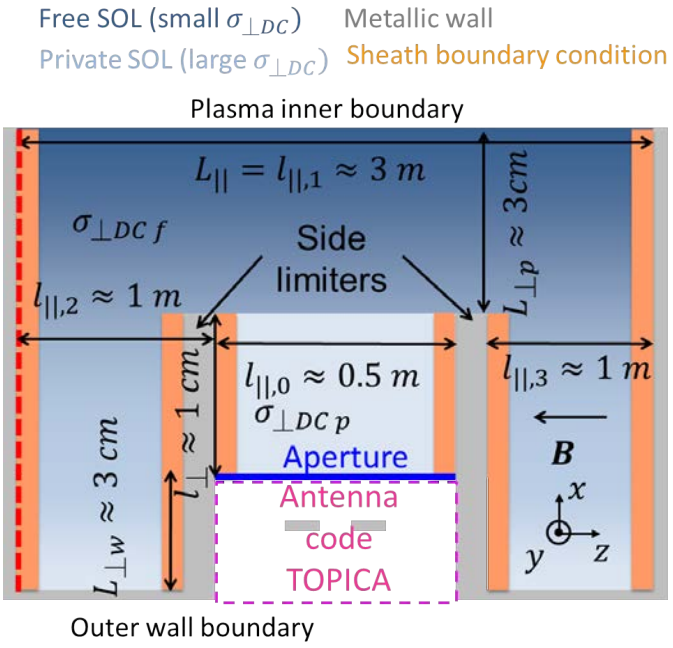

(b)

Figure 5.1: (a) 3D model of the Tore Supra antenna geometry. A parallel/radial plane is also represented to show SSWICH simulation domain. (b) 2D toroidal/radial plane domain with typical dimensions. The orange rectangles correspond to boundaries where sheaths boundary conditions are enforced. The SOL plasma is shown in level of blue with a lighter colour in the private SOL since the density is smaller. The red dashed line shows where the DC plasma potential shown for example on Figure 6.6(b) is evaluated.

Since the antenna is positioned inside the vacuum vessel, a finite density plasma can exist around the antenna. Recessed areas behind the leading edge of the limiter have to be included in the modelling, since in Tore Supra the antennas are not positioned on the vacuum vessel position.

The free SOL, where long connexion lengths exist, surrounds the antenna. A radial density profile is assumed there. The private region of the antenna, defined as the collection of field lines hitting the side limiter on both their toroidal sides, is distinguished from the rest of the SOL since the parallel connexion length is much smaller than in the free SOL. It thus has a steeper density gradient, following Stangeby's model [93]. The steeper density gradient is computed within the diffusive regime:

$$n_p(x) = n_{le} \exp\left(\frac{x_{le} - x}{\lambda_p}\right), \tag{5.1}$$

where n_p and n_{le} are respectively the density in the private SOL and at the leading edge of the side limiters, x_{le} is the radial position of the side limiter and λ_p is the characteristic length of the density gradient defined with:

$$\lambda_p = \lambda_f \sqrt{\left(\frac{l_{\parallel,0}}{l_{\parallel,1}}\right)}, \tag{5.2}$$

where λ_f is the characteristic length of the density gradient in the free SOL, $l_{\parallel,0}$ is the parallel connexion length in the private SOL and $l_{\parallel,1}$ is the parallel connexion length in the free SOL. The parallel connexion length are illustrated on Figure 5.1(b).

Due to limited computational resources (in CPU time, RAM memory and raw computing power), a multi-2D approach was applied, whereby several radial/parallel planes at different poloidal positions are solved independently. Neglecting poloidal derivative ∂_y is required. This is valid when the poloidal gradient lengths are much larger than the radial gradients lengths. The effect of the third dimension will be evaluated as a test of the multi-2D approach with a simplified version of SSWICH in Section 5.3. The third dimension is then recovered by assembling the 2D planes together. SSWICH cannot therefore compute in its present version the field at the antenna aperture that is about 0.5 m wide. It was during this thesis coupled to the TOPICA antenna code [31]. As the current SSWICH model only account for the SW in a 2D domain, it is called SSWICH-SW-2D. Let us see now the physics included in SSWICH for the self-consistent 3D modelling of RF sheaths.

5.1.2 RF wave propagation: slow wave

At the RF frequency ω_0, the SOL plasma is characterized by the cold dielectric tensor $\bar{\bar{\varepsilon}}(x, \omega_0)$ [58] given in (2.9). Let us recall that the cold plasma is gyrotropic and birefringent. Inhomogeneity can also occur in case of a density gradient in the profile. Two polarizations consequently exist in a cold plasma: the fast wave and the slow wave whose properties were summarized in Section 2.1.4.

Here we are not interested in the transverse electric field, useful for heating, but in the parallel electric field, deemed responsible of the spurious wave-plasma interactions in the vicinity of ICRH antennas. As the plasma is highly anisotropic in the parallel direction, $\varepsilon_\parallel$ is high in magnitude (highly negative) compared to other dielectric constants (i.e. $\varepsilon_\perp$ and ε_X) and squared refractive indexes ($n_\parallel^2$ and $n_\perp^2$). $E_\parallel(x, y, z, \omega_0)$ is therefore entirely due to the SW and is written in the model as an Helmholtz equation without any volume sources:

$$\varepsilon_{\parallel}\Delta_{\parallel}E_{\parallel} + \varepsilon_{\perp}\Delta_{\perp}E_{\parallel} + \varepsilon_{\parallel}\varepsilon_{\perp}\left(\omega_0/c\right)^2 E_{\parallel} = 0, \tag{5.3}$$

where Δ is the Laplace operator. Since the condition $\mathbf{B}$ perpendicular to the wall is imposed, the fast wave and the slow wave are completely decoupled. The fast wave impact can thus be neglected. However, in reality, arbitrary angles between the wall and the magnetic field $\mathbf{B}$ exist. Mode conversion of the fast wave for arbitrary angles can occur and generate a slow wave outside the private SOL [51, 92]. This aspect is here neglected. The sources terms of $E_{\parallel}$ are rejected in the boundary condition at the antenna aperture.

Boundary conditions are needed to solve the SW equation in the appropriate environment. The RF waves are emitted through an aperture in the metallic chamber wall at the radial boundary $x = 0$ of width $l_{\parallel} \approx 0.5$ m (thick blue line on Figure 5.1(b)). The RF electric field $E_{\parallel ap}(y, z)$ is prescribed at this boundary by imposing a 2D map of $E_{\parallel}$ typically produced by an antenna code in the absence of sheaths. This input map excites the whole RF+DC physical model.

At the ICRH frequencies, the parallel dielectric constants $\varepsilon_{\parallel}$ is always highly negative because of the SOL density. Therefore, plane SW are evanescent whatever the parallel wave-numbers $k_{\parallel}$ composing the excited spectrum above a critical density corresponding to $\varepsilon_{\perp} = 0$. Metallic boundary condition is thus enforced $E_{\parallel}(x = L_{\perp}, y, z) = 0$ on the main plasma side of the simulation since the SW is assumed to be completely extinguished as the density there (i.e. $\varepsilon_{\perp} < 0$) is higher than this critical density. Metallic BCs are also imposed at the outer vessel boundary outside the antenna aperture as well as all other boundaries parallel to $\mathbf{B}$. This latter condition is questionable, especially on protruding objects in the SOL, but is unfortunately imposed when working with $\mathbf{B}$ perpendicular to the wall. This condition imposes $E_{\parallel} = 0$ on both edges at the leading edge of the limiter. Thus no rectification is possible. This condition could be replaced in the RF part of the model by the full SBC [53]. The FW however could not be neglected however. The conditions to establish are more complicated due to oblique reflections, which can induce mode conversion (i.e. $\partial_x\partial_z$ spatial derivative are there to ensure this possibility). Moreover no similar conditions presently exist for the rectification in the DC part of the model.

Since the sheath (in orange on Figure 5.1(b)) is usually thinner than the typical extension of the simulation domain, its consequence on the RF field propagation is accounted for via a RF sheath boundary condition [53]. It replaces the usual metallic boundary condition for boundaries perpendicular to $\mathbf{B}$, instead of meshing finely the domain to resolve the sheaths typical scale. Sheath boundary conditions are one of the characteristic features of the SSWICH code that was developed during this thesis. Although they rigorously prevail at the sheath/plasma interface, the RF-SBCs are applied directly at the wall. Assuming that at ω_0 the RF current through the sheath is mainly a displacement current, the sheath is assimilated to a parallel plate capacitor of width δ, filled with a dielectric material of dielectric constant ε_{sh} introduced in Section 2.3.2.3. With $\mathbf{B}$ normal to the wall, the RF-SBC is given by (2.63):

$$\mathbf{E}_{\perp} = \pm\nabla_{\perp}\left(\delta\varepsilon_{\parallel}E_{\parallel}/\varepsilon_{sh}\right), \tag{5.4}$$

where the opposite signs for the opposite walls account for the reversal of the normal direction n: $+$ when $\mathbf{e_n}\cdot\mathbf{z} = +1$ and $-$ when $\mathbf{e_n}\cdot\mathbf{z} = -1$. The radial/poloidal distribution of δ, function of the radial and poloidal coordinates, needs to be determined self-consistently. The condition of the orientation of the magnetic field $\mathbf{B}$, while restrictive, allows us to avoid the fast wave, thus only keeping the slow wave. This condition is applied on boundaries perpendicular to $\mathbf{B}$.

Conservation of the RF electric displacement $\mathbf{D}$ in the SOL plasma is expressed as:

$$\nabla \cdot \bar{\bar{\varepsilon}}\mathbf{E} \approx \varepsilon_\perp \nabla_\perp \cdot \mathbf{E}_\perp - i\varepsilon_X \left(\nabla \times \mathbf{E}_\perp\right)_\parallel + \varepsilon_\parallel \partial_\parallel E_\parallel = 0. \tag{5.5}$$

Since the SW exhibits essentially a transverse magnetic polarization, the second term at the RHS of (5.5) can be neglected. $\mathbf{E}_\perp$ in (5.5) can be replaced by its expression given by (5.4).

$$\varepsilon_\perp \Delta_\perp \left(\delta \mathbf{D}_\mathbf{n}^\mathbf{pl}/\varepsilon_{sh}\right) = \pm\varepsilon_\parallel \partial_\parallel E_\parallel \left(x, y, z = z_{\text{lateral boundary}}\right), \tag{5.6}$$

where the sign + accounts for lateral boundaries with $\mathbf{e_n} \cdot \mathbf{e_z} = 1$ and the sign − accounts for lateral boundaries with $\mathbf{e_n} \cdot \mathbf{e_z} = -1$. $z_{\text{lateral boundary}}$ denotes the positions along the parallel direction corresponding to the lateral boundaries on Figure 5.1(b). The quantity $\delta \mathbf{D}_\mathbf{n}^\mathbf{pl}/\varepsilon_{sh}$ at the right hand side (RHS) of (5.6) physically defines an oscillating RF voltage V_{RF} across the sheaths that drives the rectification of the DC plasma potential. As $\mathbf{B}$ is perpendicular to the wall, it gives $\mathbf{D_n} = \mathbf{D} = \varepsilon_\parallel E_\parallel$. Assuming that the distributions on V_{RF} and δ are known along all relevant boundaries, Dirichlet boundary conditions for the $E_\parallel$ are applied on the lateral boundaries in the code using:

$$E_\parallel = \pm \frac{\varepsilon_{sh}}{\varepsilon_\parallel \delta} V_{RF}, \tag{5.7}$$

where the oscillating sheath voltage V_{RF} and the sheath width have to be determined self-consistently. The quantity $C^* = \varepsilon_{sh}/\delta$ actually defined the sheath capacitance per surface unit (2.54).

5.1.3 Oscillating sheath voltage

The oscillating sheath voltage V_{RF} makes the transition between RF wave propagation and DC biasing of the plasma. Inverting the side of the terms in (5.6) gives:

$$\varepsilon_\perp \Delta_\perp V_{RF} = \pm\varepsilon_\parallel \partial_\parallel E_\parallel \left(x, y, z = z_{\text{lateral boundary}}\right), \tag{5.8}$$

where $z_{\text{lateral boundary}}$ denotes the positions along the parallel direction corresponding to the lateral boundaries on Figure 5.1(b). The sign is chosen according to the rule for (5.6). This equation is valid whatever the dielectric tensor and in the presence of radial inhomogeneity in the density profile. It allows solving V_{RF} along the lateral boundaries without a priori knowledge of the self-consistent distribution of δ.

In (5.8), the oscillating sheath voltage is generated by the slow wave within a spatial differential equation. V_{RF} is null in the absence of sheaths. The RF voltage V_{RF} is thus treated as a unknown field independent of $E_\parallel$, the source term. The formulation makes it convenient to evaluate V_{RF} with some stability. Physically it is explained by invoking the sheath-plasma wave (SPW) [53] to excite V_{RF}. These properties can explain why the RF voltages penetration [173] in the plasma is deeper than the SW skin depth characteristic of its evanescence above its cutoff density (2.33). The penetration of RF voltage is not actually governed by the slow wave equation (5.3) but by the capacitive properties of the RF sheath, written in the SBC (5.7).

Boundary conditions are needed to complete the description and allow the resolution of (5.8) in the geometry illustrated by Figure 5.1(b). The condition $V_{RF} = 0$ is applied on the inner plasma boundary, on the outer wall as well as on any other boundary parallel to $\mathbf{B}$ such as the front face of the protruding limiters. On the lateral boundaries, a zero flux boundary condition is enforced. Even if (5.8) is solved everywhere in the domain from a numerical point of view, it only makes sense physically across a sheath that only exist along objects boundaries.

5.1.4 DC biasing of the SOL plasma

The third equation solves the electrostatic DC plasma potential $V_{DC}(x, y, z)$ by expressing the local balance of DC electric charge over the simulation volume with a partial differential equation without sources:

$$\sigma_{\parallel DC}\Delta_{\parallel}V_{DC} + \sigma_{\perp DC}\Delta_{\perp}V_{DC} = 0, \tag{5.9}$$

where $\sigma_{\parallel DC}$ is the Spitzer parallel DC conductivity and $\sigma_{\perp DC}$ a small phenomenological effective DC perpendicular conductivity, which has been discussed in Section 2.3.4. One other main novel feature in the RF sheath modelling within SSWICH is the inclusion of a finite DC conductivity tensor $\bar{\bar{\sigma}}_{DC}$ to account for exchange of DC currents between adjacent flux tubes in the SOL. Through this process, a given sheath gets coupled to its neighbours as well as with the sheath at the opposite wall along the same field line, providing a mechanism of DC current formation that will be discussed more deeply in Section 6.2.3. DC currents are thus allowed to flow both in the parallel direction and in the transverse direction. This "non-locality" was investigated in refs [43, 54] and is needed to reproduce the measured DC currents created by RF sheaths [46, 108] in the vicinity of active ICRH antennas.

In a collisionless plasma the linear DC transverse conductivity should be rigorously zero. However some transverse DC current transport was evidenced experimentally. Rigorously, the transverse DC plasma conductivity takes the form of a diffusion operator only in the case of ion-neutral collisions [112]. However, this mechanism alone cannot explain the far more intense effective transverse DC conductivity observed in the SOL of tokamak plasmas.

Two perpendicular DC conductivity are actually considered: one for the free SOL $\sigma_{\perp DCf}$ and one for the private region $\sigma_{\perp DCp}$ with $\sigma_{\perp DCf} < \sigma_{\perp DCp}$. This inequality actually considers that the turbulence level is higher in the private SOL than in the free SOL. This assumption comes a afterthought of the parallel connexion length in the SOL. In the free SOL, the parallel connexion length are rather long (several tens of m). Moreover they travel though the high field side (HFS) and the low field side (LFS) on the tokamak. We know that the curvature of magnetic field line is favourable for confinement on the HFS and unfavourable on the LFS. When averaging over the entire field line in the free SOL, the curvature is thus slightly unfavourable. Let us do the identical reasoning for the short field line in the private SOL of the antenna located at low field side in the unfavourable region. When averaging over the length of the short field line, the curvature is very unfavourable. It leads to think that the interchange turbulence level is higher in the private SOL compared to the free SOL. Such a view justify the choice of different DC conductivities in both regions of the SOL and gives more sense to a finite spatial extension in the SOL of the RF sheath effects. The effective DC conductivity that model phenomenologically the transverse transport of DC currents should thus be higher in the private SOL compared to the free SOL.

SBCs are also needed to completely define the DC part of the code and find a solution. The general DC SBCs state that the local DC current leaving the bulk plasma is the DC current into the sheath. Using (2.52) and for boundaries perpendicular to $\mathbf{B}$, the non-linear sheath I-V characteristic describing the conduction current gives:

$$\mathbf{j_{DC}} \cdot \mathbf{n} = i^{+}\left[1 - \exp\left(\frac{V_f + V_b - V_{DC}}{T_e}\right)\right], \tag{5.10}$$

with $\mathbf{n}$ the normal to the surface and the floating potential without RF V_f was defined by (2.40). This BC will make use of the oscillating sheath voltage computed previously by the

intermediate of the biasing voltage V_b given by (2.51) in Section 2.3.2. Let us recall that everything is happening as if sheath rectification was positively biasing the walls. On the inner plasma side, it is assumed that no perturbation is reaching the core plasma, so that $V_{DC} = V_f$ is enforced due to the zero current exchange between plasma and wall connected to the quasi-neutrality condition.

This expression is limited by a saturating condition when the sheath vanishes when the electron saturation current is reached. This saturation can be expressed starting from (2.40):

$$j_{max} = \left[\frac{k_B T_e}{e} \frac{1}{2\pi} \frac{m_i}{m_e} \frac{1}{1 + \frac{T_i}{T_e}} \right]^{1/2} . \tag{5.11}$$

(5.10) thus becomes:

$$\mathbf{j_{DC}} \cdot \mathbf{n} = i^+ \left[1 - \min \left(j_{max}, \exp \left(\frac{V_f + V_b - V_{DC}}{T_e} \right) \right) \right] . \tag{5.12}$$

The outer vessel boundary is assumed far away radially, so that no net perpendicular DC current is collected by the wall ($\mathbf{j_{DC}} \cdot \mathbf{n} = 0$, i.e. classical metallic BC). The model also assumes this condition for any boundary of the protruding object parallel to $\mathbf{B}$, as no working sheath model exits in that case. This is clearly something that should be improved.

Once a solution has been found for V_{DC}, the sheath width can be determined from a Child-Langmuir law given by (2.53).

The refinements proposed by Liebermann for the dynamics of a high voltage, capacitive RF sheath assuming stationary state, collisionless ion motion and inertialess electrons [103] were accounted for in SSWICH. It modifies the sheath width δ which is larger than a Child's law sheath for the same DC voltage and ion current density and the sheath dielectric constant ε_{sh} that is seen by the waves as a dielectric and not as vacuum anymore. The ratio of these two previous quantities is the effective sheath capacitance C^*_{sh} in (5.7). With δ finally determined, the self-consistent loop is closed as the sheath capacitance can be found and re-injected in the wave propagation problem. A robust starting point for the convergence process of the loop still however has to be determined.

5.1.5 Initialization: asymptotic model of SSWICH-SW

Despite the assumptions made and having only three coupled equations ((5.3), (5.8) and (5.9)), SSWICH is still fairly complex. To compute the SW fields $E_\parallel$ in presence of RF-SBCs, it is necessary to know a priori the 2D (radial/poloidal) spatial distribution $\delta(x, y)$ of the sheath widths along lateral boundaries of the simulation domain that is computed later on with the output of the third module on DC biasing via the Child-Langmuir law and the distribution of $V_{RF}(x, y)$ that is determined by the second module. Moreover to know the plasma potential patterns needed to evaluate $\delta(x, y)$ with the Child-Langmuir law, it is necessary to know the 2D map $E_\parallel(x, y)$ at the lateral boundaries.

In the first version of the self-consistent code, there were only two fluid-fields and two equations. V_{RF} was an explicit function of $E_\parallel$ and the plasma parameters:

$$V_{RF} = \frac{\varepsilon_\parallel}{\varepsilon_{sh}} \delta E_\parallel . \tag{5.13}$$

Moreover an ad-hoc constant and uniform value for the sheath width was provided as an initial condition for the self-consistent loop. The power was ramped up step by step to progressively excite sheaths starting from boundary conditions close to metallic ones when

$\delta \approx 0$. This attempt failed far away from the typical power typically operated by an ICRH antenna. The non-linearity of the equations prevent the algorithm from finding a solution in a limited number of iterations. Moreover the possibility of multiple roots was proposed in [92]. This cause a numerical problem as which root the model will take and how to jump from one root to another if case of bifurcation.

Therefore, a "first guess" into the self-consistent loop is valuable, as algorithms such as Newton-Raphson, are sensitive to the starting point for their convergence. A complete description of the asymptotic model with spectral resolution in 3D within a parallelepipedic geometry can be found in ref[173]. The same concepts are used here in the context of a more complex geometry.

For the purpose of RF sheath assessment in tokamak environment, an interesting regime is when the DC biasing gets very intense at high injected power. From Child-Langmuir law (2.53), the sheath width δ grows to very large values. In this, as we call it, "wide sheath regime" some physical quantities become nearly independent of δ [173]. The principle is then to write the field with a Taylor expansion into successive approximations:

$$E_{\parallel} = E_{\parallel}^{0} + \frac{\lambda_{crit}}{\delta} E_{\parallel}^{1} + o\left(E_{\parallel}^{2}\right), \text{ with } \frac{\lambda_{crit}}{\delta} << 1. \tag{5.14}$$

This asymptotic development helps to understand why the first attempt for the self-consistent loop failed. The formulation experiences convergence issues due to the mixing of different order in the quantities [173].

At the aperture, the same boundary condition is applied as in the RF wave propagation: a field map of the parallel electric field at the aperture $E_{\parallel,ap}$. The boundary conditions are kept the same on the plasma side and the outer wall, as well as on any other boundary parallel to $\mathbf{B}$: $E_{\parallel} = 0$. On the lateral boundaries simplified SBC in the wide sheath regime are written, instead of writing metallic condition ($\partial_{\parallel} E_{\parallel} = 0$). Postulating that the sheath width δ is large and that V_{RF} cannot increase indefinitely yield for (5.7) $E_{\parallel,as} = 0$.

This asymptotic method [173] is valid whatever the 2D input RF field map, in presence of a radial profile for the plasma parameters, and with no assumption a priori about the self-consistent 2D sheath widths distribution $\delta(x, y)$. It does not exhibit convergence issue or root selection issue as its expression is explicit. The SW module can thus be solved explicitly without prior knowledge of the DC plasma potentials before entering the self-consistent loop. Within the asymptotic regime, only one of possible roots remains. As a result, the starting point of the self-consistent loop is explicitly placed on one branch of solutions.The counterpart of the asymptotic regime is a restricted validity domain as $\lambda_{crit}/\delta << 1$ must be satisfied.

A simple criterion has been proposed and tested in rectangular geometry in Ref [173] to identify the validity domain.

$$\frac{\lambda_{crit}}{\delta} = \left| \frac{\varepsilon_{sh}}{2\varepsilon_{\perp}} \frac{l_y k_0}{\pi} \frac{l_{\perp}}{\delta} \coth\left(\frac{k_0 \left|\varepsilon_{\perp}\right|^{1/2} l_{\parallel,0}}{2} \right) \right| << 1, \tag{5.15}$$

where l_y is the poloidal dimension, λ_{crit} is the critical sheath size for the asymptotic treatment validity, k_0 is the wavenumber in vacuum, ε_{sh} is the sheath dielectric constant defined in Section 2.3.2.3 and $\varepsilon_{\perp}$ is the perpendicular component is the Stix tensor (2.9). This asymptotic solution, serving as the starting point for the coupled model, is the last missing piece in the present physical model. The model can now be implemented numerically.

5.2 Numerical implementation in Comsol Multiphysics

5.2.1 Architecture of the code in Comsol

The SSWICH model is implemented numerically in the commercial software COMSOL multiphysics [164] to take advantage of the Finite Element Method [77] for complex geometries. A commercial software Comsol was chosen before the start of this thesis for its user-friendly graphical interface, the possibility to couple several physics and to define medium with full tensor properties on the contrary to other softwares (HFSS, MWS), the ready to use natively equations or boundary conditions. Implementing the SBCs in TOPICA has been tried, but for vacuum sheaths as an arbitrary medium cannot be defined before the antenna aperture. HFSS licences are available at the IRFM institute, but this software is too specialized towards electromagnetic applications. Moreover implementing the SBCs in HFSS would have been next to impossible. Comsol and MWS remain in the list for the possible choice. However, Comsol can offer other possible applications than in electromagnetism, which is not the case of MWS. Nevertheless the Comsol Multiphysics licence is not available at CEA on high performances computer (HPC) due to the financial cost of the cluster licence for several nodes. Since the numerical resources are thus limited, only 2D applications are presently possible. Adapting the code to HPC would furthermore require time for efficient computing.

Furthermore my group do not dispose of a numerical support team whose main purpose is the development and programming of the code. Consequently, it would have been impossible to write a functioning "home-made"code during the three years of this thesis from scratch using the python, C or Fortran languages while providing at the end physical relevant results for complex geometries. As an example, the development of the TOPICA code, considered as the reference for ICRH applications started in the beginning of the years 2000 and is still an ongoing process. Furthermore my education was about physics in general and especially in plasma physics and not on numerical programming and analysis. Comsol, on the other hand, offered an efficient mean to investigate the physics without heavy code development.

The SSWICH code in its present version is combining together three equations and three-fluid fields fully coupled by RF sheaths properties. The schematic representation of the SSWICH code is shown in Figure 5.2. Each equation is modelled within its own module by including a new physics module in Comsol. There are thus four modules: one for each equation and one for the asymptotic solution of the RF wave propagation. Each module is implemented in 2D. They are called RF wave propagation, asymptotic RF wave propagation, oscillating sheath voltage and DC biasing. The variables in each module are respectively $E_\parallel$, $E_{\parallel,as}$, V_{RF}, V_{DC}. The boundary conditions are then added in each module. The modules are coupled together by RF sheath properties, explained in Section 2.3.2: the generation of oscillating sheath voltage by RF waves, RF sheath rectification and sheath capacitance.

The RF wave propagation module and its asymptotic version are modelled by a natively implemented scalar Helmholtz equation for $E_\parallel$. The dielectric tensor $\bar{\bar{\varepsilon}}$ is reduced to 2D keeping the radial and toroidal directions. It gives a anisotropic diagonal tensor. The DC biasing module is modelled with the natively available Poisson equation with no volumic sources of DC current. The DC conductivity tensor is also reduced to 2D with the same directions. Finally the oscillating sheath voltage is also modelled with a Poisson equation with a source term in $\varepsilon_\parallel/\varepsilon_\perp \partial_\parallel E_\parallel$.

It is worth mentioning that the convention in Comsol is the so-called engineer convention ($\exp(+i\omega_0 t)$), different from the one used in this thesis ($\exp(-i\omega_0 t)$). The sign of

complex number is thus changed as complex number should be replaced by their conjugate complex number. For example the dielectric tensor $\bar{\bar{\varepsilon}}$ in Comsol is the conjugate tensor of the Stix tensor in (2.9). The default frame in Comsol maybe not be the one used here. It will thus change the positioning of the elements in the tensors.

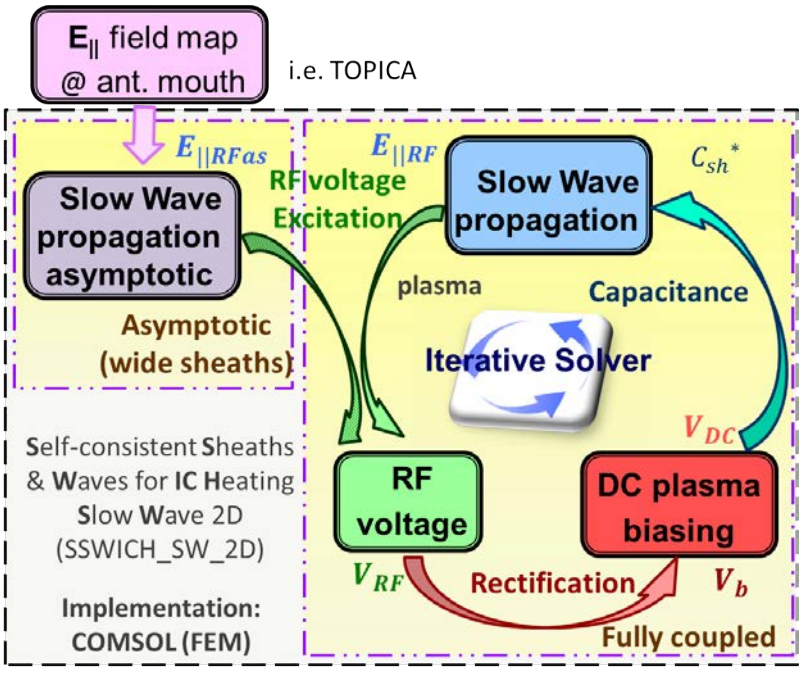

Figure 5.2: Schematic representation of the algorithm used in the SSWICH code. The three fluids are solved in their own module and are coupled together through RF sheath properties. An asymptotic version of the SW module is initiating the iterative loop to ensure convergence.

The oscillating sheath voltage module solving V_{RF} distribution implemented in 2D as the other ones could be reduced to 1D as an oscillating voltage make sense only across a sheath. Presently V_{RF} is solved everywhere. But V_{RF} only has a meaning on the lateral boundaries where sheaths exist. V_{RF}, instead of being solved with one 2D module, could thus be solved in 1D in as many modules as there are boundaries with SBCs. It would also reduce the computational resources required since 2D modelling on the entire domain is far more consuming than several 1D modelling for every lateral boundary.

5.2.2 Antenna description through an interface with the TOPICA antenna code

It has been seen that the system is excited by imposing a 2D (toroidal/poloidal) map of $E_{||}$ at an "antenna aperture", shown with a blue line in Figure 5.1(b), in the RF wave propagation module. This input map of SSWICH is one output of the antenna code TOPICA [31] computed in the absence of sheaths in vacuum with a realistic 3D geometry of the antenna. This input has to be seen as a total electric field, which mixes inward waves and backward waves. The antenna radiates on the plasma, treated as a boundary conditions, through an aperture. 3D informations are thus present in SSWICH via the input field map of the antenna. Examples of 3D antenna geometries implemented in TOPICA are shown for an antenna equipped with the classical screen and with the CBSB screen

in respectively Figure 5.3(a) and Figure 5.3(b). The different Faraday screen designs were introduced in Section 2.4.5. Nevertheless it is possible to use instead waveguide modes or input coming from other codes, as the interface is realized through a file containing the grid points of a map of the RF parallel electric field.

The near field amplitudes are scaled by the RF voltages V_{strap} imposed on the straps feeders. The same trick as in Section 4.1.3 is used in TOPICA to simulate an adapted Tore Supra antenna with TOPICA. The RF voltage is imposed on the ports connected to the capacitors lines (top and bottom) whereas the central coaxial line replacing the power loss in the resonant circuit has a null voltage.

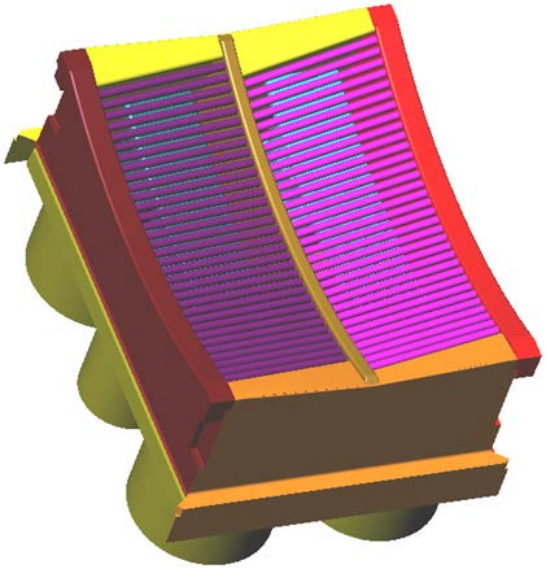

(a)

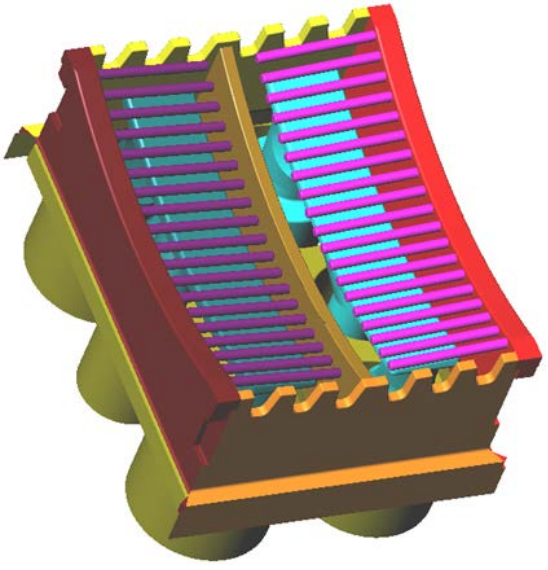

(b)

Figure 5.3: 3D model of the antenna geometry implemented in TOPICA equipped with (a) classical Faraday screen and (b) the CBSB FS.

In order to comply with the magnetic field **B** perpendicular to the wall in the SBCs, the input RF field map (see Figure 5.4(a)) was expressed in a tilted coordinate system where y and z are respectively poloidal and parallel directions. The antenna thus appears tilted as a parallelogram (see Figure 5.4(b)).

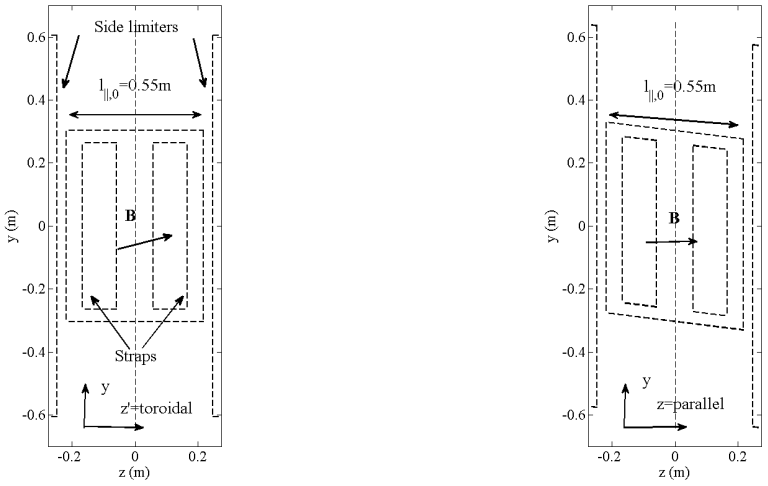

(a) (b)

Figure 5.4: (a) Toroidal/poloidal map of the antenna before tilting. (b) Parallel/poloidal map of the antenna after tilting. This tilted map is the input of SSWICH. In tilted coordinates, the antenna appears like a parallelogram.

Initially the setup on TOPICA (see Figure 5.5) included the antenna structure with the surrounding side limiters and a large domain around it. The situation was similar to the setup in Ref [48] with the addition of the limiters. The embedding of the antenna in TOPICA in between poloidal limiters change the way image currents can develop on metallic surfaces. It does not however change the density decay [93] as no density is present in the antenna. TOPICA cannot provide a solution on a plane that does intersect an object. Consequently the solution cannot be given on the Faraday screen plane but slightly in front of it. The last plasma magnetic surface (TOPICA aperture) follows the poloidal curvature of both limiters at a distance of 5 mm, and the estimated plasma ripple along the toroidal direction with curvature radius $\approx$ 1.75 m. A similar surface, called EF (electric field) surface, located 2.5 mm in front of the limiters (in vacuum) allows to compute all the components of the electric field with a better spatial resolution (8 mm for EF surface vs 34 mm on aperture). The simulation was then launched within a large domain. But in practise the results obtained from this setup had a poor resolution with small scale structures due to the mesh as the volume was larger than without the limiters. Moreover SBCs are not included in TOPICA and the antenna is placed in vacuum whereas in SSWICH a plasma surrounds the antenna and SBCs are applied as its main aim is to model RF sheaths. Intense spurious interactions on the antenna limiters attributed to RF sheaths have been observed. Therefore it makes more sense to include the antenna limiter in SSWICH than in TOPICA even with a simplified geometry. The antenna limiter in SSWICH also defines several regions in the SOL with different properties: the free and the private SOLs.

To correct this, the side limiters structures were removed from the 3D geometry in

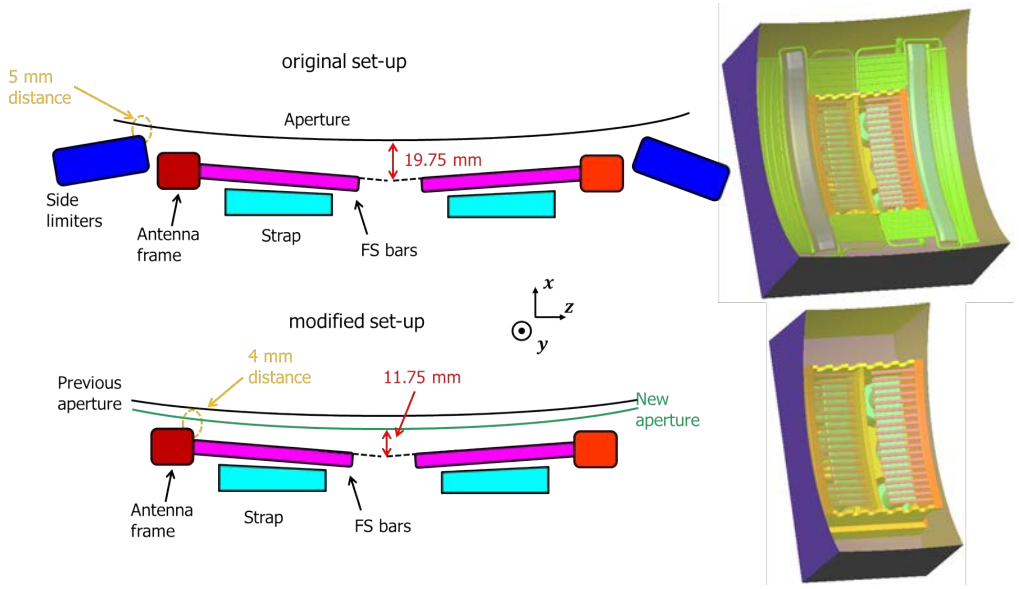

Figure 5.5: Sketch of the original setup with the side limiter surrounding the antenna frame and of the modified setup where the side limiter were removed in order to place the aperture closer and increase the resolution. The modified setup is similar to the setup used by Mendes in ref [48] (no side limiters or surrounding structures), but with a much smaller aperture and cavity to emulate the presence of limiters. The directions in the tokamak are indicated.

TOPICA. The simulation domain boundaries were placed at the location of the side limiters to emulate their presence. TOPICA aperture keeps following the poloidal curvature of both limiters (even though they are removed from the simulated domain). The absence of the side limiters and a smaller curvature radius ($\approx$ 1.65 m), again to follow toroidally the estimated plasma ripple, allowed to reduce the distance with the FS of about 8 mm. Since the domain is smaller, a better resolution is adopted for both surfaces (7.5 mm for EF surface vs 16 mm on aperture). The drawback is that we do not benefit from the detailed geometry of the limiters. Furthermore image currents developing around the antenna structure (limiter face in the free SOL and the vacuum chamber) are not taken in account. But the effect of the limiter on RF sheaths is retained as a simple rectangular limiter geometry is included in SSWICH. Figure 5.6(a) is the output of TOPICA for the antenna equipped with CBSB FS and for a 1 V input on the strap.

To take into account the distance between antenna aperture in TOPICA and the real radial position of the FS and the evanescence of the SW, the field map is extrapolated to what it should be at the FS with:

$$E_{\|FS} = E_{\|ap} \exp\left(\int_{x_{FS}}^{x_{ap}} \frac{dx}{\lambda_{skinSW}\left(n_i\left(x\right)\right)}\right), \tag{5.16}$$

where $E_{\|ap}$ is the field map at the TOPICA aperture, x_{FS} and x_{ap} are respectively the radial position of the FS and the TOPICA aperture and $\lambda_{skinSW} = c/w_{pe}$ is the skin depth for the SW with ω_{pe} the local electron plasma frequency and c the speed of light. The extrapolation coefficient is actually an average value of the evanescence of the SW over the radial density profile. The skin depth of the SW is obtained in the electrostatic limit by neglecting the ion dynamic and $k_{\|} = 0$ in the SW dispersion relation. (5.16) corrects the attenuation of the SW homogeneously for all modes contained in the field

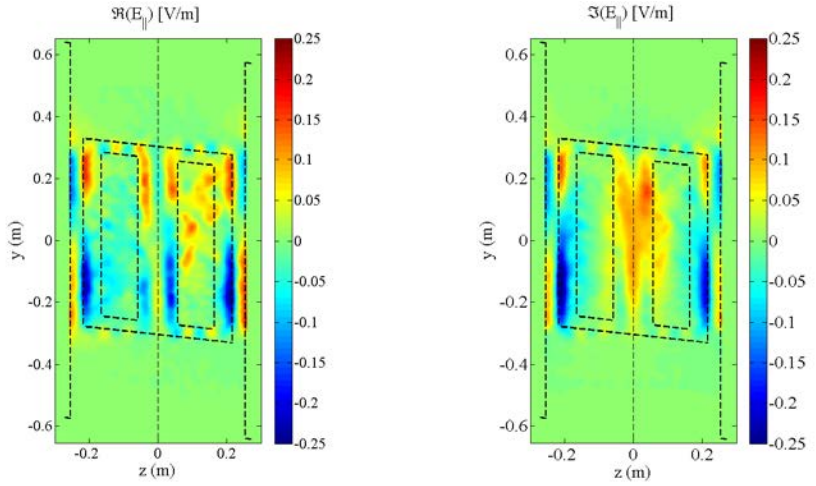

(a)

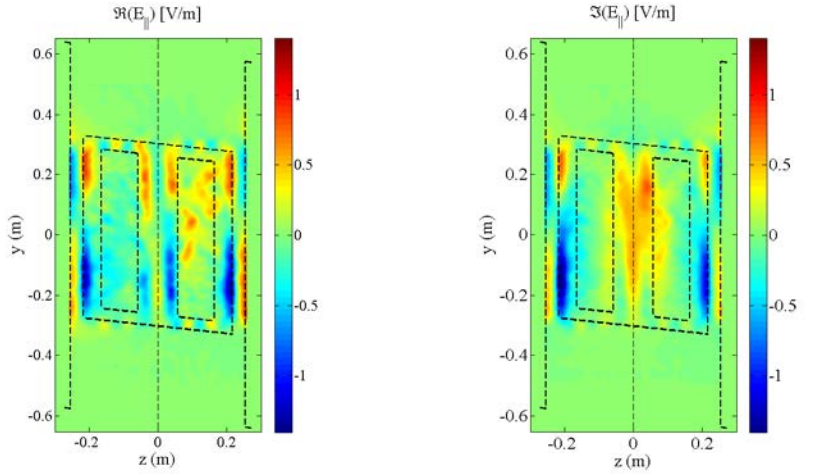

(b)

Figure 5.6: Real (left) and imaginary (right) parts of $E_{\|}$ field map for the antenna equipped with the CBSB FS (see Figure 2.14(b)) for $V_{strap} = 1$ V. (a) provided by Topica (b) after extrapolation on the Faraday screen plane with (5.16).

map with a constant positive factor, while rigorously the attenuation factor should be evaluated for all modes individually by decomposing the $E_{\|}$ field map in Fourier space. However while the deconvolution in Fourier space does not cause any particular issue, the reverse transformation gives that the high k values, ascribed to numerical noise due to finite discretization, are greatly enhanced. Moreover, when a 3D version of SSWICH will be available, this extrapolation procedure will not be necessary any more as the 3D antenna geometry will be directly imported in SSWICH and the solution will be possibly obtained on the Faraday screen plane. An illustration of (5.16) is shown on Figure 5.6(b). The evanescence factor for the SW in this case is about 5.

5.2.3 Mesh & Solver

The computational domain is meshed by default with triangular elements. A scaling factor between the directions is possible to account for the anisotropy in the plasma. It allows

reducing the number of elements and thus reduces the memory consumption and Central Processing Unit (CPU) time necessary for one simulation. Nevertheless the acceptable scaling is far below what one would expect by looking at the typical scale ratio in the plasma. The scale length are much larger in the toroidal direction than in the radial direction due to the presence of the static magnetic field for both the dielectric tensor $\bar{\bar{\varepsilon}}$ and the DC conductivity tensor $\bar{\bar{\sigma}}_{DC}$. For high scaling values of the discretization mesh, numerical instabilities near the SBCs at the lateral boundaries of a few mesh nodes have been experienced. For this reason the scaling between the radial and toroidal direction is never pushed beyond 30. Asymptotic preserving scheme [178] have being developed to overcome this well-known problem, but do not seem to be implemented with Comsol. Local mesh refinement is still possible, but the refinement has to be in both directions to keep the scaling ratio from increasing to high values.

The SSWICH-SW-2D model is solved iteratively within a self-consistent loop (see Figure 5.2) using the MUMPS [179] package (**MU**ltifrontal **M**assively **P**arallel sparse direct solver) and a segregated approach in four steps to facilitate convergence of the iterations. The first iteration solves the model within the asymptotic regime to provide a first guess of the final solution. The first three steps solve respectively the asymptotic SW wave propagation $E_{\parallel,as}$, the asymptotic sheath voltage $V_{RF,as}$ and the asymptotic DC plasma potential $V_{DC,as}$ sequentially. They provide an initial solution for the coupled non-linear model that start with the second loop. This constitutes the fourth step. As the DC biasing module is by itself non-linear, it is also iteratively solved where the convergence is stopped after a maximum number of iterations fixed at 80 if it did not converge sooner with the tolerance of the convergence fixed at 10^{-3}. For the iterative self-consistent loop, the same condition is applied with a simple convergence loop. A Newton-Raphson scheme is used.

Once convergence has been achieved, several quantities over the entire simulation domain are available that can be later used for physical interpretation of experimental observations: $E_{\parallel,as}$, $V_{RF,as}$, $V_{DC,as}$, $E_{\parallel}$, V_{RF}, V_{DC} and others derived quantities such as $j_{\parallel,DC}$, $j_{\perp,DC}$, $\partial_{\perp} V_{DC}$, $\partial^2_{\perp} V_{DC}$ and δ.

Some numerical instability was sometimes observed on a few nodes on the lateral boundaries. More robust and/or faster convergence scheme could be later tried. A numerical method such as minimum polynomial extrapolation (MPE) provide more robust and faster convergence scheme. It is not likely that such methods are implemented in Comsol. Other solver packages are available in Comsol: Pardisio and Spooles. Furthermore numerous options exist for the choice and parametrization of the solver that were left at their default value automatically determined by Comsol until now. It would nevertheless have to be verified than the numerical implementation of the model is still compatible with the convergence scheme. Adaptative meshing during the iterative resolution has not been tried yet, due to a lack of time.

It has been mentioned in Section 5.1.1 that the poloidal direction is recovered by scanning successive vertical positions during the multi-2D procedure. It is usually done with a 1 cm step far smaller than the poloidal scale length. In order to avoid a tedious manual scan, an automation was developed using the optional livelink [166] Matlab/Comsol. Matlab [180] and Comsol [166] are used in a client/server relationship with Matlab managing the simulation through a Matlab script. When the Matlab script is launched, it loads all the simulation parameters from a dedicated file before launching Comsol through this livelink. Then the order is given to the Comsol server load the Comsol file containing SSWICH. The simulations parameters are then entered in SSWICH. After achieving convergence, results (image, value, 1D grids, 2D grids,...) that have been defined previously are automatically exported in a directory with the simulation number. This livelink can

also be used to handle a job of several simulations consecutively.

5.2.4 Typical memory and CPU time requirements

Simulations were performed on a dedicated computer equipped with two Intel Xeon E560 processors and up to 24 Go of RAM memory. The domain is meshed by triangular finite elements. The 2D simulations were performed with a maximum element size of $h_{max} = 0.01$ m and a scaling in the mesh $(20-30, 1)_{(x,z)}$. The private SOL is about $0.01\ \text{m} \times 0.5\ \text{m}$ in the radial and parallel directions respectively. The free SOL is a few times larger than the private SOL: typically $3-5$ m. This is still however far from a realistic situation. The radial width of the free SOL is ≈ 0.1 m.

With $L_{\parallel} = 3.3$ m, $L_{\perp,w} = 5$ cm, $L_{\perp,p} = 3$ cm, $l_{\perp} = 0.8$ cm, $h_{max} = 0.01$ m and a scaling $(30, 1)_{(x,z)}$, it gives for the simulation domain a $0.30\ \text{m}^2$ surface with $\approx 230,000$ triangle elements. Six physics modules are included in the model (RF wave propagation, sheath RF voltage, DC biasing and their asymptotic version). In total it gives about 2.7 million degrees of freedom for the simulation with 2 degree of freedom per element and per module. It consumes during the resolution about 12 Go of RAM memory. Approximately 1 min is necessary for one iteration in the self-consistent loop. Depending on the number of iterations, whose maximum number is arbitrary fixed at 80, that are needed to reach the convergence factor, fixed at 0.01, it usually takes between ≈ 10 min and ≈ 80 min for a simulation. Scanning the entire antenna vertical dimension (i.e. $L_y = 1.3$ m) by step of 1 cm thus takes between 10 h to 25 h.

The main limitation to simulate finer geometry is the RAM memory. The main gain in RAM memory consumption would be obtained by replacing the 2D resolution of V_{RF} over the entire domain by 1D resolution along according boundaries where V_{RF} exist. That would reduce the numerical cost by almost a third. Another smaller gain could be achieve by automatically adapting the scaling with asymptotic preserving scheme [178]. CPU time consumption could, in my opinion, be optimized by choosing the best parameters for the solver and by using better conditioned matrices for the computation. Nevertheless even with optimizing the resources consumption in 2D, more resources than what is available today would be required for 3D computations. The most important feature would be to keep or increase the radial resolution for the RF sheaths. Looking in Chapter 4 at the factor between 2D and 3D simulations gives a factor about $5-6$ in the RAM consumption. Furthermore the scaling was not respected and the slow wave was not correctly resolved. The multi-2D procedure scans only one vertical position. The typical vertical size of the antenna with the limiters is ≈ 1.3 m and the typical size of the poloidal structure in Figure 5.6(b) are ≈ 1 cm. The 3D mesh in the vertical direction should have ≈ 1 cm elements for a accurate spatial resolution. That gives a factor 50-100 between 2D and 3D simulations. The CPU time necessary for one simulation would accordingly increase. Thus much fewer simulations could be performed even with more processors.

5.3 Numerical tests of SSWICH-SW-2D

Before using the SSWICH model to simulate physical relevant situations, some numerical tests are needed to validate some essential assumptions and the implementation of the ingredients in SSWICH. The aim here is not to show extensively all the tests, but to show in this section the most relevant numerical tests, in my opinion, that we have performed until now to check the implementation in SSWICH and some assumptions done in Chapter 5. Tests on the RF sheath boundary conditions, the multi-2D assumption and the validity of

the asymptotic model at high power are shown.

5.3.1 Standalone tests of the slow wave propagation module with RF sheath boundary conditions and fixed sheath width

The first tests to be performed have been on the RF wave propagation module in standalone. The aim was to verify that the implementation of sheath boundary conditions in Comsol was actually working. A simple situation, with the geometry illustrated by Figure 5.7, where simulations results can be compared to an analytical solution was identified. It consists in a rectangular waveguide filled with plasma and with a modified boundary condition: sheath boundary condition (SBC) instead of metallic boundary condition (PEC).

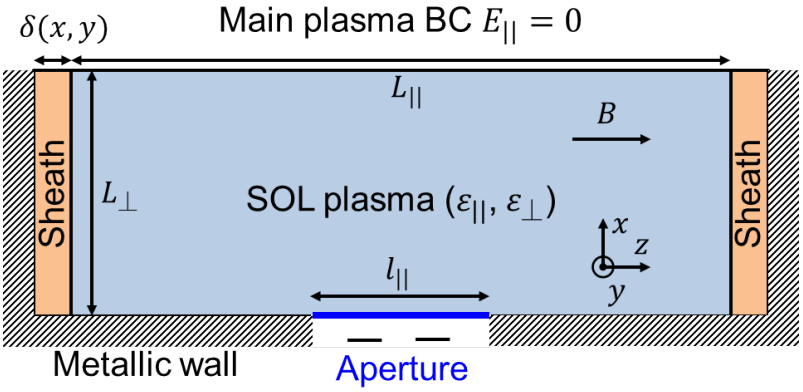

Figure 5.7: Sketch of the geometry in a 2D radial/toroidal plane of a rectangular box filled with an homogeneous plasma. Sheath boundary conditions are enforced on lateral boundaries.

It also includes a few simplifying assumptions:

- The SOL plasma is assumed homogeneous.
- Both dielectric constants $\varepsilon_{||}$ and $\varepsilon_\perp$ are assumed negative. This condition ensures the evanescence of the slow wave whatever the value of $k_{||}$ and k_y. Moreover this is actually the case in the SOL of a tokamak above a critical density $n_{c,SW}$. However below it ($\varepsilon_{||} < 0$ and $\varepsilon_\perp > 0$), it can happen that the SW becomes propagative above a critical value of $k_{||}$. The plasma is also likely to develop resonance cones [169].
- The SOL/main plasma boundary is placed far away from the evanescent region. It is then considered to be an infinity and a vanishing boundary condition for the parallel electric field $E_{||} = 0$ can be enforced. In case of propagative slow wave, it should be replaced by a radiating boundary condition at infinity.
- The self-consistency RF+DC is dismissed by assuming the sheath width δ to be constant, fixed by the user and the same at both extremities of open flux tubes.

Assuming a 2D rectangular waveguide filled with a homogeneous SOL plasma and fixed constant sheath width δ at both extremities, the problem can be solved analytically by the method of separation of variables. In order to simulate waveguide eigenmodes for this test,

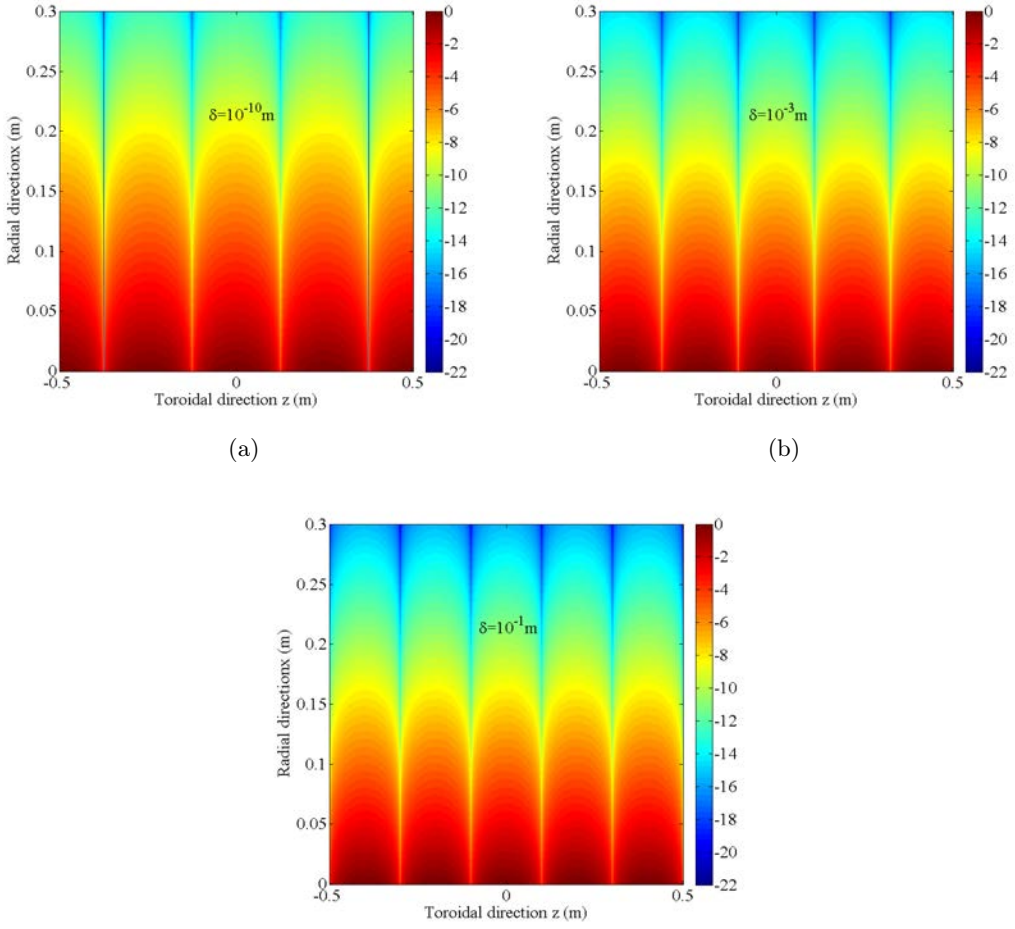

(a) (b)

(c)

Figure 5.8: 2D toroidal/radial map of $\log\left|E_{\|}\right|$ for (a) $\delta = 10^{-10}$ m, (b) $\delta = 10^{-3}$ m and (c) $\delta = 10^{-1}$ m. $f_0 = 57$ MHz, $N = 3$, $\varepsilon_{\|} = -100$, $\varepsilon_{\perp} = -10$, $h_{max} = 0.003$ m, $L_{\|} = 1$ m and $L_{\perp} = 0.3$ m.

the size of the aperture must correspond to the size of the domain: $l_{\|} = L_{\|}$. Depending on the excited mode parity, the parallel electric field of the eigenmode $E_{\|}$ reads:

$$\begin{array}{rcll} E_{\|}\left(x,y,z,\omega_0\right) & = & E\left(k_{\|},k_y\right)\cos\left(k_{\|}z\right)\exp\left(ik_y y - i\omega_0 t\right)\exp\left(-k_x x\right) & \text{for even modes,} \\ E_{\|}\left(x,y,z,\omega_0\right) & = & E\left(k_{\|},k_y\right)\sin\left(k_{\|}z\right)\exp\left(ik_y y - i\omega_0 t\right)\exp\left(-k_x x\right) & \text{for odd modes,} \end{array} \tag{5.17}$$

where both wavenumbers $k_{\|}$ and k_y are assumed to be independent of the radial direction x. As an analogy, even modes have the same toroidal properties as monopole strap phasing, whereas the same is true for odd modes with dipole strap phasing. The eigenmode parity is written with respect to $z = 0$, placed at the middle of the simulation domain. The slow wave dispersion relation given by (2.22) and the simplified sheath boundary condition given by (5.7) impose the existence of only a discrete number of possible waveguide eigenmode in the bounded simulation domain [53, 181]. The compatibility condition for $k_{\|}$ reads:

$$\begin{array}{rcll} \Lambda_0\left(\nu^2+\Lambda_1^2\right) & = & \nu\tan\left(\nu\right) & \text{for even modes,} \\ \Lambda_0\left(\nu^2+\Lambda_1^2\right)\tan\left(\nu\right) & = & -\nu & \text{for odd modes,} \end{array} \tag{5.18}$$

with

$$\nu = \frac{k_\parallel L_\parallel}{2}, \qquad \Lambda_0 = \frac{2\delta}{L_\parallel}\frac{|\varepsilon_\parallel|}{\varepsilon_{sh}}, \qquad \Lambda_1^2 = \frac{k_0^2 L_\parallel^2 |\varepsilon_\perp|}{4}, \tag{5.19}$$

where $eta = \left[N \in \mathbb{N}, \left[N\pi, \left(N+\frac{1}{2}\right)\pi\right] + 1 \text{ solution } \in \mathbb{C}\right]$. This compatibility equation is independent of k_y. The solution for the N^{th} mode is always in the domain $\left[N\pi, \left(N+\frac{1}{2}\right)\pi\right]$. But it also has a novel unique solution in the complex domain that only exist with the SBC: the sheath-plasma wave [33].

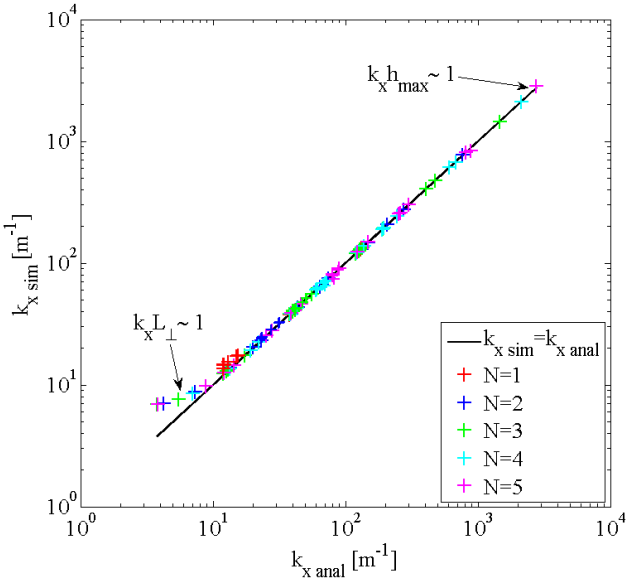

Figure 5.9: Test of the dispersion relation by comparing the analytical predictions $k_{x,anal}$ with the simulation values $k_{x,sim}$ for the first five mode numbers. Different plasma parameters $\varepsilon_\parallel, \varepsilon_\perp$ and different sheath width δ have been tried: $\varepsilon_\parallel, \varepsilon_\perp = -10^5, -10^4, -10^3, -10^2, -10$ and $\delta = 10^5$ m $\rightarrow 10^1$ m by step of 10^1 m. The maximum element size in the mesh is $h_{max} = 0.003$ m.

During the tests, the impact of the plasma parameters $\varepsilon_\parallel$ and $\varepsilon_\perp$, the sheath width δ and the maximum element size in the mesh h_{max} with the same mesh in both directions while only one wave frequency is taken $f_0 = 57$ MHz. Taking an even mode and varying the sheath width δ while retaining a waveguide eigenmode leads to observe a modification of the structure of the eigenmode in the waveguide, as illustrated by Figures 5.8(a)-(c) for $N = 3$. As δ increases, Λ_0 increases and $k_\parallel$ goes from $N\pi$ to $(N + 1/2)\,\pi$. It means that the mode goes progressively from an antinode at the lateral boundary for thin sheaths ($\delta \rightarrow 0$) to a node for wide sheaths ($\delta \rightarrow \infty$). Looking closely at the figures, it is also observed that as δ increases, the evanescence of the mode also increases. This is confirmed by the slow wave dispersion relation when injecting in it the associated compatible value for $k_\parallel$.

After this, the simulation results for k_x have been systematically compared to their prediction given by the slow wave dispersion relation (2.22). The plasma parameters and the sheath width were varied in a wide range. Figure 5.9 shows that in most cases an excellent agreement has been found between simulations and analytical predictions. There are however two exceptions in the low and high limits. For the high k_x limit, some disagreement appears when the mesh cannot resolve any more accurately the evanescence

length ($k_x h_{max} \sim 1$). A finer mesh is needed. In the low k_x cases, the evanescence length of the mode is so large ($k_x L_\perp \sim 1$) that when reaching the inner boundary condition of the domain, the vanishing boundary condition cannot be satisfied. In that case two solutions are available: take a larger domain in the radial direction or enforcing a radiating BC instead of a vanishing BC.

In some cases, it was seen that a low amplitude parasitic mode was excited once the slow wave amplitude was close to vanishing. One example is shown in Figure 5.10 with $\varepsilon_\parallel = -10^5$, $\varepsilon_\perp = -10^2$, $\varepsilon_{sh} = 1$, $\delta = 10^5$ m, $N = 3$, $L_\parallel = 1$ meter and $L_\perp = 0.3$ meter. In the region denoted as 1 in Figure 5.10, the slow wave excited an even mode at $x = 0$ is evanescent and follows the prediction given by dispersion relation (2.22). In region 2, a low amplitude parasitic mode appears with the remaining low amplitude of the evanescent slow wave. In region 3, the slow wave has completely vanished and only remains the parasitic mode. This amplitude of this mode and the subsequent error between the simulations and the analytical solution decreases as the mesh resolution increases.

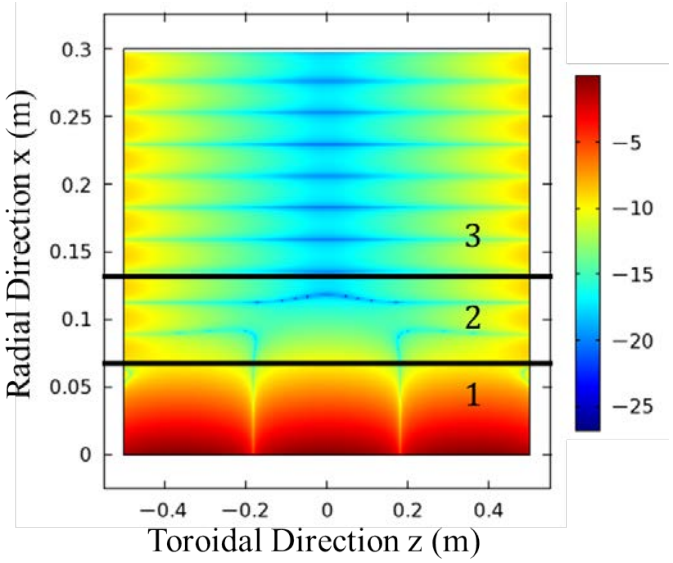

Figure 5.10: 2D toroidal/radial map of $\log\left|E_\parallel\right|$ with $\varepsilon_\parallel = -10^5$, $\varepsilon_\perp = -10^2$, $\varepsilon_{sh} = 1$, $\delta = 10^5$ m, $N = 3$, $L_\parallel = 1$ m and $L_\perp = 0.3$ m. Three specific regions are drawn to identify the presence of a low amplitude parasitic mode with the evanescent slow wave.

A second observation can be made. This mode is evanescent in the toroidal direction and propagates along the radial direction on boundaries. It disappears when the SBC reduces to PEC ($\delta = 0$ m). Moreover this parasitic mode is not modified when the wavenumber $k_\parallel$ changes. The numerical solution is therefore unique. A mode with these properties has been shown to exist with SBC: the sheath-plasma wave (SPW) [53]. An analysis of the evanescence length in the toroidal direction and of the periodicity of the propagation in the radial direction has shown that this mode has the same properties as expected from the SPW with these parameters. The amplitude of this mode is moreover changing with the mesh resolution. The finer the mesh was, the lowest the amplitude was. We thus conclude that this parasitic mode is a Sheath-Plasma Waves (SPW) excited here by numerical errors.

Since the SPW propagate along material surfaces in presence of SBC, an idea to solve potential issues between SPW and PML that was exposed as a source of concern in Section 4.3.3, is to place the plasma-PML interface far away radially in the plasma where no

material object exists. If that case, the SPW will become evanescent once the SBC ceases to exist since no wall can give a support for the propagation of the SPW.

The results shown here for the SW wave propagation module with sheath boundary condition were performed with even modes. Similar properties would nevertheless have been obtained with odd modes.

5.3.2 Comparison of multi-2D approach with 3D for Tore Supra with the asymptotic model in standalone

This test aims to verify one of the assumptions made in the establishment of SSWICH-SW-2D. To make the numerical cost acceptable in-line with our available resources, poloidal derivatives have been assumed to be negligible. We are proposing here to test this assumption with a more simplified version of SSWICH-SW that only entails the asymptotic treatment with spectral resolution of an homogeneous plasma within a parallelepipedic geometry in 3D [173]. This version of SSWICH, implemented in Matlab, provides a solution within a minute.

Since the main advantage of this version of SSWICH is its ability to handle a parallelepipedic 3D geometry, we can evaluate the impact of a finite k_y spectrum of the $E_\parallel$ field map such as Figure 5.6(a). Since only a parallelepipedic geometry is possible, the simulation domain is only the private SOL. A cut in a 2D radial/toroidal plane is shown on Figure 5.7. Extrapolating the SW evanescence for each modes individually is not an issue in this particular case since no inverse Fourier transform on the $E_\parallel$ field map is necessary. Infinite parallel DC conductivity is assumed in this model whereas no transverse DC conductivity is allowed. Since the parallel Spitzer conductivity is infinite, V_{DC} is homogeneous along field lines (i.e. flute assumption). Thus the two sides of the antenna do not need to be distinguished. The DC plasma potential $V_{DC,as}$ on one particular flux tubes exclusively depends on the biasing voltages at both extremities on this flux tube denoted by the duplet (x, y). V_{DC} is thus evaluated with the following analytic expression:

$$V_{DC,as} = \frac{1}{2}\left(V_{b,l} + V_{b,r}\right) + \ln\left[\cosh\left(\frac{1}{2}\left(V_{b,l} - V_{b,r}\right)\right)\right], \tag{5.20}$$

where $V_{b,l}$ and $V_{b,r}$ are respectively the biasing voltage on the left and the right sides of the antenna calculated with (2.51).

The simulations parameters of this test are: $n_i = 510^{17}$ m^{-3}, $T_i = 20$ eV, $T_e = 20$ eV, $L_y = 1.4$ m, $L_\parallel = 0.55$ m, $L_\perp = 1$ cm and $V_{strap} = 30$ kV. Figure 5.11(a) is a 2D map in the radial/poloidal plane of the asymptotic plasma DC potential $V_{DC,as}$ with the $E_\parallel$ field map in Figure 5.6(a). The two humps poloidal topology is characteristic of Tore Supra ICRH antennas. Further detailed discussion will occur in Chapter 6. It can also be seen that the gradient of $V_{DC,as}$ associated with each direction will have different scale-lengths. The typical gradient scale length in the poloidal direction (≈ 10 cm)is much larger than in the radial direction (≈ 1 cm). This provides a first argument for neglecting the poloidal gradient in the equations with respect to the radial gradient. Two tests cases have been then performed. One has a finite k_y spectrum defined by the $E_\parallel$ field map and in the other case $k_y = 0$ is enforced. The relative error for $V_{DC,as}$ has been evaluated and is shown on Figure 5.11(b). An error of at most 10% is expected by neglecting the poloidal derivatives for the case of a Tore Supra antenna. The maximum error is obtained in regions where the field map goes from zero to small finite value of $E_\parallel$. Moreover this is the maximum error. Over most of the 2D map, the error level is much lower at around 1%. Simulations with other parameters give similar results.

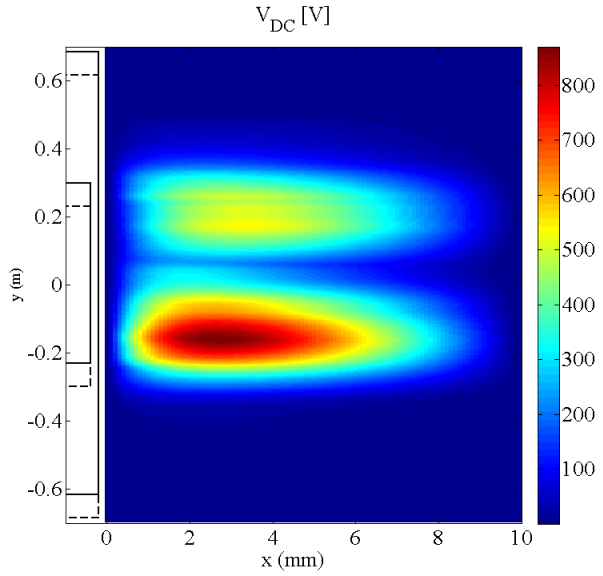

(a)

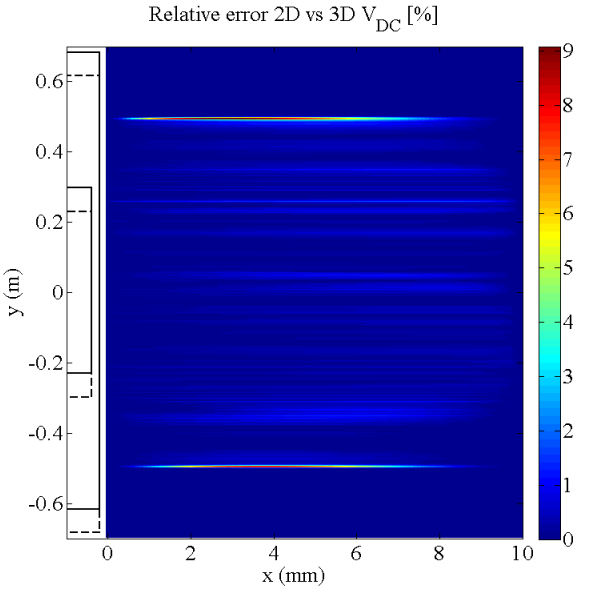

(b)

Figure 5.11: (a) 2D map in the radial/poloidal plane of the asymptotic plasma DC potential $V_{DC,as}$. (b) Comparison of the multi-2D approach with the 3D approach with the asymptotic model in Matlab using the geometry shown in Figure 5.7. The black dashed lines represent the position of the left side of the antenna (antenna box and side limiter). The same is done for the right side with black full lines. The simulations parameters are: $n_i = 510^{17}$ m^{-3}, $T_i = 20$ eV, $T_e = 20$ eV, $L_y = 1.4$ m, $L_{\parallel} = 0.55$ m, $L_{\perp} = 1$ cm and $V_{strap} = 30$ kV.

We conclude that, for the case of Tore Supra antennas in first approximation, the poloidal derivatives can indeed be neglected. The fully coupled model SSWICH-SW in 2D can thus be used with a multi-2D approach to simulate the entire 3D antenna.

5.3.3 Comparison of the fully coupled model with the asymptotic model during a power scan

The last test to be presented in this thesis consisted in comparing the solution provided at the end by the asymptotic model and the coupled model during a power scan. The amount of power is directly linked to the strap voltage. The asymptotic model was established in the wide sheaths regime at high power. Thus the discrepancy between the asymptotic model and the coupled power should get reduced as the strap voltage increases. The simulations were performed for only one vertical position. It was chosen at $y = 0.2$ m near the bottom corner of the antenna box, as illustrated by Figure 5.12.

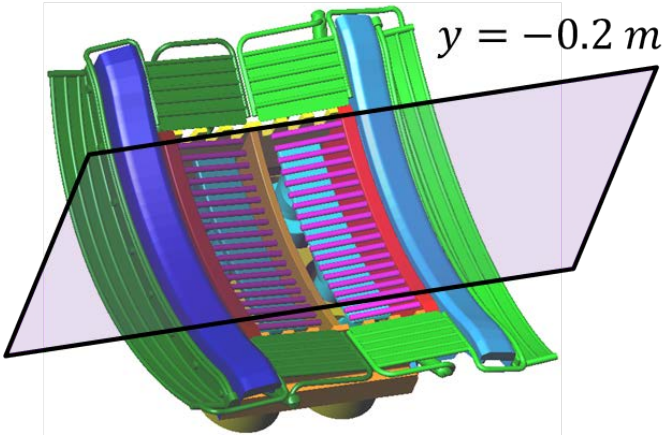

Figure 5.12: 3D model of the Tore Supra antenna geometry. A parallel/radial plane at $y = -0.2$ m, where the tests of the fully coupled version of SSWICH will be tested, is represented to show approximatively the vertical position where the maximum of V_{DC} are expected as shown on Figure 5.11(a).

This test is presented here for the classical Faraday screen, illustrated by Figure 5.3(a). The strap voltage was progressively increased step by step. For each step, the value of the DC plasma potential at the leading edge of the side limiter $V_{DC,le}$ was evaluated from the asymptotic solution and the solution of the coupled model. The results are plotted on Figure 5.13(a). The amplitude of $V_{DC,le}$ increases when V_{strap} increases. A fit gives a dependence as $V_{strap}^{2/3}$.

Looking at Figure 5.13(b), the relative error between both solutions is decreasing as V_{strap} is increasing. From a 45% error at low strap voltage, the relative error decreases to less than 10% for $V_{strap} = 50$ kV. Moreover the qualitative trend is still decreasing at this point.

At high V_{strap} numerical crashes in the loop of the coupled model was sometimes seen when a result of the type $\infty/0$ was encountered on a few nodes for one iteration always on lateral boundaries when SBCs are applied. This was ascribed to issue with the mesh since the crash do not always occur on the same nodes and that changing slightly the mesh distribution correct this issue. Being able to use finer mesh with lower scaling between directions would hopefully solve this problem.

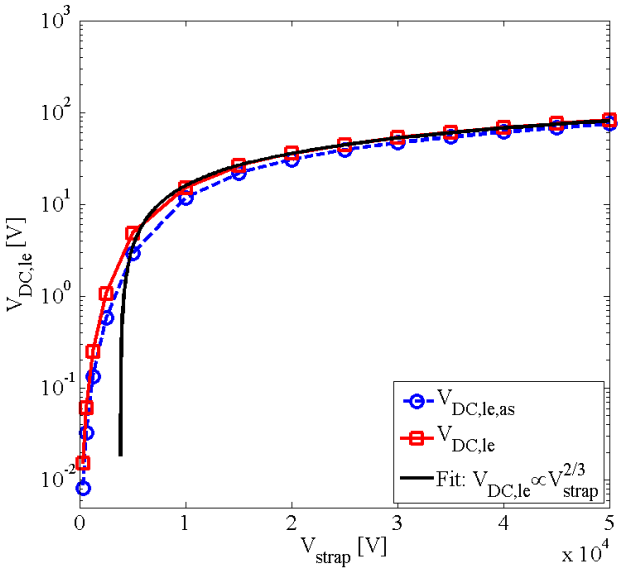

(a)

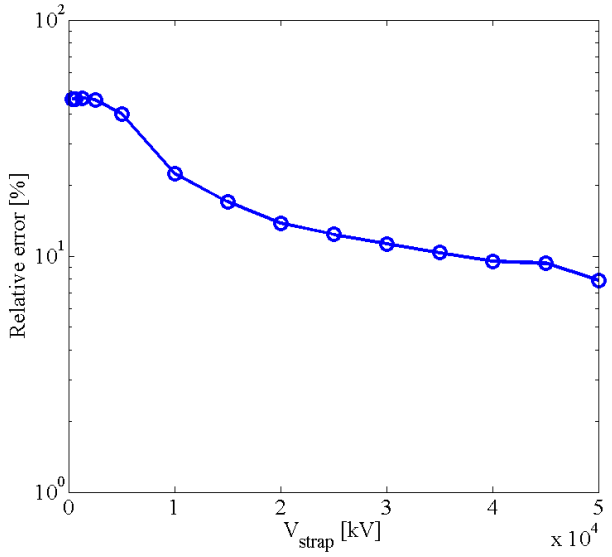

(b)

Figure 5.13: (a) Comparison of DC plasma potential at the leading edge with coupled model $V_{DC,le}$ (red straight curve with squares) and asymptotic model $V_{DC,le,as}$ (blue dashed curve with circles) versus the strap voltage. (b) Relative error versus strap voltage. Each dot represents one simulation. The other simulation parameters are: $T_e = 10$ eV, $T_i = 20$ eV, $L_\parallel = 3.3$ m, $n_{le} = 1.7$ m^{-3}, $\sigma_{\perp DC,p} = 7.110^{-8}\sigma_{\parallel,S}$ and $\sigma_{\perp DC,p} = 2.610^{-6}\sigma_{\parallel,S}$.

This test confirms that the asymptotic expansion is correct and that its validity is get better as high power which is the most interesting case for antenna since it is when the more important heat fluxes are evaluated on the antenna.

5.4 Status and prospects for SSWICH

The SSSWICH code was developed during this thesis to describe self-consistently RF sheaths. It models the interplay between the slow wave propagation and the resulting positive DC biasing of the edge of a magnetized plasma. It was seen early during the thesis than using a three field-fluid description (wave parallel electric field $E_\parallel$, oscillating sheath voltage V_{RF} and DC plasma potential V_{DC}) is better for the convergence than using only two. The code main features are sheath boundary conditions, the finite DC conductivity tensor, the full description of cold plasma, a more realistic geometry thanks to the finite element method, the ability to simulate antenna through field maps computed with TOPICA and a multi-2D procedure to recover the third direction. The model was implemented in Comsol Multiphysics. The resulting code is called SSWICH-SW-2D. To automate numerous simulations, an interaction with Matlab has been created.

Numerical tests have shown that the SBCs modify the structure of the SW. The multi-2D procedure is indeed correct as in the case of Tore Supra the poloidal derivatives can be neglected. Comparison of SSWICH-SW-2D with an analytic model of the DC biasing led us to suspect a non-linear broadening of the V_{DC} structure with the amplitude of V_{DC} due to the presence of a DC perpendicular conductivity. A comparison of the fully-coupled model with the asymptotic model during a power scan reveals that indeed the asymptotic model is true at high power.

Despite the numerical tests already performed on the individual modules and on SSWICH itself, there are still much more fundamental tests to be done on the self-consistent model concerning the uniqueness of the solution, the convergence of the iterative scheme to the solution. These fundamental nature of these open issues are first related to the multiplicity of the solution and the neighbourhood of the possible multiple solutions [92]. Second there are numerical limits to the Newton-Raphson iterative scheme due possibly to poor initial estimate, overshoot or stationary point that are identified as the major issues. For that these reasons a limit of the number of iterations was placed. Combining the method with a more robust one would bring a better mitigation capability of non-convergence or slow convergence. One other numerical issue is concerning the optimization of the mesh.

Several limitations exist in SSWICH due to some assumptions that were made to simplify the problem. These assumptions could be either removed or replaced by more realistic ones:

1. The walls are always assumed to be perpendicular or parallel to the magnetic field $\mathbf{B}$, thus restricting the possible geometries to the ones with lateral boundaries normal to $\mathbf{B}$. It is in the current model a essential assumption to neglect the fast wave and to simplify the expression of SBCs. With a shaped lateral wall or limiter, the angle is arbitrary. When the wall is arbitrarily oriented with respect to $\mathbf{B}$, it was however proved that the FW and the SW cannot be decoupled any more at the lateral boundaries of the simulation domain [171]. Both modes need to be treated simultaneously to describe the RF sheath excitation as mode conversion can occur. It means that the RHS in (5.3) would contain some source terms depending on the FW.

2. Additionally (5.3) need to be completed by a wave equation for the fast wave. A way

to damp the propagative FW would however be required at the end of the computational domain to avoid reflection on the boundaries of the domain. A technique such as the Perfectly Matched Layer [57, 150] for cold magnetized plasmas could be used. That technique has been shown to be of interest for FW coupling in a tokamak plasmas [182]. Combining the FW coupling code presented in Chapter 4 with the SSWICH code will give full self-consistent description of the waves coupling with RF sheaths. Additionally the Child-Langmuir law (2.53) would be changed to account for shaped lateral walls (e.g. Ref. [183] for cylindrical geometries). It would also be interesting to know the fraction of the power going to the slow wave lost on the antenna structure due to sheath dissipation. It requires to add an imaginary part to ε_{sh} [53]. Additionally a more refined analysis should be later done as flute assumption is considered. However the finite perpendicular DC conductivity considered in the model can possibly break the flute assumption.

3. While a radial gradient exists in the density profile, the density is assumed to be invariant in the poloidal and parallel direction (except in the private SOL). Observations however show that the density is affected by active ICRH antennae due to RF sheaths. The model thus need in a future version to include a density equation to self-consistently evaluate the DC potential pattern with the density [184]. An alternative would be to add a fourth module that would re-evaluate the density profile within the iterative loop. It will even become more critical when the FW is also included as the distance between the antenna straps and the FW cutoff density is the main parameter to determine FW coupling [182] and thus to adapt the strap voltage to couple a constant amount of power. Moreover modifying the density would also modify the sheaths boundary conditions as the density in the sheath is linked to the plasma density.

4. This issue also indicates that the code coupling TOPICA/SSWICH-SW is not self-consistent. TOPICA uses as input a radial density profile, assumed to be constant poloidally and toroidally, to compute the electric field map at the antenna aperture. This map is the input of SSWICH-SW to calculate the DC potential distribution that modifies the density by inducing poloidal gradients and toroidal gradients. A new solution should thus be computed with TOPICA using this new density profiles and so on until convergence is reached.

5. Another possible development is about a 3D version of SSWICH. Neglecting poloidal derivative would not be required anymore and a 3D antenna geometry could be directly implemented. It would however require a much greater amount of computational resources. It is finely entangled with the previous point, as modelling density convection cells has to be done in 3D.

6. Other formulae exist in the literature for the sheath capacitance [100] that could replace the current one. A sensitivity study to the formula of the sheath capacitance should be performed to identify the sensitivity of the results to the chosen model.

7. Several phenomena are moreover missing or assumed negligible here that could possibly be integrated in a full self-consistent description of RF sheaths. The radial transport of DC currents is here modelled with constant effective perpendicular DC conductivities whereas in reality there could be a spatial dependence. Moreover the transport coefficient should be described self-consistently with the rest of the model.

Secondary electron emissions, ion sputtering have also been neglected. An investigation of their impact of RF sheaths should be done to know if they enhanced or not RF sheaths. If they lower the magnitude of RF sheaths, SSWICH could be seen as predicting a worst case result.

Those are long terms prospects. SSWICH in its present version coupled with TOPICA has been used to reproduce some of the unexpected observations during the last experimental campaign on Tore Supra in 2011. Comparisons of numerical simulations with experimental observations is the purpose of Chapter 6.

Chapter 6

Comparison of SSWICH-SW-2D simulations with experimental observations on Tore Supra and predictions for ITER

Improved modelling included in the SSWICH code, presented in Chapter 5, was motivated to explain why the minimization of the integrated parallel electric field along "long field lines" predicted RF sheaths mitigation [48] for the new FS design while in practise the sheaths were significantly enhanced on the antenna structure and its side limiters.

This chapter is devoted to show that self-consistent modelling is already able to reproduce and explain some of the experimental observations along the side limiters of the antenna on Tore Supra. In order to do that, this chapter will start by recalling the major observations on the ICRH antenna during RF pulses in the 2011 campaign. Then a comparison between experimental observations and simulations results will be performed. It also proposes a possible explanation for the appearance of significant rectified potentials structures on the outer side of the antenna limiters. The design element deemed responsible for RF sheath induced enhancement of the plasma potential is presented. Finally some estimates for the parallel heat fluxes performed within a simplified geometry of the blanket shielding module of the ITER ICRH antenna are shown. Difficulties related to ITER modelling are also discussed.

6.1 Review of the experimental observations on Tore Supra during the 2011 campaign

During the latest experimental campaign on Tore Supra in 2011, several sessions were dedicated to the minimization of RF sheaths in Tore Supra [185]. Two types of FS, with different electrical designs, were compared on the same plasmas: the classical design and a proposed electrical design, shown in Section 2.4.5 supposed to mitigate RF sheaths according to the results in [48]. Multiple diagnostics on TS were available: infrared (IR) thermography [141], two-dimensional mappings by reciprocating Langmuir probes [39, 43], VUV spectroscopy [186], calorimetry of actively cooled plasma facing components [187]. The major experimental observations for RF sheaths on the ICRH antennas have been performed with infrared cameras and probes. This section is a review of the main experimental observations on the ICRH antenna that we are proposing to reproduce and interpret with

SSWICH. All these results were already published in [56, 140, 144]. The publications are indicated in the caption of each figure.

6.1.1 Comparison of two Faraday screens

All reported experiments on plasma were conducted in D(H) minority scheme with a magnetic field of 3.8 T. The antennas were configured in dipole phasing at a working frequency 57 MHz. The Last Closed Flux Surface (LCFS) was approximately circular with a minor radius $a = 0.72$ m. The plasma was leaning on a toroidal pumped limiter located at the bottom of the vacuum chamber. The leading edge of both classical and new antenna side limiters was located at $R = 3.138$ m. Macroscopic core plasma quantities (central plasma temperature, energy content, sawteeth, neutron flux and radiated power) behaved similarly for the same amount of additional power delivered by classical and new antenna in similar condition.

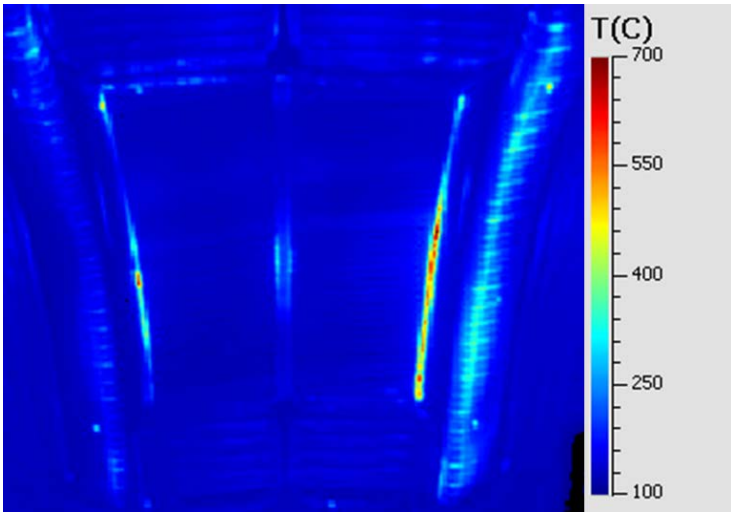

(a)

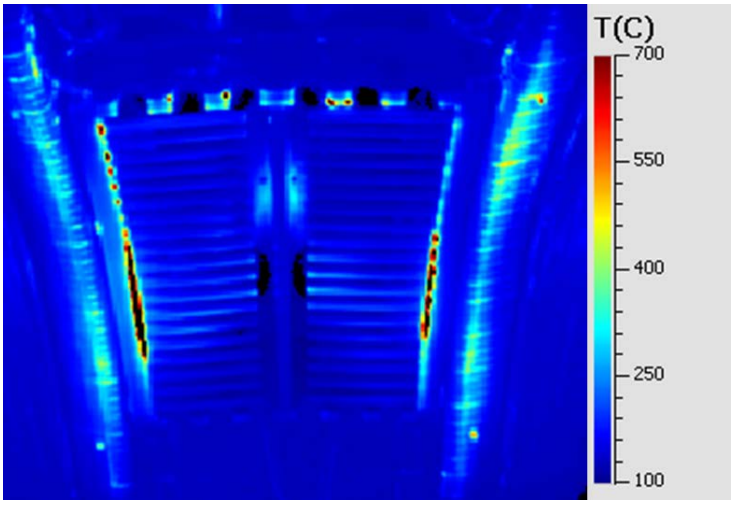

(b)

Figure 6.1: Infrared image during pulse #48268 for 3 MW of coupled power of (a) the classical ICRH antenna and (b) the ICRH antenna equipped with the CBSB Faraday screen with an unbalanced generator (57%/43%) to equalize strap RF voltages [140].

During Tore Supra plasma operation, the surface temperature T_{IR} [141] of PFCs are monitored via infrared thermography. There are much more and more intense hot spots during RF pulses on the antenna equipped with the CBSB FS (Figure 6.1(b))than on the antennas equipped with the classical FS (Figure 6.1(a)), despite the expected advantages of the CBSB FS. It resulted locally in very quick flaking [188] of the B_4C coating and numerous triggering of the IR real-time control safety system that decreases the injected power level [142]. Temperature elevations can be directly compared on the CFC side limiters. The side limiters were in fact twice hotter with the new antenna than with the classical ones. The antenna with the CBSB FS was moreover expected to be colder due the improvement in the heat exhaust capability. The impurity content was however similar with both antennae. Two mixed-up origins were evidenced for the hot spots: a strap voltage imbalance and enhanced RF sheaths.

6.1.2 Left/right symmetrisation of strap voltages and consequences on RF sheaths

The new antenna exhibited persistent left/right strap voltage imbalance [56, 140] when switched on alone. In similar conditions, the left strap (seen from plasma side) developed similar RF voltages as conventional antennae, while the values on the right strap were approximately 20% higher. The best explanation for this behaviour was provided at shut-down after the experiments. A 4 mm radial mechanical mismatch of the right strap position was observed on this antenna only as a wedge was forgotten during the assembly. It is compatible with the voltage asymmetry, as the measured voltages are higher on the strap set backwards. This misalignment of the two straps is probably responsible for the difficulties in balancing and stabilizing the strap voltage on the antenna.

In order to equalize the strap voltage of both straps, the RF power delivered to the left strap was increased from pulse to pulse, while that to the right strap was reduced by the same amount. The right/left ratio of measured strap voltages evolved from 1.15 for power sharing (left/right) = (50%/50%) to 0.9 for (63%/37%). This ratio is similar using the RF probes located at the top or at the bottom of the straps. Strap voltage balance was reached for the power distribution (left/right) = (57%/43%).

Figure 6.2 is a differential IR picture produced showing the evolution of the FS heat loads over the scan. The left side limiter heated up, while the right one cooled down, following the evolution of the voltage on the nearest strap. Heat load left/right asymmetry was reduced, but the hot spots were not fully suppressed. Moreover the floating potentials measured by the RCP on the right side limiter slightly increased [45], while the limiter was cooling down. The variations on the FS bars have a more complicated shape.

The independent behaviour of the two extremities of a short field line in the private region cannot be reproduced by any oscillating double probe model and cannot be accounted for with the variation of a single parameter. One average parameter cannot evolve differently at both extremities of a field line. It also questions the approach used to assess the FS electrical design in [48]. RF sheaths description requires a deeper understanding of the mechanisms at work to understand the failed attempt to minimize rectification on ICRH antenna. A more advanced RF sheath model should include a decoupling mechanism on both extremities in order to explain this observation and to be able to break the toroidal homogeneity. Since one parameter does not seem enough, let us try with at least two parameters: the perpendicular DC conductivity $\sigma_{\perp,DC}$ and the biasing voltage V_b.

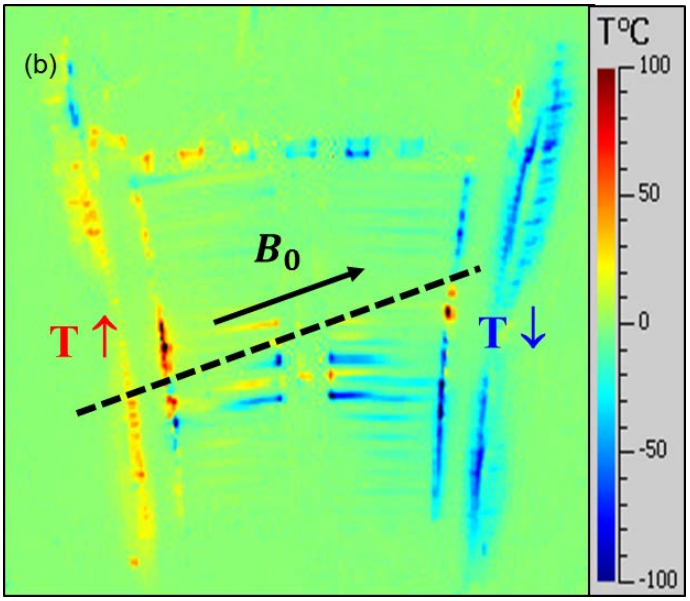

Figure 6.2: Differential IR image from two RF pulses, mapping the steady-state T_{IR} variations on new FS when (left/right) RF generator power balance was changed from (50%/50%) to (63%/37%). Superimposed: sketch of tilted open field line connecting the two side limiters [56].

6.1.3 Magnitude and topology of the enhanced RF sheaths on CBSB Faraday screen

Even with balanced strap voltages (i.e. with unbalanced generated powers 57%/43%), the antenna equipped with the CBSB FS was still hotter than the classical ones. Modelling of the thermal transients at RF switch-on and after RF, with the finite element code ANSYS V12, revealed that the FS bar heat exhaust was efficient so that faulty cooling could not explain high T_{IR} [140]. Heat fluxes of up to 750 kW/m^2 on the hottest bars (T_{IR} = 500 °C) were extracted from these calculations, versus less than 100 kW/m^2 for classical FS bars. Modelling in ANSYS gives an almost factor 2 for the parallel heat fluxes on the lateral limiters [189] between the new and the classical FSs (4.6 MW/m^2 and 2.6 MW/m^2 respectively for 2 MW of injected for each antenna). Heat fluxes calculations were the topic a post-doc by G. Ritz [189]. Flaking of the B_4C, on the lateral collectors and on upper shark teeth, are consistent with intense heat loads. This is further corroborated by calorimetry of the cooling water. Rough estimates show that the RF-induced specific energy losses over the FS and side limiters amount to about 5% of the energy delivered by the new antenna, versus about 3.5% for the classical one. Despite these high fluxes, efficient cooling allowed operating the new antenna up to 3 MW-6 s and 1 MW-19 s.

Beyond the maximum value of the surface temperature or associated heat flux, Figure 6.1(b) shows characteristic spatial distributions of the wave/plasma interactions during ICRH. On the same target plasmas, T_{IR} exhibited a two-hump poloidal variation for active antennae, with a local minimum near the equatorial plane and maxima near the top and bottom of the antenna box. Over the experimental campaign the right side limiter was systematically hotter than the left one. The T_{IR} poloidal pattern is quite different on the FS, where the hottest bars are located near the equatorial plane, a region of low strap voltage. A marked up-down T_{IR} asymmetry is visible on the shark teeth, consistent with B_4C damages only observed on the upper teeth consistent with earlier results on the

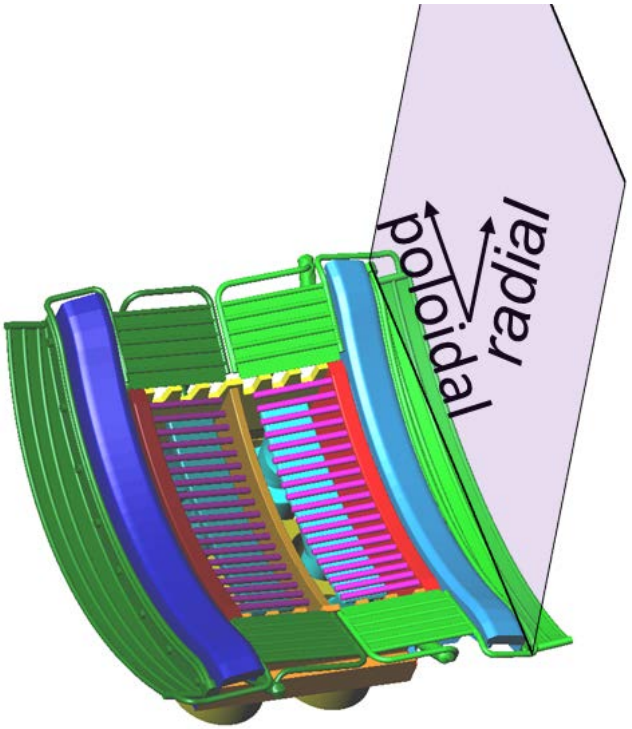

Figure 6.3: 3D model of the Tore Supra antenna geometry. A poloidal/radial plane along the outer side of the antenna side limiter indicates where the V_{float} 2D map with the probe and V_{DC} 2D map in the simulation is evaluated.

corners of conventional FS and the direction of the magnetic field [36].

Spatial heat loads measurements are complemented by reciprocating Langmuir probe (RCP) mapping [38]. The RCP is connected magnetically to the outer face of the right side limiter of the new antenna. In order to obtain a detailed 2D map, PhD topic of Martin Kubič [144], the probe is immersed into the SOL during the discharge several times. Between the plunges plasma current is decreased in little steps. As a consequence the magnetic connections of the probe to the antenna move up poloidally providing poloidal resolution. Radial resolution is achieved by the depth of the probe plunge.

The floating potential V_{float} of the probe is mapped in 2D in Figure 6.4 versus the connection point coordinates, over six 1 MW RF pulses with 7 reciprocations per shot. V_{float} reached a maximum of 170 V, while earlier measurements with a classical antenna did not exceed 100 V in similar conditions [39]. The most intense zones are located around the top and the bottom corners of the antenna box, similar to the heat loads localization on the side limiters. V_{float} was also observed to change with the density [45]. The structure however presents an up-down asymmetry. Such a mapping corresponds well to results obtained in earlier TS experiments [38]. The maximum is located surprisingly radially approximately 2 cm behind the leading edge of the side limiters, with 5 mm uncertainty in the field line tracing, while it was previously observed on Tore Supra and Alcator C-Mod [190] on the leading edge. With the classical screen, the full radial width of RF-perturbed zone is comparable to the expected uncertainty given by the magnetic reconstruction. With the prototype CBSB screen, the structure is so wide (~ 3 cm) that there can be no doubt that the probe is indeed magnetically connected to the side limiter and that high positive biasing occurs on field lines connected to the side limiter [45].

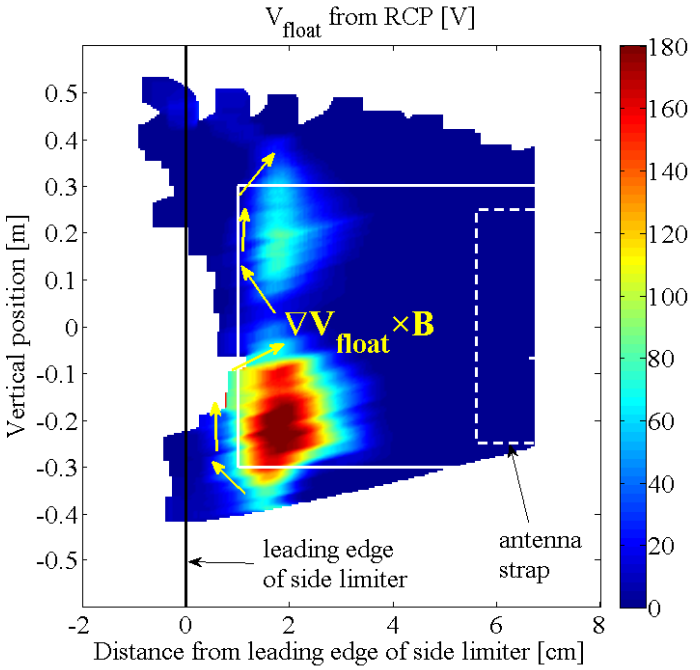

Figure 6.4: 2D mapping of RCP floating potential on flux tubes connected to the right side limiter of a powered ICRH antenna for the CBSB Faraday screen prototype. RF generator balance was (left/right) =(57%/43%). A curved coordinate system was used such that the side limiter leading edge appears as a straight vertical line. A sketch of the antenna is superimposed as well as a streamline of the $\mathbf{E} \times \mathbf{B}$ convection expected in the gradient of V_{float} [45].

Postulating that V_{float} is indicative of the DC plasma potential, stronger $\mathbf{E} \times \mathbf{B}$ density convection is expected along the iso-potentials [109]. Such particle convection, if present in the private SOL in front of the FS, could explain the poloidal concentration of the FS bar heat loads near the equatorial plane and their scaling with the square of the strap voltages, as well as the up/down asymmetry in the shark teeth damages.

These results were rather unexpected considering that one of the purposes of the new FS was to reduce these high potentials and high heat fluxes. These results are attributed to enhanced RF sheaths on "short field lines" in the private SOL between side limiters, or "lateral flux tubes" emerging from the antenna side limiters that were not envisaged in the minimization [48]. Reducing integrated $E_{\|}$ along long field lines seems to not enough to lower RF enhanced plasma potentials [109]. In order to explain the enhanced RF sheaths, several elements in the design have been proposed. The cantilevered bars, the misalignment of the bars with the magnetic field lines and the gap voltage between the bars (most likely set by the bar number and gap width) are good candidates to be investigated.

6.2 Simulations with TOPICA/SSWICH-SW-2D for Tore Supra

After obtaining these unexpected observations that were contradictory with what we thought at this time, we wanted to analyse and understand these observations from qualitative and quantitative viewpoints. The development of SSWICH provided with TOPICA the adequate tools to achieve these objectives for several reasons. First it gives a compari-

son basis for the simulations results. To be validated, a model should be able to reproduce the key observations that previous model could not. If SSWICH was unsuccessful, it would give us indications about the degree of sophistication that should be reached.

The new SSWICH procedure coupled with TOPICA was thus applied to interpret the experimental results and to analyse and compare the behaviour of the two Tore Supra FS designs, showing the compatibility and complementarity between both tools. For the first time, DC plasma potential and parallel heat fluxes measured on the antenna side limiters have been extensively compared to models predictions. Key simulations results in line with the experimental observations review exposed previously in Section 6.1 will be presented in this section.

6.2.1 Typical simulation results on the antenna side limiters

Despite the SSWICH-SW model being in 2D (radial/toroidal), results in 3D can be obtained by scanning at regular steps the vertical position along the antenna. Only one vertical position in the $E_{\|}$ field map is simulated at a time. This procedure by done here with steps of 1 cm much smaller than the expected typical poloidal scale (10 cm see Figure 5.11(a)). Then results in a 2D radial/poloidal plane was evaluated. We are interested here in what is happening on the antenna side limiters on both the inner face and on the outer face as shown on Figure 6.3.

The edge density profile is measured experimentally with a X-mode reflectometer [65], located beside the ICRH antenna. The density is thus not measured in front of the antenna but next to the antenna. The real density on the antenna can be affected by the ripple, the shadow of others objects or by the antenna itself. The radial density profile in the free

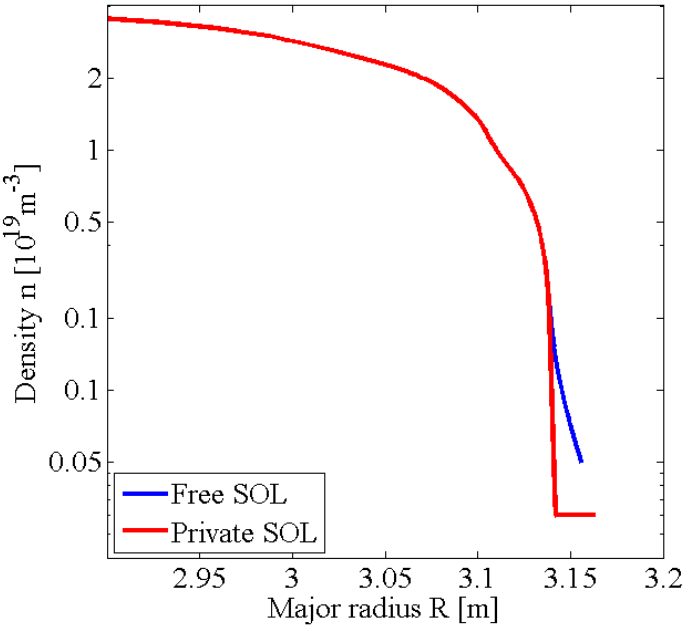

Figure 6.5: Radial density profiles. The profile in blue was measured by the reflectometer during the experiments. It corresponds to the density in the free SOL in SSWICH. The profile in red is the density profile in the private SOL in SSWICH determined with (5.1) and the density at the leading edge in the free SOL.

SOL in SSWICH is the density measured by the reflectometer. It is illustrated in blue by Figure 6.5. The density in the private SOL in red is evaluated with (5.1). The density at the leading edge of the side limiters is identical for both profiles.

Let us see now what looks like a typical result following this procedure with the field map for the CBSB FS illustrated by Figure 5.6(b). The simulation parameters were $T_e = 10$ eV, $T_i = 20$ eV, $V_{strap} = 30$ kV and $l_{\parallel,1} = 3.3$ m, $\sigma_{\perp DC,f}/\sigma_{\parallel,S} = 7.1\ 10^{-8}, \sigma_{\perp DC,f}/\sigma_{\parallel,S} = 2.5\ 10^{-6}, l_{\parallel,2} \approx 1.3$ m. The tilt of the magnetic field is 7°. Figure 6.6(b) shows the DC plasma potential evaluated on the outer face on the right side limiter with the CBSB Faraday screen (see Figure 5.3(b)) where the probes are magnetically connected. We assume that the average floating potential measured with probes is representative of the DC plasma potential. The simulation result can be then compared to the observations both qualitatively and quantitatively. Some key agreements with the experiments are recovered.

First the overall two-hump poloidal structure, observed experimentally, of the heat loads and on the floating potential on side limiters could also be reproduced. The floating potential measured on the probe is assumed to be representative of the DC plasma potential both in amplitude and in topology. The minimum is observed near the equatorial plane whereas the maximum are observed near the antenna box corners. This is a robust invariant output that was systematically observed whatever the parameters. For that reason, the poloidal topology is mainly dependent on the input $E_\parallel$ field map i.e. on the electrical design on the antenna, and not on the numerous simulation parameters. This two-hump poloidal structure could also be obtained by previous modelling [48]. So it is not by itself a discriminating test but a necessary result to obtain for any model.

Second SSWICH can obtain, with our choice of simulation parameters, a presence of DC plasma potential not only on the inner face of the side limiter in the private SOL of the antenna but also on the outer face in the free SOL. This is a new feature that did not exist in the version of SSWICH used in [174] whereas insignificant V_{DC} were evaluated in

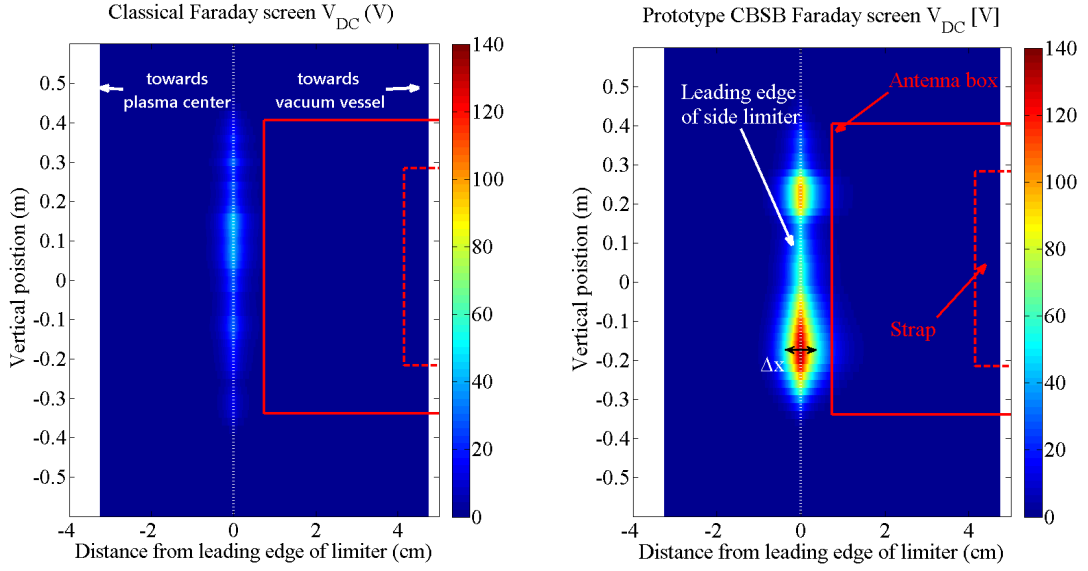

(a) (b)

Figure 6.6: 2D Map of the DC plasma potential V_{DC} obtained with SSWICH in the poloidal/radial plane at the position shown by dark dashed line in Figure 5.1(b) for (a) the conventional Faraday screen and (b) the CBSB Faraday screen prototype.

the free SOL. The topology of V_{DC} is identical on the inner face and on the outer face of the side limiters. But the amplitudes are different. This feature is rendered possible by the inclusion of a DC perpendicular conductivity in SSWICH whose role and impact on the simulation results would be detailed later on in this chapter.

Third an up-down asymmetry is also obtained similar to the experiments. A factor ≈ 2 is recovered between the maximum amplitude of the V_{DC} top peak compared to the amplitude of the bottom peak. This also corresponds to experimental observations (see Figure 6.4).

There are however some disagreements remaining. The first is on the radial position of the maximum of the V_{DC} structure that was observed for the CBSB Faraday screen in the experiments shifted outwards by 2 cm behind the leading edge and in the shadow of the limiters. However in the simulations, the maximum is always observed radially at the position of the leading edge of the limiters. There are several possible a priori explanations. The first possible explanation is an error in the reconstruction of the trajectories of the magnetic field lines. But this would not explain why this phenomenon is only observed for the antenna with the CBSB FS. The second explanation supposes the existence of an unknown physical mechanism that shift uniformly outwards by several centimeters the entire V_{DC} structure and that is significant only with high magnitude of V_{DC}. This mechanism, if it exists, has not been yet identified, and as such is not modelled within the present SSWICH code.

The second main disagreement is on the quantitative values that do not correspond exactly to the experiments results. Maximum V_{DC} value of 140 V have been obtained that has to be compared with the 170 V in the experiments (see Figure 6.4). The uncertainty of the quantitative values can be explained with two main reasons.

First, some of the simulations parameters are loosely constrained almost to the point of being free parameters for some of them. Moreover they appear to be extremely sensitive to these badly known parameters. The parallel connexion lengths in the SOL are quite difficult to obtain with accuracy due to the complex topology of the magnetic field lines and magnetic connexions to other objects.

The magnitude of the results is also sensitive to the input density. The density in the private SOL has never been measured experimentally. Instead it is evaluated from analytic considerations [93]. It is simply extrapolate from the ratio of the parallel connexion length in free in private SOLs and the density in free SOL measured by reflectometry [146] combined into a simple model [93]. However new antennas on ASDEX Upgrade [191, 192] and WEST [19] will be equipped with a reflectometer. The density in the free SOL was measured in front of the reflectometer that is placed next to the antenna and not in front of the antenna. The density in front of the reflectometer may not be the density in front of the antenna due to convection cells [38].

The quantitative values of perpendicular DC conductivity are still unknown in the SOL of tokamaks. This is only when talking about average values at zero order. A first order correction would be then to add a spatial dependence. This discussion will be further continued later in this chapter.

Second, our available resources do not allow us to simulate a more realistic set of parameters characteristic of Tore Supra. As an example, the parallel connexion length to a probe along a magnetic field line connected to the side limiter of the antenna is estimated in Tore Supra to be of the order of $10 - 15$ m. We are far from that in SSWICH as the connexion length is of the order of ≈ 1 m. Furthermore the domain of DC perpendicular conductivities compatible with the observations is not yet within our reach as the associated characteristic transverse scale lengths require finer numerical grids (i.e. more RAM

memory and more CPU time). Nevertheless relative comparisons of simulation results will be attempted.

From these 2D V_{DC} spatial distribution, DC electric field can be expected in the poloidal and radial directions, as $\mathbf{E_{DC}} = -\nabla V_{DC}$. Cross-field convection via local $\mathbf{E_{DC}} \times \mathbb{B}$ drift velocities is then evaluated with the formula $\mathbf{v} = -\nabla V_{DC} \times \mathbb{B}/B^2$ [94]. Estimates of the drift velocities give about 6000 km/s in the poloidal direction and 100 km/s in the radial direction, in agreement with observations [109].

The average sheath width δ is another possible output of the code. (a) and (b) show δ on the inner and outer face of the antenna side limiter respectively from the Child-Langmuir law (2.53) and the correction proposed by Lieberman [103]. The two density profiles distinguishing free SOL from private SOL (see Figure 6.5) are accounted for. The sheath width follows a similar pattern at the DC plasma potential. Sheath widths of a the order of 100 microns are evaluated. This is much smaller than the typical grid size in the parallel direction (i.e. 1 cm). The sheath width is of the order of the typical grid size in the radial direction. Even meshing the sheath with only one element is thus out of our reach, due to the prohibitive numerical cost. More realistically several elements (i.e. ≈ 10) would be needed to accurately mesh the sheath. Replacing metallic boundary conditions by sheath boundary conditions is thus nowadays the only way to evaluate numerically in a short time RF sheaths effects self-consistently in a domain containing an ICRH antenna in the SOL of a tokamak plasma. It also indicate that the direct measurement of the electric field in the sheath will require a high resolution spectrometer in order to do for ICRH antennas what was performed for LH antennas by Klepper [193].

6.2.2 Relative comparison of the two Faraday screens

The procedure TOPICA/Multi SSWICH-SW-2D has also been used to compare relatively the results with the two Faraday screens on Tore Supra. This relative comparison is with respect to each other with the same simulation parameters and with respect to the

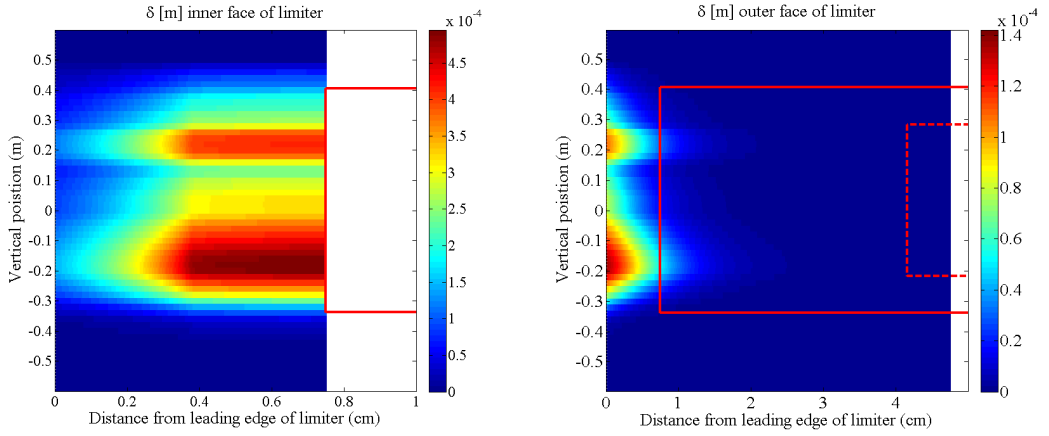

(a) (b)

Figure 6.7: 2D Map of the average sheath width δ for the CBSB Faraday screen prototype with the same parameters as in Figure 6.6(b) on (a) the inner face on the antenna side limiter and on (b) the outer face. The red solid curve denotes the antenna box while the red dashed curve denoted the strap. The sheath only exists up to the leading edge of the limiter.

relative comparison from the experiments. The simulation parameters are the same as in Section 6.2.1. The connexion length in the free SOL is much smaller in the simulations than in the experiments due to limited computational resources. At this moment the choice of perpendicular DC conductivities is arbitrary. The impact of that parameter will be discussed later and a better choice of perpendicular DC conductivities will be proposed.

The simulations results suggest that the CBSB FS enhances RF sheaths compared to the classical screen instead of reducing them, in line with the experiments. Indeed it can be seen that the magnitude of V_{DC} on Figure 6.6(b) is much higher than on Figure 6.6(a). A maximum value of ≈ 140 V is reached on the CBSB FS while only ≈ 60 V for the classical screen. The absolute values are lower than the experiments values. The density, known to impact the magnitude of V_{float} [45], and other parameters could influence the magnitude of V_{DC} in the simulations. An uncertainty thus persists on the quantitative value of the magnitude of V_{DC}. The relative comparison of the amplitude of V_{DC} however recover a factor 2 on the amplitude that is consistent with the experiments.

The maximum of the V_{DC} structure is as previously observed radially at the leading edge of the antenna side limiters for both Faraday screens. This is consistent with observations on the classical FS and on others devices [109]. It is however inconsistent with the probe measurements on the CBSB Faraday screen (see Figure 6.4).

The poloidal structure does seem however close to the equatorial plane compared to the CBSB Faraday screen. This could be related to some difficulties that were encountered when modelling the classical screen in TOPICA with the revised procedure. Indeed, the resulting $E_{\parallel}$ field map seemed more sensitive to the mesh in TOPICA especially on the regularity of the mesh. The classical FS, while having lower amplitude, has been paradoxically more difficult to handle than the CBSB Faraday screen, surely due to the situation being more subtle on the classical screen than on the CBSB screen.

Beyond V_{DC} directly known from SSWICH, the parallel heat fluxes deposited on the side limiters can be analytically evaluated [93]. The total heat flux parallel to the field lines $Q_{\parallel,tot}$ is the sum of the ion heat flux and the electron heat flux. The ions in the model are assumed to lose the same amount of energy at both extremities on a field line. The ion heat flux averaged over one RF cycle is explicitly determined with the following analytical expression [93]:

$$Q_{\parallel,i} = j^{+}\left[V_{DC}\left(x,y\right) + 2.5\frac{k_B T_i}{e}\right]. \tag{6.1}$$

The electrons population is assumed to be thermal and each electron carries an average energy $2k_B T_e/e$ [93]. The number of electrons collected by the wall is governed by the DC biasing. Multiplying (5.10) by the average energy per electron gives the electron heat flux over an RF cycle:

$$Q_{\parallel,e,k} = \frac{2k_B T_e}{e} j^{+} \exp\left[e\frac{V_f + V_{b,k}\left(x,y\right) - V_{DC}\left(x,y\right)}{k_B T_e}\right], \tag{6.2}$$

where $k = r, l$ denotes the left and right sides, j^{+}, V_f and $V_{b,k}$ are determined respectively with (2.42), (2.40) and (2.51).

With the parameters above, parallel heat fluxes on the inner face of the side limiters gives ≈ 1 MW/m^2 for the classical screen and ≈ 2.5 MW/m^2 for the CBSB screen. The correct relative comparison factor is reproduced, but the magnitude is within a factor 2 of the actual measures. The uncertainty on the quantitative values can again be ascribed to loosely constrained parameters such as the perpendicular DC conductivity in the free SOL and in the private SOL, that can changed the magnitude of V_{DC} and the parallel heat fluxes. The role of these DC conductivities will be unravelled in the next section. The

magnitude of the parallel heat fluxes is also highly dependent on the density. It could be different in front of the antenna due to the magnetic connection of the different objects and their shadowing. Moreover the density distribution is modified in presence of DC potential gradients that generate DC electric fields and $\mathbf{E}\times\mathbf{B}$ convective cells in front of the antenna [109, 172]. This phenomenon adds up to the uncertainty.

6.2.3 Different possible mechanisms to excite RF sheaths

Probes are magnetically connected to the lateral part of the antenna side limiters in the outer SOL (see Figure 6.3) where they observed significant DC plasma potential structure whenever the antenna is active. However the antenna limiters prevent a direct magnetic connection between the probes and the active elements of the antenna as no field lines enter the private SOL of the antenna. The probes thus measure phenomena of the antenna without a direct view on it.

Several (at least three) physical mechanisms could be invoked a priori to enhance significantly the DC potentials V_{DC} in the free SOL surrounding the ICRH antenna, where Langmuir probes measure large voltages: direct excitation on RF sheaths in free SOL, propagation through perpendicular DC conductivity of DC currents from the private SOL and mode conversion between slow wave and fast wave.

Direct excitation of RF sheaths in free SOL by the SW rectification mechanism does not seem prominent as the SW cannot reach the free SOL (see Figure 6.8). The typical skin depth for the SW ($c/\omega_{pe} \sim 5$ mm at most) is smaller than the perpendicular dimension of the private SOL (~ 1 cm). When taking into account the existence of sheath-plasma waves (SPW) [53] than can propagate V_{RF} (i.e. $E_{\|}$ along boundaries), that evanescence length becomes c/ω_{pi}. However the propagation stops at the leading edge of the side limiter as the SPW need a material boundary to propagate. No RF-SBC is implemented at the leading edge. The SPW thus cannot reach the free SOL either.

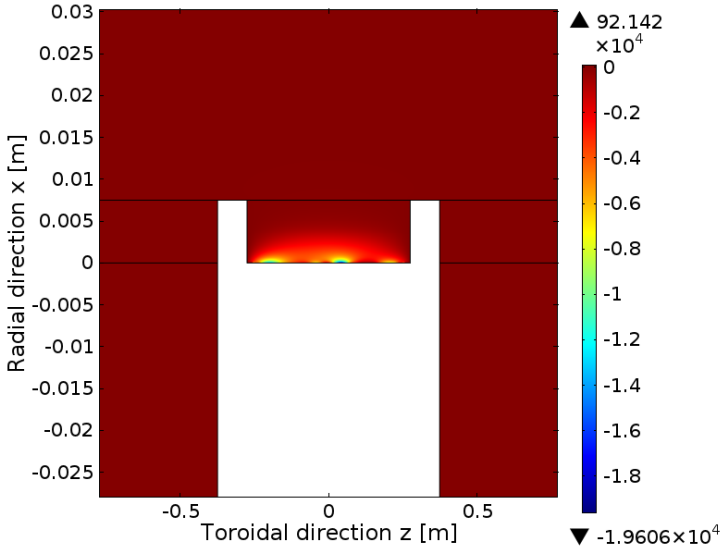

Figure 6.8: Zoom in Figure 5.1(b) around the private SOL of the wave parallel electric field $E_{\|}$ at $y = -0.2$ m.

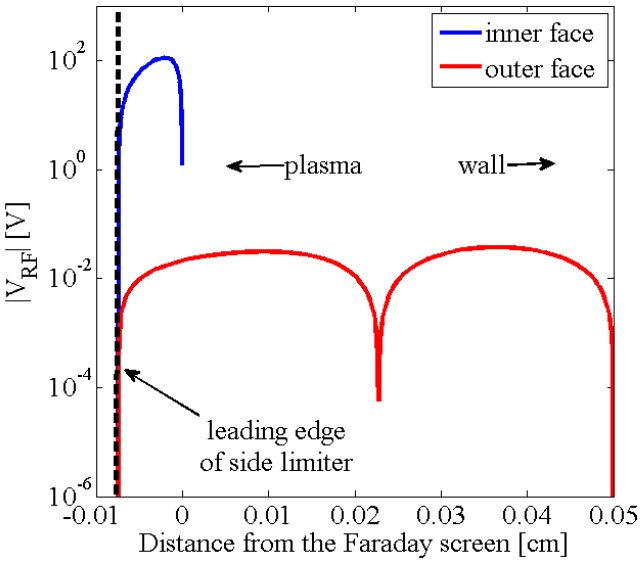

Figure 6.9: $|V_{RF}|$ vs distance from the Faraday screen on the inner face on the side limiter in blue (see blue dashed line on Figure 6.10 and on the outer face of the limiter in red (see red dashed line).

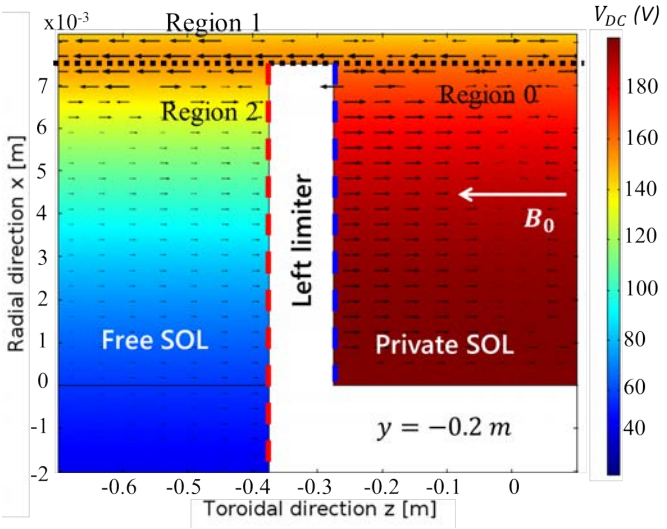

Figure 6.10: Circulation of DC currents from the private SOL to the free SOL and plasma potential around the right limiter (from the plasma) of the antenna at the vertical position $y = -0.2$ m. The axes are in meter. The black arrows represent DC currents whereas the colour scale denote the amplitude of V_{DC}. The red dashed line corresponds to the outer face of the side limiter whereas the blue dashed line denotes the inner face.

Moreover no significant RF sheath voltages are seen on the outer face of the limiter with this mechanism in SSWICH, thus confirming the fact that the slow wave does not excite sheaths in the free SOL. This is illustrated by Figure 6.9, where the oscillating voltage V_{RF} on both sides of the lateral limiter are compared. On the outer side (free SOL), the amplitude is several order (almost four orders) of magnitude lower than on the inner side of the limiter. Moreover the amplitude of V_{RF} in the free SOL is much smaller than T_e. The rectification process is thus not very efficient in the free SOL. This mechanism does not seem to have a significant enough amplitude to generate large DC potentials in the free SOL.

A second mechanism is in two steps and the topic of Appendix C. The slow wave is biasing the inner face of the limiter with the rectification process. V_{DC} is subsequently propagated outside the private SOL by the effective DC perpendicular conductivity. A circulation of DC current from the private SOL to the free SOL can be created, as seen in Figure 6.10, providing that the DC perpendicular conductivity in the private SOL is larger than in the free SOL. One possible reason is that the turbulence level could be higher in the private SOL because the short field lines are always in the bad curvature region. Confirming this assumption would require dedicated simulations involving the turbulence properties of the plasma and their impact on the radial transport, out of the scope of this thesis. This current circulation generates strong V_{DC} of the outer face of the limiter, where Langmuir probes measure large voltages, contrary to [174]. As this circulation of DC current flows in the flux tube passing in front of the leading edge of the limiter, it would also explain the location of the maximum of V_{DC} at the leading edge. The mechanism is qualitatively describes with an analytic model in Appendix C.

Mode conversion between slow and fast wave could possibly be another mechanism. It has however has yet to be included in the model. It would go together with arbitrary angles between the wall and the magnetic field and the subsequent bump profile on the front face of the limiter to spread the fluxes over a larger collection area. Recent works seem to indicate that mode conversion could be a significant mechanism [194, 195].

6.2.4 Sensitivity of the radial pattern of V_{DC} to perpendicular DC conductivity

By contrast to the poloidal pattern, the radial structure of the V_{DC} on the outer face of the limiter (radial penetration, quantitative amplitudes and radial broadening) is found highly sensitive to loosely constrained simulation parameters: transverse plasma DC conductivities, parallel connexion lengths in free SOL. The radial pattern on the inner side of the limiter is also influenced by the parameters but it always exists on the contrary to the pattern of the outer face. Indeed the patterns in the private SOL can be directly created by the evanescent SW even in the absence of perpendicular conductivity or homogeneous $\sigma_{\perp DC}$ everywhere as illustrated by the results in Ref [174, 196].

Section 6.2.3 has shown a mechanism to generate significant V_{DC} in the free SOL by transport of DC currents from the private SOL to the free SOL through different DC perpendicular conductivities in both regions. In order to know if we understand the physical mechanism, the interplay between mechanism and geometry and provide insights on the SSWICH model in Tore Supra geometry, illustrated by Figure 6.11, a simplified situation where analytic solutions exist, has been considered. It also serves as a sensitivity study to the DC perpendicular conductivity with several values in the free and private SOLs. Moreover it was anticipated that due to limited computational resources, some sets of parameters would either take too much time to calculate or either require too much memory.

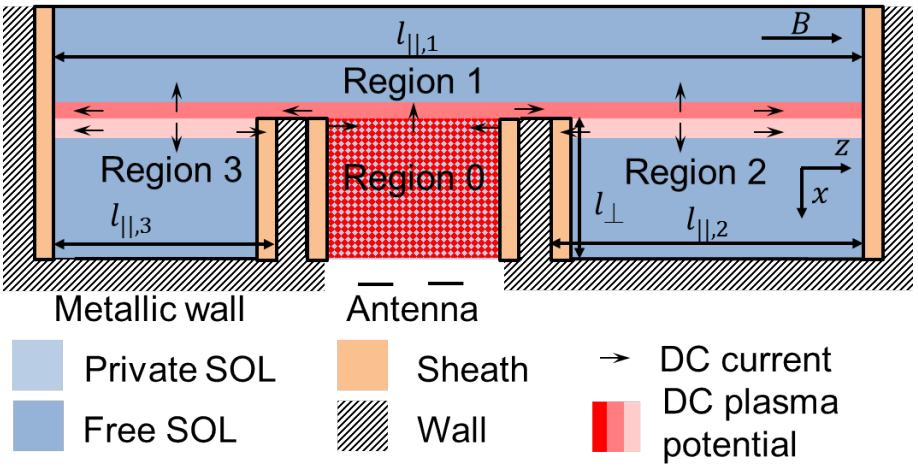

Figure 6.11: Sketch of the 4 regions geometry and main notations in a 2D radial/toroidal plane. The levels of blue are indicative of the plasma density. The levels of red are indicative of the intensity of the DC plasma potential. The black arrows indicate a circulation of DC currents from the private SOL to the free SOL.

As in Section 5.1, the magnetic field lines are either perpendicular or parallel to the boundaries. The domain is constituted of four regions: the private SOL of an ICRH antenna (region 0), the inner free SOL (region 1) and two outer free SOLs (region 2 and 3) on both toroidal sides of the antenna limiters. x is the radial direction and z is the parallel direction. Region 0 radially extends from $x = 0$ to $x = L_\perp$, whereas region 1 spans from $x = -\infty$ to $x = 0$ and region 2 and 3 from $x = 0$ to $x = +\infty$. The four regions are connected in $x = 0$.

Each region denoted by the subscript $k = 0, 1, 2, 3$ is characterized by three essential parameters assumed constant:

- the parallel connection length $l_{\parallel,k}$ of the open magnetic field lines,
- a scalar transverse DC conductivity for the DC current $\sigma_{\perp DC,k}$,
- a density n_k.

A transverse diffusion length in the region k for the DC plasma potential can thus be defined:

$$\lambda_{j,k}^2 = \frac{l_{\parallel,k}\sigma_{\perp DC,k}k_B T_e}{2ej_k^+}, \tag{6.3}$$

where j_k^+ is the ion saturation current in the region k defined by (2.42). The factor 1/2 accounts for the two sheaths at both extremities. The value of $\sigma_{\perp DC,k}$ is adjusted in order to reproduce the characteristic transverse length for the DC current associated with the physical mechanisms [112] (friction with neutrals, viscosity, inertia) briefly exposed in Section 2.3.4.

Sheath rectification of intense near RF fields is biasing the walls to a potential V_b as explained in Section 2.3.2.2. The biasing voltage V_b is assumed to exist only in the private SOL and to be homogeneous over the two sides of region 0. The wall biasing V_b is assumed to be transferred to the SOL DC plasma potential V_{DC} via the circulation of DC currents between the several regions. With this analytical model, a thin flux tube passing just in front of the antenna side limiter is transporting the DC current from the private SOL to

the free SOL. The private SOL can thus be resumed for the free SOL as a punctual source of DC currents located at the leading edge of the side limiter.

Several characteristics can then be derived. The full derivation is performed in Appendix C. This analytical model indicates that non-linear broadening with the amplitude of V_{DC} should occur. The half width at half maximum of the potential peak due to non-linear broadening reads simple expression within two asymptotic cases:

$$\frac{\Delta x_1}{\lambda_{j,1}} = \begin{cases} \ln 2 + \frac{V_{DC,le}}{12T_e} & \text{if } V_{DC,le}/T_e < 4, \\ \sqrt{2\left(\frac{V_{DC,le}}{T_e} - 1\right)} - \sqrt{\frac{V_{DC,le}}{T_e} - 2} & \text{if } V_{DC,le}/T_e > 4. \end{cases} \tag{6.4}$$

where $V_{DC,le}$ is the amplitude of the DC plasma potential at the leading edge of the side limiters. $\lambda_{j,1} \ln 2$ is the width Δx_1 that would have been obtained with the linear model whereas the second term accounts for a non-linear broadening of the potential peak for finite bias.

To test the expression of the non-linear broadening in (6.4), simulations with SSWICH-SW-2D were performed with the field maps shown in Figure 5.6(b). To limit the amount of necessary computation, only one parallel/radial plane at $y = -0.2$ m was simulated as illustrated by Figure 5.12. This vertical position was chosen since it is approximately the region where the maximum of V_{DC} are expected as shown on Figure 5.11(a).

In the simulations, region 2 and 3 in Figure 6.11 are equivalent since the geometry is symmetric and the density profile is the same. It gives $\lambda_{j,2} = \lambda_{j,3}$. The amplitude of V_{DC} at the leading edge is also evaluated. The half size at half maximum are evaluated on each side of the peak of V_{DC}. The full size at half maximum in the simulations Δx_{sim} is thus obtained by summing both half widths: $\Delta x_{sim} = \Delta x_1 + \Delta x_2$.

In the analytic model homogeneous densities are assumed in each region. This is not the case in the simulations. Instead in the simulations, the density is averaged over half the peak of V_{DC} with respect to the position of the leading edge. It therefore gives an average density higher on the plasma side of the leading edge than of the vacuum vessel wall side. The density in the private SOL is averaged.

The parallel connection length are $l_{\parallel,0} = 0.55$ m, $l_{\parallel,1} = 3.3$ m and $l_{\parallel,2} = l_{\parallel,3} = 1.275$ m with the limiter 10 cm wide. The DC perpendicular conductivities are known since they are imposed. With these parameters, the associated $\lambda_{j,k}$ can then be calculated. The predicted full widths at half maximum $\Delta x_{analytic}$ are then obtained with (6.4) where the amplitude of $V_{DC,le}$ is the one obtained from the simulations.

Figure 6.12 is the result of the comparison of the radial broadening of V_{DC} structure against the analytical predictions in (6.4).

It confirms that, within the linear regime of the sheaths, the full width at half maximum Δx of the V_{DC} structure scales as a diffusion length $\lambda_1 + \lambda_2$. Moreover a non-linear dependence of the broadening of Δx with $V_{DC,le}$ is found. The analytical formula is however always below the simulation points within an almost constant 20% margin.

A possible explanation is a violation of the flute assumption in the vicinity of the leading edge of the side limiter that is the interface along the same field line of very disparate regions since an infinitely thin flux tube is assumed in the analytic model as the mean of transport of the DC currents from the private SOL to the free SOL. In reality the tube has a finite width that is likely set by the DC perpendicular conductivity in the private SOL. This would broaden even more the V_{DC} structure.

The radial broadening is also larger on the wall side than on the plasma side, as observed in probe measurements (see Figure 6.4) and in the simulations (see Figure 6.6(b)). This analytic model can give an explanation to this phenomenon. One when looking at (6.3)

would suspect that the radial broadening is larger on the plasma side since the parallel connection length is larger on the plasma side. But one would ignore the denominator. j_k^+ is not the same in both region since a radial density gradient exist. The density is also much larger on the plasma side. This ratio of parallel connection length over the density is larger on the wall side with respect to the leading edge of the side limiter. The transverse scale length calculated with (6.3) is thus larger. This is opposite to the first intuition.

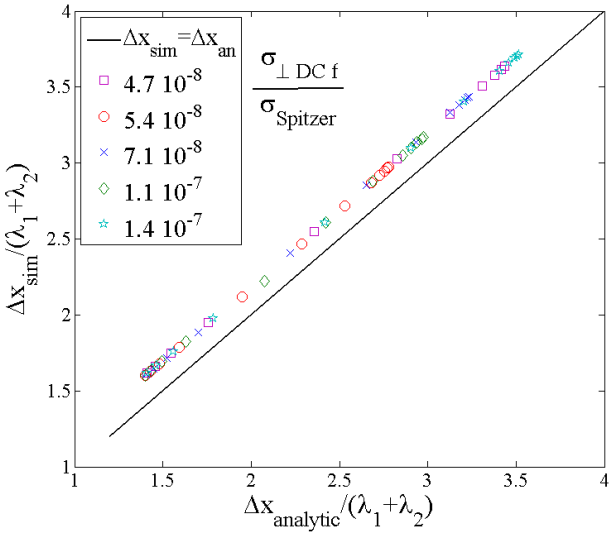

Figure 6.12: Comparison of the full width at half maximum Δx of the V_{DC} structure in the free SOL obtained with the simulations with the analytical formula (6.4) for the CBSB FS. Different values of $\sigma_{\perp DC,p}$ and $\sigma_{\perp DC,f}$ were taken. Each point represents one simulation. The others parameters are: $T_i = 20$ eV, $T_e = 20$ eV, $L_{\parallel} = 3.3$ m and $V_{strap} = 30$ kV.

The analytic model not only provides insights on the radial size of the DC potential structure but also of the amplitude of these structures. Linking the amplitude at the leading edge with the parameters in the free and private SOL has been attempted. In a linearised regime, the DC plasma potential at the leading edge reads:

$$\frac{V_{DC,le}}{V_b} = \left[1 + \frac{\lambda_{j,1} + \lambda_{j,2} + \lambda_{j,3}}{\lambda_{j,0} \tanh\left(\frac{L_\perp}{\lambda_{j,0}}\right)}\right]^{-1} . \tag{6.5}$$

The amplitude of $V_{DC,le}$ at the leading edge can be qualitatively understood by the following. The amplitude is first set by the amount of DC currents that the private SOL can draw. This total current is determined by the effective private SOL that contributes to the DC currents that are leaving the private SOL that is itself linked to the perpendicular DC conductivity in the private SOL. Second the amplitude of $V_{DC,le}$ is also set by the amount of DC currents that can flow into the free SOL that is determined by the perpendicular DC conductivity in the free SOL and the surface over which the currents can be deposited that depends on the parallel connection length in the free SOL. Third the intensity of the bias in the private SOL also has an impact on the amplitude of $V_{DC,le}$. The more intense the bias is, the more DC currents can be draw. Since the amount of current is limited in the parallel direction, then it can only flow in the perpendicular direction. This brings a refinement into the model since the amount of DC currents that can be drawn from the sheaths in the private SOL is also limited as the sheath has to exist.

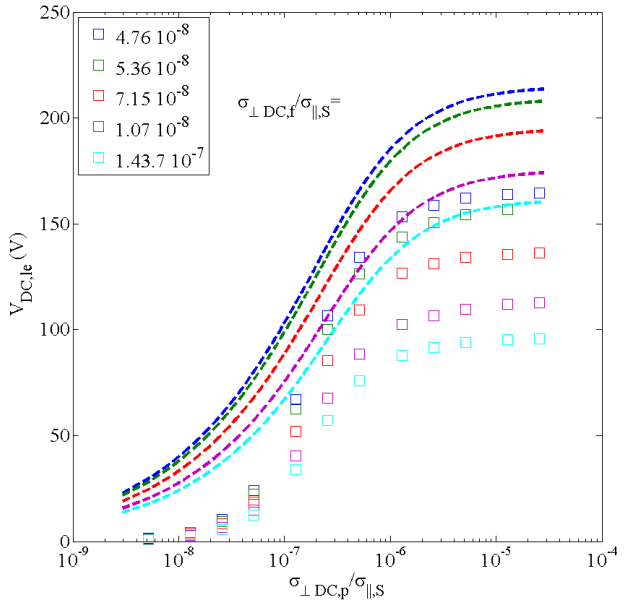

(a)

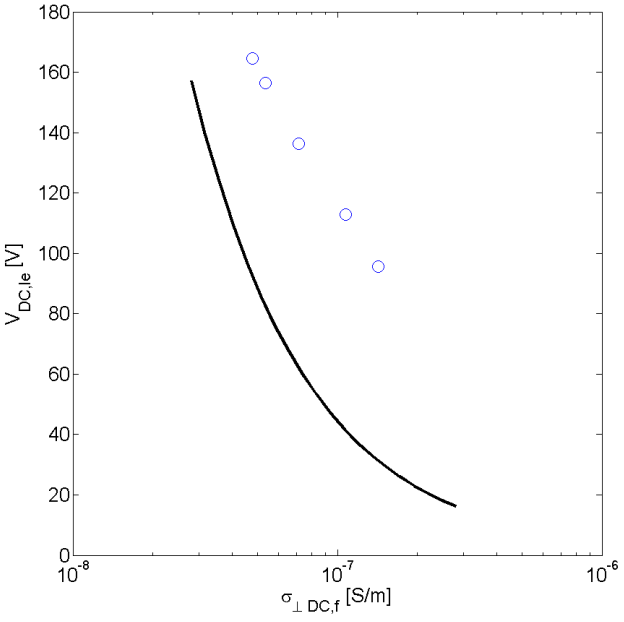

(b)

Figure 6.13: (a) Comparison of the amplitude of V_{DC} at the leading edge of the side limiters obtained with the simulations with the analytical formula (6.5) for the CBSB FS. (a) Comparison of the asymptotic amplitude of $V_{DC,le}$ at high $\sigma_{\perp DC,p}$ with the analytic formula (6.6). Different values of $\sigma_{\perp DC,p}$ and $\sigma_{\perp DC,f}$ were taken. Each point represents one simulation. The others parameters are: $T_i = 20$ eV, $T_e = 20$ eV, $L_{\parallel} = 3.3$ m and $V_{strap} = 30$ kV.

A comparison of the simulations results for the DC plasma potential at the leading edge of the side limiters with the analytic predictions of (6.5) has been performed. It is illustrated by Figure 6.13(a). The correct shape is qualitatively reproduced at least for the upper part of the curves. $V_{DC,le}$ has an asymptotic value at large $\sigma_{\perp DC,p}$. For the bottom part, it was seen a posteriori that the simulations grid was not fine enough to resolve accurately the transverse scale associated with the DC perpendicular conductivity. This is due to limited computational resources. It results in DC currents not being able to go from a grid point to an adjacent grid point in the radial direction. It should also be noted that when normalized to their asymptotic value at high $\sigma_{\perp DC,p}$, the curves coincide. They thus follow similar parametric dependences.

The predictions of the quantitative values of $V_{DC,le}$ are however loose, but within a factor 2. This can be explained by the simplicity of the analytic model that has been linearised. Moreover electron saturation, given by (5.11), is not yet accounted for. When electron saturation occurs, the sheath ceases to exist. More intense bias cannot increase the amount of currents any more. This condition is written within two extreme cases as:

$$V_{DC,le} = \begin{cases} Y\left(1+\frac{Y}{6}\right) & \text{if } Y \leq 1.5, \\ \frac{Y^2}{2}+1 & \text{if } Y > 1.5, \end{cases} \tag{6.6}$$

where

$$Y = -\frac{L_\perp}{\lambda_{j,1}+\lambda_{j,2}+\lambda_{j,3}}\frac{\langle j_{sh}\rangle}{j_0^+} \tag{6.7}$$

The predictions of analytic formula (6.6) has been then compared to the asymptotic values at high $\sigma_{\perp DC,p}$ of $V_{DC,le}$ obtained in the simulations. This comparison is illustrated by Figure 6.13(b). The analytic model does not agree with the simulations. It can be concluded that something is missing in the analytic model to understand the mechanism setting the amplitude of V_{DC}.

The parametric dependence of the amplitude and of the radial broadening of V_{DC} are extremely sensitive to the DC perpendicular conductivity that largely remain unknown in the SOL of tokamaks. However this mechanism of formation of DC plasma potential in the free SOL give some hints and constrains of the DC perpendicular conductivity, at least relatively between the private and the free SOLs. Indeed the DC perpendicular conductivity in the private SOL $\sigma_{\perp DC,p}$ has to be high enough to draw significant DC currents from the sheaths into the private SOL and allow them to leave the private SOL. This is illustrated on Figure 6.14(a) and (b) where small and large $\sigma_{\perp DC,p}$ are chosen.

With a small $\sigma_{\perp DC,p}$, the DC currents are trapped in the private SOL. V_{DC} amplitude is consequently intense in the private SOL and low in the free SOL. On the contrary with a large $\sigma_{\perp DC,p}$, DC currents can flow into the free SOL in addition to the private SOL and generate significant V_{DC} in the free SOL. The amplitude of V_{DC} is consequently lower in the private SOL.

The relationship between the amplitude V_{DC} in the private SOL and the amplitude of V_{DC} at the leading edge with the SOL plasma parameters remain unknown. Satisfying simultaneously the requirements on amplitude and size of V_{DC} on the outer face of the side limiter where probes are connected structure cannot be accomplished with an homogeneous $\sigma_{\perp DC}$ in the whole SOL as illustrated by Figure 6.14(a). The DC perpendicular conductivity in the free SOL $\sigma_{\perp DC,f}$ should however be relatively smaller compared to $\sigma_{\perp DC,p}$ as to limit the flow of DC currents radially. Indeed no significant V_{DC} amplitude has been measured in the plasma. To obtain a significant V_{DC} amplitude in the free SOL, we thus have to postulate a higher transport level in the private SOL compared to the free SOL.

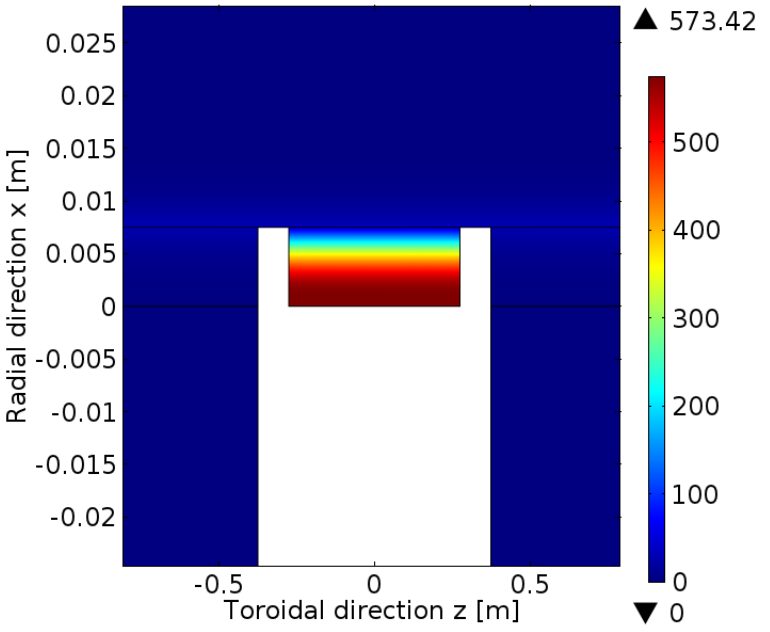

(a)

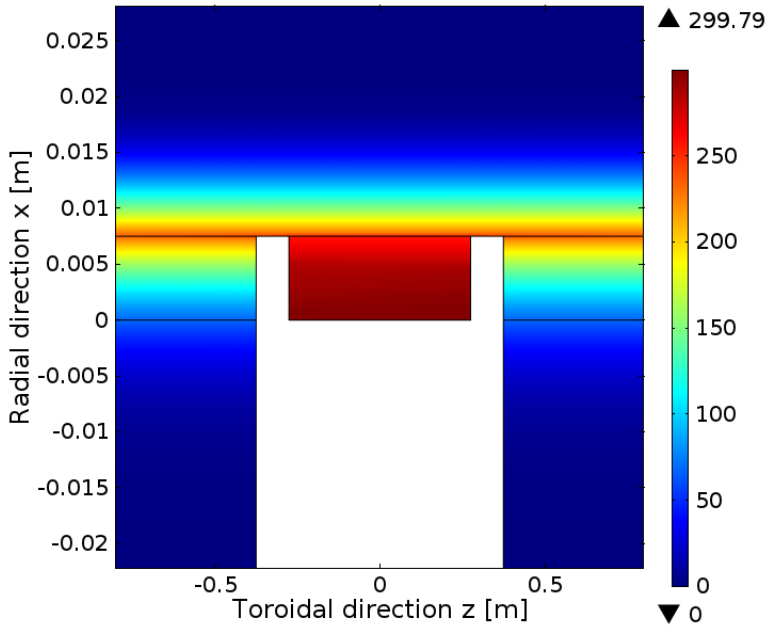

(b)

Figure 6.14: Zoom in Figure 5.1(b) of the DC plasma potential V_{DC} at $y = -0.2$ m for (a) small $\sigma_{\perp DC,p} = \sigma_{\perp DC,f} = 7.110^{-8}\sigma_{\parallel,S}$ and (b) large $\sigma_{\perp DC,p} = 2.610^{-6}\sigma_{\parallel,S}$ and $\sigma_{\perp DC,f} = 7.110^{-8}\sigma_{\parallel,S}$. The colour scale represents the amplitude of V_{DC}. The black arrows, whose lengths are in logarithmic scale, denote the DC currents. The other parameters are $T_e = 10$ eV, $T_i = 20$ eV, $V_{strap} = 30$ kV and $L_\parallel = 3.3$ m.

6.2.5 Estimation of values of perpendicular DC conductivity consistent with observations

It was shown that the radial pattern of the V_{DC} structure is highly sensitive to loosely constrained parameters such as the perpendicular DC conductivity. Our approach is therefore to treat the inverse problem and to try to estimate a domain of perpendicular DC conductivity whose values are compatible with the measured experimental broadening. In order to accomplish this task, we need to consider the real connection length of a probe magnetically connected to the outer face of the side limiter: $l_{\parallel,2} \approx 10 - 15$ m. This thus require a domain whose total size in the parallel direction $L_\parallel$ is of the order of $20 - 30$ m.

The model with a domain length of this magnitude cannot be solved due to our limited numerical resources. Despite the fact that we do not have the numerical resources, an analytical model of non-linear DC biasing in a four regions domain is available. The complete analytic derivation is presented in Appendix C. This analytic model was furthermore benchmarked against SSWICH-SW-2D simulations in Section 6.2.4. Instead of simulations in Comsol, we will reproduce the experimental broadening of the radial structure of V_{DC} by analytic considerations.

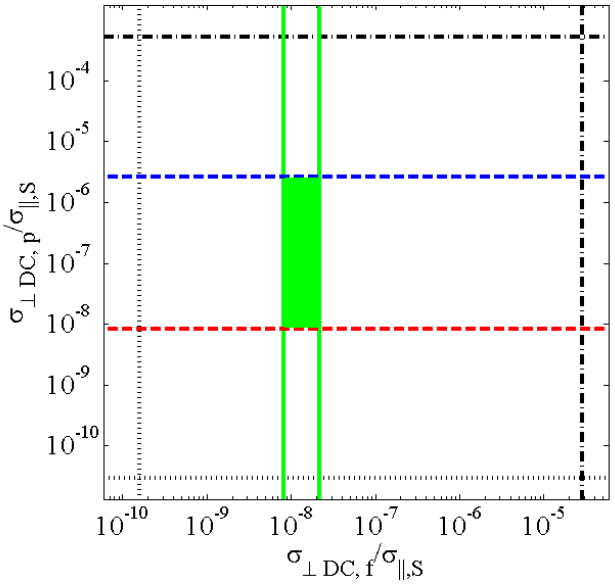

Figure 6.15: $\sigma_{\perp DC,p}/\sigma_{\parallel,S}$ versus $\sigma_{\perp DC,f}/\sigma_{\parallel,S}$. The perpendicular DC conductivity domain compatible with experiments is represented by a green rectangle. The lines represent the different limits.

When trying to determine a domain of compatible value of perpendicular DC conductivities in the free and private SOLs, the first thing one can do is think about the minimum and maximum value that they can take. The minimum value is determined through the Larmor radius, as the minimum transverse scale cannot be smaller than the ion Larmor radius (1.6). For deuterium ion at the Bohm speed with $B = 2.93$ T and $T_i = 20$ eV, it gives $\rho_s = 0.27$ mm. The other parameters are $T_e = 10$ eV, $l_{\parallel,0} = 0.55$ m, $l_{\parallel,2} = 10$ m and the density at the leading edge $n_{le} = 1.7\ 10^{18}$ m^{-3}. For the perpendicular DC conductivity it reads, reversing (6.3), in the free SOL $\sigma_{\perp DC,f,m}/\sigma_{\parallel,S} = 1.6\ 10^{-10}$ and in the private SOL $\sigma_{\perp DC,f,m}/\sigma_{\parallel,S} = 3\ 10^{-9}$. They are represented on Figure 6.15 by black dotted lines.

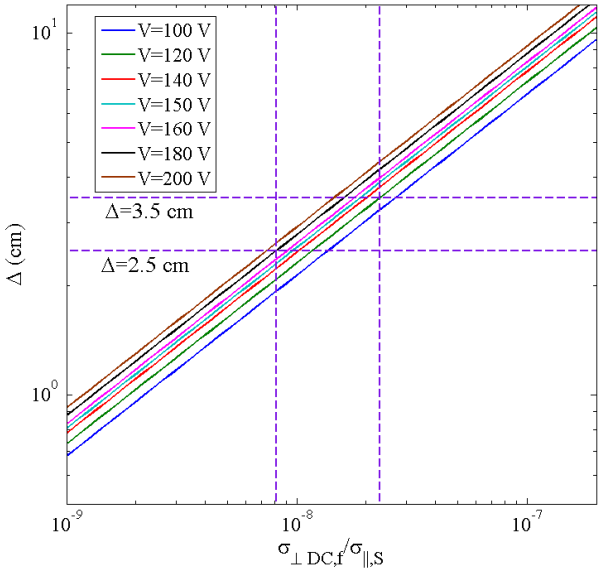

Figure 6.16: Radial extension of the V_{DC} structure (in cm) versus the perpendicular DC conductivity in the free SOL $\sigma_{\perp DC,f}$ normalized to the parallel Spitzer DC conductivity (1.7). Different amplitude are tried to account for the non-linear broadening in (6.4).

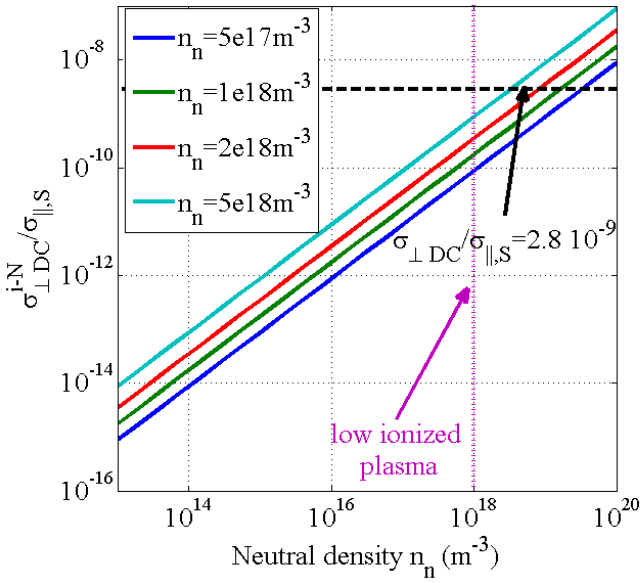

Figure 6.17: $\sigma_{\perp DC}$ normalized to $\sigma_{\parallel,S}$ versus the neutral density n_n (in m^{-3}) assuming that the transverse DC conductivity is entirely generated by friction between ions and neutrals.

The maximum transverse scale cannot be larger than the total radial SOL dimension (≈ 10 cm) as the main plasma is unperturbed. The same procedure gives the maximum allowed perpendicular DC conductivity $\sigma_{\perp DC,p,M}/\sigma_{\parallel,S} = 5.2\ 10^{-4}$ in the private SOL and $\sigma_{\perp DC,f,M}/\sigma_{\parallel,S} = 2.9\ 10^{-5}$ in the free SOL. They are represented on Figure 6.15 by black dashed and dotted lines. This gives a first large domain.

Let us see if we can reduce the surface of the domain with the analytic model in Section 6.2.4. The application of (6.4) is shown on Figure 6.16 for different $V_{DC,le}$ amplitude. To obtain the observed extension (3 ± 0.5 cm) with the measured maximum amplitude (150 ± 30 V) and $l_{\parallel_2} \sim 10$ m, (6.4) indicates that $\sigma_{\perp DC,f}/\sigma_{\parallel,S} = [0.8 - 2.1]10^{-8}$ is required. They are represented by green full lines on Figure 6.15.

The link between amplitude of the V_{DC} at the leading edge and conductivity has not been yet fully understood as well as its dependence with the parallel connexion length. Nevertheless a private perpendicular DC conductivity higher than in the free SOL is required. Then we know that $\sigma_{\perp DC,p}/\sigma_{\parallel,S} \geq 0.82\ 10^{-8}$, shown with a red dashed line on Figure 6.15, is required to create a significant DC currents circulation from the private SOL to the free SOL. This current circulation is saturating when DC currents are drawn from the entire radial extension of the private SOL (≈ 1 cm). It is represented by the blue dashed line on Figure 6.15. The average density in the private SOL is $\langle n_p \rangle = 7.6\ 10^{17}$ m^{-3}. It gives $\sigma_{\perp DC,p,sat}/\sigma_{\parallel,S} \approx 2.6\ 10^{-6}$).

These values of perpendicular DC conductivities cannot be explained invoking friction ion-neutrals alone ever when taking a low ionized plasma and a high neutral density (i.e. neutral density $n_n = 10^{18}$ m^{-3}). There is still at least one order of magnitude missing. Beyond collisions, they are also hard to explain with classical or neo-classical mechanisms. The most likely origin comes from anomalous transport [113].

6.2.6 Effect of unbalanced strap voltage on the distribution left/right of the heat fluxes on inner face of the lateral limiters

An original experiment was shown in Section 6.1.2 to balance the strap voltages since the right strap was positioned radially 4 mm behind the left strap. When changing the power balance on the generators to equalize the strap voltage, it was observed that the relative variation of the surface temperature T_{IR} of the antenna was evolving in opposite direction between the left side and the right side of the antenna. Both extremities of the same short field lines did not have the variation relative evolution when changing the power balance of the generators. This could not be explained by the variation of one integrated parameter such as $\int E_\parallel dl$ or any others. We then supposed that at least two independent parameters must be involved.

Let us now check, with the TOPICA/SSWICH-SW-2D procedure, if we can do better and reproduce then explain what is happening. Unfortunately we cannot at the moment reproduce the misalignment of both straps since the 4 mm mismatch is of the order of one element in TOPICA simulations (5 mm). TOPICA would thus see the straps as aligned with this kind of grids. We can however change the strap voltage balance. Instead of having V_{strap} on both straps, we thus have $V_{strap} \pm 15\%$ or $V_{strap} \mp 15\%$. It is thus equivalent at having a power balance on the straps 57%/43% and 43%/57% respectively. This test was only performed for one vertical position ($y = -0.2$ m), such as the situation illustrated on Figure 5.12. The $E_\parallel$ was computed in TOPICA with the CBSB FS geometry as it was on the antenna equipped with this FS that this was observed.

The simulation parameters were $T_e = 10$ eV, $T_i = 20$ eV, $V_{strap} = 30$ kV and $l_{\parallel,1} = 3.3$ m, $\sigma_{\perp DC,f}/\sigma_{\parallel,S} = 2.5\ 10^{-8}, \sigma_{\perp DC,f}/\sigma_{\parallel,S} = 2.5\ 10^{-6}, l_{\parallel,2} \approx 1.3$ m.

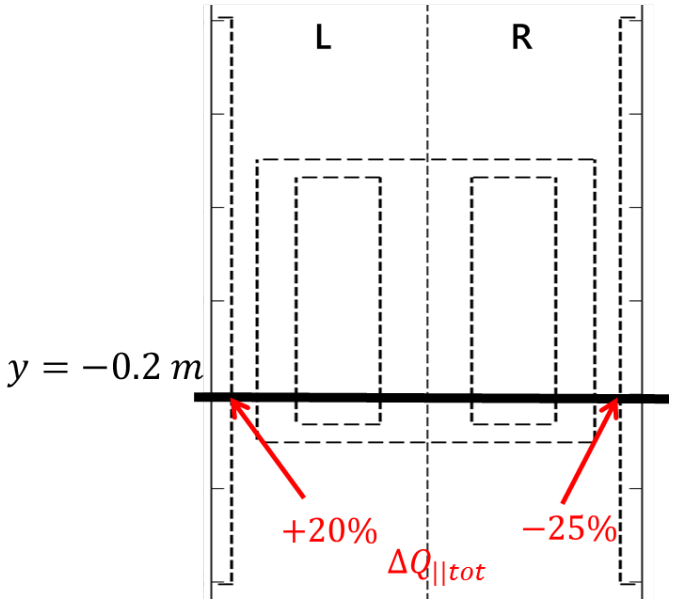

Figure 6.18: Comparison with TOPICA/SSWICH of the effect of unbalancing the strap voltages on the parallel heat fluxes evaluated on the inner side of the antenna side limiters.

The total heat fluxes were then evaluated on the inner face of the side limiters with (6.1) and (6.2). The evaluated heat fluxes were of the order of $2 - 2.5$ MW $\perp$ m^2, again within a factor 2 of the measured heat fluxes on the limiters. It results that unbalancing the strap voltage by +15%/-15% gives $\pm$20% variations on the heat fluxes deposited on the inner sides of the antenna limiters as shown on Figure 6.18. It corresponds qualitatively to the observations (see Figure 6.2). The left side that heats up during the power balance scan is also in the simulations the side that receives more parallel heat fluxes. This is due to subtle changes in the $E_{||}$ field map that induces slightly modifications in the biasing voltages V_b on left and on the right that are different. This is comparable to the situation in [54] where asymmetric drive can draw net DC currents. Moreover DC current flows are also allowed in the radial direction. It results in changes in the electronic heat fluxes (6.2).

6.2.7 Comparison of intermediate electrical designs of the antenna in order to identify the weak element in the CBSB FS

A direct comparison of the results with the two different Faraday screens has been performed. The simulations results correspond to the observations, at least qualitatively and relatively. There is however still some uncertainty on the quantitative values due to two main reasons: loosely constrained parameters and limited computational resources.

For given values of the effective transport coefficients in SSWICH, it was nevertheless found that the relative variation of simulation results for two input field maps was quite independent of the DC conductivity. The same is also true for the other simulation parameters, such as the parallel connexion length. This robust property allows relative comparisons between antenna designs, despite the sensitivity of quantitative results to DC current diffusion. A hierarchy in the designs can be established by comparing them with the same parameters ($\sigma_{\perp DC}$, $L_{||}$, $L_{\perp}$, etc...), assuming that the antenna design does not affect the transport coefficients.

With this setup, the two Faraday screen designs have been compared. A proposal in order to identify which element (or combination of elements) of the CBSB FS design

enhances the sheaths was to create hybrid electrical designs in between classical and CBSB FSs. In order to do this, we have identified the major electrical differences in the FS design between the classical screen and the CBSB screen. Of course, two main differences are already contained in the acronym. The differences in the electric design are:

1. the cantilevered bars that are not connected to the central septum,
2. the slotted frame with the, so-called, shark teeth,
3. the tilt of the bars not present on the CBSB screen, clearly visible when comparing Figure 2.14(a) with Figure 2.14(b),
4. the gap between FS bars related to the number of bars and their individual size.

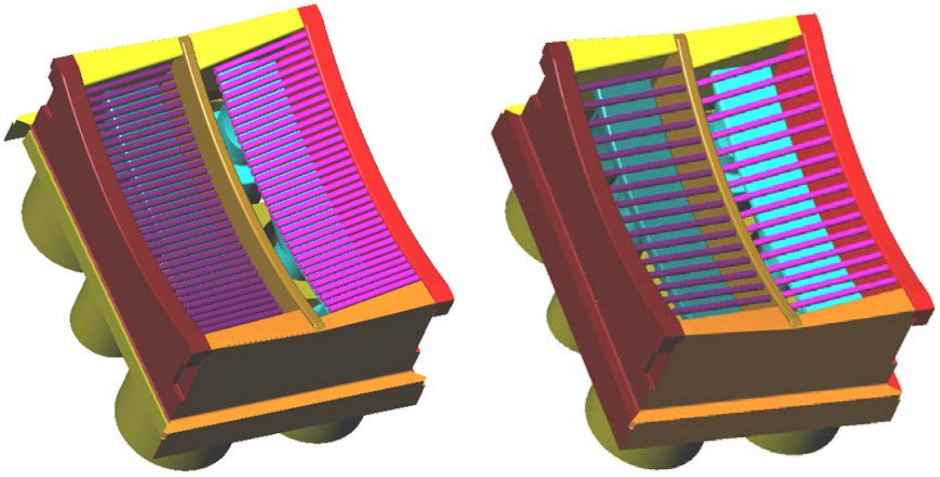

(a) (b)

Figure 6.19: 3D model of the hybrid geometry in between the classical FS and the CBSB FS implemented in TOPICA to identify the faulty element the difference. (a) classical screen with cantilevered FS bars and (b) classical screen with half the bars with constant gap between bars.

The first step consisted in creating a 3D model of the hybrid design starting from the classical screen as a reference where one element is modified at a time. It resulted in two hybrid geometries illustrated in Figures 6.19(a) and (b). The impact of the shark teeth was considered to be only local and for this reason was not studied. For the tilt of the bars, removing the tilt of the bars in the classical screen geometry would have been a long and painful process to ensure all proper electrical connections to the septum as not only the tilt has to be changed but also the bars parameters and positioning. Adding an electrical connection to the septum for the bars on the CBSB screen would have similarly encounter the same difficulties. Instead we kept identical the 3D models of the classical and the CBSB screens and we changed the tilt of the magnetic field in the TOPICA simulations. Instead of 7° tilt, -7°, 0° were enforced for the CBSB screen whereas it was 0° and 14° for the classical screen.

Simulations results show that reducing the number of bars (i.e. increasing the gap between bars) is marginal on the impact of RF sheaths on the DC plasma potential with the present version of SSWICH (see Figure 6.20(b)). The conclusion is identical for the tilt of the bars (see Figure 6.21(a)-(d)). It should be noted that high tilt (14°) increases

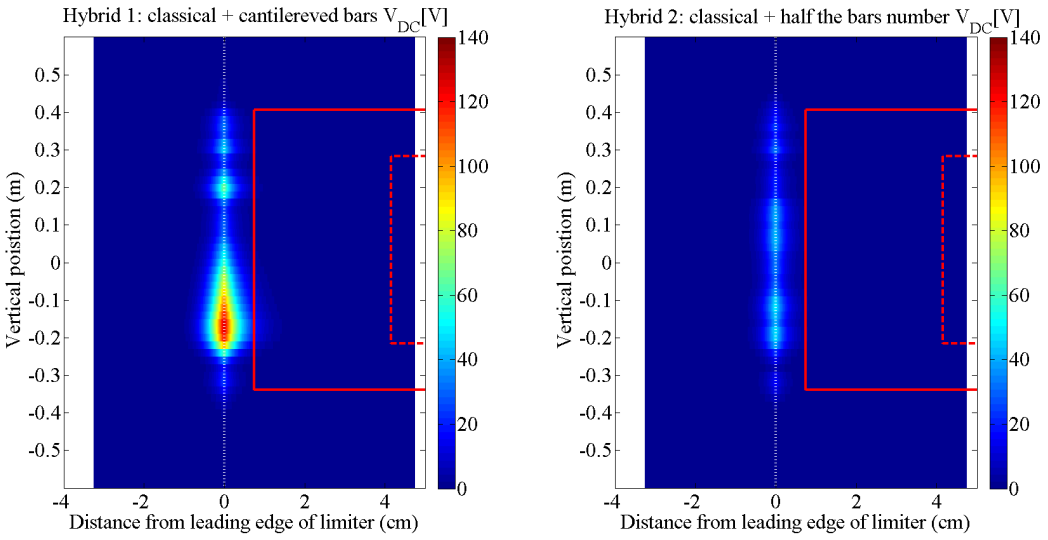

(a) (b)

Figure 6.20: 2D Map of the DC plasma potential V_{DC} obtained with SSWICH in the poloidal/radial plane at the position shown by dark dashed line in Figure 5.1(b) for hybrid electrical designs: (a) classical screen with cantilevered bars and (b) classical screen with half the bars number.

slightly the amplitude of V_{DC} for the classical screen (see Figure 6.21(b)). Some preliminary results with the asymptotic model only has however indicated a sensitivity to the density when looking at the impact of the tilt of the bars, especially at low density. Up to 20% difference has been evaluated. This would have to be confirmed and studied deeper with self-consistent version of SSWICH. The alignment of the bars with the magnetic field can only be perfectly realized for one plasma current value. Nevertheless, as it has been shown on Alcator C-Mod, the impurity content seems to be not directly correlated to the DC plasma potential [109, 190]. Moreover, it remains to be determined if the potential gain from the electrical point of view justifies the added mechanical complexity of the design.

Simulations however suggest (see Figure 6.20(a)) that creating numerically an hybrid configuration by cutting the bars on the classical screen enhanced greatly the RF sheaths in the vicinity of the antenna when the side limiters are also taken into account. This configuration gives results that are the closest to the CBSB Faraday screen for both the spatial topology and the amplitude of V_{DC}.

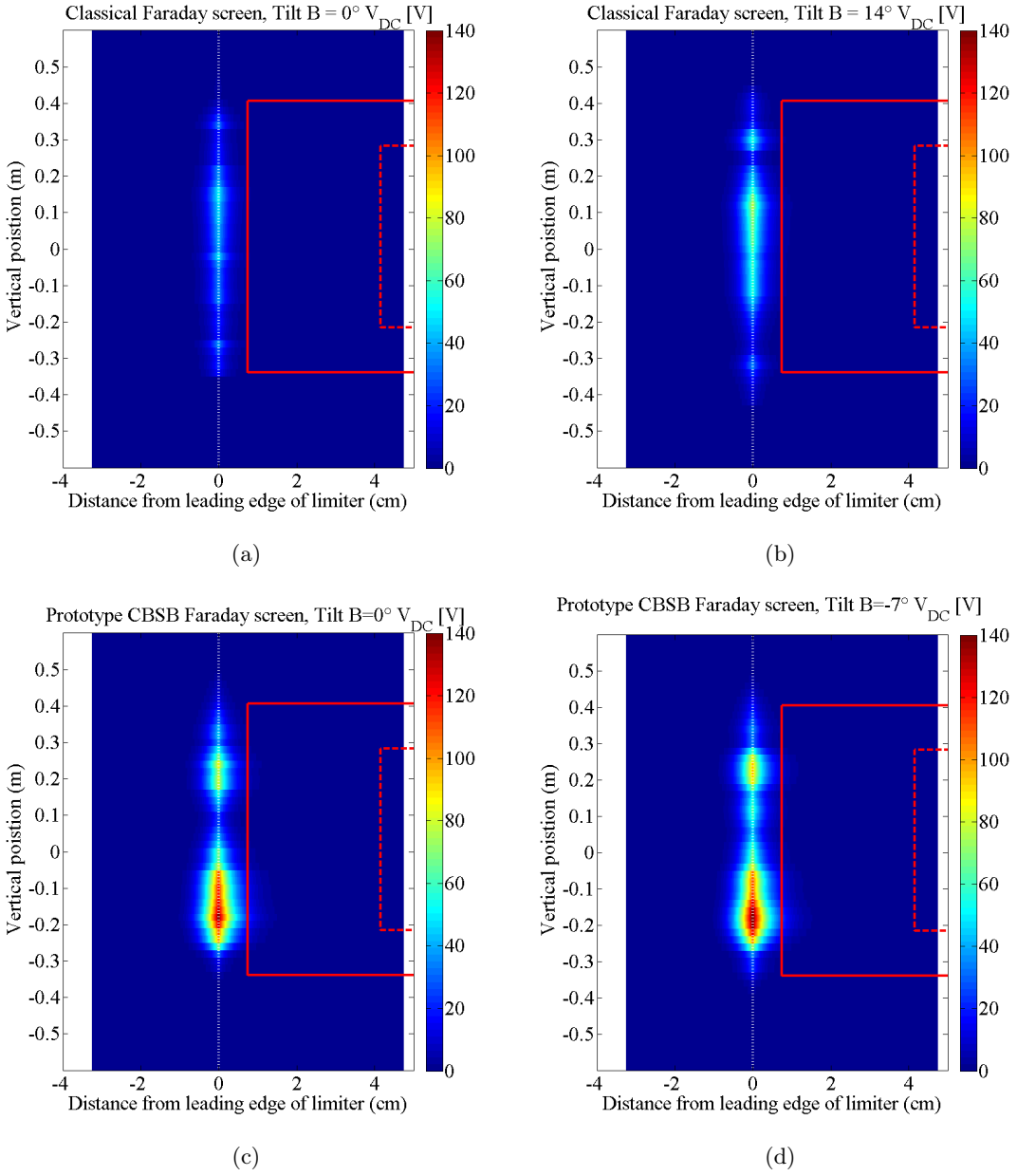

Figure 6.21: 2D Map of the DC plasma potential V_{DC} obtained with SSWICH in the poloidal/radial plane at the position shown by dark dashed line in Figure 5.1(b) when changing the tilt of the magnetic field for: (a) classical screen with 0° tilt, (b) classical screen with 14°, (c) CBSB screen with 0° and (d) CBSB screen with -7°.

6.3 Estimations of parallel heat fluxes on the blanket shielding modules (BSM) for ITER

In parallel to activities on Tore Supra, the IRFM institute is actively involved in the activities concerning the support the ITER design development and preparation for operations. Beyond the work for Tore Supra for the purpose of code validation against experimental observations and interpretation of observations, the formalism implemented in SSWICH was applied to ITER to estimate the parallel heat fluxes on the blanket shielding modules (BSM) that surround the ITER ICRH antenna (see Figure 6.22). Within only the asymptotic formalism exposed in Chapter 5 the RF wave propagation in the bounded SOL plasma is described self-consistently with the DC biasing of the SOL from both ends of open magnetic field lines. Pessimistic assumptions are made in terms of plasma parameters and BSM geometry in order to estimate an upper bound of the expected heat fluxes.

This section is intended to be remembered as preliminary work and estimations for the ITER ICRH antenna than as final results. Indeed due to lack of time and the complexity of the modelling an ICRH antenna bringing difficulties that will be further detailed, more work is required to refine the results. A lot of prospects can be contemplated to continue this preliminary estimations.

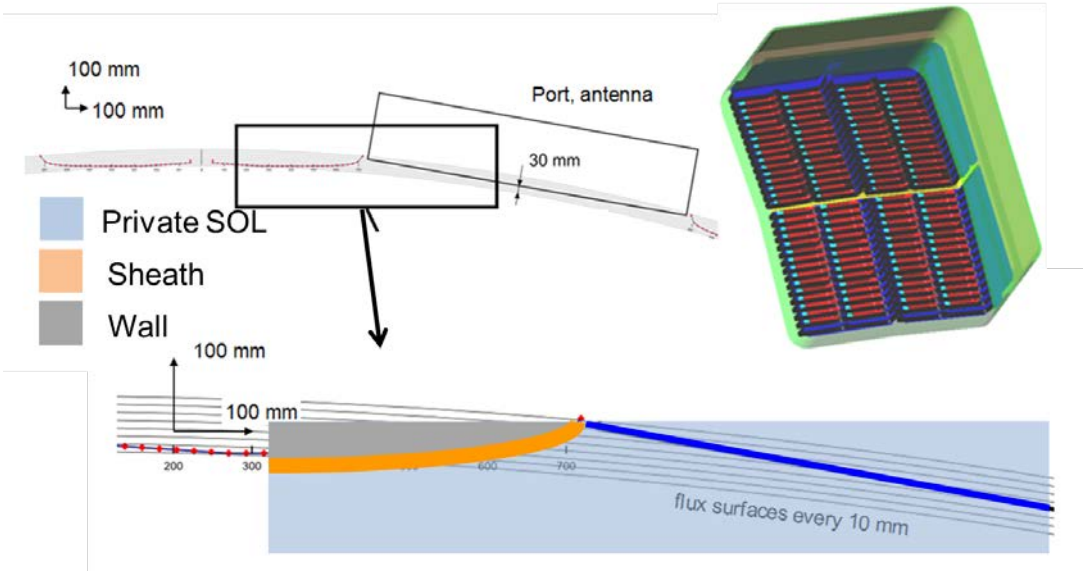

Figure 6.22: Geometry of the blanket shielding modules (BSMs) in ITER. On the top right is the ITER ICRH antenna composed of 4×6 straps.

6.3.1 Modelling of ITER ICRH antenna

The same procedure as for Tore Supra simulations was applied. As a first step in the simulation, near RF $E_{\|}$ field maps are produced using the TOPICA antenna code [31]. The TOPICA aperture represents the plasma edge. In order to remove any additional vacuum layer, the plasma edge is located 5 mm in front of the FS bars, following the V-shaped profile (both toroidally and poloidally) of the front part of the launcher. The complex RF field maps (real and imaginary parts) extrapolated from TOPICA to the reference radial plane are imposed at the SSWICH aperture, represented by a thick blue line in Figure 6.23 in order, to excite the sheaths.

The complex RF field maps are evaluated at the mid-band RF frequency $f_0 = 47.5$ MHz. They were normalized for 20 MW RF power coupled to plasma in matched conditions. The ITER antenna features a 6×4 phased strap array as seen on Figure 6.22. Five toroidal strap phasings were studied: $[0, \pi, 0, \pi]$, $[0, 0, \pi, \pi]$, $[0, \pi, \pi, 0]$, CD^+ and CD^-. The straps are grouped by triplets in the poloidal direction and the poloidal phasing between triplets is fixed at $\breve{}\pi/2$.

To be consistent, the plasma profile, the position of the plasma edge in front of the launcher and imposed coupled power to the plasma (20 MW) have been kept constant for both designs and for all five simulated phasings.

6.3.2 Simplified geometry of the BSM in SSWICH

The ITER ICRH antenna is surrounded by blanket shielding modules creating a private SOL around the ICRH launcher in the same way as the antenna limiters on Tore Supra (see Figure 6.22). The curvature of the BSM makes a realistic modelling of the geometry out of our reach at the present time since field line must be either parallel or perpendicular the walls. The main consequence is that the formalism cannot handle curved field lines connecting the Faraday screen bars to the BSM. Instead, the sheath-related parallel heat fluxes are estimates on the two BSMs, assimilated to flat plates normal to $\mathbf{B}$. The geometry of the ITER antenna was flattened in both toroidal and poloidal directions. Parallel heat loads of similar magnitude are expected in front of FS bars. For our estimates the simulation domain is restricted to a parallelepipedic zone representing the private SOL shadowed by the two BSMs surrounding the ITER antenna (see Figure 6.23). This zone is not parallelepipedic in a realistic geometry as shown in Figure 6.22.

Since the asymptotic treatment alone is adopted here and the simulation domain only consists in the private SOL between the BSM, the 3D parallelepipedic geometry is similar to the one shown in Figure 5.7 with different dimensions. The radial recess of the antenna behind the BSM modules, averaged over the antenna surface (i.e. 1 cm) is the radial depth $l_\perp$ of the private SOL. The sensitivity of the results to $l_\perp$ was studied in Ref [173]. In practice the TOPICA aperture extends over $l_{TOP} = 1.72$ m. Here $l_\parallel = 1.75$ m. The simulation results were moreover shown to be very sensitive to the gap between the lateral sides of the TOPICA aperture and the location of the walls [173]. The parallel connection

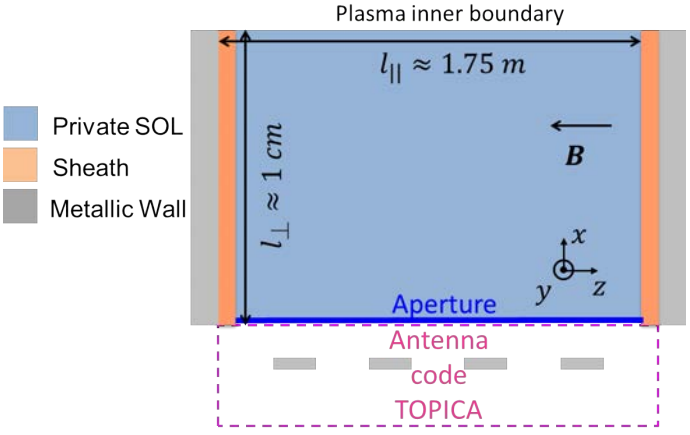

Figure 6.23: Simplified geometry of the BSMs for the sheath assessment with SSWICH. The aspect ratio was not preserved.

length $l_{\parallel}$ in the private SOL was thus chosen as small as possible, in order to minimize the toroidal gap to the lateral walls, thus providing "pessimistic estimates" for the RF-related heat loads.

6.3.3 Estimation of parallel heat fluxes

With the simplified geometry of the BSMs shown in Figure 6.23, a first run of simulations were performed within the asymptotic model framework. All five phasing were considered.

The local plasma in the private SOL is treated as homogeneous with $n = 210^{18}$ m^{-3}, $T_e = 10$ eV, $T_i = 20$ eV, $B = 3.93$ T and $\varepsilon_{\parallel} = -72182$ and $\varepsilon_{\perp} = -23.25$. For these parameters the slow wave is evanescent whatever the duplet $\left(k_{\parallel}, k_y\right)$. The DC plasma potential was evaluated with (5.20) and the parallel heat fluxes with (6.1) and (6.2)

For the "reference" sheath estimates, the field map were extrapolated in a reference radial plane located midway between the TOPICA aperture and the FS. The simulation results are summarized in Table 6.1 for the maximum of the oscillating sheath voltage on both sides, the DC plasma potential and the parallel heat fluxes on both sides.

The first thing that can be said is that we retrieve a similar hierarchy in toroidal phasing as for JET antennas [177]. The heat fluxes expected on both sides are similar. They are in the range $2 - 4$ MW/m^2. It should be nevertheless reminded that these results were obtained at the TOPICA aperture and extrapolated on the FS plane. Thus the impact of the SW evanescence is uncertain. Sensitivity study of the extrapolation length has shown high sensitivity on the results. For example an extra extrapolation of 5 mm (i.e. approximately at the FS location) has resulted in an increase of up to 50 % of $Q_{\parallel,max}$ [196]. Furthermore the simulations here were performed without any DC conductivity. Thus non-local effects are not included.

Phasing	$[0, \pi, 0, \pi]$	$[0, 0, \pi, \pi]$	$[0, \pi, \pi, 0]$	CD$^+$	CD^-
$\lvert V_{RF,l,max}\rvert$ (V)	319	560	413	265	692
$\lvert V_{RF,r,max}\rvert$ (V)	191	668	331	316	641
$V_{DC,max}$ (V)	313	658	406	311	683
$Q_{\parallel,l,max}$ (MW/m^2)	2.2	3.9	2.7	2.0	4.3
$Q_{\parallel,r,max}$ (MW/m^2)	2.0	4.1	2.5	2.2	4.1

Table 6.1: Summary of the sheaths properties with five toroidal strap phasings.

6.3.4 Difficulties for modelling the antenna and estimating heat fluxes on the BSM

These estimations are only preliminary as many difficulties appear when one to model and estimate the heat fluxes on the BSM. The first difficulty is related to the geometry that is quite complex. It was here greatly simplified assuming the worst case scenario when the fluxes are incident to the material surfaces and not spread over a larger surface with oblique incidence.

A second difficulty is due to the size of the huge antenna that makes it costly to simulate entirely. The mesh resolution is thus limited. On the $E_{\parallel}$ field maps produced by TOPICA, the near field structure looks dominated by small scale features hardly related to a particular element of antenna design. The variations with antenna phasing are also difficult to explain. This situation is specific of the "high-density target plasma" and is in contrast with the typical maps obtained at low density. In these circumstances, specific $E_{\parallel}$

field patterns can be clearly associated with the strap phasing, the different antenna boxes as well as the end of FS bars.

Moreover with our current resources, attempting to simulate the entire ITER antenna with the multi-2D procedure in SSWICH-SW-2D was not done due to the excessive time it would take. The RAM memory consumption would also be an issue as high mesh resolution is needed in the radial direction and the scaling between directions cannot be chosen arbitrary high. The mesh should also be able to resolve the effective transport scale of the DC currents. Finally the CPU time has to be shared with other tasks and others users. Despite these limitations, a few simulations have been performed in Comsol with finite DC conductivities at one vertical position for a phasing CD^{-}. With a homogeneous perpendicular DC conductivity, the heat loads remain in the range $3-4$ MW $\perp$ m^2 despite a variation over several orders of magnitude. The ion heat fluxes however were found to be decreasing with increasing perpendicular DC conductivity which might be beneficial to reduce sputtering.

Another difficulty is the number of possible toroidal phasings that render difficult a detail study on the parametric dependence which take lots of time. On top of this the design of the antenna is constantly changing, as it is still of course in the design phase. This renders difficult a follow up in the study as well as ascribing a result to a modification in the design or to the numerous parameters.

The results are, as for Tore Supra simulations, highly sensitive to loosely constrained parameters. The estimations on the heat fluxes are also highly sensitive to the density profile that is itself a prediction. As for Tore Supra, the field maps are not produced on the Faraday screen plane but a few millimeters in front of it. The field maps are thus extrapolated on the Faraday screen plane with an evanescence factor of the SW. Only detailed parametric scans can thus provide an accurate description of the situation to estimate the heat fluxes. The number of possible combinations is thus enormous.

All these difficulties related to uncertainties led us to take lots of cautions by assuming the worst case scenario. This could lead to overestimating the actual heat fluxes on the BSMs and consequently overestimating the necessary heat exhaust capability of the antenna cooling system.

6.4 Summary and Prospects

This chapter has first reviewed the major experiments results on Tore Supra during the test on plasmas of a prototype Faraday screen that was supposed to minimize the magnitude of RF sheaths. In reality, it was found unfortunately found that this Faraday screen enhanced RF sheaths.

SSWICH combined with TOPICA in the multi-2D procedure has been applied to Tore Supra to see if these unexpected observations could be unravelled by more advanced RF sheaths modelling. Key experimental observations have been reproduced with a novel modelling of RF sheaths in SSWICH. Enhanced magnitude of RF sheaths is found with the CBSB Faraday screen compared to the classical screen with SSWICH. The poloidal topology is a robust and invariant result that mainly depends on the electrical design but not on the numerous parameters. The radial topology is however greatly dependent on the simulations parameters whose some of them are loosely constrained. The radial topology on the outer face of the side limiter is also dependent on a mechanism to generate significant V_{DC}. One possible mechanism, proposed here, is a circulation of DC currents from the private SOL to the free SOL through an effective perpendicular DC conductivity higher in the private SOL than is the free SOL. For this feature to be valid, a higher turbulence level

in the private SOL needs to be postulated. A qualitative disagreement between experiments and simulations is on the radial position of the radial structure of V_{DC} that is found on the leading edge in the simulations but 2 cm behind in the experiments for the CBSB Faraday screen only. An explanation has been yet found.

Qualitative results have been correctly reproduced. Quantitative results however are highly dependent on the simulations parameters. Results for the parallel heat fluxes and DC plasma potential are nevertheless found in the correct range. Using the observations and a benchmarked analytical model of the transport of DC currents, a window of DC perpendicular conductivities compatible with the observations has been found. SSWICH combined with TOPICA has also found that strap unbalance can lead to changes in electron heat fluxes on the inner face of the side limiter.

These simulations results affirm that the lateral limiters should be accounted for in the RF sheaths assessment. The topology of the magnetic field lines are different with a limiter. Short field lines have to be distinguished from long field lines. It also implies that the more important RF sheaths consequences occur on short field lines connected to the lateral limiters, on the contrary to the assessment performed during the design phase of the CBSB FS [48] that only focused on long field lines. An investigation of the electrical design of the CBSB Faraday screen suggests that the cantilevered bars are the elements in the design enhancing the magnitude of RF sheaths and its spurious effects.

Preliminary results for ITER with the asymptotic model only have been performed in a worst case scenario basis assuming an overly simplified geometry of the blanket shielding modules normal to the field lines. Several antenna phasing were tested. Maximum heat fluxes of 5 MW $\perp$ m^2 are expected. More work is however required to study the impact of loosely constrained parameters on the predictions. This study will continue in parallel with the evolution of SSWICH to refine the estimations with more accurate ones. Tore Supra results could also be refined with newer version of SSWICH or with more realistic/constrained simulation parameters.

Conclusion

Heating the tokamak central plasma to fusion relevant conditions requires external heating systems such as RF systems. ICRH antennas, injecting into the plasma several MW of power, are commonly used in large tokamaks. To design an ICRH antenna able to couple efficiently and reliably large amount of RF power into a magnetized plasma for long pulses (or in steady state) in a metallic environment, it is necessary to understand the interactions between wave and the edge plasma: wave coupling and RF sheaths formation.

This PhD thesis aimed at proposing a common framework in which a sophisticated description of RF sheath formation in the vicinity of ICRH antenna in SOL of tokamak plasmas could be modelled self-consistently with wave coupling. Indeed, previous modelling and antenna design relied on the minimization of $\int \left| E_{\parallel} \cdot dl \right|$ from antenna codes without sheaths. This approach had some successes since the antennas do work and could explain some phenomena. But RF sheaths description was not self-consistent as they were only treated a posteriori of the calculation of the wave radiation pattern by the antenna with a crude rectification model. The design of the prototype Faraday screen [140] for Tore Supra with this approach on long field lines led to cutting the bars thinking that interrupting the path of parallel currents would reduce RF sheaths oscillations. Experiments prove the contrary as the magnitude of measured sheaths effects (heat loads, probe floating potentials) were significantly enhanced compared to the classical Faraday screen. Moreover the design of a field aligned antenna for Alcator C-Mod considering symmetry did not reduce the amplitude of the plasma potentials measured by emissive probes but still somehow lowered the impurity content (less sputtering). RF sheaths also have a feedback impact on the coupling properties on the antenna since the density can be locally modified changing the size of the evanescence layer in front of the antenna. The strap voltage for a constant coupled power thus also changes, in turn changing the amplitude of the RF sheaths. This problem should thus be treated ideally simultaneously and fully consistently. Due to the complexity of the problem, the limited resources and manpower and the three year limitations of this thesis, these two phenomena were however, modelled, for this first step, separately but in compatible approaches to anticipate the development of a single code combining both. Two codes were thus successfully developed during this thesis: one for fast wave coupling without sheaths and one for self-consistent RF sheaths formation and slow wave propagation.

The choice of modelling with the commercial software Comsol Multiphysics was made before the start of this thesis to ease the development strains. The multiphysics purpose and the finite element feature of Comsol make it easy to be used by numerous people and to model multiphysics problems such as these ones in complex geometries. It also gives the freedom of modifying the equations. Moreover the three years constrain on the duration of this thesis in addition with the requirement to provide physical relevant results did not give the freedom of writing a code. The counterpart is the impossibility to access the inner working of the equation solver and the limitation to run it on only one workstation as part

of the licence agreements.

The first code is modelling fast wave coupling to the plasma. It contains a full description of a cold plasma with anisotropic, gyrotropic and inhomogeneity properties in the dielectric tensor. Tore Supra ICRH antennas simplified geometries were implemented at the same time in 2D and in 3D. Realistic density and magnetic field radial profiles were included for the simulations. The fast wave being propagative above some critical density, the perfectly matched layer technique in frequency domain, commonly used for classical dielectrics, was implemented for magnetized plasmas to mimic single pass-absorption without numerical reflections of outgoing propagative waves. The PML concept relies on the transformation of the real space coordinates to complex stretched coordinates in the direction of absorption.

The PML was first tested on homogeneous plasmas with monochromatic plane waves. It was seen that low reflection could be achieved provided that the PML satisfies some constraints. First the PML is only perfectly reflectionless for the exact wave equation. Discretization inevitably induces some reflection. This phenomenon can be reduced by a finer mesh closer to the exact wave equation. Second no singularity should be present in the PML. Third the PML should not be placed next to a cutoff since it would significantly increase the numerical cost. For plane waves, a numerical formula tested against simulations indicates that the PML depth must be of the order value of the wavelength in the PML direction to have low reflection. Near a cutoff, the wavelength is huge, requiring a large PML. Fourth the current PML formulation cannot handle forward and backward waves simultaneously. This issue arises in some anisotropic media where several eigenmodes exist, whose group velocity vector is not collinear to the phase velocity. This issue can be resolved in our situation by letting the plasma reflect the evanescent SW above some critical density and thus placing the PML interface where the SW is extinguished and only the FW subsists. Fifth the PML should only be used with convex domains since once a wave enters the PML it should not be allowed to leave the PML or cross again the studied medium.

After checking that the reflection coefficient only defined for plane waves could be replaced by tracking the modulations of the coupling resistance, easier to obtain for spectrum of plane waves, the PML technique was implemented into a code to evaluate the coupling resistance of phased strap arrays. Simulations with Tore Supra antennas were compared to experimental measurements of the coupling resistance and to the TOPICA antenna code. The qualitative trends are correctly reproduced, but the magnitude is always overestimated by a factor 1.5-2 by both codes due probably to uncertainties on the actual size of the evanescence layer. The necessary degree of sophistication of the antenna geometry was also investigated: the strap thickness, the presence of passive antenna elements in addition to active elements.

TOPICA provides results closer to the experiments than this new wave coupling code, since the antenna geometry in TOPICA is much more detailed at the expense of the numerical cost. This FW coupling code however can provide a fair result within a minute in 2D. Very fine and numerous parameters scans can thus be considered before using TOPICA for accurate results on a few cases during the design phase of an antenna. This procedure is currently being used for the design of new ICRH antennas for WEST.

Improvements of the PML formulation should be considered to resolve the issue with simultaneous propagating forward and backwards waves. Handling the concave plasma curvature could very likely to be the harder issue to handle in order to simulate realistic plasmas. A more appropriate coordinate system than Cartesian coordinate can be contemplated.

This approach with PMLs and full plasma description is in principle compatible with the presence of a finite density inside the antenna box. Including RF sheath modelling into this code can therefore be contemplated for the future. There is however the ongoing issue on the way to cross the lower hybrid resonance.

The second part of the thesis objectives, carried on in parallel, consisted in developing an innovative model of the interplay, due to RF sheaths, of RF wave propagation and the resulting positive DC biasing of the edge plasma in the vicinity of an ICRH antenna. The model, called SSWICH, rests on previous works realized by Myra and D'Ippolito for sheath boundary condition and Lieberman for the description of the sheath capacitance. This model considers that some RF wave propagation effects occur on the rapid time-scale and the DC biasing of the plasma on the slow time-scale. The two time-scales are coupled together by the RF sheaths. The RF sheaths are seen as an electrical circuit composed of a capacitance and a diode in parallel. The RF effects acts only on the capacitance whereas the DC effects act only on the diode. That approach accounts for the rapidly varying RF electric field and the slowly varying electrostatic electric field responsible for zero order flows. However the density is treated up to now as being invariant poloidally and unchanged by the RF sheaths even if the radial gradient is accounted for. An equation (or system of equations) describing the evolution of the density over the slow time scale is missing. Moreover the plasma inductance and the sheath resistivity are neglected compared to the sheath capacitance. Keeping them as first order terms in the expansion could be beneficial. It would however break the association capacitance/displacement current/fast time scale on one side and diode/conduction current/ slow time scale on the other side.

The description of the slow time-scale in SSWICH is more rigorous than in previous models while still being coupled to the fast time-scale. An effective DC conductivity tensor is considered. The parallel DC conductivity is the usual Spitzer conductivity that allows flows of DC currents in the parallel direction in case of asymmetric biasing. An effective perpendicular DC conductivity is added in the description to allow exchange of DC currents between adjacent flux tubes and thus propagate the DC biasing. This choice was motivated by measuring during experiments significant DC currents flows when the antenna is active. The nature of transverse transport of DC currents is however most likely not diffusive but anomalous (turbulence). It cannot thus be described in principle with a conductivity. The perpendicular DC conductivity is nevertheless considered here as an effective phenomenological transport coefficient enough for a zero order description of the DC currents flows. The values found to agree with the experiments can only be explained with anomalous transport. It is thus likely that the nature of the transport of DC currents do not obey a Fick's law. An effective conductivity can thus only quantify a zero order approximation.

Moreover an investigation of the relevancy of a spatial dependence should be done. The transport could be modified by the presence of an antenna and the fact that it is active or not. The transport coefficient should in that case be described self-consistently with the rest of the model. A recent study with the code TOKAM-2D [197] on the impact of polarized probes in the ionic regime in the SOL has shown that the turbulence characteristics are not only modified locally near the probe but that oscillations occur also far away [198]. It was also observed that two probes have an asymmetrical mutual influence on each other.

Despite this more sophisticated description, SSWICH is still quite simple compared to the full complexity of the RF sheath formation. Significant improvements can still be added. Only the slow wave has been included until now. The fast wave would have to be included as well. It implies a way to handle outgoing propagative waves and describe fast wave coupling. This aspect will be provided by the perfectly matched layer technique

already implemented in the fast wave coupling code developed during this thesis. Including the fast wave will also induce mode conversion with the slow wave. It requires the full description of a cold plasma and provides another mechanism to generate significant DC plasma potential at the leading edge of the antenna side limiter. Another improvement would be to add a density equation in the model to account for transport of the density through convection cells in addition to transport of DC currents. This requires a 3D description of the full model. Local density inhomogeneity near the antenna are also triggered by a ponderomotive effect [199], that was also investigated in the context of non-linear coupling for LH [70]. To model fast wave coupling together with RF sheaths, a feedback at constant coupled power should also be developed to emulate the behaviour of the antenna experimentally and replace the present condition in SSWICH with a given strap voltage.

The geometry implemented in SSWICH accounts for the geometry the SOL in the vicinity of the antenna as well as the topology of the magnetic field lines due to the inclusion in the assessment of the side limiters that distinguish long field lines and short field lines. The geometrical description of the antenna environment, while more complex that what was done until now, is still far from the real one. More detailed objects shape and dimensions of the vicinity of the ICRH antenna would be a nice contribution. It goes in line with an arbitrary orientation of the magnetic field compared to the objects boundaries and the inclusion of the fast wave.

From this viewpoint, RF sheath models in cold plasma discharge benefits from a simpler geometry that can also be exactly known. The understanding of the mechanisms behind the formation of RF sheaths in plasma processing discharges is more advanced than in tokamaks. Other phenomena, included in plasma processing, such as secondary electron emission, sputtering, that has been neglected in tokamaks until now, should be studied as least sequentially to evaluate if they favour or not the magnitude of RF sheaths. Secondary electron emission (i.e. similarly to emissive probes) would a priori lower the sheath potential. Sputtering will add species in the plasma. The multi-species plasma would thus change the Bohm criterion for the ions. The description of sheaths in plasma processing is more advanced on these aspects, as explained in the following review paper [200]. If they favour the magnitude of RF sheaths, they must be included in the modelling for a worst case scenario. The underlying properties are the same. The power is however lower (kW) than in tokamaks (MW) even compared to the temperature (1 eV and 10 eV in the SOL of tokamaks). The RF excitation is also much different as it is a biasing electrode with a RF potential.

Nothing in the formalism a priori prevents modelling the far-field sheaths [92] with the near-field sheaths. The fast wave as well as arbitrary angles with the magnetic field is however missing. The biggest challenge, in my opinion, would be to handle the natural reflection of the fast wave coming from the main plasma due to low single pass absorption that can be caused for example by steep density gradient, improper minority concentrations in the plasma.

Improvements can also be performed on the computational resources consumption. The focus until now has been on obtaining a working model. For a given case, an optimization of the model to consume less memory and less CPU time can now be accomplished. The sheath oscillating module could be modelled in 1D along lateral boundaries instead of in 2D. The memory consumption would be thus reduced. Applying more sophisticated/refined solver options could lead to better computing performances and faster convergence. More robust numerical convergence scheme would also provide better performances and avoid the numerical instabilities related to the mesh or the interaction of the mesh with the sheath

boundary conditions sometimes encountered. Moreover the ever increasing computing power will allow more realistic cases to be run. These processes are necessary to go to a 3D description with more physics of the electrical behaviour of an ICRH antenna facing a magnetized plasma in realistic conditions.

One must not forget that one of the most important criterion of the success of a code is the user interface. On the way, a user-friendly interface for the code should also be considered. At some point, this code should become an engineer tool. The code should thus at that point be easy to parametrize in order to evaluate the heat fluxes, DC potentials, sputtering yield on the antenna. This code would provide the limits that an antenna should have to handle while facing a plasma and the electrical design, thermo-mechanical design defined accordingly.

SSWICH has been coupled with TOPICA in the cases of Tore Supra antennas. First some validation tests have been performed. The poloidal derivatives have been confirmed as negligible on first approximation. The dimensionality reduction to 2D is thus justified. A power scan has also proved that the asymptotic model can provide an accurate picture rapidly at high power. There subsists however still unknowns on the inner working of the coupled model. Only part of the model has been tested against simple models where analytic solutions exist. The starting point of the simulations has been changed to achieve convergence at high power with an asymptotic model. The entry point in the coupled convergence loop is thus different than at first thoughts. It also determines the solution branch on which the coupled model is initially starting the iterative loop. The possibility of multiple roots is still under examination. A possible study would be to check the multiplicity of the solutions when starting from high power regime and low power regime.

An extensive direct comparison between simulations and experiments has been performed for the first time. This has been made possible since realistic antenna geometries have been modelled and experimentally measured profiles have been input in SSWICH. Results can consequently be directly compared. Key experimental observations have been reproduced numerically and have good agreement with experiments. The more robust result is the poloidal topology of RF sheaths that is invariant with the simulation parameters and mainly determined by the electrical design of the antenna via the TOPICA field map. The maximum amplitude of the DC plasma potential is observed near the top and bottom of the antenna box structure, whereas the minimum is observed on the equatorial plane. An up-down asymmetry was recovered. The relative comparison of two Faraday screen designs tested on Tore Supra also corresponds to experiments. Decoupling the sheaths at both extremities of the same open field line was possible as both extremities on a field line in the private SOL evolve differently during the power balance scan on the straps. This is ascribed to the finite DC perpendicular conductivity and the asymmetric DC biasing of both extremities that introduces subtle changes in the electronic parallel heat fluxes.

One important result is that the lateral limiters influence the electrical behaviour of the antenna. Long field lines should be discriminated from short field lines in the SOL for future RF sheaths assessments. More globally the immediate environment of the antenna, that can modify the SOL properties in the vicinity of the antenna, should be accounted for. In general the magnetic connections of the antennas to neighbouring objects are asymmetric whereas for simplicity the geometry was considered as symmetric in this thesis.

Some other observations are still under examination. The radial position of the DC plasma potential structure was always found on the leading edge on the lateral limiter in the simulations whereas it was found for the CBSB screen only located behind by ≈ 2 cm in the experiments. This result was only observed once as for the classical screen on Tore Supra and probe measurements on other tokamaks the maximum is always found on the leading

edge as in the simulations. It remains until now unexplained. A possible explanation could be an unidentified mechanism shifting the structure of the DC plasma potential. Another possibility is that we are overestimating the confidence with which we are evaluating the magnetic connections of the probe on the limiter.

While the qualitative results are in good agreement with the experiments, the quantitative results are highly sensitive to loosely constrained simulation parameters, such as the effective perpendicular DC conductivity in the SOL of a tokamak. The parallel connection lengths are estimated in the range $10 - 15$ m on Tore Supra. Moreover the parallel heat fluxes are also highly dependent on the density and the temperatures. The density profile is assumed to be unchanged in front of the antenna with respect to the reflectometer, located far from the ICRH antenna. This is not the case in reality as the shadow of the different objects will change the magnetic topology in the SOL. Moreover a significant DC plasma potential amplitude will induce convective cells of the density in front of the antenna. This could also be partially linked to the numerical limits that do not allow us to simulate realistic connection lengths and perpendicular DC conductivities. This is why the quantitative values are hard to obtain and the confidence in their reliability is questionable. Nevertheless quantitative values are found in the correct range. Parallel heat fluxes are found for example within a factor 2 of the measured ones.

Comparison of simulation results with an analytic model of transport of DC currents in a four region geometry was successful. It gives insights on the inner working of SSWICH and proves that we have understood qualitatively the mechanism at work to generate significant DC plasma potentials in the free SOL. Circulation of DC currents from the private SOL to the free SOL is a possible mechanism to generate significant DC plasma potential on the outer face of the lateral limiters if an effective DC conductivity tensor with finite conductivities in both parallel and transverse directions is included in the model. Parametric analytic dependencies with the DC conductivity, density, the parallel connexion length (and other quantities) have also been identified and compared to simulations. Since the quantitative value for the DC plasma potential given by simulations are highly sensitive to loosely constrained parameters, we reversed the procedure. Instead of guessing the "correct" value for the DC conductivity in both regions, we looked for a window of perpendicular DC conductivity values consistent with the experiments data on the width and amplitude of the DC plasma potential structure. Since realistic parameters cannot be simulated due to computing capabilities limitations, the analytic model of transport of DC currents was used instead. It gave at the end a domain of conductivities compatible with the amplitude and the broadening of the DC plasma potential structure measured during the experiments with probes. It would have to be checked experimentally. The domain of perpendicular DC conductivities found cannot be explained invoking a collisional process.

State of the art 2D probe mapping of the floating potential and the ion energy and infrared systems looking at the antennas are available on Tore Supra. This made of Tore Supra, in my opinion, one of the best devices presently to study RF sheaths. The free SOL on Tore Supra benefits thus of a good characterization. These measurements have allowed benchmarking some features of SSWICH at least qualitatively and relatively when comparing two Faraday screens. Despite the quality of these diagnostics, the properties of the private SOL, essential for the quantitative results even in the free SOL, remain largely unknown. As an example, probes cannot be magnetically connected to the private SOL due to the presence of the limiters. The only informations are indirect through the infrared cameras that are difficult to link to the evolution of several parameters simultaneously and from DC currents measured when the antenna is active. Moreover the radial resolution is limited by the line of sight of the camera. The metallic impurity content of the plasma

when the antenna is active is different. This is however difficult to link to one parameter or to one region of the antenna. The density and the temperature in the private SOL are almost unknown. They have been, until now, defined through analytic considerations. The connexion lengths in the SOL are approximately known, but more accuracy would be useful.

It has to be conceded that measuring the properties of the private SOL is not an easy task. More efforts should however be devoted to provide more informations to characterize more accurately RF sheaths and the SOL plasma in the private SOL and to obtain an estimation of the loosely constrained parameters. Besides linking measurements in the free SOL with measurements in the private SOL would provide a better interpretation of the present observations. To address at least partially this issue, it is proposed to install a reflectometer(s) on the antenna itself in ASDEX Upgrade [191] and WEST [19]. The density could be thus measured in between the antenna limiters. Another possibility is a direct measurement of the electric field in the sheaths with a spectrometer [193]. The main issues are the signal/noise ratio and the resolution of the spectrometer. The ion velocity distribution in the sheath could be measure by Laser Induced Fluorescence [201]. It remains to be seen if these diagnostics are compatible with tokamak usage.

This would reduce the discrepancy in the quantitative values and would require fewer simulations as the value of the parameters would be known within a more restrain domain. Moreover a more extensive database for several machines with very different plasma parameters and different antenna designs should be constituted to test the models and the relevancy of new additions in the models. It would provide precious informations to understand the level of sophistication in the physics ingredients needed to obtain an accurate description of RF sheaths, discriminate the models and justify a posteriori the choices made in the model development. With several antenna designs, a relationship between the electrical design and the sheaths properties could be established. Moreover it would provide a guideline for the development of the models to privilege some ideas and save development time. Small devices dedicated to the study of RF sheaths such as ALINE or ISHTAR are sorely needed to bring progress to the description of RF sheaths as it will be easier to obtain data than on larger tokamaks in dedicated experiments with a limited number of pulses such as Tore Supra, JET or ASDEX-Upgrade where some parameters are moreover unknown (perpendicular DC conductivity, temperature ion and electron and density in private SOL). However SSWICH and other models should be tested and benchmarked in the meantime on several machines to bring universality in the description of RF sheaths. While waiting for more data to be produced, my personal opinion would be to compare codes, as a first step, on a common case, that has still to be defined. Collaboration would thus be facilitated.

Despite the uncertainty of the quantitative values, the TOPICA/SSWICH procedure has already been applied to preliminary estimations for ITER. These results should however consider really carefully: the magnitude is uncertain as a lot of assumptions are made about the plasma parameters. However the assumed geometry is a worst case scenario with incident heat fluxes. These results are more indicative than predictive in the magnitude. However the relative comparisons are more reliable if the same parameters can be assumed for the comparison of different electrical designs. This was assumed to be the case and it suggested that the cantilevered bars on the CBSB Faraday screen on Tore Supra are the guilty elements in the electrical design for the enhancement of the magnitude of RF sheaths. The same procedure could be used to guide the design of future antennas during the conception phase (such as the Faraday screen for the WEST antennas) by looking at the relative evolution of the results.

There was not enough time during this thesis to couple together the FW coupling code and the RF sheaths code. This would constitute the topic of another PhD. The goal then would be to simulate self-consistently the RF sheaths with the feedback on FW coupling for a constant coupled power to the plasma that was exposed as a possible prospect for improvement of SSWICH-SW-2D. This, if achievable, would render more reliable the quantitative predictions made with the code and more strongly guide the antenna design. Including a convective model of density transport is also considered for this new PhD thesis. Simulating in 3D a model containing more physical ingredients and a more realistic geometry of the region in the vicinity of the ICRH antenna (including oblique RF sheath physics) with realistic plasma parameters will require more computing power. Antenna matching could also be added.

Appendix A

Error between exact solution and PML solution in the semi-infinite problem

$\hat{E}_{PML}\left(t_x, k_y, k_\parallel\right)$ is the analytical solution of the semi-infinite problem with the domain plasma + PML + PEC written using (3.20), (3.21) and (3.22).

$$\begin{aligned}\hat{E}_{PML}\left(t_x, k_y, k_\parallel\right) &= \frac{1}{1-\eta}\hat{E}_0\left(k_y, k_\parallel\right)\left[\exp\left(ik_x t_x\right)\right. \\ &- \left.\eta\exp\left(-ik_x t_x\right)\right]. \end{aligned} \tag{A.1}$$

To further quantify the error made when using PMLs, let us now evaluate the difference $\hat{E}_{PML}\left(t_x, k_y, k_\parallel\right) - \hat{E}_{exact}\left(x, k_y, k_\parallel\right)$ in the main simulation domain given respectively by (3.20) and (3.17):

$$\hat{E}_{PML}\left(t_x, k_y, k_\parallel\right) - \hat{E}_{exact}\left(x, k_y, k_\parallel\right) = \frac{2i\eta}{1-\eta}\sin\left(k_x x\right)\hat{E}_0\left(k_y, k_\parallel\right), \tag{A.2}$$

The infinite norm is now taken:

$$\begin{aligned}\left\|\frac{\hat{E}_{PML}\left(t_x, k_y, k_\parallel\right)}{\hat{E}_{exact}\left(x, k_y, k_\parallel\right)} - 1\right\|_\infty &= \max\left(\left|\frac{2i\eta}{1-\eta}\frac{\sin\left(k_x x\right)}{\exp\left(ik_x x\right)}\right|\right)_{x\in[0;L_1]} \\ &= \left|\frac{2\eta}{1-\eta}\right|\max\left(\left|\frac{\sin\left(k_x x\right)}{\exp\left(ik_x x\right)}\right|\right)_{x\in[0;L_1]} \end{aligned} \tag{A.3}$$

The maximum relative error for propagating waves (real k_x) over the main simulation domain is bounded by:

$$\left\|\frac{\hat{E}_{PML}\left(t_x, k_y, k_\parallel\right)}{\hat{E}_{exact}\left(x, k_y, k_\parallel\right)} - 1\right\|_\infty < \left|\frac{2\eta}{1-\eta}\right|. \tag{A.4}$$

A similar analysis can be done for evanescent waves ($k_x = i\left|k_x\right|$). It thus reads, provided $2|k_x|L_1 >> 1$:

$$\left\|\frac{\hat{E}_{PML}\left(t_x, k_y, k_\parallel\right)}{\hat{E}_{exact}\left(x, k_y, k_\parallel\right)} - 1\right\|_\infty \approx \left|\frac{\eta}{1-\eta}\right|\exp\left(2\left|k_x\right|L_1\right). \tag{A.5}$$

Appendix B

Analytic link between reflection coefficient and Poynting vector in the case of a plane wave

This appendix is devoted to show the full demonstration of the formal analytic relationship between oscillations in the radial component of the Poynting vector and reflection coefficient in the case of radial propagation of a plane wave with the polarization of the fast wave. The electric field with both incident and reflected waves reads:

$$\mathbf{E}\left(x, k_{\parallel}, k_y\right) = \left[\mathbf{E}^{+} \exp\left(ik_x x\right) + \mathbf{E}^{-} \exp\left(-ik_x x\right)\right] e^{ik_z z + ik_y y}. \tag{B.1}$$

As in the ICRH applications, the fast wave carries the RF power to be deposited in the plasma, it will be the one treated. The electric field of a wave can thus be rewritten by factorizing by the y component as:

$$\mathbf{E} = E_y \begin{pmatrix} i\alpha \\ 1 \\ i\beta \end{pmatrix}, \tag{B.2}$$

where [58]

$$\begin{aligned} \alpha &= \frac{E_x}{E_y} = \frac{\varepsilon_X}{\varepsilon_\perp - n_\parallel^2}, \\ \beta &= \frac{E_z}{E_y} = -\frac{\varepsilon_\parallel}{n_\parallel n_\perp}, \end{aligned} \tag{B.3}$$

with α and β real numbers. $\bar{\bar{\mu}} = \bar{\bar{1}}$ is assumed for the sake of simplicity, so $\mathbf{B} = \mu_0 \mathbf{H}$. The total magnetic induction vector yields assuming a plane wave:

$$\mathbf{H} = \mathbf{H}^{+} + \mathbf{H}^{-} = \frac{c}{\mu_0} \mathbf{n}^{+} \times \mathbf{E}^{+} + \frac{c}{\mu_0} \mathbf{n}^{-} \times \mathbf{E}^{-} \tag{B.4}$$

where the incident (index $+$) and reflected wave (index $-$) propagate in opposite radial directions:

$$n^{+} = \begin{pmatrix} n_x \\ n_y \\ n_z \end{pmatrix}, \; n^{-} = \begin{pmatrix} -n_x \\ n_y \\ n_z \end{pmatrix}. \tag{B.5}$$

The total electric field and magnetic induction yields:

$$\mathbf{E} = \mathbf{E}^{+} + \mathbf{E}^{-} = E \begin{pmatrix} i\alpha \\ 1 \\ i\beta \end{pmatrix} \tag{B.6}$$

and

$$\mathbf{H} = \frac{c}{\mu_0} \begin{pmatrix} in_y\beta E - n_\parallel E \\ in_\parallel \beta E - in_x \beta F \\ n_x F - in_y \alpha E \end{pmatrix}, \tag{B.7}$$

with

$$\begin{aligned} E &= E_y^+ + E_y^-, \\ F &= E_y^+ - E_y^-. \end{aligned} \tag{B.8}$$

The time average Poynting vector is defined as:

$$\mathbf{P} = \frac{1}{2} \Re \left(\mathbf{E} \times \mathbf{H}^* \right). \tag{B.9}$$

The relationship between the total electric field and the incident electric field reads:

$$E_y = E_y^+ \left(1 + \eta e^{i\varphi} \right), \tag{B.10}$$

where η is the reflection coefficient and φ the phase between incident and reflected waves. Together they form the complex reflection coefficient $\Gamma \equiv \eta \exp(i\varphi)$.

Combining (B.7) and (B.8) in (B.9) yields:

$$\mathbf{P} = \frac{\varepsilon_0 c}{2} \Re \begin{pmatrix} n_x \left(1+\beta^2\right) EF^* - n_\parallel \alpha\beta EE^* + in_y \alpha EE^* \\ n_y \left(\alpha^2+\beta^2\right) EE^* - in_\parallel \beta EE^* - in_x \alpha EF^* \\ n_\parallel \left(1+\alpha^2\right) EE^* - n_x \alpha\beta EF^* + in_y \beta EE^* \end{pmatrix}, \tag{B.11}$$

with

$$\begin{aligned} EE^* &= \left|E_y^+\right|^2 \left[1 + 2\eta\cos\left(2k_x x - \varphi\right) + \eta^2\right], \\ EF^* &= \left|E_y^+\right|^2 \left[1 - 2i\eta\sin\left(2k_x x - \varphi\right) - \eta^2\right]. \end{aligned} \tag{B.12}$$

Only the radial component is of interest. The radial component of the time average Poynting vector P_x thus yields:

$$P_x = \frac{\varepsilon_0 c}{2} \Re \left[n_x \left(1+\beta^2\right) EF^* - n_\parallel \alpha\beta EE^* + in_y \alpha EE^* \right]. \tag{B.13}$$

The imaginary terms disappear and (B.13) gives:

$$P_x = \frac{\varepsilon_0 c}{2} \left|E_y^+\right|^2 \left[n_x \left(1-\eta^2\right) - \beta\alpha n_\parallel \left(1 + 2\eta\cos\left(2k_x x - \varphi\right) + \eta^2\right) + \beta^2 n_x \left(1-\eta^2\right) \right]. \tag{B.14}$$

For the fast wave, a common choice is to consider $\beta \to 0$. This means that the fast wave electric field has a very low parallel component. (B.14) gets further simplified:

$$P_x = \varepsilon_0 c \frac{\left|E_y^+\right|^2}{2} n_x \left(1-\eta^2\right). \tag{B.15}$$

Since a homogeneous plasma is considered for a plane wave, the radial component of the Poynting vector is conserved when moving radially. The subscript 0 denotes a quantity at $x = 0$. We take the poloidal electric field E_y imposed at the position $x = 0$. Multiplying (B.10) by its complex conjugate yields:

$$\left|E_{y_0}\right|^2 = \left|E_{y_0}^+\right|^2 \left(1 + 2\eta\cos\left(\varphi\right) + \eta^2\right). \tag{B.16}$$

Combining (B.16) with (B.15) gives the final expression:

$$P_x = \varepsilon_0 c \frac{\left|E_{y_0}\right|^2}{2} n_x \frac{1-\eta^2}{1 + 2\eta\cos\left(\varphi\right) + \eta^2}. \tag{B.17}$$

Oscillations of the radial component of the Poynting vector are following the evolution of the reflection coefficient and the phase between incident and reflected wave. The cosine can change sign in the denominator, thus giving a damped oscillatory behaviour of the coupled power as the reflection coefficient η approaches unity.

One unknown remains in (B.17): the phase between incident and reflected waves. It can be evaluated by the following way. The two waves can interfere constructively and the resulting amplitude E_{max} is the sum of their amplitudes:

$$E_{max} = E^{+}\left(1+\eta\right). \tag{B.18}$$

At $x = 0$, (B.1) becomes:

$$\mathbf{E_0} = \mathbf{E_0^{+}} + \mathbf{E_0^{-}} = \mathbf{E_0^{+}}\left[1+\eta\exp\left(i\varphi\right)\right]. \tag{B.19}$$

Keeping only the poloidal component yields: At $x = 0$, (B.1) becomes:

$$E_{y_0} = E_{y_0}^{+} + E_{y_0}^{-} = E_{y_0}^{+}\left[1+\eta\exp\left(i\varphi\right)\right]. \tag{B.20}$$

The square of (B.20) reads:

$$\left|E_{y_0}\right|^2 = \left|E_{y_0}^{+}\right|^2\left[1+2\eta\cos\left(\varphi\right)+\eta^2\right]. \tag{B.21}$$

Combining (B.18) in (B.21) yields:

$$\left|E_{y_0}\right|^2 = \frac{\left|E_{max}\right|^2}{\left(1+\eta^2\right)}\left[1+2\eta\cos\left(\varphi\right)+\eta^2\right]. \tag{B.22}$$

Finally the cosine of the phase can be expressed as:

$$\cos\left(\varphi\right) = \frac{1}{2\eta}\left[\left(1+\eta\right)^2\frac{\left|E_0\right|^2}{\left|E_{max}\right|^2} - 1 - \eta^2\right]. \tag{B.23}$$

$\cos\left(\varphi\right)$ can thus be evaluated by looking at the electric field at $x = 0$, the maximum of the electric field E_{max} and the amplitude of the reflection coefficient η. Alternatively, $\cos\left(\varphi\right)$ could be determined by looking at the spatial location of the maximum of the amplitude of E_y, corresponding to $2k_x x + \varphi = 2n\pi$.

Appendix C

Non-linear DC plasma potential diffusion analytical model with a DC conductivity tensor in a simplified 4 regions geometry

C.1 Outline of the 4 regions model

This appendix treats only analytically the DC part of the more general SSWICH model. To provide insights into the SSWICH model in Tore Supra geometry, a simplified situation is considered where analytical solutions exist, as illustrated by Figure C.1. Due to limited computational resources, some sets of parameters are either taking too much simulations time or either require too much memory. For that reason, an analytical model benchmark against simulations would be useful to extrapolate to what is happening in these cases out of our present reach. Such a model could also permit to evaluate the impact of future refinements on the limiter geometry and the accuracy of a simulation at the border of numerical stability. Moreover an analytical model takes much less time and resources to solve and offers a good opportunity to test if the physical mechanisms have been correctly modelled and understood.

As in Section 5.1, the magnetic field lines are either perpendicular or parallel to the boundaries. The domain (see Figure C.1) is constituted of four regions: the private SOL of an ICRH antenna (region 0), the inner free SOL (region 1) and two outer free SOLs (region 2 and 3) on both toroidal sides of the antenna limiters. x is the radial direction and z is the parallel direction. Region 0 radially extends from $x = 0$ to $x = L_\perp$, whereas region 1 spans from $x = -\infty$ to $x = 0$ and region 2 and 3 from $x = 0$ to $x = +\infty$. The four regions are connected in $x = 0$.

Each region denoted by the subscript $k = 0, 1, 2, 3$ is characterized by three essential parameters assumed constant:

- the parallel connection length $l_{\parallel,k}$ of the open magnetic field lines,
- a transverse DC conductivity for the DC current $\sigma_{\perp DC,k}$,
- a density n_k.

The geometry is not assumed symmetrical on both sides of the antenna. In reality, the topology of magnetic field lines in the SOL is rather complicated, as some objects are

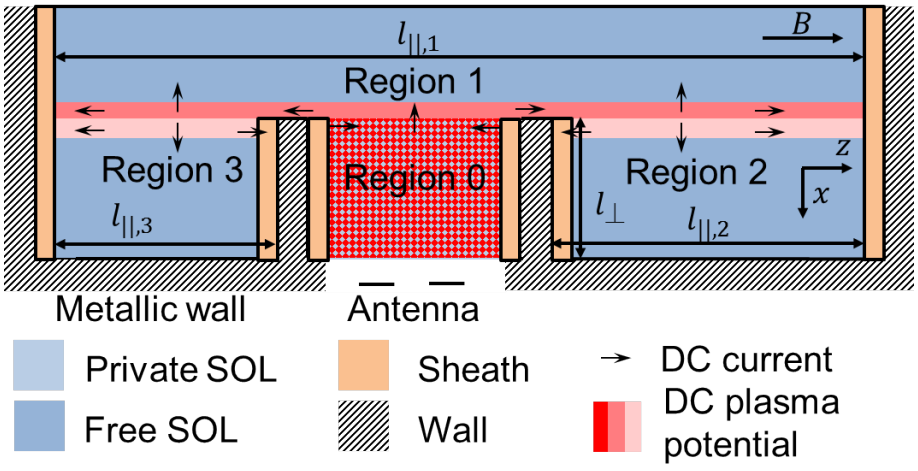

Figure C.1: Sketch of the 4 regions geometry and main notations in a 2D radial/toroidal plane. The levels of blue are indicative of the plasma density. The levels of red are indicative of the intensity of the DC plasma potential. The black arrows indicate a circulation of DC current from the private SOL to the free SOL.

magnetically connected to others on one side but not one the other side. Moreover, as the objects can be moved relatively to others, the connexion lengths are also modified. This model aim at understanding the SOL behaviour in the vicinity of the leading edge of the side limiters $x = 0$. The analytic treatment will in practise consider homogeneous regions with the radial average density in each region. For example, the ICRH antenna on Tore Supra can be connected to an LH antenna.

To ease calculations the transverse DC conductivity is treated here as via Ohm's law, but its value is adjusted so that it can reproduce the characteristic transverse length for the DC current associated with the physical mechanisms [112] (friction with neutrals, viscosity, inertia) briefly exposed in Section 2.3.4. With these parameters as well as the ion and electron temperatures T_i and T_e (assumed constant over the entire domain), a transverse diffusion length for the DC plasma potential can be defined:

$$\lambda_{j,k}^2 = \frac{l_{\|,k}\sigma_{\perp DC,k}k_B T_e}{2ej_k^+}, \tag{C.1}$$

where j_k^+ is the ion saturation current in the region k defined by (2.42). The factor 2 accounts for the two sheaths at both extremities. The radial size of the region coloured in level of red thus depends on the corresponding transverse diffusion length.

This analytical model assumes that the DC bias of the I-V sheath characteristics (due e.g. to RF oscillations) mostly exist in the private SOL of the antenna. In the private SOL, due to sheath rectification of intense near RF fields, the walls (grounded in practice) are assumed to behave as if they were biased to a potential V_b as explained in Section 2.3.2.2. For the sake of simplicity V_b is assumed homogeneous over the two sides of region 0. It is supposed that this wall biasing is present only in the private SOL, i.e. in the free SOL the two toroidal extremities of the open field lines are assumed to be connected via sheaths to electrically grounded walls. This is the reason why the level of red is shown as darker on Figure C.1. The wall biasing V_b is assumed to perturb the entire SOL by being transferred to the SOL DC plasma potential V_{DC} via the circulation of DC currents between the several regions allowed by a finite DC conductivity tensor with elements in the parallel and in the

perpendicular directions.

If the perpendicular DC conductivity in the private SOL is large enough, so the transverse diffusion length in the private SOL is larger than the radial depth of the private SOL $l_\perp$, then the entire private SOL is drawing transverse currents that can flow in the free SOL.

Assuming that no volumic charge exist and stationnary state, the charge conservation reads $\nabla \cdot J = 0$. In order to simplify the problem, in each region it is supposed that the plasma potential is homogeneous toroidally (flute assumption in z direction). Truthfully the assumption is not exactly satisfied since a small toroidal inhomogeneity in the plasma potential is needed to create parallel currents connecting the regions together with the large parallel Spitzer conductivity ((1.7)). The third direction (poloidal in a tokamak) is also ignored. The situation can thus be seen as a tube with finite width of DC current just in front of the antenna limiter distributing current from the private SOL to the free SOL. The balance of DC currents inside each region individually reads:

$$j_{sh}(x) = l_{\parallel,l}\sigma_{\perp,k}\partial_{xx}^2 V_{DC,k} = j_k^+ \left[1 - \exp\left(e\frac{V_{b,k} + V_f - V_{DC,k}(x)}{k_B T_e}\right)\right], \tag{C.2}$$

with the biasing voltage defined as:

$$V_{b,k} = \begin{cases} V_b & \text{if } k = 0, \\ 0 & \text{if } k = 1, 2, 3. \end{cases} \tag{C.3}$$

As in Section 5.1, the current in the sheath is assumed to be saturating when the sheath vanishes. This brings a maximum value of the electronic contribution (exponential term in (C.2)) given by (5.11). (C.2) is an approximation of the vorticity equation [43] with the vorticity $\Omega = \nabla_\perp^2 \phi$. Moreover the convective term in the vorticity equation $v \cdot \nabla\Omega$ is approximated by $\sigma_{\perp DC,k}\Omega$. The convective non-linearity is neglected. However the sheath non-linearity on the right hand side of (C.2), associated with the Boltzmann factor, is retained. Normalized quantities are defined as:

$$\phi_k = e\frac{V_{DC,k} - V_f}{k_B T_e}, \qquad \phi_b = \frac{eV_b}{k_B T_e}. \tag{C.4}$$

It simplifies the expression of (C.2):

$$\lambda_{j,i}^2 \phi_i'' = 1 - \exp(\phi_b - \phi_i), \tag{C.5}$$

where prime denotes the derivative with respect to x. In the geometry described by Figure C.1, the DC plasma potential in the free SOL has a peak centered on $x = 0$ in the radial direction. The aim in the following is to characterize analytically in a simple manner the amplitude and the radial broadening of the peak in each region as well as the dependence on the parameters ($\lambda_{j,k}$, ϕ_b, $l_\perp$, $\sigma_{\perp DC,k}$,...).

C.2 DC plasma potential radial variation in the private SOL

Let us start by looking at the private SOL (region 0). The differential expression given in (C.5) for region 0 (private SOL)is rather complicated:

$$\lambda_{j,0}^2 \phi_0'' = 1 - \exp(\phi_b - \phi_0). \tag{C.6}$$

The outer boundary of the private SOL in $x = L_\perp$ is supposed electrically insulated. The enforced boundary condition thus reads:

$$\phi_0^{'}\left(x = L_\perp\right) = 0. \tag{C.7}$$

Integrating (C.6) with the boundary condition (C.7) yields:

$$\lambda_{j,0}^2 \phi_0^{'}\left(x = 0\right) = -\int_0^{L_\perp} \frac{j_{sh}\left(x\right)}{j_0^+} dx = -L_\perp \frac{\langle j_{sh} \rangle}{j_0^+} \tag{C.8}$$

(C.6) can nevertheless be solved analytically in the linear regime. Linearising (C.6) yields:

$$-\lambda_{j,0}^2 \partial_{xx}^2 \phi_0 + \phi_0 = \phi_b. \tag{C.9}$$

The solution of the linearised differential equation in region 0 given by (C.9) subject to boundary condition (C.7) reads:

$$\phi_0\left(x\right) = \phi_b - \phi_0 \cosh\left(\frac{L_\perp - x}{\lambda_{j,0}}\right). \tag{C.10}$$

The integration constant ϕ_0, unknown at this moment, will be determined later by connecting the private SOL to the free SOL assuming continuity in the plasma potential.

C.3 Radial extension of the DC plasma potential in the free SOL

In the inner free SOL (region 1), (C.5) reads:

$$\lambda_{j,1}^2 \phi_1^{''} = 1 - \exp\left(-\phi_1\right). \tag{C.11}$$

The inner plasma is at the floating potential far away from the biased region:

$$\phi_1\left(x \to -\infty\right) = 0. \tag{C.12}$$

Multiplying (C.11) by $\phi_1^{'}$, one finds for $x < 0$:

$$\frac{d}{dx}\left[\frac{\left(\lambda_{j,1}^2 \phi_1^{'}\right)^2}{2} - \phi_1 - \exp\left(-\phi_1\right)\right] = 0. \tag{C.13}$$

The boundary conditions at infinity defined in (C.12) is then used to determine the proper integration constant:

$$\frac{1}{2}\left(\phi_1^{'}\right)^2 - \phi_1 - \exp\left(-\phi_1\right) = -1. \tag{C.14}$$

Integrating (C.14) gives access to the radial profile of the normalized DC plasma potential in the region 1 under the form $x\left(\phi_1\right)$ provided that the potential at the antenna limiter leading edge $\phi\left(0\right)$ is known:

$$x\left(\phi_1\right) = -\lambda_{j,1} \int_{\phi_1}^{\phi(0)} \frac{d\psi}{\left[2\left(\psi - 1 - \exp\left(-\psi\right)\right)\right]^{1/2}}. \tag{C.15}$$

If $\phi(0) \ll 1$, the sheaths characteristic can be linearised and (C.15) explicitly inverted. Linearising yields $\exp(-\psi) \sim 1 - \psi + \psi/2 + o(\psi^3)$. Inserting this linearisation into (C.15) gives:

$$\frac{x(\phi_1)}{\lambda_{j,1}} \approx \ln\left(\frac{\phi_1}{\phi(0)}\right) \Leftrightarrow \frac{\phi_1}{\phi(0)} \approx \exp\left(\frac{x}{\lambda_{j,1}}\right). \tag{C.16}$$

The DC plasma potential decreases with the distance to the antenna limiter leading edge. The half width at half maximum Δx_1 is defined as the radial position where the potential $\phi(0)$ is halved. It yields for (C.15):

$$\Delta x_1(\phi_1) = -\lambda_{j,1}(\sigma_{\perp DC,1}) \int_{\phi(0)/2}^{\phi(0)} \frac{d\psi}{[2(\psi - 1 - \exp(-\psi))]^{1/2}}. \tag{C.17}$$

Explicit expression can be found within two extreme cases: $\phi(0) \ll 1$ and $\phi(0) \gg 1$. The two solutions read:

$$\frac{\Delta x_1}{\lambda_{j,1}} = \begin{cases} \ln 2 + \frac{\phi_1}{12} & \text{if } \phi_1 < 4, \\ \sqrt{2(\phi_1 - 1)} - \sqrt{\phi_1 - 2} & \text{if } \phi_1 > 4. \end{cases} \tag{C.18}$$

$\lambda_{j,1} \ln 2$ is the width Δx_1 that would have been obtained with the linearised model given by (C.16) whereas the second term accounts for a non-linear broadening of the potential peak for finite bias proportional to the amplitude of the bias. The second expression is valid for high bias. In that case the broadening is following the square root of the amplitude of the bias.

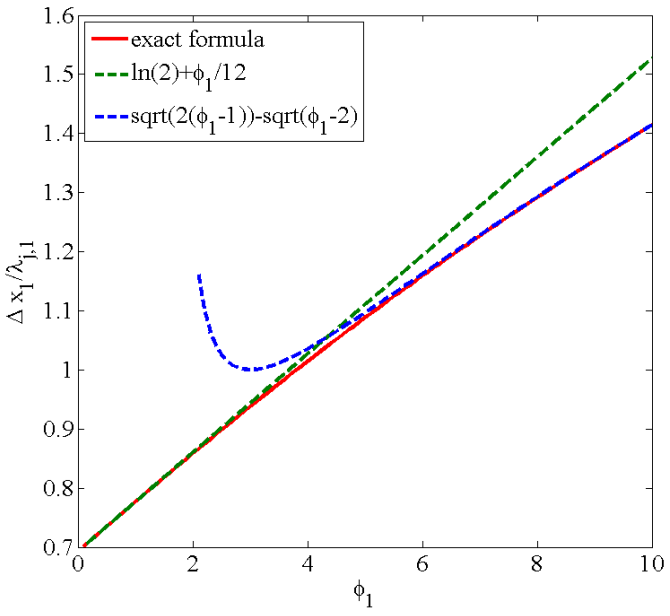

Figure C.2: Half width at half maximum normalized to the DC potential diffusion length in region 1 $\lambda_{j,A}$ versus the normalized DC potential peak in region 1 at the leading edge of the antenna limiter ($x = 0$) ϕ_1. The exact numerical solution (C.17) is shown, as well as two approximate formulas (C.18)

Figure C.2 plots the half width at half maximum normalized to the DC potential diffusion length in region 1 $\Delta x_1/\lambda_{j,1}$ versus the normalized DC potential peak in region

1 at the leading edge of the antenna limiter ϕ_1. It verifies that the two approximate expressions in (C.18) provide fair predictions of the exact formula (C.17) over the wide range of DC potentials. The transition from one approximate expression to the other seems to occur around $\phi_1 \approx 4$.

Similar results are found for the region 2 and 3 for the normalized potential ϕ_2 and ϕ_3 by replacing respectively $\lambda_{j,1}$ by $\lambda_{j,2}$ and $\lambda_{j,3}$ and $\Delta_{HWHM,1}$ by and $\Delta_{HWHM,2}$ and $\Delta_{HWHM,3}$.

C.4 Connection between the 4 regions at the antenna limiter leading edge

A form of solutions has been obtained for each of the four regions individually with one unknown quantity remaining. In order to obtain a self-consistent solution of the DC plasma potential over the whole spatial domain, the regions in the SOL must be connected at the interface $x = 0$ corresponding here to the leading edge of the antenna limiter. To achieve this aim, continuity of the DC plasma potential is enforced at $x = 0$:

$$\phi_0(0) = \phi_1(0) = \phi_2(0) = \phi_3(0) = \phi(0). \tag{C.19}$$

$\phi(0)$ is then determined from the balance of transverse DC current across the interface $x = 0$. The net DC current flowing in region 1 is the difference between the current coming from region 0 (private SOL) and the DC current lost to region 2 and region 3. Mathematically, it yields:

$$l_{\parallel,1}\sigma_{\perp DC,1}\partial_x V_{DC,1}(x=0) = \sum_{k=0,2,3} l_{\parallel,k}\sigma_{\perp DC,k}\partial_x V_{DC,k}(x=0) \tag{C.20}$$

Using the normalized quantity given by (C.4), (C.20) is similarly written:

$$\lambda_{j,1}^2\phi_1'(x=0) = \sum_{k=0,2,3} \lambda_{j,k}^2\phi_k'(x=0). \tag{C.21}$$

When the sheath characteristic are linearised, the current balance equation given by (C.21) can be explicitly solved. It yields:

$$\lambda_{j,1}\phi(0) = \lambda_{j,0}[\phi_b - \phi(0)]\tanh\left(\frac{L_\perp}{\lambda_{j,0}}\right) - \lambda_{j,2}\phi(0) - \lambda_{j,3}\phi(0). \tag{C.22}$$

It thus gives for the normalized DC plasma potential at the interface $x = 0$:

$$\frac{\phi(0)}{\phi_b} = \frac{1}{1 + \frac{\lambda_{j,1}+\lambda_{j,2}+\lambda_{j,3}}{\lambda_{j,0}\tanh\left(\frac{L_\perp}{\lambda_{j,0}}\right)}}. \tag{C.23}$$

Considering that the electron saturation regime has been reached for the sheaths in region 0, another expression can be obtained. The quantity $\langle j_{sh}\rangle$ is assumed to be known. In the free SOL, (C.14) is used as well as (C.8) in the private SOL. The DC current balance is re-expressed as:

$$\begin{aligned} -L_\perp\frac{\langle j_{sh}\rangle}{j_0^+} &= (\lambda_{j,1}+\lambda_{j,2}+\lambda_{j,3})\sqrt{2\left(\exp\left(-\phi(0)\right)+\phi(0)-1\right)} \\ &= (\lambda_{j,1}+\lambda_{j,2}+\lambda_{j,3})F(\phi(0)). \end{aligned} \tag{C.24}$$

The normalized DC potential in $x = 0$ is then deduced as:

$$\phi(0) = F^{-1}\left(-\frac{L_\perp}{\lambda_{j,1}+\lambda_{j,2}+\lambda_{j,3}}\frac{\langle j_{sh}\rangle}{j_0^+}\right). \tag{C.25}$$

(C.25) has a solution if $\langle j_{sh}\rangle < 0$ i.e. if on average over region 0, an electronic current goes into the sheaths. As electron saturation is assumed, neither $\lambda_{j,0}$ nor V_b appear in (C.26). In (C.25), $\phi(0) = F^{-1}(Y)$ can be approximated as follows:

$$\phi(0) = \begin{cases} Y\left(1+\frac{Y}{6}\right) & \text{if } Y \leq 1.5, \\ \frac{Y^2}{2}+1 & \text{if } Y > 1.5. \end{cases} \tag{C.26}$$

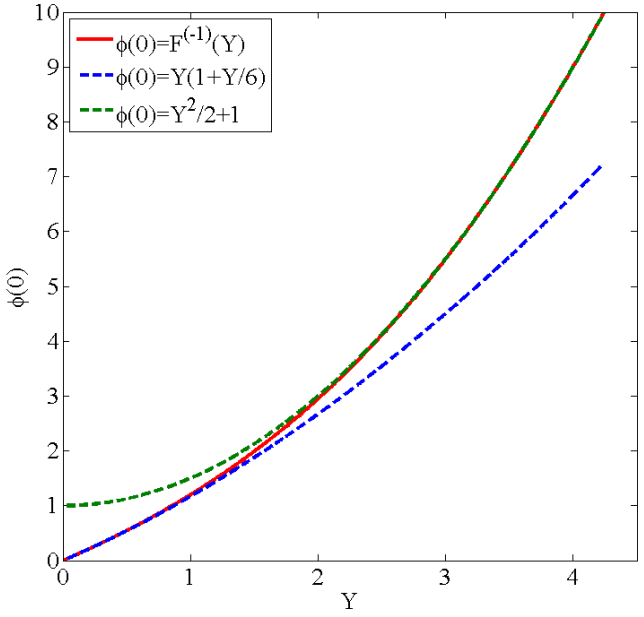

Figure C.3: Amplitude of the normalized DC plasma potential at the leading edge of the antenna limiter $\phi(0)$ versus Y. The exact solution (C.25) as well as two approximate solution are shown.

Figure C.3 confirms that the two expressions in (C.26) are good approximations of the exact solution (C.25). The transition from one approximation to the other seems to occur around $Y \approx 1.5$. These expressions of $\phi(0)$ neglect the self-consistency between $\langle j_{sh}\rangle < 0$ and $\phi(0)$. Non-linear solution keeping the self-consistency still has to be found.

Bibliography

[1] J. Ongena and G. Van Oost. Energy for Future Centuries - Prospects for Fusion Power as a Future Energy Source. *Fusion Science and Technology*, 53 (2T), 3-15, Feb 2008. http://www.ans.org/pubs/journals/fst/a_1686.

[2] G. Van Oost and E. Rebhan. Thermonuclear Burn Criteria. *Fusion Science and Technology*, 53 (2T), 16-26, Feb 2008. http://www.ans.org/pubs/journals/fst/a_1687.

[3] J. Wesson. *Tokamaks, 3rd ed.* Clarendon Press-Oxford, 2004.

[4] J.D. Lawson. Some Criteria for a Power Producing Thermonuclear Reactor. *Proc. Royal Physical Society B*, 70, 6-10, 1957.

[5] R.R. Weynants. Fusion Machines. *Fusion Science and Technology*, 53 (2T), 37-43, Feb 2008. http://www.ans.org/pubs/journals/fst/a_1689.

[6] D.A. Hartmann. Stellerators. *Fusion Science and Technology*, 53 (2T), 44-55, Feb 2008. http://www.ans.org/pubs/journals/fst/a_1690.

[7] U. Samm. Plasma-Wall Interactions in Magnetically Confined Fusion Plasmas. *Fusion Science and Technology*, 53 (2T), 223-228, Feb 2008. http://www.ans.org/pubs/journals/fst/a_1708.

[8] R. Koch. Fast Particle Heating. *Fusion Science and Technology*, 53 (2T), 184-193, Feb 2008. http://www.ans.org/pubs/journals/fst/a_1703.

[9] E. Westerhof. Electron Cyclotron Waves. *Fusion Science and Technology*, 53 (2T), 202-209, Feb 2008. http://www.ans.org/pubs/journals/fst/a_1694.

[10] R.J. La Haye. Neoclassical tearing modes and their control. *Physics of Plasmas*, 13, 055501 (18pp), May 2006.

[11] C.C. Hegna and Callen J.D. On the stabilization of neoclassical magnetohydrodynamics teraing modes using current drive or heating. *Physics of Plasmas*, 4, 2940-2946, May 1997.

[12] A. Mück *et al* . Sawtooth control experiments on ASDEX Upgrade. *Plasma Physics and Controlled Fusion*, 47, 1633-1655, Oct. 2005.

[13] M. Bornatici *et al* . Electron-cyclotron emission and absorption in fusion plasmas. *Nuclear Fusion*, 23, 1153-1257, Sept. 1983.

[14] R. Prater. Heating and current drive by electron cyclotron waves. *Physics of Plasmas*, 11, 2349-2376, Apr 2004.

[15] R.A. Cairns. *Radiofrequency heating of plasmas*. IOP Publishing, Bristol, 1991.

[16] D. Van Houtte *et al* . Recent fully non-inductive operation results in Tore Supra with 6 minute, 1 GJ plasma discharges. *Nuclear Fusion*, 44, L11-L15, Apr 2004.

[17] M. Chatelier and Equipe Tore Supra. Integration of high power, long pulse operation in Tore Supra in prparation for ITER. *Nuclear Fusion*, 47, S579–S589, Oct. 2007.

[18] D. Van Houtte *et al* . The West Project: a Major Upgrade of Tore Supra for Preparing ITER Operation in a Tungsten Environment. In *Proc. IEE 25th Symposium on Fusion Engineering (SOFE), San Francisco, CA, USA*, pages (WO1–6), 2013. http://advprojects.pppl.gov/SOFE2013/SOFE_Presentations/12_Wednesday/WO1-6vanHoutte.pdf.

[19] D. Guilhem *et al* . Radio frequency additional heating systems issues for the Tore-Supra WEST project. *Proc. IEE 25th Symposium on Fusion Engineering (SOFE), San Francisco, CA, USA*, 2013.

[20] A. Becoulet. Heating and current drive regimes in the ion cyclotron range of frequency. *Plasma Physics Controlled Fusion*, 38, A1-A11, Dec. 1996.

[21] F.W. Perkins. ICRH Heating Theory. *IEEE Transactions on Plasma Science*, 12, 53-63, June 1984.

[22] M. Brambilla. *Kinetic theory of plasma waves*. Oxford science publications, 1998.

[23] D. Zarzoso. *Kinetic description of the interaction between energetic particles and waves in fusion plasmas*. PhD thesis, Ecole Doctorale de l'Ecole Polytechnique (France), 2012.

[24] G. Bosia. On the automatic control of the ITER ion cyclotron system. *Fusion Engineering and Design*, 82, 662-665, Oct. 2007.

[25] A. Argouarch *et al* . ICRH ITER like antenna tested on TS commissioning, electrical modeling and load resilience studies. *Fusion Engineering and Design*, 84, 275-278, 2009.

[26] M. Brambilla. Numerical simulations of ion cyclotron waves in tokamaks plasmas. *Plasma Physics and Controlled Fusion*, 41, 1-34, Jan 1999.

[27] D. Borba W. and Kerner. CASTOR-K: Stability Analysis of Alfvén Eigenmodes in the Presence of Enegetic Ions on Tokamaks. *J. Computional Physics*, 153, 101-138, March 1999.

[28] E.F. Jaeger *et al* . Self-consistent full-wave and Fokker-Planck calculations for ion cyclotron heating in non Maxwellian plasmas. *Physics of Plasmas*, 13, 056101 (9pp), May 2006.

[29] R.J. Dumont. Variational approach to radiofrequency waves in magnetic fusion devices. *Nuclear Fusion*, 49, 075033 (14pp), July 2009.

[30] A. Messiaen *et al* . Performance of the ITER ICRH system as expected from TOPICA and ANTITER II modelling. *Nuclear Fusion*, 50, 025026 (21pp), Feb. 2010.

[31] V. Lancellotti *et al* . TOPICA: an accurate and efficient numerical tool for analysis and design of ICRF antennas. *Nuclear Fusion*, 46, S476-S499, July 2006.

[32] S. Pécoul *et al* . Numerical modeling of the coupling of an ICRH antenna with a plasma with self-consistent antenna currents. *Computer Physics Communications*, 146, 166-187, July 2002.

[33] J.R. Myra *et al* . Nonlinear ICRF-plasma interactions. *Nuclear Fusion*, 46, S455-S468, July 2006.

[34] J.M. Noterdaeme and G. Van Oost. The interaction between waves in the ion cyclotron range of frequencies and the plasma boundary. *Plasma Physics and Controlled Fusion*, 35, 1481-1511, Nov. 1993.

[35] D.A. D'Ippolito *et al* . A model of sheath-driven impurity by ICRH antennas. *Plasma Physics and Controlled Fusion*, 33, 607-642, June 1991.

[36] L. Colas *et al* . Ion Cyclotron Resonant Heating in Tore Supra. *Fusion Science and Technology*, 56, 1173-1204, Oct 2009. http://www.ans.org/pubs/journals/fst/a_9173.

[37] R. Van Nieuwenhove and G. Van Oost. Experimental study of sheath currents on the scrape-off-layer durin ICRH of TEXTOR. *Plasma Physics and Controlled Fusion*, 34, 525-532, April 1992.

[38] L. Colas *et al* . 2-D mapping of ICRH-induced SOL perturbations in Tore Supra tokamak. *J. Nuclear Materials*, 363–365, 555–559, June 2007.

[39] M. Kubič *et al* . Attenuation of ICRH-induced potentials in the SOL of Tore Supra. *Proc. 19th Topical Conf. on Radio Frequency Power in Plasmas, 1-3 June, Newport, RI, USA, AIP Conf. Proc.*, 1406, 215-218, June 2011.

[40] S.J. Wukitch *et al* . RF plasma edge interactions and their impact on ICRF antenna performance in Alcator C-Mod. *J. Nuclear Materials*, 363-365, 491-497, 2007.

[41] L. Colas *et al* . Key results of long pulse ICRH operation in Tore Supra. *Nuclear Fusion*, 46, 500-513, July 2006.

[42] V. Bobkov *et al* . ICRF antenna-plasma interactions and its influence on W sputtering in ASDEX upgrade. *Journal of Nuclear Materials*, 415, S1005-S1008, Sep. 2011.

[43] D.A. D'Ippolito *et al* . Modelling of mixed-phasing antenna-plasma interactions on JET A2 antennas. *Nuclear Fusion*, 42, 1357-1365, Dec. 2002.

[44] A. Ekedahl *et al* . Density Convection near Radiating ICRF Antennas and its Effect on the Coupling of Lower Hybrid Waves. *Proc. 15th Top. Conf. on Radio Frequency Power in Plasmas (19-21 May 2003, Moran, Wyoming 2003) AIP Conf. Proc.*, 694, 259–262, 2003.

[45] M. Kubič *et al* . Measurements of RF-induced SOL modifications in Tore Supra tokamak. *Proc. 20th International Conference on Nuclear Engineering and the ASME 2012 Power Conference (ICONE20-POWER2012) 30 July-3 August, Anaheim, CA, USA*, 5, 191-197, 2012.

[46] J. Gunn *et al* . Power and particle fluxes at the plasma edge of ITER: Specifications and Physics Basics. In *Proc. 22nd IAEA Fusion Energy Conference - 50th Anniversary of Controlled Nuclera Fusion, Geneva (Switzerland) 13/10-18/10, EXP/P6-32*, 2008.

[47] M. Bures *et al* . The modification of the plasma edge and impurity production by antenna phasing during ICRH heating on JET. *Plasma Physics and Controlled Fusion*, 30, 1496-167, Feb. 1988.

[48] A. Mendes *et al* . Reduction of RF-sheaths potentials by compensation or suppression of parallel RF currents on ICRF antennas. *Nuclear Fusion*, 50, 025021 (17pp), Feb. 2010.

[49] M.L. Garrett and S.J. Wukitch. Mitigation of radio frequency sheaths through magnetic field-aligned ICRF antenna design. *Fusion Engineering and Design*, 87, 1570-1575, 2012.

[50] J.R. Myra *et al* . Sheath-plasma waves and anamalous loading in ion-Bernstei-wave experiments. *Physical Review Letters*, 66, 1173–1176, 1991.

[51] D.A. D'Ippolito *et al* . Far-field sheaths due to fast waves incident on material surfaces. *Physics of Plasmas*, 15, 102501 (12pp), Oct. 2008.

[52] R.L. Stenzel. Instability of the sheath-plasma resonance. *Physical Review Letters*, 60, 704-707, Feb. 1988.

[53] D.A. D'Ippolito and J.R. Myra. A radio-frequency sheath boundary condition and its effect on slow wave propagation. *Physics of plasmas*, 13, 102508 (12pp), Oct. 2006.

[54] A. Ngadjeu *et al* . Generation of DC currents by ICRH near fields in the Scrape-off-Layer. *J. Nuclear Materials*, 415, S1009-S1012, Aug. 2012.

[55] J. Jacquot *et al* . Radio-frequency sheaths physics: Experimental characterization on Tore Supra and related self-consistent modeling. In *Proc. 20th Topical Conference on Radio Frequency Power in Plasmas, Sorrento, Italy, June 25-28 2013, submitted to Physics of Plasmas*, 2013. Invited Talk I3.7.

[56] L. Colas *et al* . RF-sheath patterns modification via novel Faraday screen and strap voltage imbalance on Tore Supra ion cyclotron antennae. *J. Nuclear Materials*, 438, S330-S333, July 2013.

[57] J.-P. Bérenger. A perfectly matched layer for the absorption of electromagnetic waves. *J. Computional Physics*, 114, 185-200, Oct. 1994.

[58] T.H. Stix. *The Theory of Plasma Waves, second edition.* AIP, 1992.

[59] I.B. Bernstein. Waves in a Plasma in a Magnetic Field. *Physical Review*, 109, 10-21, Jan 1958.

[60] D.G. Swanson. *Plasma Waves, second edition.* IoP series on Plasma Physics, Taylor & Francis, 2003.

[61] L. Chen. Alfvén waves: a journey between space and fusion plasmas. *Plasma Physics Controlled Fusion*, 50, 124001 (14pp), Dec. 2008.

[62] R. Koch. A global solution of the ICRH problem based on the combined use of a planar coupling model and hot-plasma ray-tracing in tokamak geometry. *Computer Physics Communications*, 40, 1-22, May 1986.

[63] S. Pécoul *et al* . Selfconsistent determination of currents on ICRH antennae taking into account magnetic shielding. *Proc. 25th EPS conf. Praha ECA vol.22C p.1586*, 1998.

[64] A. Messiaen and R. Weynants. ICRH antenna coupling physics and optimum plasma edge density profile. Application to ITER. *Plasma Physics and Controlled Fusion*, 53, 085020 (29pp), Aug. 2011.

[65] F. Clairet *et al* . ICRF coupling and edge density profile on Tore Supra. *Plasma Physics and Controlled Fusion*, 46, 1567-1580, Oct. 2004.

[66] P. Descamps *et al* . Excitation of global modes in textor and comparison with theory. *Plasma Physics Controlled Fusion*, 33, 1109-1133, Sep. 1991.

[67] L. Colas. *H.D.R.: Linear and non-linear Physics of high power radio-frequency waves in the edge of magnetized plasmas*. PhD thesis, U.F.R. Sciences et Techniques de la Matière et des Procédés, Ecole doctorale EMMA, 2009.

[68] D. Milanesio *et al* . TOPLHA: an accurate and efficient numerical tool for analysis and design of LH antennas. *Nuclear Fusion*, 52, 013008 (7pp), Jan. 2012.

[69] J. Hillairet *et al* . ALOHA: an Advanced LOwer Hybrid Antenna coupling code. *Nuclear Fusion*, 50, 125010 (17pp), Dec. 2010.

[70] M. Preynas *et al* . Experimental characterization and modelling of non-linear coupling of the lower hybrid current drive power on Tore Supra. *Nuclear Fusion*, 53, 013012 (18pp), Jan. 2013.

[71] `http://www.ansoft.com/products/hf/hfss/`.

[72] `https://www.cst.com/Products/CSTMWS`.

[73] P.U. Lamalle *et al* . Recent developments in ICRF antenna modelling. *Nuclear Fusion*, 46, 432-443, April 2006.

[74] F. Louche *et al* . Eigenmode analysis of the ITER ICRF antenna plug and electrical solution to the grounding of the antenna. *Nuclear Fusion*, 49, 065025 (11pp), May 2009.

[75] F. Louche *et al* . 3D electromagnetic optimization of the front face of the ITER ICRF antenna. *Nuclear Fusion*, 51, 103002 (20pp), Aug. 2011.

[76] K.S. Yee. Numerical solution of initial boundary value problems involving Maxwell's equations in isotropic media. *IEEE Transactions on Antennas Propagation*, 14, 302-307, May 1966.

[77] G. Strang and G. Fix. *An Analysis of The Finite Element Method*. Prentice Hall, 1973.

[78] C. Christopoulos. *The Transmission Line Modeling Method: TLM*. Piscataway, NY, IEEE Press, 1995.

[79] S.G. Johnson. Notes on Perfectly Matched Layers (PMLs).

[80] M.J. Grote and J.B. Keller. Non reflecting boundary conditions for Maxwell's equations. *J. Computational Physics*, 139, 327-342, Jan. 1998.

[81] A. Taflove and M.E. Brodwin. Numerical solution of steady-state electromagnetic scattering problems using the time-dependant Maxwell's equations. *IEEE Transactions on Microwave Theory and Techniques*, 23, 623-630, Aug. 1975.

[82] R. Holland. THREDE - Free-Field EMP coupling and scattering code. *IEEE Transactions on Nuclear Science*, 24, 2416-2421, Dec. 1977.

[83] B. Engquist and A. Majda. Absorbing boundary conditions for the numerical simulation of waves. *Mathematics of Computation*, 31, 629-651, July 1977.

[84] G. Mur. Absorbing boundary conditions for the finite-difference approximation of the time-domain electromagnetic field equations. *IEEE Transactions on Electromagnetic Compatibility*, 23, 377-382, Nov. 1981.

[85] L.N. Trefethen and L. Halpern. Well-posedness of one-way wave equations and absorbing boundary conditions. *Mathematics of Computation*, 47, 421-435, Oct. 1986.

[86] R. Higdon. Numerical absorbing boundary conditions for the wave equations. *Mathematics of Computation*, 49, 65-90, July 1987.

[87] O.M. Ramahi. Complementary operators: A method to annihilate artificial reflections arising from the truncation of the computational domain in the solution of partial differential equations. *IEEE Transactions on Antennas Propagation*, 43, 697-704, July 1995.

[88] H.S. Butler and G.S. Kino. Plasma Sheath Formation by Radio-Frequency Fields. *Physics of Fluids*, 6, 1346-1355, Sept. 1963.

[89] F.W. Perkins. Radiofrequency sheaths and impurity generation by ICRH antennas. *Nuclear Fusion*, 29, 583-592, Apr. 1989.

[90] T. Hellsten *et al* . Influence of coupling to spectra of weakly damped eigenmodes in the ion cyclotron range of frequencies on parasitic absorption in rectified radio frequency sheaths. *Physics of Plasmas*, 12, 032505 (9pp), March 2005.

[91] J.R. Myra *et al* . Far-field sheaths from waves in the ion cyclotron range of frequencies. *Physics of Plasmas*, 1, 2890-2900, Sept. 1994.

[92] H. Kohno *et al* . Numerical analysis of radio-frequency sheath-plasma Interactions in the ion cyclotron range of frequencies. *Physics of Plasmas*, 19, 012508 (9pp), Jan 2012.

[93] P.C. Stangeby. *The Plasma Boundary of Magnetic Fusion Devices*. IOP, 2000.

[94] A.L. Lieberman and A.J. Lichtenberg. *Principles of Plasma Discharges and Material Processing, Second Edition*. Wiley-Interscience, Inc Publication, 2005.

[95] K.-U. Riemann. The Bohm criterion and sheath formation. *J. Physics D: Applied Physics*, 24, 493-518, April 1991.

[96] R. Chodura. Plasma-wall transition in an oblique magnetic field. *Physics of Fluids*, 25, 1628-1633, Sept. 1982.

[97] K.-U. Riemann. Theory of the plasma–sheath transition in an oblique magnetic field. *Contribution to Plasma Physics*, 34, 127-132, Feb. 1994.

[98] E. Ahedo. Structure of the plasma-wall interaction in an oblique magnetic field. *Physics of Plasmas*, 4, 4419-4430, Dec. 1997.

[99] E. Faudot *et al* . Parametric study of two-dimentional potential structures induced by radio-frequency sheaths coupled with transverse currents in front of the Ion Cyclotron Resonance Heating antenna. *Physics of Plasmas*, 13, 042512 (16pp), Apr. 2006.

[100] V.A. Godyak and N. Sternberg. Dynamic model of the electrode sheaths in symmetrically driven rf discharges. *Physical Review A*, 42, 2299-2312, Aug. 1990.

[101] C.D. Child. Discharge from hot CaO. *Physics Review (Series I)*, 32, 492-511, May 1911.

[102] I. Langmuir. The effect of space charge and residual gases on thermionic currents in high vacuum. *Physical Review*, 2, 450-486, Dec. 1913.

[103] M.A. Lieberman. Analytical Solution for Capacitive RF Sheath. *IEEE Transactions on Plasma Science*, 16, 638-644, Dec. 1988.

[104] H. Kohno. *Numerical Analysis of Radio-Frequency Sheath-Plasma Interactions in the Ion Cyclotron Range of Frequencies*. PhD thesis, Massachussets Institute of Technology (USA), 2011.

[105] D. Van Eester *et al* . Connection coefficients for cold plasma wave propagation near metallic surfaces. *Plasma Physics and Controlled Fusion*, 55, 055001 (17pp), May 2013.

[106] K. Günther and A. Carlson. Fluid theory of Langmuir probes in magnetized plasma with open flux tubes. *Contribution to Plasmas Physics*, 34, 484-489, Feb. 1994.

[107] J. Cornelis *et al* . Predicting the radial electric field imposed by externally driven radial currents in tokamaks. *Nuclear Fusion*, 34, 171-183, Feb. 1994.

[108] V. Bobkov *et al* . Assessment of compatibility of ICRF antenna operation with full W wall in ASDEX Upgrade. *Nuclear Fusion*, 50, 035004 (11pp), March 2010.

[109] S.J. Wukitch *et al* . Characterization and performance of a field aligned ion cyclotron range of frequency antenna in Alcator C-Mod. *Physics of Plasmas*, 20, 056117 (8pp), May 2013.

[110] D.A. D'Ippolito *et al* . Analysis of rf sheaths interactions in TFTR. *Nuclear Fusion*, 38, 1543-1563, Oct. 1998.

[111] S.I. Braginskii. Transport processes in a plasma. *Review of Plasma Physics*, 1, 205-311, 1965.

[112] V.A. Rozhansky V.D. Shafranov and O.G. Bakunin. *Review Plasma Physics: Mechanisms of Transverse Conductivity and Generation of Self-Consistent Electric Fields in Strongly Ionized Magnetized Plasma*, volume 24. ed. Springer, 2008.

[113] Ph. Ghendrih *et al* . Theoretical analysis of the influence of external biasing on lon range turbulent transport in the scrape-off-layer. *Nuclear Fusion*, 43, 1013-1022, Oct. 2003.

[114] V.A. Godyak and A.A. Kuzovnikov. Rectifying properties of rf discharges. *Soviet J. Plasma Physics*, 1, 276-280, May-June 1975.

[115] E.F. Jaeger *et al* . Power deposition in high-density inductively coupled plasma tools for semiconductor processing. *Physics of Plasmas*, 2, 2597-2604, June 1995.

[116] M.D. Carter *et al* . Combined rf and transport effects in in magnetized capacitive discharges. *J. of Applied Physics*, 100, 073305 (13pp), Oct. 2006.

[117] R. Maggiora. Efficient 3D/1D selfconsistent integral-equation analysis of ICRH antennae. *Nuclear Fusion*, 44, 846-868, Aug. 2004.

[118] B. Van Compernolle *et al* . Implementation of sheath effects into TOPICA. In *Proc. 35th EPS Conference on Plasma Physics, HerVonissos, Crete, Greece, 9-13 June 2008*, volume 32 ECA, pages 1106–1109, 2008.

[119] D. Smithe *et al* . 3D TimeDomain Simulations of ITER Antenna Modules with Edge Plasma. *Proc. 19th Topical Conf. on Radio Frequency Power in Plasmas, 1-3 June, Newport, RI, USA, AIP Conf. Proc.*, 1406, 65-68, 2011.

[120] D. Smithe *et al* . Quantitative modelling of ICRH antennas with integrated time domain RF sheath and plasma physics. In *Proc. 20th Topical Conf. on Radio frequency Power in Plasma, Sorrento*, 2013.

[121] C. Nieter and J.R. Cary. VORPAL: a versatile plasma simulation code. *J. Computational Physics*, 196, 448-473, May 2004.

[122] D. Smithe. Finite-difference time-domain simulation of fusion plasmas at radiofrequency times scales. *Physics of Plasmas*, 14, 056104 (7pp), Apr. 2007.

[123] T.G. Jenkins *et al* . Time-domain simulation of nonlinear radiofrequency phenomena. *Physics of Plasmas*, 20, 012116, Jan. 2013.

[124] E. Faudot *et al* . Fluid modeling of radio frequency and direct currents in a biased magnetized plasma. *Physics of Plasmas*, 20, 043514 (14pp), Apr. 2013.

[125] J. Voge. *Les tubes aux hyperfréquences: Triodes et tétrodes, klystrons, magnétrons, tubes à onde progressive, amplificateurs paramétriques et quantiques*. Éditions Eyrolles, 1959.

[126] L. Delpech *et al* . Design and validation of a 700 kW/CW water load for 3.7 GHz klystrons. *Fusion Engineering and Design*, 86, 815-818, Oct. 2011.

[127] E. Westerhof. Electron cyclotron resonance heating on TEXTOR. *Nuclear Fusion*, 43, 1371-1383, Nov. 2003.

[128] A.G.A. Verhoeven. The design of an ECRH system for JET-EP. *Nuclear Fusion*, 43, 1477-1486, Nov. 2003.

[129] D. Guilhem *et al* . Manufacturing process and tests of a Lower Hybrid Passive Active Multijunction launcher for long pulses experimenents on Tore Supra. *Fusion Engineering and Design*, 86 (6-8), 513-517, Oct. 2011.

[130] H. Kuus *et al* . The ICRH system for Tore Supra. *Proc. 15th SOFT*, 1988.

[131] THALES. Technical Note Tetrode TH 525/TH 525A. https://www.thalesgroup.com/sites/default/files/asset/document/TH525_A%20.pdf.

[132] T.L. Owens T.L. *et al* . ICRF antenna and feedthrough development at the Oak Ridge National Laboratory. *Proc. 6th Topical Conf. on RF Plasma Heating*, 1985.

[133] H. Wilson. Edge Localized Modes in Tokamaks. *Fusion Science and Technology*, 53 (2T), 161-169, Feb 2008. http://www.ans.org/pubs/journals/fst/a_1702.

[134] I. Monakhov. Tests of load-tolerant external conjugate-T matching system for A2 ICRH antenna at JET. *Fusion Engineering and Design*, 74, 467-471, Nov. 2005.

[135] K. Vulliez *et al* . Tore Supra ICRH antenna prototype for next step devices. *Fusion Engineering and Design*, 66-68, 531-535, Sep. 2003.

[136] K. Vulliez *et al* . First results of the Tore Supra ITER like ICRH antenna prototype. *Fusion Engineering and Design*, 74, 267-271, Nov. 2005.

[137] K. Vulliez *et al* . Validation of the load-resilient ion cyclotron resonance frequency antenna concept on Tore Supra plasmas. *Nuclear Fusion*, 48, 065007 (6pp), 2008.

[138] G. Agarici *et al* . First plasma experiments in Tore Supra with a new generation of high heat flux limiters for RF antennas. *Fusion Engineering and Design*, 49-50, 145-150, Nov. 2000.

[139] D.W. Faulconer. Adverse shielding of the heating field and high ohmic loss introduced by electrostatic shields employed in radio-frequency heating of plasma. *J. Applied Physics*, 54, 3810-3817, July 1983.

[140] Y. Corre *et al* . Characterization of heat flux generated by ICRH heating with cantilevered bars and a slotted box Faraday screen. *Nuclear Fusion*, 52, 103010(11pp), Oct. 2012.

[141] D. Guilhem *et al* . Tore-Supra infrared thermography system, a real steady-state diagnostic. *23rd Symposium on Fusion Technology (SOFT 23), Venice, Italy, Fusion Engineering and Design*, 74, 879-883, Nov. 2005.

[142] Ph. Moreau *et al* . RF heating optimization on Tore Supra using feedback control of infrared measurements. *Fusion Engineering and Design*, 82, 1030-1035, March 2007.

[143] G. Berger-By. Arc security system on harmonics detection for the Tore Supra ICRH transmitter. *Fusion Engineering and Design*, 82, 716-722, 2007.

[144] M. Kubič *et al* . Measurement of sheath potential in RF-biased flux tubes using a retarding field analyser in Tore Supra tokamak. *J. Nuclear Materials*, 438, 509–512, July 2013.

[145] G. Hornung. *Étude de la turbulence plasma par réflectométrie à balayage ultra rapide sur le tokamak Tore Supra*. PhD thesis, Aix-Marseille Université (France), 2013.

[146] F. Clairet *et al* . Edge density profile measurements by X-mode reflectometry on Tore Supra. *Plasma Physics and Controlled Fusion*, 43, 429-441, April 2001.

[147] J.-P. Bérenger. *Perfectly Matched Layer (PML) for Computational Electromagnetics*. Morgan & Claypool, 2007.

[148] A. Taflove S.C. Hagness. *Computational Electrodynamics: The Finite-Difference Time-Domain Method, 3rd ed.* Artech House Publishers, 2005.

[149] Jin Jianming. *The Finite Element Method in Electromagnetisms, 2nd Edition*. Wiley-IEEE Press, 2002.

[150] F.L. Teixeira and W.C. Chew. General Closed-Form PML Constitutive Tensors to Match Arbitrary Bianisotropic and Dispersive Linear Media. *IEEE Microwave and Guided Wave Letters*, 8, 1804-1807, June 1998.

[151] N.A. Gondarenko *et al* . Perfectly matched layers for radio wave propagation in inhomogeneous magnetized plasmas. *J. Computational Physics*, 194, 481-504, March 2004.

[152] Mario Augusto Velasco Sanchez. *Improvements to a solver of the Helmholtz Equation*. PhD thesis, Erasmus Mundus Program on Nuclear Fusion Science and Engineering Physics, Université Henri Poincaré, 2009.

[153] F.L. Teixeira and W.C. Chew. Unified analysis of perfectly matched layers using differential forms. *Microwave and Optical Technology Letters*, 20, 124-126, Jan. 1999.

[154] F.L. Teixeira and W.C. Chew. Complex space approach to perfectly matched layers: a review and some new developments. *International J. of Numerical Modelling: Electronic Networks, Devices and Fields*, 13, 441-455, Sep. 2000.

[155] W.C. Chew and W. Weedon. A 3D perfectly matched medium from modified Maxwell's equations with stretched coordinates. *Microwave and Optical Technology Letters*, 7, 599-604, Jan. 1994.

[156] Z.S. Sacks *et al* . A perfectly matched anisotropic absorber for use as an absorbing boundary condition. *IEEE Transactions on Antennas and Propagation*, 43, 1460-1463, Dec. 1995.

[157] S.D. Gedney *et al* . An anisotropic perfectly matched layer absorbing media for the truncation of FDTD latices. *IEEE Transactions on Antennas and Propagation*, 44, 1630-1639, Dec. 1996.

[158] F.L. Teixeira and W.C. Chew. Split-Field and Anisotropic-Medium PML-FDTD Implementations for Inhomogeneous Media. *IEEE Transactions on Microwave Theory and Techniques*, 50, 30-35, January 2002.

[159] F.L. Teixeira and W.C. Chew. On causality and dynamic stability of perfectly matched layers for FDTD simulation. *IEEE Transactions on Antennas Propagation*, 47, 775-785, 1999.

[160] I. Singer and E. Turkel. A perfectly matched layer for the Helmholtz equation in a semi-infinite strip. *J. Computional Physics*, 201, 439-465, Dec. 2004.

[161] S.G. Johnson *et al* . Adiabatic theorem and continuous coupled-mode theory for efficient taper transitions in photonic crystals. *Physical Review E*, 66, 066608, Dec. 2002.

[162] A.F. Oskooi. The failure of perfectly matched layers, and towards their redemption by adiabatic absorbers. *Optics Express*, 16, 11376-11392, July 2008.

[163] C. Balanis. *Antenna Theory: analysis and design*. Wiley 3rd, 2005.

[164] R.W. Pryor. *Multiphysics modeling using COMSOL: a first principles approach*. Jones and Bartlett Publishers, 2011.

[165] E. Becache *et al* . Stability of perfectly matched layers, group velocities and anisotropic waves. *J. Computational Physics*, 188, 399-433, July 2003.

[166] http://www.comsol.com/.

[167] D. Milanesio *et al* . Analysis of the Tore Supra ICRF antenna with TOPICA. *Plasma Physics and Controlled Fusion*, 49, 405-419, April 2007.

[168] R.K. Fisher and R.W. Gould. Resonance Cones in the Field Pattern of a Short Antenna in an Anisotropic Plasma. *Physical Review Letter*, 22, 1093-1095, May 1969.

[169] J.R. Myra and D.A. D'Ippolito. Resonance cone interactions With a Self-Consistent Radio-Frequency Sheath. *Physical Review Letter*, 101, 195004 (4pp), Nov. 2008.

[170] P.M. Bellan. *Fundamental of Plasma Physics*. Cambridge University Press, Cambridge, England, 2006.

[171] D.A. D'Ippolito and J.R. Myra. Analytic model of near-field radio-frequency sheaths. I. Tenuous plasma limit. *Physics of Plasmas*, 16, Feb. 2009.

[172] L. Colas *et al* . RF current distribution and topology of RF sheath potentials in front of ICRF antennae. *Nuclear Fusion*, 45, 767-782, Aug. 2005.

[173] L. Colas *et al* . Self consistent radio-frequency wave propagation and peripheral direct current plasma biasing: Simplified three dimensional non-linear treatment in the "wide sheath" asymptotic regime. *Physics of Plasmas*, 19, 092505 (15pp), Sept. 2012.

[174] J. Jacquot *et al* . Recent advances in self-consistent RF sheath modeling and related physical properties: Application to Tore Supra IC antennae. *Proc. 39th EPS ECA vol.32 P-2.105*, 2012. http://ocs.ciemat.es/EPSICPP2012PAP/pdf/P2.038.pdf.

[175] R.J. Dumont and D. Zarzoso. Heating and current drive by ion cyclotron waves in the activated phase of ITER. *Nuclear Fusion*, 53, 013002 (12pp), Nov. 2013.

[176] M. Lassas and E. Somersalo. Analysis of the PML equations in general convex geometry. In *Proc. Royal Society Edinburgh Sect. A*, volume 131(5), pages 1183–1207, 2001.

[177] P. Jacquet *et al* . Heat loads on JET plasma facing components from ICRF and LH wave absorption in the SOL. *Nuclear Fusion*, 51, 103018 (16pp), Oct. 2011.

[178] C. Besse *et al* . Efficient Numerical Methods for Strongly Anisotropic Elliptic Equations. *J. Scientific Computing*, 55, 231-254, Apr. 2013.

[179] P.R. Amestoy *et al* . Multifrontal parallel distributed symmetric and unsymmetric solvers. *Computer Methods in Applied Mechanics and Engineerin*, 184, 501-520, Apr. 2000.

[180] http://www.mathworks.com/products/matlab/.

[181] L. Colas. Note de Travail: Self-Consistent description of near RF field propagation and DC sheath potential build-up in tokamak SOL plasma. Technical report, CEA, IRFM, 2009.

[182] J. Jacquot *et al* . 2D and 3D modeling of wave propagation in cold magnetized plasma near the Tore Supra ICRH antenna relying on the Perfectly Matched Layer technique. *Plasma Physics and Controlled Fusion*, 55, 115004 (17pp), Nov. 2013.

[183] I. Langmuir and K. Blodgett. Currents limited by space charge between coaxial cylinders. *Physical Review*, 22, 347-356, Oct. 1923.

[184] V. Rozhansky *et al* . Plasma Depletion and Electron Current Saturation for Positively Biased Flush-Mounted Probe in Magnetic Field. In *26th EPS Conf. on Controlled Fusion and Plasma Physics, Maastricht, 14 - 18 June 1999, ECA*.

[185] X. Litaudon *et al* . Physics and technology in the ion-cyclotron range of frequency on Tore Supra and TITAN test facility: implication for ITER. *Nuclear Fusion*, 53, 083012 (11pp), Aug. 2013.

[186] O. Meyer *et al* . Impurity production monitoring during RF experiments in Tore Supra. *J. Nuclear Materials*, 390-391, 879-883, June 2009.

[187] M. Chantant *et al* . Calorimetry measurements during high energy discharges at Tore Supra. *Fusion Engineering and Design*, 74, 897-902, Nov. 2005.

[188] Y. Corre *et al* . Heat flux calculation and problem of flaking of boron carbide coatings on the Faraday screen of the ICRH antennas during Tore Supra high power, long pulse operation. *Fusion Engineering and Design*, 86, 429-441, June 2011.

[189] G. Ritz *et al* . Calculation of heat fluxes induced by radio frequency heating on the actively cooled protections of ion cyclotron resonant heating (ICRH) and lower hybrid (LH) antennas in Tore Supra. *Fusion Engineering and Design*, 88, 899-902, 2013.

[190] I. Cziegler *et al* . Ion-cyclotron range of frequencies in the scrape-of-layer: fine structure radial electric fields. *Plasma Physics and Controlled Fusion*, 54, 105019 (9pp), Oct. 2012.

[191] A. Kallenbach *et al* . Recent ASDEX Upgrade Results and Future Extension Plans. *IEEE Transactions on Plasma Science*, 40, 605-513, March 2012.

[192] V. Bobkov *et al* . ICRF operation with improved antennas in ASDEX Upgrade with W wall. *Nuclear Fusion*, 53, 093018 (9pp), Aug. 2013.

[193] C. Klepper *et al* . Dynamic Stark Spectroscopic Measurements of Microwave Electric Fields Inside the Plasma Near a High-Power Antenna. *Physical Review Letters.*, 110, 215005 (5pp), May 2013.

[194] D.A. D'Ippolito *et al* . Modeling far-field RF sheaths in Alcator C-Mod. In *Proc. 20th Topical Conf. on Radio frequency Power in Plasma, Sorrento, Italy*, 2013.

[195] J.R. Myra *et al* . Role of magnetic field tangency in ICRH sheath interactions. In *Proc. 20th Topical Conf. on Radio frequency Power in Plasma, Sorrento, Italy*, 2013.

[196] L. Colas *et al* . RF sheath estimates on blanket shielding modules surrounding the ITER Ion Cylotron Antenna using the SSWICH asymptotic model. Technical report, CEA, IRFM, 2011.

[197] Y. Sarazin. *Etude de la turbulence de bord dans les plasmas de tokamaks*. PhD thesis, Université Joseph Fourier - Grenoble 1 (France), 2012.

[198] C. Colin. Modélisation umérique des mesures de flux par sonde mobile dans le plasma de bord des tokamaks, 2012. Master thesis Université Henri Poincaré Nancy-Metz (France).

[199] D. Van Eester *et al* . Ion cylotron resonance heating-induced density modifications near antennas. *Plasma Physics and Controlled Fusion*, 55, 025002 (12pp), Feb. 2013.

[200] S. Robertson *et al* . TOPICAL REVIEW: Sheaths in laboratory and space plasmas. *Plasma Physics and Controlled Fusion*, 55, 093001, Sep. 2013.

[201] B. Jacobs *et al* . Temporally resolved ions velocity distribution measurements in a radio-frequency plasma sheath. *Physics of Plasmas*, 18, 053503 (5pp), May 2011.

List of Publications

1st author

J. Jacquot et al . Radio-frequency sheaths physics: Experimental characterization on Tore Supra and related self-consistent modeling. *In Proc. Invited Talk 20th Topical Conference on Radio Frequency Power in Plasmas, Sorrento, Italy, June 25-28 2013, submitted to Physics of Plasmas*

J. Jacquot et al. 2D and 3D modeling of wave propagation in cold magnetized plasma near the Tore Supra ICRH antenna relying on the Perfectly Matched Layer technique. *Plasma Physics and Controlled Fusion*, **55**, 115004 (17pp), Nov. 2013.
http://dx.doi.org/10.1088/0741-3335/55/11/115004

J. Jacquot et al. Recent advances in self-consistent RF sheath modeling and related physical properties: Application to Tore Supra IC antennae. *Proc. 39th EPS ECA* vol.**32** P-2.105, 2012.
http://ocs.ciemat.es/EPSICPP2012PAP/pdf/P2.038.pdf

J. Jacquot et al. Self-consistent non-linear radio-frequency wave propagation and peripheral plasma biasing. *Proc. 19th Topical Conf. on Radio Frequency Power in Plasmas, 1-3 June, Newport, RI, USA, AIP Conf. Proc.* **1406**, p.211-214, 2011.
http://dx.doi.org/10.1063/1.3664962

Co-author

D. Guilhem et al. Radio frequency additional heating systems issues for the Tore-Supra WEST project. *Proc. IEE 25th Symposium on Fusion Engineering (SOFE), San Francisco, CA, USA*, 5pp, 2013.
http://dx.doi.org/10.1109/SOFE.2013.6635379

A. Bécoulet et al. Science and technology research and development in support to ITER and the broader approach. *Nuclear Fusion*, **53**(8), 104023(17pp), Oct. 2013.
http://dx.doi.org/10.1088/0029-5515/53/10/104023

X.Litaudon et al. Physics and Technology in the Ion-cyclotron Range of Frequency on Tore Supra and TITAN test facility: implication for ITER. *Nuclear Fusion*, **53**(8), 083012(11pp), Aug. 2013.
http://dx.doi.org/10.1088/0029-5515/53/8/083012

M. Kubič et al. Measurement of sheath potential in RF-biased flux tubes using a retarding field analyser in Tore Supra tokamak. *J. Nuclear Materials*, **438**, p.509–512, July 2013.
http://dx.doi.org/10.1016/j.jnucmat.2013.01.105

L. Colas et al. RF-sheath patterns modification via novel Faraday screen and strap voltage imbalance on Tore Supra ion cyclotron antennae. *J. Nuclear Materials*, **438**, S330-S333, July 2013.
http://dx.doi.org/10.1016/j.jnucmat.2013.01.061

Y. Corre et al. Characterization of heat flux generated by ICRH heating with cantilevered bars and a slotted box Faraday screen. *Nuclear Fusion*, **52**, 103010(11pp), 2012.
http://dx.doi.org/10.1088/0029-5515/52/10/103010

L. Colas et al. Self consistent radio-frequency wave propagation and peripheral direct current plasma biasing: Simplified three dimensional non-linear treatment in the "wide sheath" asymptotic regime. *Physics of Plasmas*, **19**, 092505 (15pp), Sept. 2012.
http://dx.doi.org/10.1063/1.4750046

A. Koehn et al. Full-wave modeling of the O-X mode conversion in the Pegasus toroidal experiment. *Physics of plasmas*, **18**(8), 082501 (9pp), Aug. 2011.
http://dx.doi.org/10.1063/1.3609828

Long résumé

Ce travail de thèse s'inscrit dans le contexte global de la fusion thermonucléaire. Le but est de domestiquer sur Terre l'énergie des étoiles afin de produire de l'énergie en abondance sur des échelles de temps très longs et sans déchet difficile à gérer. Une voie pour réaliser ce type de production d'énergie sur Terre est d'utiliser des bouteilles magnétiques fermées sur elle-mêmes appelées tokamaks. Dans ce tokamak, il devrait être possible de maintenir des très hautes températures de l'ordre de 100 millions de degrés pour atteindre des conditions permettant la fusion d'un noyau de deutérium avec un noyau de tritium. Ces deux éléments correspondent aux deux isotopes de l'hydrogène. A ces températures la matière existe sous forme de plasma, dans lequel les électrons sont détachés des noyaux. Dans ce milieu plasma, les interactions électromagnétiques dominent bien que ce milieu soit globalement neutre et conduisent à un comportement collectif des particules face à une perturbation. Ce comportement collectif, résumé dans un tenseur diélectrique gyrotrope, se traduit par l'existence de modes d'oscillation permettant de transporter de l'énergie dans le plasma. Différentes techniques sont possibles pour chauffer le plasma à ces températures extrêmes nécessaires à la fusion des noyaux. Un chauffage par des ondes radio-fréquences (RF) est possible dans le domaine des fréquences cyclotroniques ioniques (FCI) $(30 - 100\ \mathrm{MHz})$ afin d'atteindre les températures requises dans un plasma de fusion. Les grands tokamaks sont pour la plupart équipés de systèmes de chauffage FCI permettant d'injecter plusieurs MWde puissance additionnelle dans le plasma. Les antennes FCI sont composées d'un réseau phasé de rubans métalliques parcourus par un courant RF.

Afin d'obtenir un chauffage efficace du plasma central, une bonne compréhension des interactions entre les ondes et le plasma de bord est cependant nécessaire. Comme les ondes FCI sont évanescentes à basse densité, elles doivent traverser par effet tunnel une couche d'évanescence [65]. L'antenne, pour avoir un couplage efficace, doit donc être placée près du plasma. Des interactions non-linéaires, dues aux gaines RF [34] déterminent alors souvent les limites opérationnelles des systèmes de chauffage. Ces effets délétères ont été observés sur différents tokamaks [40–42] sous différentes formes telles que des points chauds sur les antennes [36], de l'érosion [35], des modifications locales de la densité au voisinage des antennes par des cellules de convection [37]. Or l'efficacité du couplage de l'onde est principalement déterminée par la largeur de la zone d'évanescence. Comme les asservissements du point de fonctionnement de l'antenne sont conçus pour délivrer une puissance couplée au plasma constante, la tension appliquée à l'antenne est donc changée, ce qui va aussitôt modifier l'amplitude des gaines RF et ainsi de suite. De forts courants DC (Direct Current) ont également été mesurés quand les antennes sont actives [42]. Il a également été observé des interactions non-linéaires avec d'autres antennes [44]. Il est primordial que ces phénomènes soient compris afin que le système de chauffage soit parfaitement contrôlé et fiable à haute puissance sur de très longues durées dans un environnement métallique afin d'obtenir des plasmas stables satisfaisant aux conditions nécessaires aux réactions de fusion du deutérium et du tritium..

Une modélisation auto-cohérente des gaines RF dans un code de couplage de l'onde n'a encore jamais été réalisée. Chacun de ces deux problèmes est en soi-même ardu. Les objectifs de cette thèse étaient de modéliser séparément mais de façon compatible le couplage d'onde et la formation de gaines RF afin de les coupler au sein d'un unique code.

Les simulations ont été réalisées avec le logiciel commercial sous licence Comsol Multiphysics [166]. Ce choix a été fait avant mon arrivée en thèse afin d'éviter un fastidieux développement numérique qui n'était pas réalisable en 3 ans avec la main d'œuvre disponible tout en produisant une analyse physique pertinente d'observations expérimentales. L'aspect élément finis [77] a été un élément prépondérant dans le choix puisque qu'il permet d'inclure des géométries complexes en 3D. Le logiciel Comsol a aussi été choisi pour son aspect multi-physique qui en fait un outil disponible pour d'autres utilisateurs menant d'autres travaux en parallèle comme le problème de dissipation thermique dans l'antenne ou le calcul des contraintes mécaniques induites lors d'une disruption. Comme le problème à traiter présente en lui-même des aspects multi-physiques, ce choix s'est imposé de lui-même. Ici, les équations génériques à résoudre correspondent aux équations de Helmholtz et Poisson. L'interface graphique est également ergonomique et simple d'utilisation et permet aussi des sous-niveaux avec plus d'options. Les équations (ou leurs formes) nativement implémentées ne répondent pas cependant forcément à nos besoins. Cette limitation est interne à Comsol, ce qui réduit les choix possibles pour l'équation générique à résoudre. Il est cependant possible de les modifier légèrement dans les sous-niveaux. Ce choix présente cependant certaines contraintes, la principale étant le manque de contrôle du solveur permettant la résolution des équations. Les problèmes de convergence et de stabilité sont donc difficiles à maîtriser.

Des restrictions internes au CEA (Commissariat à l'énergie atomique et aux énergies alternatives) existent aussi. Le coût de la licence limite le nombre d'heures par utilisateur et le nombre de processeurs. Une autre limite est à caractère numérique est due à la taille mémoire disponible et le temps de calcul sur les stations déterminant directement le nombre d'éléments maximum pour les simulations (ces contraintes interviennent rapidement lors du passage en 3D).

Le plasma du tokamak de forme torique est déplié d'abord sous forme de cylindre qui est lui-même déplié sous forme de plan, afin d'éliminer des effets de courbure dans la direction toroidale et dans la direction poloidale. Cette hypothèse se justifie partiellement car la taille des domaines étudiés a des dimensions plus faibles que les caractéristiques géométriques du plasma de tokamak. La propagation d'onde est ici modélisée dans la Section à l'Ombre des Limiteurs (SOL) du plasma d'un tokamak, où les lignes de champs magnétiques sont ouvertes et connectées à des objets matériels. La propagation d'ondes aux fréquences considérées dans la SOL peut être décrite dans l'approximation plasma froid. Au contraire, le plasma central est bien confiné par des lignes de champs fermées. Dans ce cas le tenseur diélectrique, communément appelé tenseur de Stix [58], caractérisant les propriétés du plasma magnétisé, la réponse du courant plasma RF à un champ électrique RF est locale en espace et non-locale en temps. Pour une onde monochromatique sa modélisation passe par l'écriture d'un tenseur dépendant uniquement de la fréquence. Ce tenseur présente une très grande anisotropie. Cela provient simplement du libre déplacement des particules chargées dans la direction du champ magnétique. Il présente aussi une gyrotropie puisque certains éléments non diagonaux sont non nuls traduisant la présence de l'effet Hall. En présence de champ magnétique DC les particules chargées n'oscillent pas nécessairement dans une direction colinéaire au champ RF. Ce tenseur est également inhomogène traduisant la présence des gradients radiaux du champ magnétique et de la densité. Les éléments du tenseur peuvent donc changer de signe.

Dans ce milieu biréfringent, pour une même direction de propagation deux types d'ondes peuvent coexister simultanément [58]. Dans ce domaine de fréquences FCI, elles sont appelées onde rapide et onde lente. L'onde rapide est progressive alors que l'onde lente est régressive. Une onde est dite progressive quand sa vitesse de phase et sa vitesse de groupe sont colinéaires. L'onde rapide est évanescente en dessous d'une densité critique alors que l'onde lente l'est au-dessus d'une autre densité critique. Ces propriétés peuvent être facilement retrouvées à partie des relations de dispersions [22]. Dans les conditions de notre étude, l'onde rapide a une polarisation transverse électrique. Elle peut donc se propager transversalement au champ magnétique jusqu'au centre du plasma où par résonance cyclotronique avec les ions, l'énergie de l'onde est transmise au plasma. Les antennes FCI sont conçues en conséquence pour générer l'onde rapide avec des rubans de courant phasé verticaux. L'onde lente est générée de façon parasite du fait des courants induits sur la structure d'antenne et son environnement.

Une bonne compréhension dans l'ensemble de couplage d'onde est à présent acquise, du moins en régime linéaire en l'absence des interactions indirectes non-linéaires. Toutefois les manières de modéliser le couplage [30–32, 66] sont difficilement compatibles avec une étude détaillée et réaliste des gaines RF de manière auto-cohérente. La première étape de la thèse a été consacrée à trouver une manière nouvelle de modéliser le couplage d'ondes FCI au plasma qui puisse être compatible a priori avec un ajout futur de la modélisation de gaines RF [182]. Cette partie linéaire utilise les équations de Maxwell macroscopiques en présence d'un plasma froid magnétisé et d'objets de géométrie complexes.

L'effet des gaines RF étant supposé principalement lié à la présence de l'onde lente, nous sommes seulement intéressés au comportement du plasma au voisinage de l'antenne. A cause de ressources numériques limitées, la propagation d'ondes loin de l'antenne et l'absorption dans le chaud plasma de cœur sont généralement inclus seulement en tant que conditions aux limites. Pour ces raisons, seulement une fraction du volume du tokamak est simulée. Il devient nécessaire de trouver une manière d'absorber les ondes propagatives au frontière du domaine afin d'émuler l'absorption dans le cas où l'absorption par passage est quasi-totale. Sans ces conditions de bord, des réflexions d'origine numérique se produisent aux frontières du domaine. En dépit du fait que de nombreux scénarios de chauffage ont une faible absorption par passage, les études de conception d'antenne sont toutes réalisées en faisant l'hypothèse d'une forte absorption par passage. Différentes stratégies existent pour éviter la réflexion numérique. Des collisions artificielles peuvent être ajoutées [70]. Dans ce cas, la réflexion n'est pas contrôlée. La manière la plus courante est de traiter le plasma en tant que conditions aux limites avec des admittances de surface [66]. Cette méthode est capable de gérer des basses absorptions par passage. Elle réclame cependant un coût numérique important du fait de la nécessité de faire correspondre les modes dans le vide avec les modes du plasma. De plus les antennes sont face à un plasma tout en étant placées dans le vide. Or une gaine ne peut pas exister dans le vide. Une autre manière est de fabriquer une zone absorbante sans saut d'indice. La meilleure technique de ce point de vue est la technique des couches parfaitement adaptées (CPA plus connues sous l'acronyme anglais PML signifiant perfectly matched layer) [57]. C'est une méthode communément employée avec des milieux classiques afin de gérer les ondes sortantes propagatives sans réflexion numérique.

Pour appliquer ce type de conditions de bord, il faut savoir que les plasmas magnétisés ont des propriétés assez originales : anisotropie, gyrotropie, inhomogénéité, vitesses de groupe des deux modes avec des signes opposés. Il est possible de remplacer le plasma par un diélectrique équivalent [73, 74]. En conséquence de quoi, la contribution de l'un des deux modes est perdu. Les CPA ont notablement avancé au point de tenter de les appliquer aux

plasmas de fusion [150, 151]. Dans le domaine fréquentiel, le concept des CPA repose sur une transformation de l'espace des coordonnées réelles vers des coordonnées complexes tout en étirant l'espace afin d'amener ce qui peut être considéré comme l'infini à une distance finie. Cette distance représente la taille de la CPA. Cette transformation ne modifie pas les propriétés du plasma. La partie complexe de la transformation agit sur les ondes propagatives tandis que la partie réelle agit sur les ondes évanescentes. La transformation dans une direction dépend uniquement de la coordonnée dans cette direction. La magnitude de l'étirement permet de moduler le taux d'absorption de l'onde dans la CPA. La formulation trouvée des CPA est élégante et facile à implémenter. En effet la CPA peut être vue comme un matériau artificiel ayant des tenseurs diélectrique et perméabilité magnétique particuliers. Les champs dans les équations de Maxwell ne sont pas modifiés dans le plasma mais correspondent à des champs artificiels dans la CPA [157]. Des transformations de type polynômial ont été employées pour implémenter les CPA dans Comsol.

Cette technique a tout d'abord été testée sue des plasmas magnétisés homogènes dans une boîte rectangulaire pour lesquels une solution analytique avec des ondes planes existe afin de pouvoir comparer les prédictions analytiques pour le coefficient de réflexion avec les simulations. Le coefficient de réflexion est uniquement défini pour des ondes planes. Ces tests ont permis de vérifier des intuitions données par une formule analytique sur l'impact des paramètres des CPA et du plasma. Une grande CPA diminue la réflexion. Un conseil usuel est de choisir une CPA de la taille de l'ordre de la longueur d'onde pour satisfaire aux conditions d'application de la méthode WKB, nécessaire pour éviter les réflexions d'origine numérique liées à une trop grande variation de l'indice. Un polynôme d'ordre faible est préférable. Par la suite un ordre 2 est choisi. Les coefficients d'étirement doivent être préférablement choisi grands. Cependant de trop grandes valeurs induisent également des réflexions numériques du fait de l'inadéquation de l'étirement avec le maillage du fait d'une trop grande variation spatiale des champs sur la taille d'une maille de calcul.

Ces tests académiques ont aussi permis de mettre en évidence certaines limites des CPA. Les CPA peuvent être parfaitement sans réflexion seulement pour l'équation d'onde exacte. La discrétisation du problème en vue d'une résolution numérique induit un certain niveau de réflexion d'origine numérique. Un maillage raffiné permet de se rapprocher de cette limite sans réflexion. Il a aussi été identifié qu'une singularité ne doit pas être présente dans les CPA. Placer une CPA à proximité d'une coupure,où l'onde est réfléchie naturellement par le milieu, génère un surcout numérique qui peut être évité en éloignant la CPA. Il a été également vu qu'un niveau de réflexion acceptable peut être atteint dans les cas absorbés. La gyrotropie, mêlant différentes directions du fait d'éléments non-diagonaux, de augmente la réflexion ainsi que la présence de modes poloidaux. Un maillage avec une meilleure résolution permet de corriger ces effets. L'impossibilité de la coexistence simultanée d'une onde progressive et d'une onde régressive a été constatée. Cela est dû au choix du signe du coefficient d'étirement de la partie imaginaire de la transformation. Un choix doit donc être fait. Dans un tokamak, un gradient radial de densité existe. Or l'onde lente est évanescente au-delà d'une densité critique [58]. Le mieux est alors de laisser le plasma réfléchir naturellement l'onde lente et de concevoir la CPA pour l'onde rapide uniquement.

Dans les expériences, l'efficacité à laquelle est réalisée le couplage de la puissance véhiculée par l'onde au plasma est évaluée par la résistance de couplage. Une équivalence entre coefficients de réflexion et oscillations de la résistance de couplage dans les simulations a été établie analytiquement et vérifiée pour des ondes planes. Dans le cas d'une antenne rayonnant un spectre d'ondes planes, les oscillations de la résistance de couplage avec les paramètres de la CPA sont plus commodes à surveiller que le coefficient de réflexion strictement valable pour une onde plane.

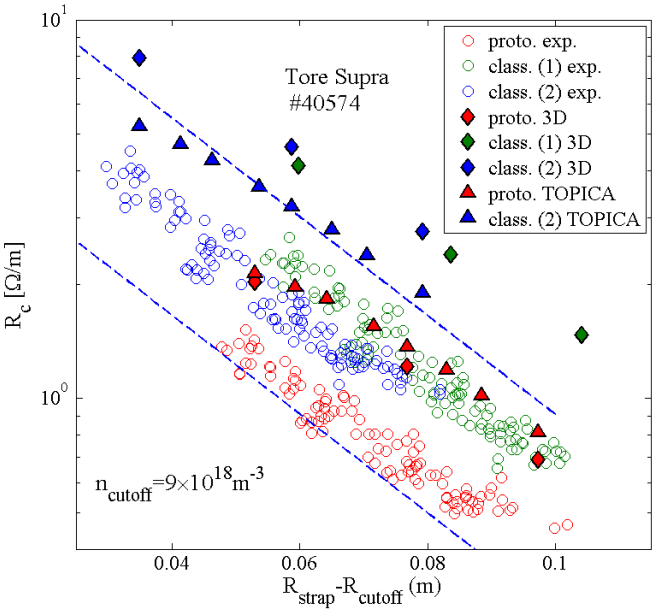

FIGURE C.4 – Résistance de couplage en fonction de la distance entre ruban de courant et densité de coupure pour le choc 40574. Valeurs expérimentales (cercles). Chacune des couleurs représente une des 3 antennes actives. Comparaison avec Comsol en 3D (diamants) et TOPICA (triangles). Les deux lignes bleues en pointillés montrent la sensibilité de la résistance de couplage envers un changement de ±2 cm de la distance ruban-coupure pour les résultats expérimentaux.

Les CPA ont ensuite été employées au sein d'un code modélisant le couplage de l'onde rapide au plasma avec les géométries d'antennes existantes et des profils de densité réalistes mesurés expérimentalement avec un réflectomètre. Liées aux capacités de calculs limitées des stations disponibles, des modèles simplifiés en 2D et en 3D d'antennes de Tore Supra avec moins de détails géométriques ont été implémentés dans Comsol. Plusieurs types de CPA sont nécessaires : une pour chaque combinaison de directions en 2D et en 3D. La CPA dans la direction radiale est ensuite placées de façon adéquate à une position où l'onde lente a été réfléchie par le plasma et à une position où les modes contribuant au rayonnement de l'antenne sont propagatifs. Les problèmes dus aux résonances ion-ion et hybride basse sont résolus respectivement par la présence d'une seule espèce d'ions dans le plasma et un saut de densité entre le vide et une densité supérieure à la densité de la résonance hybride basse. Pour économiser de la mémoire RAM, seulement la moitié de l'antenne est simulée en considérant une condition de symétrie ou d'antisymétrie pour l'autre côté. Un test en 2D a vérifié la validité de cette hypothèse valable si une symétrie existe. D'autres tests sur les paramètres des CPA ont vérifié que les oscillations de la résistance de couplage disparaissent quand la taille des CPA est suffisante.

Le résultats fournis par le code ont été comparés à des efficacités de couplage expérimentales avec des géométries 2D et 3D des antennes Tore Supra afin de connaître la sophistication nécessaire de la géométrie pour reproduire le plus fidèlement possible les résultats expérimentaux. L'épaisseur des rubans de courants est cruciale ainsi que la présence des objets passifs de la structure d'antenne générant des courants images. Les simulations reproduisent les tendances qualitatives mais surestiment toujours par un facteur de l'ordre de 2 l'efficacité de couplage en 3D par rapport aux expériences, comme illustré par la figure

1. Ce facteur diminue avec la sophistication de la description de la géométrie de l'antenne. Une comparaison avec le code référence de couplage FCI TOPICA [31] comportant une géométrie très réaliste donne également un facteur 1.5. Cette différence est expliquée par le plus grand raffinement de TOPICA allant de pair avec un maillage plus fin mais nécessitant un coût numérique plus important en mémoire et en temps de calcul. Ce facteur entre simulations et expériences est probablement dû à une incertitude sur la réelle largeur de la couche d'évanescence. L'influence de l'écran de Faraday causant un écrantage magnétique [32] a été aussi négligée.

Dans l'immédiat ce code est utilisable tel quel pour des calculs de couplage d'ondes. Il va être utilisé en complément de TOPICA pour concevoir de nouvelle antenne pour projet WEST, étant une transformation majeure de Tore Supra. Même sans atteindre le degré de sophistication de TOPICA, ce code de couplage peut donner un résultat pertinent en quelques minutes en 2D ou en quelques heures en 3D sur une simple station de travail alors que TOPICA réclame sur un supercalculateur plusieurs heures pour un cas. Un grand nombre d'études paramétriques très détaillées peut donc être envisagées pour identifier les domaines de paramètres pertinents avant de confirmer avec TOPICA. A terme, ce code a vocation à être intégré dans un code plus global modélisant de manière auto-cohérente couplage d'ondes et gaines RF [33, 34].

Parallèlement une description novatrice auto-cohérente des gaines RF modélisant la propagation d'ondes RF et la polarisation DC positive résultante du bord d'un plasma magnétisé a été développée durant cette thèse. La physique des gaines RF est un sujet extrêmement ardu étudié depuis plusieurs décennies. Ceci étant dû à un comportement hautement non-linéaire. La gaine classique/thermique [93] est une région dont l'épaisseur est très fine comparée aux dimensions caractéristiques du plasma. Cette zone tampon chargée positivement permet de préserver la quasi-neutralité du plasma se trouvant à l'intérieur d'une enveloppe matérielle. Lorsque la gaine est soumise à un potentiel RF d'amplitude supérieure au potentiel flottant, elles se mettent à osciller [103], permettant alors la génération d'un potentiel continu.

Des progrès ont été réalisés dans leur compréhension en complexifiant peu à peu leur description. La description des gaines RF nécessite plusieurs échelles de temps, plusieurs échelles de longueurs et la prise en compte de l'orientation du champ magnétique. Les première études ont d'abord porté sur la description de l'interaction entre les ondes RF entrant dans la gaine et le potentiel électrostatique. Cela a conduit au mécanisme de rectification des potentiels RF qui induit un phénomène d'auto-polarisation DC du plasma [114] modifiant ainsi les conditions de bord vu par l'onde. La propagation d'ondes RF modifie le plasma. Les modèles précédents négligeaient cependant la rétroaction du plasma sur la propagation des ondes rapides et lentes.

Pour éviter de mailler les gaines nécessitant des grilles très fines et donc un coût numérique prohibitif, des conditions aux limites de type gaine du point de vue RF ont été développées par Myra et D'Ippolito [53]. Des conditions similaires existent pour les plasmas de décharges non magnétisés. Ces conditions sont appliquées à la place de conditions métalliques sur les parois alors que strictement elles ne sont valides qu'à l'entrée de la gaine. Un essai a été fait afin d'inclure ce type de conditions dans TOPICA mais pour des gaines dans le vide [118]. Ces conditions considèrent dans l'approximation électrostatique que du point de vue des ondes RF à la fréquence fondamentale, la gaine de taille moyenne temporellement δ peut être vue comme un capacité plane avec un matériau de constante diélectrique ε_{sh} entre les plaques de la capacité. Le courant dans la gaine est principalement un courant de déplacement. Cette description est appropriée puisque la gaine est une région vidée d'électrons assimilable au vide. Cela a mis en évidence la propriété de capacité de la

gaine RF. Cette capacité varie de façon inversement proportionnelle à la taille de gaine et au potentiel électrostatique selon la loi de Child-Langmuir [102].

La description auto-cohérente des gaines RF plus proche des premiers principes a seulement commencé il y a quelques années. Il est supposé que les échelles de temps rapide et lente peuvent être séparées. Certaines propriétés clés sont connues : la redressement de courant RF en courant DC et la capacité. Du point du vue électrique, les gaines sont donc vues comme une diode et une capacité en parallèle. La diode permet de passer de l'échelle de temps rapide à l'échelle de temps lent. L'inverse est vrai pour la capacité.

Une modélisation auto-cohérente a été réalisée par Kohno [92] en combinant ces principes. La description de l'échelle de temps lente était cependant simpliste. En effet, les courants DC n'étaient pas autorisés puisque le tenseur de conductivité DC était nul. L'onde rapide et l'onde lente ont toutefois été prises en compte et l'orientation arbitraire du champ magnétique autorisait la conversion de mode.

Un projet similaire a été entrepris durant cette thèse [55]. Ce projet de modélisation auto-cohérente de la propagation d'onde et la polarisation DC du plasma de bord est appelé SSWICH (Self-consistent Waves and Sheaths for Ion Cylotron heating). La géométrie du modèle est une représentation simplifiée du voisinage d'une antenne FCI dans Tore Supra. La forme des objets est simplifiée afin que les lignes de champ magnétiques soient perpendiculaires à la surface des objets (i.e. parallèle à la normale de la surface) ou parallèle à la surface des objets. Cette restriction est due à l'écriture des conditions aux limites de ce modèle qui ne tolèrent pas pour le moment une orientation arbitraire de champ magnétique. Deux types de plasmas de bord sont considérés. La zone entre les limiteurs entourant l'antenne pour la protéger des flux provenant du plasma est appelée SOL privée. Les lignes de connexion étant courtes, la densité décroit plus rapidement que dans la SOL libre à l'extérieur des limiteurs, selon le modèle élaboré par Stangeby [93]. Les longueurs de connexion sont plus longues que dans la SOL privée. Seule l'onde lente est donc prise en compte. Toutefois, lorsque l'anisotropie du plasma est très grande, il peut être dit que le champ électrique parallèle à l'origine des gaines RF est principalement dû à l'onde lente. Le modèle est limité à deux dimensions dans le plan radial/toroidal pour l'instant à cause de limitations dans les ressources informatiques. La troisième dimension peut être cependant prise en compte au travers d'une procédure multi-2D où les positions verticales sont successivement changées. Cela nécessite cependant de négliger les dérivées poloidales (modèle en tranches). Cette hypothèse fut testée par la suite dans un contexte simplifié. Pour ces raisons, la version actuelle de SSWICH est appelée SSWICH-SW-2D (SSWICH pour l'onde lente en deux dimensions).

Le modèle actuel le plus développé durant cette thèse contient le minimum d'ingrédients physiques nécessaires pour une description auto-cohérente de la formation des gaines RF. Il est implémenté dans Comsol sous forme de modules couplés. Il s'agit d'une description fluide couplant trois quantités : le champ électrique parallèle, la tension de gaines oscillantes et le potentiel électrostatique du plasma. Chaque module décrit un phénomène traduisant une propriété de gaines RF.

Le premier module modélise la propagation d'ondes RF dans un plasma froid magnétisé. Pour l'instant, les conditions de type gaine sont implémentées pour les cas où les lignes de champ magnétique sont perpendiculaires à la paroi. Une carte de champ électrique est imposée à l'embouchure de l'antenne. Cette carte est produite dans TOPICA sans gaine avec une géométrie 3D. Le modèle est donc capable de prendre en compte des cartes de champs réalistes. Le couplage entre SSWICH et TOPICA n'est cependant pas auto-cohérent.

Un deuxième module calcule les tensions de gaines oscillantes à partir de la distribution

de champ électrique parallèle traitée comme terme source de cette tension de gaine. Ce module pourrait être amélioré pour consommer beaucoup moins de ressources puisque qu'une tension de gaine ne peut exister qu'au voisinage d'une paroi. A l'heure actuelle, la résolution se déroule dans tout le domaine. A la place ce module en 2D pourrait être remplacé par plusieurs modules en 1D le long des parois où une tension oscillante de gaine peut être évaluée.

Le troisième module modélise la conservation des courants DC dans le plasma. La condition aux limites sur les parois latérales est similaire à la caractéristique courant-tension d'une diode. Une tension redressée est cependant ajoutée par le processus de redressement. Tout se passe donc comme si les ondes RF polarisaient positivement la paroi. Cette auto-polarisation est ensuite diffusée à travers le plasma par un tenseur de conductivité DC non nul. Il a été montré qu'une asymétrie dans ces tensions redressées aux extrémités d'une même ligne de champ pouvait générer des courants parallèles du côté où la tension redressée est la plus importante vers l'autre côté [54]. Du transport de courant DC transversalement au champ magnétique est de plus possible ici à travers une conductivité DC perpendiculaire effective modélisant de manière phénoménologique des processus ayant une origine liée à la présence de la turbulence [113].

La non-linéarité du problème rend la convergence de la boucle auto-cohérente très difficile avec un schéma de type Newton-Raphson. Pour faciliter la convergence le point d'entrée dans la boucle a été changé en remplaçant la solution initiale nulle par une solution asymptotique valide dans le cas des gaines ayant une étendue spatiale importante existant à haute puissance, pertinent dans le cas de chauffage FCI. Dans ce cas, les conditions aux limites du module de propagation d'ondes RF sont simplifiées puisque la taille de gaine δ disparait. Il n'est plus nécessaire de connaître a priori la distribution des potentiels électrostatiques. Cela permet de donner un solide point de départ assez proche du point de convergence de la solution finale. Une comparaison de la solution asymptotique avec la solution de modèle couplé a été réalisée lors d'une étude en puissance en changeant la tension sur l'antenne.

Ce modèle a été couplé avec le code d'antenne TOPICA pour le cas des antennes Tore Supra de façon interprétative avec des simulations numériques afin d'éclaircir des observations inattendues sur un écran de Faraday dont le schéma électrique minimisait prétendument les gaines RF [48]. Un écran de Faraday est un objet monté sur l'antenne. Ces deux rôles sont d'agir comme un polariseur pour filtrer le champ électrique parallèle [139], responsable des gaines RF, et de protéger l'antenne des flux provenant du plasma [40].

Certaines observations clés ont pu être reproduites. Le motif poloidal du potentiel plasma DC est un résultat robuste qui dépend essentiellement du schéma électrique de l'antenne alors que le motif radial est très sensible à des paramètres très mal connus. La conductivité DC perpendiculaire, négligée jusqu'à présent, est un mécanisme possible de transport de courants DC dans la SOL en conjonction avec la polarisation DC asymétrique de tubes de flux. L'onde lente, évanescente ne peut donc pas atteindre la SOL libre. Par contre elle peut polariser la SOL privée par le processus de rectification. Le potentiel redressé est ensuite propagé à la SOL libre par transport radial de courants DC avec la conductivité DC perpendiculaire. Cela permet d'obtenir des potentiels électrostatiques significatifs sur la face extérieure des limiteurs où les sondes sont connectées durant les expériences [45]. Pour que ce mécanisme fonctionne, un niveau de turbulence plus élevé dans la SOL privée que dans la SOL libre est requis contrairement à [174]. En pratique la conductivité DC perpendiculaire est plus élevée dans la SOL privée.

Une comparaison de SSWICH avec un modèle analytique de la partie DC du problème

a mis en évidence un élargissement non linéaire des structures radiales du potentiel électrostatique avec l'amplitude du potentiel. Cela pourrait expliquer pourquoi les structures sont beaucoup plus larges avec l'écran de Faraday prototype où l'amplitude du potentiel est également plus importante. Ce modèle analytique permet aussi d'expliquer pourquoi l'élargissement est plus important dans l'ombre du limiteur que du côté du plasma.

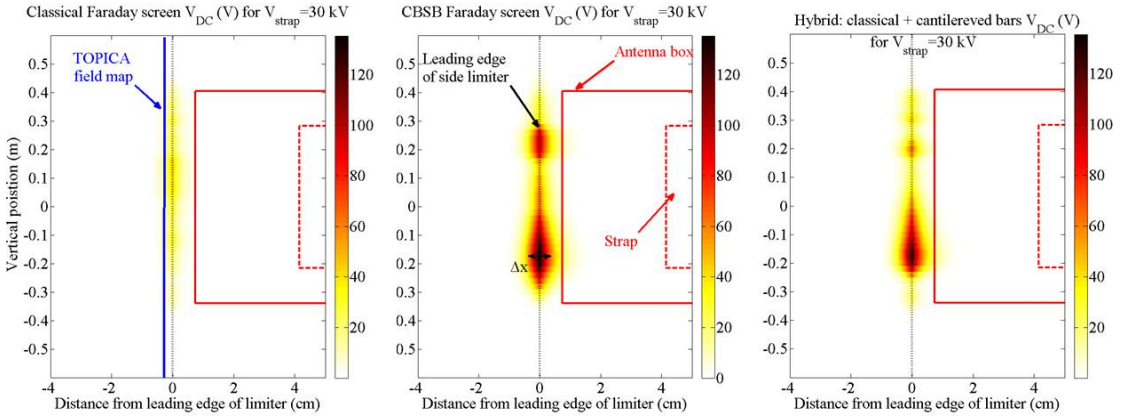

FIGURE C.5 – Carte 2D du potentiel électrostatique obtenu avec les données TOPICA pour un calcul effectué à l'aide de SSWICH sur la face extérieure du limiteur de l'antenne pour Tore Supra pour l'écran classique (gauche), écran prototype (milieu) et hybride écran classique avec barreaux coupés (droite).

Une comparaison relative des écrans de Faraday avec la procédure TOPICA/SSWICH a reproduit les facteurs relatifs entre les deux écrans pour les potentiels et les flux de chaleur parallèles. La figure 2 montre la comparaison. SSWICH indique que le concept de l'écran prototype amplifie l'amplitude des gaines RF en accord avec les expériences. Cela a pu être obtenu grâce aux cartes de champs réalistes associés à chaque géométrie.

Un autre test discriminant sur la sophistication de modèle est sa capacité à expliquer comment les deux extrémités d'une ligne de champ dans la SOL privée peuvent évoluer de manière différente lors d'une même étude. En changeant l'équilibre des tensions sur les deux rubans de courant des antennes Tore Supra, il fût observé qu'un côté s'échauffait plus pendant que l'autre refroidissait. Avec TOPICA/SSWICH, il a été évalué que la conductivité DC perpendiculaire avec des tensions de polarisation DC différentes des deux côtés peuvent modifier les flux de chaleur électronique.

Comme déjà mentionné, la sensibilité à des paramètres non mesurés précisément (ou mal mesurable) induisent une incertitude trop importante pour considérer que l'évaluation faite soit quantitative. Par exemple, les flux de chaleur très sensibles à la densité sont trouvés avec un facteur 2 par rapport aux expériences.

La position du maximum de la structure radiale du potentiel électrostatique pour l'écran prototype est mesurée avec les sondes dans l'ombre des limiteurs approximativement à 2 cm du bord d'attaque. Dans les simulations, le maximum est toujours évalué au niveau du bord d'attaque ainsi que sur l'autre écran et dans d'autres tokamaks [190].

Les simulations avec des géométries d'écran intermédiaires entre l'écran classique et l'écran prototype ont permises aussi d'identifier les barreaux coupés [48] comme étant l'élément de la conception électrique de l'écran responsable de l'augmentation de la magnitude des gaines RF sur l'écran de Faraday, comme illustré par la figure 2.

Les objectifs de cette thèse étaient de proposer un cadre commun dans lequel une

description sophistiquée des gaines RF dans le voisinage d'une antenne FCI puisse être construite de manière auto-cohérente avec le couplage d'onde. A cause de la complexité du problème, les ressources limitées et la durée limitée de trois ans de cette thèse, ces deux phénomènes n'ont pas pu être couplés. Par contre, ils ont été modélisés séparément avec des méthodes qui permettent d'envisager un couplage. Il en résulte le développement de deux codes durant cette thèse : un pour le couplage et un pour les gaines RF, avec de plus un projet réalisable puisque des comparaisons à l'expérience ont pu être réalisé.

Le code de couplage repose sur l'utilisation des CPA pour gérer les ondes sortantes propagatives sans réflexion. Les simulations ont été comparées avec des résultats expérimentaux et un autre code, TOPICA, qui utilise des matrices d'impédance de surface. Sa description est plus avancée et les géométries utilisables sont plus détaillées mais il requière beaucoup de ressources numériques. Ajouter une description réaliste des gaines RF y est très difficile. Au contraire le code de couplage développé durant cette thèse consomme poins de ressources. Ce code de couplage peut être amélioré en ajoutant un écran de Faraday à la géométrie ou en raffinant la géométrie avec plus de détails. La technique des CPA peut aussi évoluer en résolvant l'incompatibilité entre ondes propagatives progressives et régressives. Étendre la technique en prenant en compte la courbure du plasma est envisageable. Cependant les domaines doivent être convexes. Appliquer les CPA à d'autres domaines de fréquences du plasma est également possible et fait l'objet de collaborations. L'intérêt premier pour ce travail de thèse est de pouvoir y ajouter la description des gaines RF.

En dépit d'une description des gaines RF plus sophistiquée que par le passé, SSWICH est encore relativement simple, comparé à la globalité de la richesse de la physique de gaines RF. Des améliorations significatives peuvent être attendues. Jusqu'à présent seule l'onde lente est incluse. L'onde rapide pourrait être ajoutée, ce qui nécessite la présence de CPA. Cela permettrait de pouvoir prendre en compte la conversion de mode qui peut être un autre mécanisme pouvant expliquer des potentiels électrostatiques significatifs sur la face extérieure des limiteurs. Une autre amélioration serait d'inclure une équation sur la densité qui n'est pas invariante en présence de gradients de potentiel générant des cellules de convection. La géométrie peut être encore complexifiée pour apporter plus de réalisme. Cela va de pair avec une orientation arbitraire du champ magnétique et l'ajout de l'onde rapide. L'impact d'autres effets physiques comme l'ionisation, l'émission secondaire ou le sputtering devrait être également évalué au moins de manière séquentielle et de voir s'il existe des synergies. De ce point de vue, les travaux en physiques des décharges sont plus avancés [200]. Par exemple, l'émission électronique secondaire va avoir tendance a priori de diminuer le potentiel de gaine. Le sputtering va induire de l'ionisation dont l'influence devrait être évaluée. La situation est cependant plus aisée en physique des décharges du fait d'une meilleur connaissance des paramètres géométriques et du plasmas. L'excitation des gaines, bien que partageant les mêmes principes fondamentaux, est également différente. En effet un potentiel oscillant est imposé sur une électrode.

SSWICH couplé à TOPICA a déjà apporté des résultats significatifs et a permis de reproduire des observations expérimentales clés inexpliquées jusque là. Les simulations suggèrent que les barreaux coupés de l'écran prototype augmentent la magnitude des gaines RF. L'inclusion des limiteurs est également nécessaire [109]. Ils devront être pris en compte à l'avenir pour des calculs de conception et prédiction. Il ne faut pas cependant oublier que d'autres explications sont proposées [109] et devront être testées, en particulier les hypothèses associer à ces modélisations. Un autre aspect, qui a permis à ce travail d'être d'un grand intérêt, est l'existence de diagnostics, disponibles sur Tore Supra, permettant d'obtenir des cartes 2D du potentiel DC et de la thermographie infrarouge sur les antennes. Cela fait de Tore Supra une des machines les mieux équipés pour l'étude des gaines RF.

Les propriétés de la région privée de l'antenne reste cependant assez mystérieuse. Un manque relatif de données expérimentales sur la région privée de l'antenne est à constater et a causé des soucis pour l'avancée de la thèse. La tâche n'est pas aisée. Des effort supplémentaires devraient être fournis pour caractériser les gaines RF dans cette zone avec des données supplémentaires. Cela permettrait aussi de donner une meilleure interprétation au résultats actuellement obtenus. Dans cette perspective, de petites machines telles que ISHTAR ou ALINE dédiées à l'étude des gaines RF dans un environnement plus simple et plus facilement maîtrisable que la SOL d'un tokamak représente une excellente opportunité. Une comparaison des différents codes dans un cadre d'étude commun devrait également être entrepris pour identifier le degré de sophistication nécessaire ou des ingrédients à ajouter. Pour terminer, une attention particulière devrait être apportée à l'interface utilisateur du code car l'utilisation d'un code est fortement lié à sa clarté et sa capacité à être mis en œuvre facilement.

Résumé

Une bonne compréhension des interactions entre les ondes à la fréquence cyclotronique ionique (FCI) ($40 - 80$ MHz) et le plasma de bord est nécessaire pour injecter de façon fiable de fortes puissances dans un plasma de fusion en continu. Les objectifs de cette thèse étaient de modéliser séparément, avec Comsol Multiphysics, mais de façon compatible le couplage d'ondes et la formation de gaines radio-fréquences (RF), qui rétroagissent sur le couplage, pour aboutir à terme à une modélisation auto-cohérente.

Modéliser le couplage de l'onde rapide nécessite une description détaillée de l'antenne émettrice (2D ou 3D) et du plasma environnant par une approche pleine onde en plasma froid. L'absorption des ondes sortant du domaine de simulation est émulée par des couches parfaitement adaptées, rendues compatibles avec un tenseur diélectrique plasma. Les tendances expérimentales des résistances de couplage des antennes de Tore Supra sont qualitativement reproduites mais l'efficacité de couplage est surestimée probablement à cause d'une incertitude sur la largeur réelle de la couche d'évanescence des ondes FCI.

Parallèlement une description novatrice auto-cohérente, incluant les effets des gaines RF, de la propagation de l'onde lente et de la polarisation DC (Direct Current) résultante du bord d'un plasma magnétisé a été développée avec le minimum d'ingrédients physiques. Dans le cas des antennes Tore Supra, le couplage du code avec TOPICA a permis d'expliciter qualitativement certaines observations inattendues sur un écran de Faraday dont le schéma électrique visait à minimiser les gaines RF. Un transport de courants DC dans la SOL est apparu nécessaire pour expliquer les structures radiales des mesures. Les barreaux coupés sont les éléments de l'antenne responsable de l'augmentation du potentiel plasma.

Mots-clés : gaine, onde, auto-cohérent, conditions aux limites, plasma, magnétisé, polarisation, Tore Supra, antenne, FCI, modélisation, Comsol

Abstract

A correct understanding of the interactions between the edge plasma and the ion cyclotron (IC) waves ($40 - 80$ MHz) is needed to inject reliably large amount of power required for self-sustainable fusion plasmas. These thesis objectives were to model separately, with Comsol Multiphysics, but in compatible approaches the wave coupling and the RF sheath formation to anticipate development of a single code combining both.

Modelling of fast wave coupling requires a detailed description of the antenna (2D or 3D) and of the plasma environment by a full wave approach for a cold plasma. Absorption of outgoing waves is emulated by perfectly matched layers, rendered compatible with a plasma dielectric tensor. Experimental trends for the coupling resistance of the antennas of Tore Supra are qualitatively reproduced but the coupling efficiency is overestimated, most probably due to uncertainty of the real evanescence length of IC waves.

In parallel a novel self-consistent description, including RF sheaths, of the interplay between the cold wave propagation and DC (Direct Current) biasing of the magnetized edge plasma of a tokamak was developed with the minimum set of physics ingredients. For Tore Supra antenna cases, the code coupled with TOPICA allowed to unveil qualitatively some unexpected observations on the latest design of Tore Supra Faraday screens whose electrical design was supposed to minimize RF sheaths. From simulations, a DC current transport appears necessary to explain the radial structures of measurements. Cantilevered bars have been identified as the design element in the antenna structure enhancing the plasma potential.

Keywords: sheath, wave, self-consistent, boundary conditions, plasma, magnetized, polarization, Tore Supra, antenna, ICRH, modelling, Comsol